

**UNIVERSITATEA TEHNICĂ A MOLDOVEI**

Cu titlu de manuscris  
C.Z.U.: 622.361.16:621.798

**SIMINEL NIKITA**

**STRUCTURI CLAY-POLYMER NANOCOMPOSITE PENTRU  
AMBALAJE ALIMENTARE**

**253.06 Tehnologii biologice și chimice în industria alimentară**

Teză de doctor în științe inginerești

Conducător științific: STURZA Rodica  
m. cor. AȘM, dr. hab., prof. univ.

Comisia de îndrumare: GHENDOV-MOȘANU Aliona  
dr. hab., conf.univ.  
BAERLE Alexei  
dr.conf.univ.  
SIMINIUC Rodica  
dr.conf.univ.

Autor: SIMINEL Nikita

**CHIȘINĂU 2023**

© Siminel Nikita, 2023

# Contents

<b>ADNOTARE</b>	<b>x</b>
<b>ANNOTATION</b>	<b>xi</b>
<b>List of Figures</b>	<b>xii</b>
<b>List of Tables</b>	<b>xvii</b>
<b>List of Abbreviations</b>	<b>xix</b>
<b>Introducere</b>	<b>xx</b>
Actualitatea temei investigate . . . . .	xx
Descrierea situației în domeniul de cercetare . . . . .	xx
Scopul și obiectivele cercetării . . . . .	xxi
Obiectivele cercetării . . . . .	xxi
Ipoteza de cercetare . . . . .	xxii
Metodologia cercetării științifice . . . . .	xxii
Noutatea și originalitatea științifică . . . . .	xxii
Rezultatele științifice principale înaintate spre susținere . . . . .	xxiii
Aprobarea lucrării la foruri științifice naționale și internaționale . . .	xxiii
Publicații la tema tezei . . . . .	xxiii
Volumul și structura lucrării . . . . .	xxiii
<b>Introduction</b>	<b>xxiv</b>
The actuality of the investigated topic . . . . .	xxiv
Identification of research problems . . . . .	xxiv
Aim and objectives of the research . . . . .	xxv
Research objectives . . . . .	xxv
Research hypothesis . . . . .	xxv
Scientific research methodology . . . . .	xxvi
Scientific novelty and originality . . . . .	xxvi
Main scientific results submitted for defense . . . . .	xxvii
Approval of work at national and international scientific conferences .	xxvii
Publications on the thesis topic . . . . .	xxvii
Volume and structure of the work . . . . .	xxvii

<b>1</b>	<b>Clay Minerals and Clay-based Composites</b>	<b>1</b>
1.1	Structure and Properties of Clay Minerals . . . . .	1
1.1.1	The Elementary Structure: Sheets . . . . .	1
	The Tetrahedral Sheet . . . . .	1
	The Octahedral Sheet . . . . .	2
	Adjustments of the Tetrahedral and Octahedral Sheets . . . . .	4
	The Interlayer Sheet . . . . .	4
	The Layer Charge . . . . .	4
1.1.2	Common Patterns of Layer Structure . . . . .	6
	1:1 Structure: Kaolinite . . . . .	6
	2:1 Structure without an Interlayer Sheet: Talc and Pyrophyllite . . . . .	7
	2:1 Structure with an Interlayer Sheet: Smectite, Mica . . . . .	8
1.1.3	The Swelling of the Clay Interlayer . . . . .	10
	Clay-Water Interactions . . . . .	10
	Swelling Isotherms . . . . .	11
1.2	Polymer/Clay Nanocomposites . . . . .	12
1.2.1	Structure of Polymer/Clay Nanocomposites . . . . .	13
	Phase Separated Structure . . . . .	13
	Intercalated Structure . . . . .	13
	Exfoliated Structure . . . . .	14
1.2.2	Barrier Properties of Polymer/Clay Nanocomposites . . . . .	14
1.2.3	Preparation Techniques . . . . .	14
1.3	Chapter Summary . . . . .	15
<b>2</b>	<b>Methods and Computational Models</b>	<b>16</b>
2.1	Molecular Dynamics . . . . .	17
2.1.1	Initialisation . . . . .	21
	Equilibration . . . . .	21
2.1.2	The Integration Algorithm . . . . .	22
	Time Step . . . . .	23
2.1.3	Molecular Dynamics in Different Environments . . . . .	23
	Thermostat and Barostat . . . . .	24
2.1.4	Practical Aspects . . . . .	25
	Boundary Conditions and the Minimum Image Convention . . . . .	25
	Cutoff and Verlet Neighbour List . . . . .	25
	Ewald Summation . . . . .	26
	Partial Charges . . . . .	27
2.1.5	Measuring System Properties . . . . .	27
	Pair Distribution Function . . . . .	27
	Coordination Number . . . . .	28
	Hydration Energy . . . . .	28
	Mean Square Displacement . . . . .	28

	Radius of Gyration and Chain End-to-End Distance . . . . .	29
2.1.6	The DL_POLY Molecular Simulation Package . . . . .	29
2.1.7	Visualisation . . . . .	30
2.2	Force fields . . . . .	33
2.2.1	Force Field for Clays Minerals . . . . .	33
2.2.2	Force Field for Water . . . . .	37
2.2.3	Force Field for Organic Materials . . . . .	37
2.2.4	Deriving Cross Terms . . . . .	38
2.2.5	Validating the Potential Models . . . . .	38
2.3	Experimental Techniques . . . . .	40
2.3.1	X-ray Diffraction Analysis . . . . .	40
2.3.2	Thermogravimetric Analysis . . . . .	41
2.3.3	Thermogravimetry Mass Spectrometry Analysis . . . . .	42
2.4	Chapter Summary . . . . .	42
<b>3</b>	<b>Hydration of Clay Layers</b>	<b>43</b>
3.1	Simulation Details . . . . .	43
3.2	Results and Discussion . . . . .	46
3.2.1	Swelling and Hydration Energetics . . . . .	48
3.2.2	Interlayer Structure of Hydrated Montmorillonites . . . . .	52
	Atomic Density Profiles . . . . .	52
	Radial Distribution Functions . . . . .	60
3.2.3	Dynamics of the Interlayer . . . . .	61
3.3	Conclusions and Chapter Summary . . . . .	65
<b>4</b>	<b>Adsorption of Poly(ethylene) Glycol onto Montmorillonite</b>	<b>66</b>
4.1	Introduction . . . . .	66
4.2	The Exfoliated System . . . . .	68
4.2.1	Simulation Details . . . . .	68
4.2.2	Results and Discussion . . . . .	70
	Structure at the Interface . . . . .	70
	Mobility at the Interface . . . . .	73
4.2.3	Conclusions . . . . .	76
4.3	The Intercalated Systems . . . . .	77
4.3.1	Details of Experimental and Simulated Systems . . . . .	77
	Preparation of PEG200/Clay Films . . . . .	77
	Simulation Details . . . . .	77
4.3.2	Experimental Characterisation of PEG/water/Mt Intercalated Films	80
	Thermal Decomposition of PEG in Nanocomposites . . . . .	80
	Conclusions . . . . .	86
4.3.3	Molecular Simulation of PEG/clay Intercalated System . . . . .	87
	Swelling Energetics and Interlayer Structures . . . . .	87
	Preferential Intercalation of Poly(ethylene glycol) and its Morphologies	88

4.4	Conclusions and Chapter Summary . . . . .	92
<b>5</b>	<b>Synergistic Adsorption of Poly(ethylene glycol) and Amylose onto Montmorillonite</b>	<b>93</b>
5.1	Introduction . . . . .	93
5.2	Simulation Details . . . . .	94
5.3	Results and Discussion . . . . .	98
5.3.1	AML/Mt binary system . . . . .	98
	Thermodynamics of the Intercalation . . . . .	98
	Swelling Dynamics and Interlayer Structure . . . . .	99
	<b>General Conclusions</b>	<b>102</b>
	Recommendations . . . . .	103
	<b>Concluzii Generale</b>	<b>104</b>
	Recomandări . . . . .	105
	<b>Bibliography</b>	<b>106</b>
	<b>Appendices</b>	<b>118</b>
<b>A</b>	<b>Force Field Parameters</b>	<b>118</b>
A.1	TIP3P/Fs . . . . .	118
A.2	AMBER . . . . .	118
A.3	CLAYFF . . . . .	119
<b>B</b>	<b>Cross Terms</b>	<b>121</b>

# Cuprins

<b>ADNOTARE</b>	<b>x</b>
<b>ANNOTATION</b>	<b>xi</b>
<b>Lista abrevierilor</b>	<b>xvii</b>
<b>Introducere</b>	<b>xix</b>
Actualitatea temei investigate .....	xix
Descrierea situației în domeniul de cercetare .....	xix
Scopul și obiectivele cercetării .....	xx
Obiectivele cercetării .....	xx
Ipoteza de cercetare .....	xxi
Metodologia cercetării științifice .....	xxi
Noutatea și originalitatea științifică .....	xxi
Rezultatele științifice principale înaintate spre susținere .....	xxii
Aprobarea lucrării la foruri științifice naționale și internaționale .....	xxii
Publicații la tema tezei .....	xxii
Volumul și structura lucrării .....	xxii
<b>Introduction</b>	<b>xxiii</b>
The actuality of the investigated topic .....	xxiii
Identification of research problems .....	xxiii
Aim and objectives of the research .....	xxiv
Research objectives .....	xxiv
Research hypothesis .....	xxiv
Scientific research methodology .....	xxv
Scientific novelty and originality .....	xxv
Main scientific results submitted for defense .....	xxvi
Approval of work at national and international scientific conferences ...	xxvi
Publications on the thesis topic .....	xxvi
Volume and structure of the work .....	xxvi
<b>1 Minerale de argilă și structure din material compozite</b>	<b>1</b>
1.1 Structura și proprietățile mineralelor argiloase .....	1
1.1.1 Structura elementară: Strat .....	1
Stratul tetraedric .....	1

Stratul octaedric .....	2
Interacțiunea straturilor tetraedrice și octaedrice .....	4
Stratul intermediar .....	4
Încărcarea stratului .....	4
1.1.2 Modele comune ale structurii argiloase .....	5
Structură 1:1: Caolinit .....	5
Structură 2:1 Talc și pirofilită .....	6
Structură 2:1 Smectită, Mica .....	7
1.1.3 Gonflarea stratului intermediar de argilă .....	10
Interacțiuni argilă-apă .....	10
Izoterme de gonflare .....	11
Nanocompozite polimer/argilă .....	12
1.2.1 Structura nanocompozitelor polimer/argilă .....	13
Structură separate .....	13
Structură intercalată .....	13
Structura exfoliate .....	14
1.2.2 Proprietăți de barieră ale nanocompozitelor polimer/argilă .....	14
1.2.3 Metode de pregătire .....	14
1.3 Rezumatul capitolului .....	15
<b>2 Metode și modele de calcul</b> .....	<b>16</b>
2.1 Dinamica moleculară .....	17
2.1.1 Inițializare .....	21
Echilibrare .....	21
2.1.2 Algoritm de integrare .....	22
Timestep .....	23
2.1.3 Dinamica moleculară în medii diferite .....	23
Termostat și Barostat .....	24
2.1.4 Aspecte practice .....	25
Condiții la limită .....	25
Cutoff și Verlet Neighbour List .....	25
Ewald Summation .....	26
Sarcine parțiale .....	27
2.1.5 Proprietățile sistemului .....	27
Funcția de distribuție .....	27
Număr de coordonare .....	28
Energie de hidratare .....	28
Mean Square Displacement .....	28
Radius of Gyration and Chain End-to-End Distance .....	29
2.1.6 Pachetul de simulare moleculară DL_POLY .....	29
2.1.7 Vizualizare .....	30
2.2 Force fields .....	33
2.2.1 Force Field pentru minerale argiloase .....	33
2.2.2 Force Field pentru apă .....	37

2.2.3	Force Field pentru materiale organice .....	37
2.2.4	Deriving Cross Terms .....	38
2.2.5	Validating the Potential Models .....	38
2.3	Metode experimentale .....	40
2.3.1	Analiza difracției cu raze X .....	40
2.3.2	Analiza termogravimetrice .....	41
2.3.3	Termogravimetrie Analiza prin Mass spectrometrie .....	42
2.4	Rezumatul capitolului .....	42
<b>3</b>	<b>Hidratarea straturilor de argilă</b> .....	<b>43</b>
3.1	Detalii de simulare .....	43
3.2	Rezultate și discuții .....	46
3.2.1	Energetică de gonflare și hidratare .....	48
3.2.2	Structura interstratului .....	52
	Profiluri de densitate atomică .....	52
	Funcții de distribuție radial .....	60
3.2.3	Dinamica stratului intermediar .....	61
3.3	Concluzii și rezumatul capitolului .....	65
<b>4</b>	<b>Adsorbția de plastificant pe Montmorillonit</b> .....	<b>66</b>
4.1	Introducere .....	66
4.2	Sistemul exfoliat .....	68
4.2.1	Detalii de simulare .....	68
4.2.2	Rezultate și discuții .....	70
	Structura la interfață .....	70
	Mobilitate la interfață .....	73
4.2.3	Concluzii .....	76
4.3	Sistemele intercalate .....	77
4.3.1	Detalii ale sistemelor experimentale și simulate .....	77
	Prepararea PEG200/Clay nanocomposite .....	77
	Detalii de simulare .....	77
4.3.2	Caracterizarea experimentală a filmelor intercalate PEG/apă/Mt .....	80
	Descompunerea termică a PEG în nanocomposite .....	80
	Concluzii .....	86
4.3.3	Simularea moleculară a sistemului intercalat PEG/argilă .....	87
	Energetică de gonflare și structuri interstrat .....	87
	Intercalarea preferențială a plastificantului .....	88
4.4	Concluzii și rezumatul capitolului .....	92
<b>5</b>	<b>Adsorbția sinergică a plastificantului și a biopolimerilor pe Montmorillonit</b> .....	<b>93</b>
5.1	Introducere .....	93
5.2	Detalii de simulare .....	94
5.3	Rezultate și discuții .....	98
5.3.1	Sisteme binare AML/Mt .....	98

Termodinamica intercalării .....	98
Dinamica gonflării și structura interstratului .....	99
<b>General Conclusions</b>	<b>102</b>
Recommendations .....	103
<b>Concluzii Generale</b>	<b>104</b>
Recomandări .....	105
<b>Bibliografie</b>	<b>106</b>
<b>Anexe</b>	<b>118</b>
<b>A Force Field Parameters</b>	<b>118</b>
A.1 TIP3P/Fs .....	118
A.2 AMBER .....	118
A.3 CLAYFF .....	119
<b>B Cross Terms</b>	<b>121</b>

## ADNOTARE

**Siminel Nikita:** Structuri clay-polymer nanocompozite pentru ambalaje alimentare, teză de doctor în științe inginerești, Chișinău, 2023.

**Structura tezei:** Teza înaintată spre susținere a fost elaborată în cadrul Universității Tehnice a Moldovei, Chisinau 2023, este scrisă în limba engleză și constituită din introducere, cinci capitole, concluzii generale și recomandări, bibliografie din 166 titluri, 110 pagini de text de bază, 71 figuri și 7 tabele. Rezultatele obținute au fost publicate în 12 lucrări științifice, dintre care 3 articole în reviste internaționale, 2 articole în reviste naționale și 7 articole în lucrările unor conferințe naționale și internaționale.

**Cuvinte cheie:** Montmorillonit, biopolimeri, polietilenglicol (PEG), amiloză, nanocompozite, ambalaje biodegradabile.

**Scopul lucrării:** Dezvoltarea de noi biopolimeri pe bază de argile  $\text{Na}^+$ - și  $\text{Ca}^{2+}$ - montmorillonit, polietilenglicol și amiloză; elucidarea funcțiilor argilei, plastifiantului, amidonului și apei în formarea straturilor nanocompozite cu ajutorul tehnicilor experimentale și de simulare pe calculator (dinamica moleculară); cercetarea afinității reciproce a componentelor și structurilor formate asupra proprietăților de barieră și vitezei de transfer a vaporilor de apă în vederea stabilirii domeniului de aplicare a biopolimerilor în domeniul ambalajelor ecologice.

**Obiectivele cercetării:** Influența mărimii încărcăturii stratului de argilă și a distribuției acesteia asupra dinamicii de hidratare a mineralelor de argilă smectită în vederea dezvoltării și optimizării modelor potențiale de biopolimeri pe bază de polietilenglicol, amiloză și argile  $\text{Na}^+$ - și  $\text{Ca}^{2+}$ - montmorillonit. Investigații experimentale și computaționale ale structurii moleculare a nanocompozitelor în vederea îmbunătățirii proprietăților de barieră și mecanice ale straturilor depuse pe baza acestor materiale biodegradabile. Absorbția simultană a trei adsorbanti - apă, plastifiant și amidon, determinarea afinității relative a componentelor și a modului în care aceasta este influențată de mărimea, localizarea și densitatea încărcăturii stratului și de tipul de cationi schimbabili din stratul intermediar al argilei. Reducerea vitezei de transfer a vaporilor de apă prin spațiul interstrat în vederea creării barierei pentru diminuarea penetrării vaporilor de apă prin materialele de ambalaj destinate produselor alimentare uscate.

**Noutatea și originalitatea științifică:** Au fost elaborate structuri clay-polymerice care oferă o înțelegere cuprinzătoare a comportamentului nanocompozitelor polimer-argilă și a potențialelor lor aplicații ca acoperiri de barieră, ceea ce se așteaptă să aibă implicații semnificative pentru industria ambalajelor alimentare și pentru domeniile mai largi de știința materialelor și fizica polimerilor.

**Rezultatele principale:** S-a investigat efectul substituției izomorfe din  $\text{Na}^+$ - și  $\text{Ca}^{2+}$ - montmorillonita asupra dinamicii de absorbție și a stabilității că argile cu o cantitate mai mare de substituții tetraedrice ar putea avea o capacitate puternică de a reține moleculele de biopolimerice. S-a observat o structură ordonată a lanțurilor de polimeri PEG, paralelă cu suprafața argilei, în modelul de calcul al sistemului PEG/Mt. S-a demonstrat că filossilicații cu o sarcină de strat de  $< 0,4$  electroni pe unitate de formulă pot găzdui amidonul și oferi cea mai mare barieră la vaporii de apă în stratul de acoperire formulat. Pe baza datelor obținute, a fost creat un strat de barieră de 80 de ori mai eficient.

**Problema științifică principală solutionată:** dezvoltarea și optimizarea modelelor potențiale ale biopolimerilor (polietilenglicol și amiloză) și ale argilelor montmorillonite  $\text{Na}^+$  și  $\text{Ca}^{2+}$  pentru a înțelege structura moleculară a compozitelor bazate pe aceste materiale și pentru a îmbunătăți proprietățile de barieră ale acoperirilor formulate folosind aceste bio-compozite.

**Semnificatia teoretica si valoarea aplicativa a lucrării:** Pentru prima dată a fost dezvoltat și optimizat modele de biopolimeri pe bază de polietilenglicol, amiloză și argile  $\text{Na}^+$ - și  $\text{Ca}^{2+}$ -montmorillonit; studiile experimentale și computaționale au descris comportamentul de gonflare al mineralelor argiloase în prezența plastifiantului și afinitatea relativă a apei și polimerului pentru diferiți cationi; o combinație specifică de biopolimer și argilă a fost propusă, care a redus permeabilitatea stratului obținut cu un factor de 80. A fost obținut 1 brevet de invenție.

**Implementarea rezultatelor științifice:** Rezultatele cercetărilor au fost implementate în producția de acoperiri barieră © Cailar, produse la Barrcoat AB, Karlstad, Suedia

## ANNOTATION

**Siminel Nikita:** Nanocomposite clay-polymer structures for food packaging, PhD thesis in engineering sciences, Chisinau, 2023.

**Thesis structure:** The thesis submitted for defense was prepared at the Technical University of Moldova, Chisinau 2023, is written in English and consists of an introduction, five chapters, general conclusions and recommendations, bibliography of 166 titles, 110 pages of basic text, 71 figures and 7 tables. The results were published in 12 scientific papers, including 3 articles in international journals, 2 articles in national journals and 7 articles in national and international conference proceedings.

**Keywords:** Montmorillonite, biopolymers, polyethylene glycol (PEG), amylose, nanocomposites, biodegradable packaging.

**Aims:** Development of new biopolymers based on  $\text{Na}^+$ - and  $\text{Ca}^{2+}$ -montmorillonite clays, polyethylene glycol and amylose; elucidation of the functions of clay, plasticizer, starch and water in the formation of nanocomposite layers using experimental and computer simulation techniques (molecular dynamics); investigation of the mutual affinity of the formed components and structures on the barrier properties and water vapour transfer rate in order to determine the scope of application of the biopolymers in the field of eco-friendly packaging.

**Research objectives:** Influence of clay layer loading size and its distribution on hydration dynamics of smectite clay minerals in order to develop and optimize potential biopolymer modes based on polyethylene glycol, amylose and  $\text{Na}^+$ - and  $\text{Ca}^{2+}$ -montmorillonite clays. Experimental and computational investigations of the molecular structure of nanocomposites in order to improve the barrier and mechanical properties of layers deposited on the basis of these biodegradable materials. Simultaneous adsorption of three adsorbents - water, plasticiser and starch, determination of the relative affinity of the components and how this is influenced by the size, location and charge density of the layer and the type of exchangeable cations in the clay interlayer. Reducing the rate of water vapour transfer through the interlayer space to create a barrier to reduce water vapour penetration through dry food packaging materials.

**Scientific novelty and originality:** Clay-polymer structures have been developed that provide a comprehensive understanding of the behaviour of polymer-clay nanocomposites and their potential applications as barrier coatings, which is expected to have significant implications for the food packaging industry and the wider fields of materials science and polymer physics.

**Main results:** The effect of isomorphic substitution of  $\text{Na}^+$ - and  $\text{Ca}^{2+}$ - montmorillonite on adsorption dynamics was investigated and it was determined that clays with a higher amount of tetrahedral substitutions could have a strong ability to retain biopolymer molecules. An ordered structure of PEG polymer chains parallel to the clay surface was observed in the computational model of the PEG/Mt system. It was shown that phyllosilicates with a layer charge of  $< 0.4$  electrons per formula unit can accommodate starch and provide the highest barrier to water vapor in the formulated coating layer. Based on the data obtained, an 80-fold barrier layer was created.

**The main scientific problem solved:** Developed and optimized potential models of biopolymers (polyethylene glycol and amylose) and montmorillonite  $\text{Na}^+$  and  $\text{Ca}^{2+}$  clays to understand the molecular structure of composites based on these materials and to improve the barrier properties of coatings formulated using these bio-composites.

**Theoretical significance and applicative value of the work:** For the first time biopolymer models based on polyethylene glycol, amylose and  $\text{Na}^+$ - and  $\text{Ca}^{2+}$ -montmorillonite clays were developed and optimized; experimental and computational studies described the swelling behavior of clay minerals in the presence of plasticizer and the relative affinity of water and polymer for different cations; a specific combination of biopolymer and clay was proposed, which reduced the permeability of the obtained coating by a factor of 80. 1 patent was obtained.

**Implementation of scientific results:** The research results have been implemented in the production of barrier coatings © Cailar, produced at Barrcoat AB, Karlstad, Sweden.

# List of Figures

1.1	Diagrammatic sketch showing (a) a single silicon tetrahedron and (b) the sheet structure of silicon tetrahedra arranged in a hexagonal network . . . . .	2
1.2	Diagrammatic sketch showing (a) a single octahedron and (b) the sheet structure of octahedra . . . . .	3
1.3	Diagrammatic sketch of an octahedral sheet showing the <i>cis</i> - and <i>trans</i> - octahedron topologies. Adapted from [1] . . . . .	3
1.4	Diagrammatic sketch of (a) a trioctahedral sheet and (b) a dioctahedral with vacant sites. Adapted from [1] . . . . .	3
1.5	Deformation of tetrahedral sheet through rotation by $\alpha$ . Adapted from [2] . . . . .	5
1.6	Structure of the interlayer cation. (a) Theoretical - due to the position of cation in ditrigonal cavities of tetrahedral sheet of clay. (b) Distortions of the tetrahedral sheet brings the coordination from 12 down to 6. Adapted from [2] . . . . .	5
1.7	Isomorphic substitutions in tetrahedral and octahedral sheets with corresponding charge localisation. Adapted from [3] . . . . .	7
1.8	Schematic representation of the three aluminosilicate layer types. Adapted from [2] . . . . .	7
1.9	Diagrammatic sketch of the structure of smectite . . . . .	9
1.10	Variation in d-spacing of a Wyoming montmorillonite as a function of the water partial pressure ( $p/p_0$ ) [2] . . . . .	11
1.11	Adsorption of water by clays. a) Diagram showing that layers 2 and 3 can "nucleate" before completion of layer 1. b) Influence of saturation by different interlayer cations [2] . . . . .	12
1.12	Different types of composites arising from interaction of polymer and clay . . . . .	13
1.13	Schematic illustration of tortuosity for a diffusing penetrant introduced to exfoliated clay, layered in a polymer matrix . . . . .	14
2.1	Simulation methods for materials systems, with associated time- and length scales. Pictures are taken from * [4]; ** [5] . . . . .	16
2.2	Variation in bond energy with interatomic separation . . . . .	18
2.3	Empirical Potential Energy Functions . . . . .	19
2.4	The Lennard-Jones potential and its repulsive ( $\alpha r^{-12}$ ) and attractive ( $\alpha r^{-6}$ ) component . . . . .	31
2.5	A schematic representation of periodic boundary conditions in two dimensions . . . . .	31
2.6	The cutoff sphere and the Verlet neighbour list skin around a central particle. Particles 1-12 are in the list of central particle. Only particles 1-7 are within the range of the potential . . . . .	32

2.7	Schematic diagram of the series used in the Ewald summation method. The total Coulombic contribution to the non-bonded potential is calculated from two sums: the $U_{real}$ sum consists of point and smoothly varying screening charges (performed in real space); and the $U_{reciprocal}$ sum of smoothly varying screening background (adapted from [6]) . . . . .	32
2.8	Octahedral O–Al–O angle-bending potential that allows multiple equivalent minima [7]	35
2.9	Structure of (001) surface of pyrophyllite minimised by (a) CLAYFF model and (b) DFT ab-initio method. Colours: O red; Si yellow; H white [8] . . . . .	36
2.10	Comparison of adsorption energies for a dimethylether with a calcite surface calculated with potential model (squares) and DFT method (circles) [9]. The Ca–C separation is the distance between molecular carbon and the calcite surface . . . . .	39
2.11	(a) Schematic diagram of an X-ray diffractometer; (b) Bragg’s condition . . . . .	40
2.12	Thermogravimetric analysis (direct curve and derivative) of a saturated Na-montmorillonite showing two low temperature dehydration stages and the dehydroxylation stage [2] .	41
3.1	Construction and simulation flow of studied systems. Here a NaMt cell containing $30.5 \text{ H}_2\text{O} \cdot \text{uc}^{-1}$ in the interlayers (460 water molecules in each interlayer) is shown. Colours: Na blue; Si, yellow; Mg cyan; Al pink; O red; H white . . . . .	45
3.2	Basal spacing evolution of $104.4 \text{ meq NaMt}$ clay model containing $30.5 \text{ H}_2\text{O} \cdot \text{uc}^{-1}$ in the interlayers as a function of simulation time. First 250 ps of the equilibration process are shown . . . . .	46
3.3	Simulated and experimental basal spacing of (a) $113 \text{ meq NaMt}$ with octahedral charge and (b) $104 \text{ meq CaMt}$ with octahedral charge as a function of increasing water content <sup>a</sup> Experimental data for NaMt taken from Fu et al. [10]. Structural formula of the clay used in the experiment is $\text{Na}_{0.82}[\text{Al}_{3.1}\text{Fe}_{0.3}\text{Mg}_{0.6}][\text{Si}_{7.84}\text{Al}_{0.16}]\text{O}_{20}(\text{OH})_4$ <sup>b</sup> MD simulation data for CaMt taken from Teich-McGoldrick et al. [11] <sup>c</sup> Experimental data for octahedrally charged CaMt with net layer charge of $0.86 e \cdot \text{uc}^{-1}$ is taken from Sato et al. [12] . . . . .	47
3.4	$\text{Na}^+$ -montmorillonite swelling curves (left) and hydration energies (right) as a function of water content from MD simulations at 300 K and 1 atm . . . . .	48
3.5	$\text{Ca}^{2+}$ -montmorillonite swelling curves (top) and hydration energies (bottom) as a function of water content from MD simulations at 300 K and 1 atm . . . . .	51
3.6	Atomic density profiles from MD simulations at 300 K and 1 atm for NaMt of water ( $\text{O}_{\text{water}}$ ) and sodium ( $\text{Na}^+$ ). Left to right increases the water contents in the interlayer space of clay. Vertical dashed lines designate the planes of basal oxygens; $0 \text{ \AA}$ corresponds to the centre of the interlayer . . . . .	53
3.7	Snapshots of clay surface (yz plane) showing configurations of adsorbed calcium cations in (a) anhydrous, (b) inner-sphere (IS), and (c) outer-sphere (OS) water complexes on the $\text{Ca}^{2+}$ -montmorillonite. Colours as in Figure 3.1 . . . . .	54
3.8	Atomic density profiles of water hydrogen ( $\text{H}_{\text{water}}$ ) for NaMt (top) and CaMt (bottom). Left to right increases the water contents in the interlayer space of clay . . .	55
3.9	Spatial arrangements of cation and water molecules in the bilayer hydrate on the example of NaMt with a) octahedral charge (OS configuration) and b) tetrahedral charge (combination of IS and OS configuration) . . . . .	55

3.10	Distribution of water dipole showing major orientations of water molecules in the bilayer hydrate interlayer. Note that angle is with respect to the $c$ -axis vector which is perpendicular to clay layer . . . . .	56
3.11	Atomic density profiles from MD simulations at 300 K and 1 atm for CaMt of water ( $O_{\text{water}}$ ) and calcium ( $\text{Ca}^{2+}$ ). Left to right increases the water contents in the interlayer space of clay. Vertical dashed lines designate the planes of basal oxygens; 0 Å corresponds to the centre of the interlayer . . . . .	58
3.12	Evolution of the water and interlayer cation distribution in the 104.4 meq (a) NaMt and (b) CaMt clay interlayer during the swelling process. The graphs represent corresponding atomic density as a function of the layer spacing. Colour scheme: black–blue–red–yellow from lowest to highest density . . . . .	59
3.13	Radial distribution functions (solid lines) and the corresponding coordination numbers (dashed lines) for atomic pairs in the interlayer of 104.4 meq NaMt at different water content: $\text{Na}^+ - \text{O}_{\text{H}_2\text{O}}$ (top) and $\text{Na}^+ - \text{O}_{\text{basal}}$ (bottom) . . . . .	60
3.14	Radial distribution functions (solid lines) and the corresponding coordination numbers (dashed lines) for atomic pairs in the interlayer of 104.4 meq CaMt at different water content: $\text{Ca}^{2+} - \text{O}_{\text{H}_2\text{O}}$ (top) and $\text{Ca}^{2+} - \text{O}_{\text{basal}}$ (bottom) . . . . .	61
3.15	Overlapped final 500 ps snapshots from MD simulations at 300 K and 1 atm of 113.1 meq octahedrally charged NaMt and CaMt at different water contents. It can be observed that the overlapped trajectories of $\text{Ca}^{2+}$ and their accompanying coordinated water molecules are much denser than is the case for $\text{Na}^+$ . Colours are as follows: $\text{Na}^+$ blue, $\text{Ca}^{2+}$ cyan, $O_{\text{water}}$ red . . . . .	62
3.16	Diffusion as a function of cation concentration of cation (top) and $O_{\text{water}}$ (bottom) for a) NaMt; b) CaMt . . . . .	64
4.1	Graphical representation of poly(ethylene glycol) of $\text{MW} = 194.2 \text{ g}\cdot\text{mol}^{-1}$ (PEG200). Colours: C cyan; O red; H white . . . . .	67
4.2	Schematic representation of models of PEG intercalation in smectites: a) helical conformation of PEG chains [13]; b) double layer planar conformation [14] . . . . .	67
4.3	Energy minimisation of PEG200/Mt exfoliated system; After $\sim 600$ ps the structure is minimised. The total energy during equilibration of the bulk PEG200 system is shown in the inset . . . . .	69
4.4	Snapshot obtained after 1 ns of MD simulation at 300K following the annealing cycle for an exfoliated PEG/NaMt system. Colours: Na blue; Si yellow; Mg cyan; Al pink; C cyan; O red; H white . . . . .	69
4.5	Atomic density profiles of the exfoliated PEG/NaMt nanocomposite species from MD simulation at 300 K. Vertical dashed line designate the plane of basal oxygens . . . . .	71
4.6	Gaussian fits to end-to-end distributions of PEG200 chains forming different layers above the clay surface of 104 meq NaMt and in molten bulk (dashed line) . . . . .	72
4.7	Fragments of clay surface of exfoliated a) PEG200/NaMt and b) PEG200/CaMt systems showing structural conformations of PEG molecules in complexes with exchangeable cations in the 1 <sup>st</sup> layer. Distortion in measured and visual distances are due to 2D orthographic projection; cations can be positioned at different distances from the clay surfaces. Colours: Na blue; Ca purple; Si yellow; Mg cyan; Al pink; C cyan; O red; H white . . . . .	74

4.8	The mean square displacement (MSD) of the PEG carbon atoms as a function of time for exfoliated PEG/NaMt nanocomposite. MSD for PEG carbon atoms in the bulk system has been added for comparison purposes . . . . .	75
4.9	Basal spacing evolution of 104.4 meq NaMt clay with Oh charge containing 34 PEG200 and 180 H <sub>2</sub> O molecules in the interlayer as a function of simulation time. First 500 ps of the equilibration process are shown . . . . .	79
4.10	Simulation flow of the intercalated PEG200/Mt systems. Here a NaMt cell containing 34 PEG200 molecules (0.28 g <sub>PEG</sub> /g <sub>clay</sub> ) and 180 H <sub>2</sub> O molecules in each interlayer are shown. Colours as in Figure 4.4 . . . . .	79
4.11	XRD patterns of PEG/Mt with 0–27 wt% PEG200 for a) Na <sup>+</sup> -cloisite <sup>®</sup> and b) Ca <sup>2+</sup> -cloisite <sup>®</sup> . . . . .	81
4.12	Summary of d-spacing observed in the XRD traces of PEG200/Mt for a) Na <sup>+</sup> -cloisite <sup>®</sup> and b) Ca <sup>2+</sup> -cloisite <sup>®</sup> . . . . .	82
4.13	Thermograms of PEG200/Mt with different wt% PEG200 for a) Na <sup>+</sup> -cloisite <sup>®</sup> and b) Ca <sup>2+</sup> -cloisite <sup>®</sup> . . . . .	82
4.14	TGA negative derivatives of PEG200/Mt with different wt% PEG200 for a) Na <sup>+</sup> -cloisite <sup>®</sup> and b) Ca <sup>2+</sup> -cloisite <sup>®</sup> . . . . .	83
4.15	Weight losses associated with peaks 1–4 defined in Figure 4.14 for a) Na <sup>+</sup> -cloisite <sup>®</sup> and b) Ca <sup>2+</sup> -cloisite <sup>®</sup> . . . . .	83
4.16	Mass chromatograms obtained from volatile degradation products during the thermal degradation of a PEG200/NaMt mixture (27 wt%) . . . . .	85
4.17	Simulated and experimental basal spacing of (a) NaMt and (b) CaMt as a function of increasing poly(ethylene glycol) (PEG200) content in the interlayer. Amount of water in the interlayer was selected according to experimental findings presented in Table 4.5 . . . . .	88
4.18	Dehydrated NaMt with PEG of different MW . . . . .	88
4.19	Fragments of NaMt surface (110) of intercalated PEG200/Mt system showing predominant polymer conformations in (a) low charge clay – "crown" conformation and (b) high charge clay – "planar extended" conformation. Overlapped trajectories are shown over last 500 ps. Colours as in Figure 4.4 . . . . .	90
4.20	Influence of magnitude and location of clay layer charge on the interlayer conformations of PEG200 . . . . .	91
5.1	Graphical representation of amylose of MW = 828.7 g·mol <sup>-1</sup> (PEG200). Colours: C cyan; O red; H white . . . . .	94
5.2	Snapshots of equilibrated configurations of AML/clay intercalated nanocomposite obtained in NPT and NVT MD simulations. NaMt interlayer consists of 8 AML molecules (0.28 g <sub>AML</sub> /g <sub>clay</sub> ) and 100 H <sub>2</sub> O molecules (0.07 g <sub>H<sub>2</sub>O</sub> /g <sub>clay</sub> ). Colours: Na blue; Si yellow; Mg cyan; Al pink; C cyan; O red; H white . . . . .	96
5.3	Snapshots of equilibrated configurations of AML-PEG/clay intercalated nanocomposite obtained in NPT and NVT MD simulations. NaMt interlayer consists of 4 AML molecules (0.14 g <sub>AML</sub> /g <sub>clay</sub> ), 26 PEG200 molecules (0.21 g <sub>PEG200</sub> /g <sub>clay</sub> ) and 100 H <sub>2</sub> O molecules (0.07 g <sub>H<sub>2</sub>O</sub> /g <sub>clay</sub> ). Colours as in Figure 5.2 . . . . .	96

5.4	Starting structure of the AML/Mt adsorption model. The centre of mass of single amylose molecule in aqueous environment is positioned at 3.5 Å above the clay surface. Colours as in the Figure 5.2 . . . . .	97
5.5	Definition of the AML orientations of te AML/Mt adsorption model. The amylose molecule is oriented along (a) [010] and (b) [100]. Colours as in Figure 5.3 . . . . .	97
5.6	Variation of (a) $E_{\text{int}}$ and (b) RMSD of amylose molecules adsorbed onto 104.4 meq NaMt with octahedral charge in different adsorption configurations with simulation time . . . . .	98
5.7	Simulation cell for molecular dynamics simulations of amorphous AML containing 100 molecules. Simulation was equilibrated at 300 K and 1 atm . . . . .	99
5.8	Swelling curves of NaMt as a function of amylose content in the interlayer from MD simulations at 300 K and 1 atm. Swelling curves are shown for clays with various net charge distribution . . . . .	99
5.9	Swelling curves of CaMt as a function of amylose content in the interlayer from MD simulations at 300 K and 1 atm. Swelling curves are shown for clays with various net charge distribution . . . . .	100
5.10	Atomic density profiles from MD simulations at 300 K and 1 atm for AML/NaMt nanocomposite. Amylose backbone carbon atom ( $C_{\text{AML}}$ - blue curve), sodium ( $\text{Na}^+$ - black curve) and water ( $\text{O}_{\text{water}}$ - red curve). Left to right increases clay layer charge	101

# List of Tables

2.1	CLAYFF and DFT pyrophyllite bond lengths (Å) compared with experiment [15]	36
2.2	Comparison of adsorption energies of organic molecules onto pyrophyllite and Na-montmorillonite using both the potential model and DFT methods [8]	39
3.1	Cation exchange capacity, charge location and chemical composition of clay models used in this work	44
3.2	Values of basal d-spacing (Å) from MD simulations at 300 K and 1 atm for Montmorillonite with various layer charge as a function of interlayer cation compared with previous experiments	49
3.3	Experimental ion radii and hydration enthalpies, and water contents for 1W and 2W states in montmorillonite from MD simulations at 300 K and 1 atm	50
3.4	Percentage of exchangeable cations in each adsorption layer of bilayer hydrate interlayers ( $\sim 0.2 \text{ g}_{\text{water}}/\text{g}_{\text{clay}}$ )	56
3.5	Cation and water diffusion coefficients ( $10^{-10} \text{ m}^2\text{s}^{-1}$ ) from MD simulations and experiment for a CEC of 104 meq	63
4.1	Distribution of carbon PEG200 atoms as a function of centre of mass location of polymer chain. The results presented for Mt with 104.4 meq layer charge in the octahedral sheet	71
4.2	Root mean end-to-end distance and radius of gyration of PEG200 chains in different layers of exfoliated PEG/Mt systems. Values for montmorillonites with CEC of 104.4 meq are presented	73
4.3	Diffusion coefficients ( $(10^{-10} \text{ m}^2\text{s}^{-1})$ ) of PEG200 chains carbons in each layer as a function of clay layer charge location and exchangeable cation. Values for clay with CEC of 104.4 meq are shown	75
4.4	Diffusion coefficients ( $(10^{-10} \text{ m}^2\text{s}^{-1})$ ) of exchangeable cations located in the first polymer layer of the exfoliated PEG/Mt system. Values for clays with different charge distribution are presented	75
4.5	Amounts of PEG and water adsorbed from water solution on NaMt and CaMt, as determined by thermogravimetry	86
4.6	Root mean end-to-end distance of PEG200 chains intercalated in various clays	90
4.7	Percentage of characteristic polymer conformations in bilayer polymer structure ( $0.25 \text{ g}_{\text{PEG200}}/\text{g}_{\text{clay}}$ )	91
A.1	Nonbond Parameters for the TIP3P/Fs Force Field [16]	118
A.2	Bond Parameters for the TIP3P/Fs Force Field [16]	118
A.3	Nonbond Parameters for AMBER Force Field [17]	118

A.4	Bond Parameters for the AMBER Force Field [17]	119
A.5	Nonbond Parameters for the CLAYFF Force Field [18]	120
A.6	Bond Parameters for the CLAYFF Force Field [18]	120
B.1	Nonbonded Cross Terms for water–organic, water–mineral and organic–mineral interactions	121

## List of Abbreviations

<b>MD</b>	Molecular Dynamics
<b>DFT</b>	Density Function Theory
<b>PBC</b>	Periodic Boundary Conditions
<b>CG</b>	Coarse-grained
<b>LJ</b>	Lennard-Jones
<b>FF</b>	Force Field
<b>ESP</b>	Electrostatic Potential
<b>RDF</b>	Radial Distribution Function
<b>CN</b>	Coordination Number
<b>ADP</b>	Atomic Density Profile
<b>MSD</b>	Mean Square Displacement
<b>TGA</b>	Thermogravimetric Analysis
<b>TGMS</b>	Thermogravimetric Mass Spectroscopy Analysis
<b>XRD</b>	X-ray Diffraction
<b>NMR</b>	Nuclear magnetic resonance spectroscopy
<b>RH</b>	Relative Humidity
<b>MW</b>	Molecular Weight
<b>pph</b>	Parts per Hundred
<b>FWHM</b>	Full Width at Half Maximum
<b>Mt</b>	Montmorillonite
<b>NaMt</b>	Na <sup>+</sup> -montmorillonite
<b>CaMt</b>	Ca <sup>2+</sup> -montmorillonite
<b>CEC</b>	Cation Exchange Capacity
<b>Oh</b>	Octahedral Charge
<b>Th</b>	Tetrahedral Charge
<b>Oh/Th</b>	Mixed Octahedral and Tetrahedral Charge
<b>IS</b>	Inner-sphere Adsorption complex
<b>OS</b>	Outer-sphere Adsorption complex
<b>PEG</b>	Poly(ethylene glycol)
<b>PEO</b>	Poly(ethylene oxide)
<b>AML</b>	Amylose
<b>OW</b>	Oxygen of H <sub>2</sub> O molecule
<b>HW</b>	Hydrogen of H <sub>2</sub> O molecule
<b>1W</b>	Monolayer Hydrate
<b>2W</b>	Bilayer Hydrate
<b>3W</b>	Three Layer Hydrate

# Introducere

## Actualitatea temei investigate

În ultimele decenii, producția și utilizarea materialelor plastice derivate din petrol a crescut enorm, ceea ce creează probleme atât din punct de vedere ecologic, cât și din punct de vedere economic. Industria europeană a ambalajelor are o valoare de piață de aproximativ 80 miliarde EUR și crește în fiecare an [19]. Ambalarea alimentelor este un concept important pentru satisfacția consumatorului și pentru creșterea duratei de valabilitate a produselor alimentare. Introducerea de noi materiale de ambalare a alimentelor a devenit o tendință emergentă în ultimii ani, care s-ar putea datora în principal poluării mediului cauzată de ambalajele din plastic și pentru a reduce risipa alimentară. Astfel de noțiuni, precum ambalaje biodegradabile, biocompatibile, ecologice devin din ce în ce mai frecvente în literatura de specialitate referitoare la ambalaje. Reglementările stricte privind reciclarea deșeurilor și reciclabilitatea materialelor au determinat cerințe ale industriei alimentare pentru materiale de ambalare mai eficiente.

Necesitatea materialelor biodegradabile regenerabile capabile să înlocuiască materialele plastice convenționale, obținute pe bază de petrol, prezintă un domeniu de cercetare în plină dezvoltare, deoarece oferă un avantaj important pentru creșterea durabilă a industriei ambalajelor. Dintre acestea, amidonul este unul dintre cele mai promițătoare materiale biopolimerice, deoarece este regenerabil, are un preț scăzut, este complet biodegradabil și, cel mai important, este permis pentru contactul cu alimentele [20–23]. Acoperirile pe hârtie, realizate pe bază de amidon, au demonstrat o ameliorare a proprietăților de barieră, reducând rata de transmitere a vaporilor de apă (WVTR) de la 800 g/m<sup>2</sup>.zi pentru hârtia netratată la 400 g/m<sup>2</sup>.zi [19]. Poli(etilenglicolul) a fost utilizat ca plastifiant pentru amidon, care este cunoscut ca fiind fragil.

Argilele sunt un alt material promițător. Mineralele argiloase sunt o familie de materiale stratificate. Acestea reprezintă o clasă de materiale anizotrope, ai căror atomi intrastrat sunt fixați prin legături chimice, în timp ce atomii din straturile adiacente interacționează prin forțe fizice (Van der Waals). Argilele au o gamă largă de utilizări potențiale și actuale, datorate, în parte, capacității lor de a intercala o varietate largă de specii anorganice și organice. În comparație cu materialele de umplutură tradiționale obținute pe bază de materiale compozite, aceasta oferă avantaje substanțiale în ceea ce privește creșterea aderenței. Actualmente materialele compozite pe bază de argilă au numeroase aplicații comerciale și potențiale în sectoarele de exploatare a automobilelor, îngrijirii sănătății, acoperirilor și pigmentilor, precum și în alte industrii [24]. Încorporarea nanoargilelor în matricea ambalajelor îmbunătățește proprietățile mecanice și de barieră și în același timp prelungeste biodegradarea materialului de ambalare [25]. Caracteristicile mecanice, de barieră și antibacteriene ale materialelor de ambalare a alimentelor pe bază de nanoargilă pot fi ameliorate semnificativ [26].

## Descrierea situației în domeniul de cercetare

Argilele ne gonflabile sunt utilizate în tehnologiile tradiționale de acoperire a hârtiei, deoarece acestea exercită un efect nesemnificativ asupra proprietăților reologice ale straturilor formate [27]. Analiza proprietăților peliculelor de montmorilonit și amidon și a demonstrat, prin teste de migrare, că acestea pot fi utilizate în mod satisfăcător în conformitate cu reglementările europene actuale privind ambalajele biodegradabile [21]. S-a demonstrat, că prezența argilelor gonflabile în cadrul unei matrici polimerice influențează semnificativ proprietățile de barieră ale acoperirilor formulate [10]. Această abordare a fost dezvoltată în continuare de Breen et al. [19], care au identificat o combinație specială de

argile, amidon și plastifiant pentru a forma un înveliș durabil. Acoperirile aplicate pe substratul de hârtie au prezentat un WVTR remarcabil de  $10 \text{ g/m}^2 \cdot \text{zi}$  [19, 23], fiind competitive cu unele dintre latexurile convenționale [28].

Tehnicile experimentale actuale dețin o performanță limitată pentru investigarea materialelor stratificate intercalate. Doar rareori se obțin cristale suficient de mari pentru determinarea structurală completă prin difracție de raze X convențională [29]. Difracția pulberilor cu raze X (PXRD) oferă unele informații cu privire la structura globală a materialului (de exemplu, distanța dintre straturi), dar, în general, structurile intercalate de argilă se caracterizează prin absența unei ordini semnificative cu rază lungă de acțiune. Aranjamentele dintre straturi (de exemplu, orientarea adsorbitului) pot fi uneori estimate din distanța dintre straturi determinată prin măsurători PXRD, dar, de obicei, acestea sunt estimări bazate pe dimensiunile moleculare presupuse ale adsorbantului [30]. De asemenea, nu este posibil să se stabilească dacă amidonul sau plastifiantul pot concura în mod eficient cu apa pentru un loc în sfera de coordonare primară a cationilor din galerie. De asemenea, este foarte dificil sau imposibil să se identifice ce proporție de amidon și de plastifiant este prezentă în galeria argilelor care se umflă [31].

Din cauza acestor limitări, a crescut interesul pentru utilizarea metodelor de calcul pentru studierea acestor solide stratificate și a intercalatelor. Rolul acestor cercetări constă în putea raționalizarea experimentelor și prezicerea proprietățile fizice și chimice ale structurilor nanocompozite formate. Dezvoltarea tehnicilor de simulare pe calculator aplicate materialelor argiloase oferă o perspectivă asupra structurii, dinamicii și reactivității sistemelor de argilă polimerică [32, 33].

### **Scopul și obiectivele cercetării**

Scopul lucrării a constat în dezvoltarea de noi biodegradabile nanocompozite pe bază de argile  $\text{Na}^+$ - și  $\text{Ca}^{2+}$ -montmorillonit, polietilenglicol și amiloză; elucidarea funcțiilor argilei, plastifiantului, amidonului și apei în formarea straturilor nanocompozite cu ajutorul tehnicilor experimentale și de simulare pe calculator (dinamica moleculară); cercetarea afinității reciproce a componentelor și structurilor formate asupra proprietăților de barieră și vitezei de transfer a vaporilor de apă în vederea stabilirii domeniului de aplicare a biopolimerilor în domeniul ambalajelor ecologice.

### **Obiectivele cercetării**

1. Influența mărimii încărcăturii stratului de argilă și a distribuției acesteia asupra dinamicii de hidratare a mineralelor de argilă smectită în vederea dezvoltării și optimizării modelor potențiale de biopolimeri pe bază de polietilenglicol, amiloză și argile  $\text{Na}^+$ - și  $\text{Ca}^{2+}$ -montmorillonit.
2. Investigații experimentale și computaționale ale structurii moleculare a nanocompozitelor în vederea îmbunătățirii proprietăților de barieră și mecanice ale straturilor depuse pe baza acestor materiale biodegradabile.
3. Absorbția simultană a trei adsorbanti - apă, plastifiant și amidon, determinarea afinității relative a componentelor și a modului în care aceasta este influențată de mărimea, localizarea și densitatea încărcăturii stratului și de tipul de cationi schimbabili din stratul intermediar al argilei.
4. Reducerea vitezei de transfer a vaporilor de apă prin spațiul interstrat în vederea creării barierei pentru diminuarea penetrării vaporilor de apă prin materialele de ambalaj destinate produselor alimentare uscate.

## **Ipoteza de cercetare**

Ambalajele pentru alimente uscate realizate din nanocompozite pe bază de argile  $\text{Na}^+$  și  $\text{Ca}^{2+}$ -montmorillonit, polietilenglicol și amiloză, utilizate drept acoperiri de barieră, ar contribui la reducerea permeabilității oxigenului și umidității, majorând astfel termenul de păstrare pe raft a produselor și ar diminua impactul asupra mediului prin substituirea materialelor de ambalaje derivate din petrol.

## **Metodologia cercetării științifice**

Suportul teoretic al tezei a fost realizat în baza analizei pentru literatura de specialitate accesată din bibliotecile electronice ale Universității Tehnice a Moldovei, precum și prin accesarea online a revistelor științifice și a articolelor cu acces liber.

În vederea realizării obiectivelor tezei de doctorat au fost utilizate următoarele metode de cercetare:

- ▷ Metoda dinamicii moleculare (MD). Această tehnică a fost aplicată pentru a calcula proprietățile de echilibru și transport ale sistemelor multicomponente prin utilizarea legilor mecanicii clasice și cuantice, cu integrarea acestor efecte.
- ▷ Metoda simulării tridimensionale Ewald, aplicată pentru calcularea interacțiunilor Van-deer-Waals și rezolvarea problemei convergenței lente.
- ▷ Software DL\_POLY, pentru simulările MD ale macromoleculelor, polimerilor, sistemelor ionice și soluțiilor pe un computer paralel cu memorie distribuită.
- ▷ Modelul CLAYFF, care a fost aplicat pentru a simula parametrii cristalografici realiști ai mineralelor argiloase.
- ▷ Metoda difracției cu raze X, aplicată pentru studiul comportamentului de gonflare asociat al nanocompozitelor polimer/argilă.
- ▷ Analiza termogravimetrică (TGA), care a fost utilizată pentru cercetarea distribuției apei și materialelor organice în probele compozite polimer/argilă.
- ▷ Spectrometria de masă cu termogravimetrie (TGMS), care a fost aplicată pentru determinarea compoziției elementare a probelor examinate.

## **Noutatea și originalitatea științifică**

- ▷ Teza de doctorat se axează pe dezvoltarea de modele potențiale pentru simularea pe calculator a nanocompozitelor polimer-argilă, care este o zonă de cercetare relativ nouă și promițătoare.
- ▷ Studiul explorează efectul diferitelor parametri, inclusiv concentrația de argilă, matricea polimerică și condițiile de prelucrare asupra proprietăților nanocompozitelor, ceea ce oferă informații valoroase despre comportamentul acestor materiale.
- ▷ Teza investighează aplicarea nanocompozite drept acoperiri de barieră pentru aplicații de ambalaje alimentare, care este o zonă de cercetare relativ nouă și emergentă, cu perspectivă de a îmbunătăți semnificativ durata de raft a produselor ambalate și de a reduce risipa alimentară.
- ▷ Lucrarea utilizează o combinație de metode teoretice și experimentale, care prezintă o abordare inovatoare și permite o înțelegere mai cuprinzătoare a comportamentului nanocompozitelor polimer-argilă.
- ▷ Rezultatele cercetării demonstrează eficacitatea acestor nanocompozite utilizate drept acoperiri de barieră pentru materiale de ambalare, cum ar fi reducerea permeabilității oxigenului și umidității, ceea ce reprezintă o contribuție semnificativă pentru domeniul ambalajelor alimentare.

- ▷ În ansamblu, teza oferă o înțelegere cuprinzătoare a comportamentului nanocompozitelor biopolimer-argilă și a potențialelor lor aplicații drept acoperiri de barieră, ceea ce preconizează atât implicații semnificative pentru industria ambalajelor alimentare, cât și pentru domeniile știința materialelor și fizica polimerilor.

**Problema științifică rezolvată** constă în dezvoltarea și optimizarea modelelor de biopolimeri pe bază de polietilenglicol, amiloză și argile  $\text{Na}^+$  și  $\text{Ca}^{2+}$ -montmorillonit, descrierea comportamentului de umflare, afinitatea apei și biopolimerului pentru diferiți cationi; reducerea permeabilității și îmbunătățirea proprietăților de barieră ale acoperirilor formulate pe bază de aceste bio-compozite.

### **Rezultatele științifice principale înaintate spre susținere**

1. Modelele au fost adaptate pentru a simula sistemele terțiare argilă-PEG-biopolimer-apă cu o cantitate optimă de materiale.
2. Efectul dezordinii rotaționale asupra parametrilor energetici și structurali ai argilei.
3. Efectul substituției izomorfe din  $\text{Na}^+$ - și  $\text{Ca}^{2+}$ -montmorillonit asupra dinamicii de absorbție și distribuție a moleculelor de apă și polimer intercalate.
4. Efectul cationilor schimbabili și al substituției izomorfe asupra formării nanocompozitelor argilă-biopolimer.
5. Distribuția biopolimerilor în nanocompozite, influența suprafeței minerale și a structurii argilei asupra interfeței polimer-argilă.
6. Formarea structurilor de barieră și reducerea permeabilității gazelor și vaporilor.
7. Afinitatea argilelor față de biopolimeri în funcție de structura și sarcina de strat.
8. Structura și proprietățile de barieră ale nanocompozitelor în funcție de masa moleculară și natura biopolimerului.

### **Aprobarea lucrării la foruri științifice naționale și internaționale**

Principalele rezultate ale tezei de doctorat au fost prezentate la 12 conferințe naționale și internaționale: Conferința internațională „MTFI”, Chisinau (2022); Simpozion Internațional “European Kesterite Hybrid Workshop”, Copenhagen, Denmark (2022); Conferința internațională “Materials Science and Condensed Matter Physics”, Chisinau (2018); Conferința Internațională “Clay Science and Technology Euroclay”, Edinburgh (2018); Simpozion “CCP5 Annual Meeting”, Edgmond (2017); Conferința Studenților, Masteranzilor și Doctoranzilor (2020, 2022); Conferința Internațională “Nanotechnologies and Biomedical Engineering” (2021, 2023); Conferința internațională “TIM”, Timisoara (2021, 2022), Romania; The XXV International Scientific Conference of Young Scientists and Specialists (2021), Almaty, Republic of Kazakhstan.

### **Publicații la tema tezei**

Rezultatele principale ale cercetării au fost publicate în 12 lucrări științifice, dintre care 3 articole în reviste internaționale, 2 articole în reviste naționale și 7 articole și teze în lucrările unor conferințe naționale și internaționale, a căror listă completă este prezentată la sfârșitul acestui Rezumat și în Anexa I a tezei.

### **Volumul și structura lucrării**

Teza este constituită din introducere, cinci capitole, concluzii generale și recomandări, bibliografie din 166 titluri, 110 pagini de text de bază, 71 figuri și 7 tabele.

**Cuvinte-cheie:** *montmorillonit, biopolimeri, polyetilenglycol (PEG), amiloză, nanocompozite, ambalaje biodegradabile.*

## Introduction

### The actuality of the investigated topic

In recent decades, the production and use of petroleum-derived plastics has increased enormously, creating both environmental and economic problems. The European packaging industry has a market value of around €80 billion and is growing every year [19]. Food packaging is an important concept for consumer satisfaction and increasing the shelf life of food products. The introduction of new food packaging materials has become an emerging trend in recent years, which may be mainly due to environmental pollution caused by plastic packaging and to reduce food waste. Such notions as biodegradable, biocompatible, eco-friendly packaging are becoming increasingly common in the packaging literature. Strict regulations on waste recycling and material recyclability have led to demands from the food industry for more eco-efficient packaging materials.

The search for renewable biodegradable materials to replace conventional oil-based plastics is a fast growing research area as it provides an important factor for sustainable growth of the packaging industry. Amongst these, starch is one of the most promising biopolymer materials, because it is renewable, low in price, fully biodegradable and, rather importantly, approved for food contact [20–23]. Starch based paper barrier coatings showed improvement of barrier properties when applied alone on paper reducing the Water Vapour Transmission Rate (WVTR) from 800 g/m<sup>2</sup>.day for untreated paper down to 400 g/m<sup>2</sup>.day for paper coated with starch and poly(ethylene glycol) [19]. Poly(ethylene glycol) was utilised as a plasticiser for starch which is notoriously brittle.

Clays are another promising material. Clay minerals are a family of layered materials; they are a class of highly anisotropic materials comprising sheets whose atoms are linked by chemical bonds, whereas the atoms of adjacent sheets interact by non-bonded, physical forces. Clays have a wide range of potential and actual uses due, in part, to their ability to intercalate a variety of inorganic and organic species. Compared with traditional fillers in composite materials, this offers substantial advantages in terms of improved adhesion and lower required filler volume to achieve equivalent properties. As such, clay containing composite materials have numerous current and potential commercial applications in the automotive, packaging, health care, coatings and pigments sectors, as well as in other industries [24]. Incorporation of nanoclays into the packaging matrix improves mechanical and barrier properties [25]. The mechanical, barrier and antibacterial characteristics of nanoclay based food packaging materials can be significantly improved [26].

### Identification of research problems

Non-swelling clays have been used in traditional paper coating technologies for many years because these exert the least effect on the rheological properties of a formulated coating [27]. However, Avella et al. [21] studied the properties of starch-montmorillonite films and showed, through migration tests, that the films could be satisfactorily used according to the current European regulations for biodegradable packaging. The presence of swelling clays within a polymer matrix has been shown to significantly influence the barrier properties of formulated coatings. This approach was further developed by Breen et al. [19] who identified a particular combination of swelling clays, starch and plasticiser to form a sustainable coating that exhibited a remarkable WVTR of 10 g/m<sup>2</sup>.d [19,23] when applied on the paper substrate, and is already competitive with some of the conventional latexes [28].

Unfortunately, current experimental techniques are lacking in performance for the investigation of intercalated layered materials. Only rarely are sufficiently large crystals for full structural determination by conventional X-ray diffraction obtained. Powder X-ray diffraction (PXRD) gives some indication of the bulk structure of the material (e.g., the spacing between layers), but in general clay intercalates are characterised by the absence of significant long-range order [29]. Interlayer arrangements (e.g., orientation of the adsorbate) may, however, sometimes be estimated from the interlayer spacing determined from PXRD measurements, but usually these are estimations based on the assumed molecular dimensions of the adsorbent [30]. Likewise, it is not possible to ascertain whether the starch or the plasticiser can compete effectively with water for a place in the primary coordination sphere of the gallery cations. It is also very difficult or impossible to identify what proportion of starch and plasticiser is present in the gallery of the swelling clays [31].

Because of these limitations, interest in the use of computational methods for studying these layered solids and their intercalates has increased in order that observed physical and chemical properties may be rationalised and predicted [32,33]. The development of computer simulation techniques applied to clay materials provides insight into the structure, dynamics and reactivity of polymer clay systems.

### **Aim and objectives of the research**

The aim of the work was to develop new biodegradable composites based on Na<sup>+</sup>- and Ca<sup>2+</sup>-montmorillonite clays, polyethylene glycol and amylose; to elucidate the functions of clay, plasticizer, starch and water in the formation of nanocomposite layers using experimental and computer simulation techniques (Molecular Dynamics); Investigation of the mutual affinity of the components and structures formed on the barrier properties and water vapour transfer rate in order to determine the scope of application of biopolymers in the field of eco-friendly packaging.

### **Research objectives**

1. Influence of clay layer loading size and its distribution on the hydration dynamics of smectite clay minerals in order to develop and optimize potential biopolymer modes based on polyethylene glycol, amylose and Na<sup>+</sup>- and Ca<sup>2+</sup>-montmorillonite clays.
2. Experimental and computational investigations of the molecular structure of nanocomposites in order to improve the barrier and mechanical properties of layers deposited on the basis of these biodegradable materials.
3. Simultaneous adsorption of three adsorbents - water, plasticiser and starch, determination of the relative affinity of the components and how this is influenced by the size, location and charge density of the layer and the type of exchangeable cations in the clay interlayer.
4. Reducing the rate of water vapour transfer through the interlayer space to create a barrier to reduce water vapour penetration through dry food packaging materials.

### **Research hypothesis**

Dry food packaging made of nanocomposites based on Na<sup>+</sup>- and Ca<sup>2+</sup>-montmorillonite clays, polyethylene glycol and amylose, used as barrier coatings, would contribute to reduc-

ing oxygen and moisture permeability, thereby increasing shelf-life of products, and would decrease environmental impact by substituting petroleum-derived packaging materials.

### **Scientific research methodology**

The theoretical support of the thesis was made based on the analysis of the literature accessed from the electronic libraries of the Technical University of Moldova, as well as by accessing online scientific journals and open access articles.

In order to achieve the objectives of the thesis the following research methods were used:

- ▷ Molecular Dynamics (MD) method. This technique was applied to calculate the equilibrium and transport properties of multicomponent systems using the laws of classical and quantum mechanics, with the integration of these effects.
- ▷ The three-dimensional Ewald simulation method applied to calculate Van-deer-Waals interactions and solve the slow convergence problem.
- ▷ DL\_POLY software, for MD simulations of macromolecules, polymers, ionic systems and solutions on a parallel computer with distributed memory.
- ▷ CLAYFF model, which was applied to simulate realistic crystallographic parameters of clay minerals.
- ▷ X-ray diffraction method, applied to study the associated swelling behaviour of polymer/clay nanocomposites.
- ▷ Thermogravimetric analysis (TGA), which was used to investigate the distribution of water and organic materials in polymer/clay composite samples.
- ▷ Thermogravimetric mass spectrometry (TGMS), which was applied to determine the elemental composition of the examined samples.

### **Scientific novelty and originality**

- ▷ The PhD thesis focuses on the development of potential models for computer simulation of polymer-clay nanocomposites, which is a relatively new and promising area of research.
- ▷ The study explores the effect of different parameters including clay concentration, polymer matrix and processing conditions on the properties of nanocomposites, which provides valuable insights into the behaviour of these materials.
- ▷ The thesis investigates the application of nanocomposites as barrier coatings for food packaging applications, which is a relatively new and emerging area of research with the prospect of significantly improving the shelf life of packaged products and reducing food waste.
- ▷ The paper uses a combination of theoretical and experimental methods, which presents an innovative approach and enables a more comprehensive understanding of the behaviour of polymer-clay nanocomposites.
- ▷ The research results demonstrate the effectiveness of these nanocomposites used as barrier coatings for packaging materials, such as reducing oxygen and moisture permeability, which is a significant contribution to the field of food packaging.
- ▷ Overall, the thesis provides a comprehensive understanding of the behaviour of biopolymer-clay nanocomposites and their potential applications as barrier coatings, which predicts both significant implications for the food packaging industry and the fields of materials science and polymer physics.

**The scientific problem solved** consists in developing and optimizing biopolymer models based on polyethylene glycol, amylose and Na<sup>+</sup> and Ca<sup>2+</sup>-montmorillonite clays, describing the swelling behavior, water and biopolymer affinity for different cations; reducing the permeability and improving the barrier properties of coatings formulated based on these bio-composites.

### **Main scientific results submitted for defense**

1. The models were adapted to simulate tertiary clay-PEG-biopolymer-water systems with an optimal amount of materials.
2. Effect of rotational disorder on energetic and structural parameters of clay.
3. Effect of isomorphic substitution of Na<sup>+</sup>- and Ca<sup>2+</sup>-montmorillonite on the adsorption and distribution dynamics of intercalated water and polymer molecules.
4. Effect of exchangeable cations and isomorphic substitution on the formation of clay-biopolymer nanocomposites.
5. Distribution of biopolymers in nanocomposites, influence of mineral surface and clay structure on polymer-clay interface.
6. Formation of barrier structures and reduction of gas and vapour permeability.
7. Affinity of clays towards biopolymers as a function of layer structure and charge.
8. Structure and barrier properties of nanocomposites as a function of molecular weight and nature of biopolymer.

### **Approval of work at national and international scientific conferences**

The main results of the PhD thesis have been presented at 12 national and international conferences: International Conference "MTFI", Chisinau (2022); International Symposium "European Kesterite Hybrid Workshop", Copenhagen, Denmark (2022); International Conference "Materials Science and Condensed Matter Physics", Chisinau (2018); International Conference "Clay Science and Technology Euroclay", Edinburgh (2018); Symposium "CCP5 Annual Meeting", Edgmond (2017); Conference of Students, Masters and PhD Students (2020, 2022); International Conference "Nanotechnologies and Biomedical Engineering" (2021, 2023); International Conference "TIM", Timisoara (2021, 2022), Romania; The XXV International Scientific Conference of Young Scientists and Specialists (2021), Almaty, Republic of Kazakhstan.

### **Publications on the thesis topic**

The main results of the research have been published in 12 scientific papers, including 3 articles in international journals, 2 articles in national journals and 7 articles and theses in the proceedings of national and international conferences, the full list of which is presented at the end of this Abstract and in Appendix I of the thesis.

### **Volume and structure of the work**

The thesis consists of an introduction, five chapters, general conclusions and recommendations, a bibliography of 166 titles, 110 pages of basic text, 71 figures and 7 tables.

**Keywords:** *montmorillonite, biopolymers, polyethylene glycol (PEG), amylose, nanocomposites, biodegradable packaging.*

# 1 Clay Minerals and Clay-based Composites

Clay minerals belong to the phyllosilicate group (from the Greek “phylon” – leaf, and from the Latin “silic” – flint) [2]. Silicates are the largest class of minerals present on Earth, comprising the majority of its crust and representing 30% of all minerals [1].

Clay minerals are highly anisotropic materials. They are made up of sheets whose atoms are linked by chemical bonds, whereas the atoms of adjacent sheets interact by non-bonded, physical forces. Clays have been known and utilised for a very long time and are indispensable in modern living, through their use in porcelain, bricks, tiles and sanitary ware [34]. However, their range of applications is not limited to these arenas. Clay minerals are extensively used as filamentous components in polymer based composites, partly because of their ability to intercalate a variety of inorganic and organic species. Compared with traditional composite materials, this results in a unique property-enhancement profile in terms of various mechanical, barrier, and fire resistance behaviours and requires lower filler volumes (5 wt% clay vs 20–40 wt% traditional filler) to achieve equivalent outcomes [19]. As a result, clay materials have numerous current and potential commercial applications in the automotive, packaging, health care, coatings and pigments sectors, as well as in other industries [24].

It is important to understand why the micro structure of clay minerals affords them such compositional and metrological diversity. To this end, this chapter focuses on introducing the fundamentals of common clay crystal structures. Firstly, a summary is given of common clay structures and properties. Following this, the field of clay-polymer nanocomposites is reviewed.

## 1.1 Structure and Properties of Clay Minerals

Whilst the structures of phyllosilicate minerals appear to be very complex, the various levels of organisation they adopt can be characterised via two basic features:

- ▷ Sheets: These are formed by three ionic planes within which each cation is framed by  $O^{2-}$  or  $(OH)^-$  anions. Examples are tetrahedral, octahedral and interlayer sheets;
- ▷ Layers: These result from the association of several sheets, e.g. linkage of tetrahedral and octahedral sheets in various combinations. Some phyllosilicates also include an interlayer sheet.

Three types of coordination determine the elementary “building blocks” that make up various sheets within the clay crystal structure [2]:

- ▷ 4-fold coordination ( $SiO_4^{4-}$  or  $AlO_4^{5-}$  tetrahedra);
- ▷ 6-fold coordination (octahedra occupied by a tri- or divalent cation:  $Al^{3+}$ ,  $Fe^{3+}$ ,  $Mg^{2+}$ ,  $Fe^{2+}$ );
- ▷ 12-fold coordination (dodecahedra occupied by an exchangeable cation:  $Na^+$ ,  $K^+$ ,  $Ca^{2+}$ ).

### 1.1.1 The Elementary Structure: Sheets

#### The Tetrahedral Sheet

The basic unit of a phyllosilicate tetrahedral sheet (Th) is the silicon tetrahedron  $SiO_4^{4-}$  (Fig. 1.1(a)). Each tetrahedron consists of a  $Si^{4+}$  cation, coordinated to four oxygen  $O^{2-}$  anions, such that the total bond energy of each oxygen is equal to two silicon–oxygen bonds. This condition causes adjacent tetrahedra to link up by sharing the oxygens on the triangular



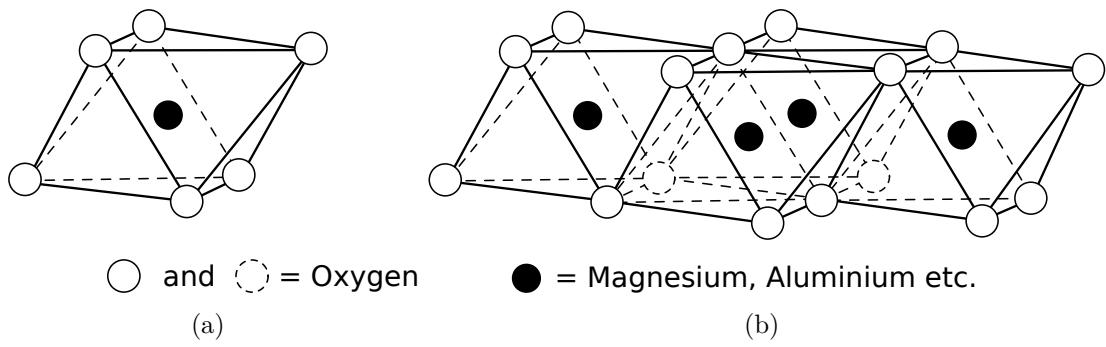


Figure 1.2: Diagrammatic sketch showing (a) a single octahedron and (b) the sheet structure of octahedra

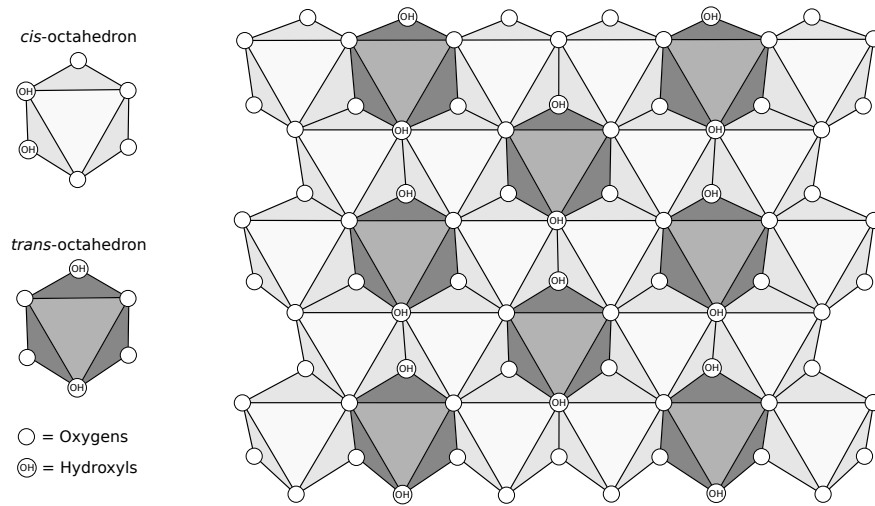


Figure 1.3: Diagrammatic sketch of an octahedral sheet showing the *cis*- and *trans*-octahedron topologies. Adapted from [1]

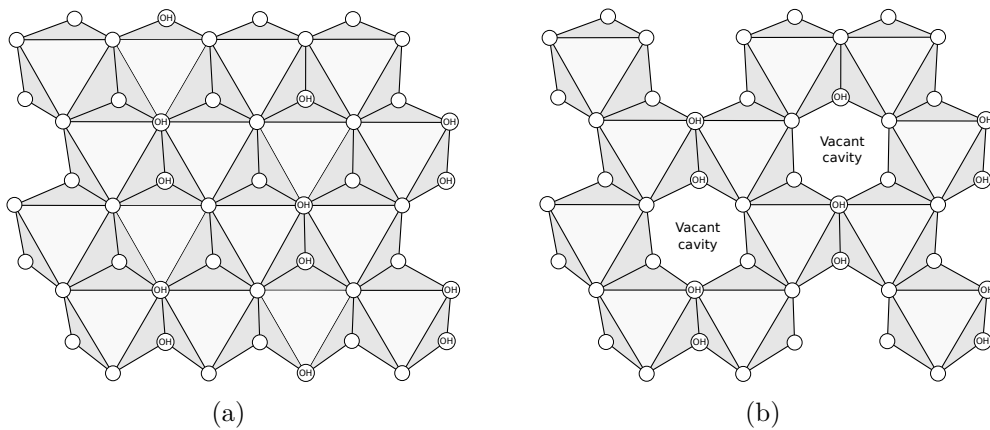


Figure 1.4: Diagrammatic sketch of (a) a trioctahedral sheet and (b) a dioctahedral sheet with vacant sites. Adapted from [1]

are filled.

The edge-length of each octahedron corresponds to the ionic diameter of the appropriate  $O^{2-}$  or  $OH^-$  anions. Bond lengths can be approximated as the sum of the ionic radii of the octahedral cation ( $Mg^{2+} - 0.86 \text{ \AA}$ ,  $Al^{3+} - 0.68 \text{ \AA}$  [2]) and of the 6-fold coordination  $O^{2-}$  anion ( $1.26 \text{ \AA}$  [2]). Therefore, the edge length of a Mg octahedron is calculated as  $3.00 \text{ \AA}$  and that of an Al octahedron as  $2.74 \text{ \AA}$  while their respective thickness are  $2.45$  and  $2.24 \text{ \AA}$  [2]. Resultant lattice parameters are  $a \times b = 5.44 \times 9.43 \text{ \AA}$  for trioctahedral sheet and  $a \times b = 4.98 \times 8.64 \text{ \AA}$  for dioctahedral sheets.

### Adjustments of the Tetrahedral and Octahedral Sheets

The theoretical unit cell dimensions calculated for the tetrahedral sheet ( $5.35 \times 9.27 \text{ \AA}$ ) and for the tri- and dioctahedral sheets ( $5.44 \times 9.43 \text{ \AA}$  and  $4.98 \times 8.64 \text{ \AA}$  respectively) differ significantly [2]. These mismatches lead to deformations in one or both sheets and deviations from ideal hexagonal symmetry when they are combined into layers [2, 36]. Layer distortion usually follows three different mechanisms [35]: (i) the rotation of adjacent tetrahedra about axes perpendicular to the basal plane as evaluated by the angle  $\alpha$  (Fig. 1.5); (ii) the increase in thickness of the tetrahedral sheet, thereby reducing the edge length of individual tetrahedra; (iii) the tilting of the tetrahedral basal oxygen plane. As a consequence of these distortions, the symmetry of the tetrahedral sheet becomes ditrigonal.

Di- and trioctahedral sheets undergo deformations as well. Individual octahedra experience elongation of their edges and become asymmetrical. Vacancies within the dioctahedral sheet cause even stronger adjustments. As a result of these deformations, the internal energy of the crystal is increased by the associated additive elastic energy.

### The Interlayer Sheet

In some phyllosilicates, electrical neutrality of the crystal structure is achieved by the incorporation of a cation interlayer sheet. Interlayer sheets can be formed by cations which are not bonded to each other (smectites, vermiculites and micas) or can take the form of an octahedral sheet which has no shared vertices with the tetrahedral sheets (chlorites) [2]. Cations reside in hexagonal or ditrigonal cavities formed by the  $O^{2-}$  anions of the adjacent tetrahedral sheets (Fig. 1.6(a)). As a result, the cations are 12-fold coordinated. However, when distortions of tetrahedral sheets are taken into account, the actual coordination of the cations is reduced to 6 (Fig. 1.6(b)).

### The Layer Charge

When the tetrahedral and octahedral sheets are joined in a layer, the resulting structure can be either electrically neutral or negatively charged. Electrical neutrality is achieved if:

- ▷ tetrahedral sheets have  $Si^{4+}$  cations resident in all tetrahedra;
- ▷ dioctahedral sheets have only trivalent cations (e.g.  $Al^{3+}$ ,  $Fe^{3+}$ ); and
- ▷ trioctahedral sheets are formed of divalent cations only (e.g.  $Mg^{2+}$ ).

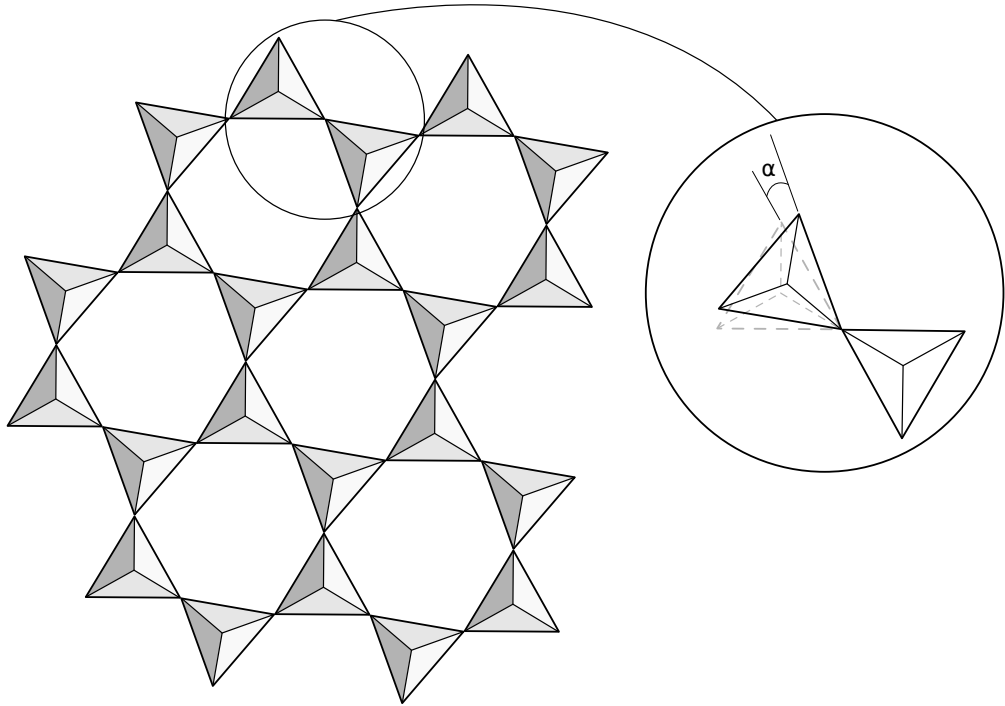


Figure 1.5: Deformation of tetrahedral sheet through rotation by  $\alpha$ . Adapted from [2]

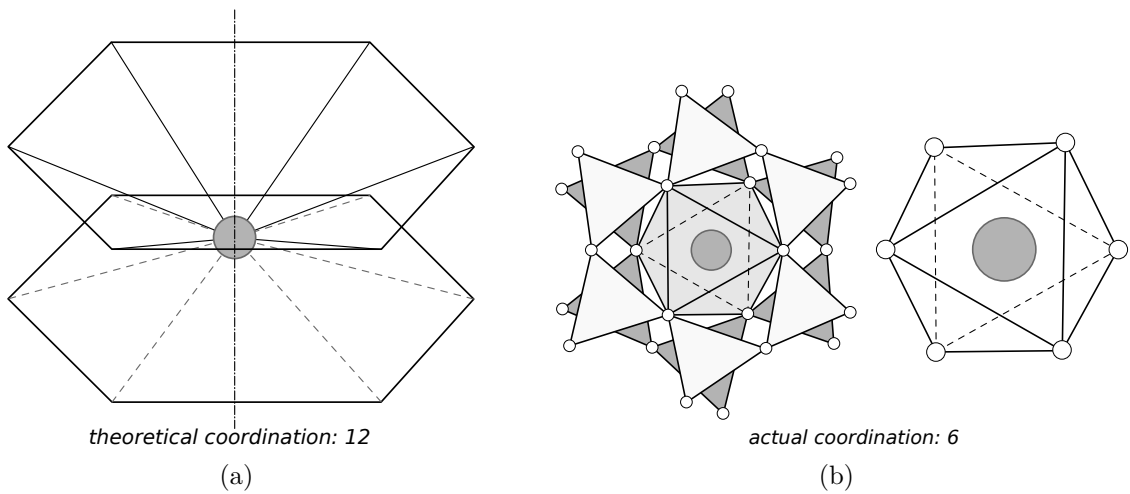


Figure 1.6: Structure of the interlayer cation. (a) Theoretical - due to the position of cation in ditrigonal cavities of tetrahedral sheet of clay. (b) Distortions of the tetrahedral sheet brings the coordination from 12 down to 6. Adapted from [2]

However, negative layer charges arise from various degrees of substitution:

- ▷ substitution of  $\text{Al}^{3+}$  for  $\text{Si}^{4+}$  in tetrahedral sites;
- ▷ substitution of  $\text{Al}^{3+}$  in dioctahedral sheets, or  $\text{Mg}^{2+}$  in trioctahedral sheets, for lower charge cations; or
- ▷ the presence of vacancies in the tetrahedral or octahedral sheets.

Substitution in a tetrahedral sheet is characterised by a localised charge distribution over three oxygen atoms (Fig. 1.7). In the case of octahedral substitution, in contrast, the delocalisation of layer charge is spread over a region of 10 basal oxygen atoms [3,37]. Charge localisation, and the diversity of its location and composition is considered to be one of the most important qualities of phyllosilicates, because of the effect this has on the exchangeable cations in the interlayer space of the clay [1, 2, 24].

The Cation Exchange Capacity (CEC) is a measurable quantity that is related to the layer charge of the clay and corresponds to the number of hydrogen cations ( $\text{H}^+$ ) needed to balance the negative charge of the clay layers [35]. The CEC also depends on the nature of the cations adsorbed between the clay layers. It is expressed in centimols of positive charge per kg of dry clay mineral ( $\text{cmol} \cdot \text{kg}^{-1}$ ), which is numerically equal to the traditional units of the milliequivalents per 100 g of clay ( $\text{meq}/100\text{g}$ ). The CEC can be calculated as follows:

$$CEC = (\text{charge}/\text{mass}) \times 1000 \times 100 \quad [\text{meq}/100\text{g}], \quad (1.1)$$

where the *charge* and *mass* of the half unit cell are considered.

Experimental work [19] which motivated this study found that the CEC was an important parameter for formation polymer/clay nanocomposites and for coating packaging materials. For this reason, the effect of the CEC is studied in detail in Chapters 4,5 and 6.

### 1.1.2 Common Patterns of Layer Structure

The make up of all phyllosilicates is based on two main types of layer structure: 1:1 layers, in which one tetrahedral sheet is joined to one octahedral sheet; and 2:1 layers, in which one octahedral sheet is sandwiched between two tetrahedral sheets (Fig. 1.8).

The group symmetry to which a particular phyllosilicate belongs depends on the way in which its 1:1 or 2:1 layers are linked. As indicated previously, layer linkage always leads to some deformation of bond angles and lengths. Therefore, the symmetries of phyllosilicates range from highest to lowest as follows: *hexagonal*, *rhombohedral*, *orthorhombic*, *ditrigonal*, *monoclinic* and *triclinic* [2].

#### 1:1 Structure: Kaolinite

The clay minerals in the kaolin group consist of dioctahedral 1:1 layer structures with a general composition of  $\text{Al}_2\text{Si}_2\text{O}_5(\text{OH})_4$ . One surface of the layer consists entirely of basal oxygen atoms belonging to the tetrahedral sheet, while the other surface is mainly composed of OH groups from the octahedral sheet. In 1:1 phyllosilicates the layer charge is usually close to zero. The negative charge of the oxygen anion framework is balanced by the positive charge of the tetrahedral and octahedral cations. The unit cell includes six octahedral sites and four tetrahedral sites, such that the dimensions of kaolinite are  $a \times b = 5.15 \times 8.95 \text{ \AA}$  [2].



Pyrophyllite is characterised by the presence of a vacancy in the *trans*-octahedra. The unit cell is formed from six octahedral sites and eight tetrahedral sites and its measurable cell dimensions are:  $a \times b = 5.160 \times 8.966 \text{ \AA}$ . Tetrahedral sheets from adjacent pyrophyllite layers are bonded through Van der Waals interactions. The basal spacing of the 2:1 layer varies from 9.10 to 9.43  $\text{\AA}$  [2, 36].

Due to the absence of an octahedral vacancy in the talc structure, deformations of the tetrahedral and octahedral sheet are limited. This results in unit cell dimensions of  $a \times b = 5.290 \times 9.173 \text{ \AA}$  [2].

Structural differences between pyrophyllite and talc arise due to their disparate structural configurations of OH radicals. In the dioctahedral structure, the net negative charge is compensated for by two adjacent cations. This causes the O-H bonds to be inclined towards the direction of the vacancy. In the trioctahedral structure, each OH radical is balanced by three neighbouring cations. In this case, the O-H bond is oriented perpendicular to the hexagonal cavity of the tetrahedral sheet.

### 2:1 Structure with an Interlayer Sheet: Smectite, Mica

The crystal structure of smectite and mica clays derives from that of pyrophyllite through cationic substitution of  $\text{Al}^{3+}$  for  $\text{Si}^{4+}$  in the tetrahedral layer and of  $\text{R}^{2+}$  for  $\text{R}^{3+}$  in octahedral layer [1, 2, 36]. The general formula for dioctahedral smectites is  $(\text{M}_{x+y}^{n+} \times m\text{H}_2\text{O})(\text{R}_{2-y}^{3+}\text{R}_y^{2+})(\text{Si}_{4-x}^{4+}\text{Al}_x^{3+})\text{O}_{10}(\text{OH})_2$  where  $x$  and  $y$  indicate the layer charges resulting from each type of substitution;  $\text{R}^{n+}$  refers to a generic di- ( $\text{Mg}^{2+}$ ,  $\text{Ni}^{2+}$ ,  $\text{Zn}^{2+}$ ) or trivalent octahedral cation ( $\text{Al}^{3+}$ ,  $\text{Fe}^{3+}$ );  $\text{M}^{n+}$  refers to a generic interlayer cation ( $\text{Na}^+$ ,  $\text{K}^+$ ,  $\text{Ca}^{2+}$ ,  $\text{Mg}^{2+}$ ). These substitutions lead to the formation of a negative charge framework in the 2:1 layer which is compensated for by the addition of a cation interlayer sheet in the crystal structure (Fig. 1.9). The interlayer cations are situated in the ditrigonal cavities captured by two opposite tetrahedral sheets (Fig. 1.6). The negative charge of the 2:1 mica layer is very high. As a result, interlayer cations serve as "locks" which strongly bond layers together. Due to this, no expansion of the interlayer sheet is possible [1, 2].

One of the most important and widely used in various industries dioctahedral smectite is Montmorillonite (Mt) [1], the idealised composition of which is  $(\text{M}_y^+ \times n\text{H}_2\text{O})(\text{Al}_{2-y}^{3+}\text{Mg}_y^{2+})(\text{Si}_4^{4+})\text{O}_{10}(\text{OH})_2$ . In nature, negative layer charge excess is compensated for by inorganic cations  $\text{M}^+$  (e.g.  $\text{Na}^+$ ,  $\text{K}^+$  or  $\text{Ca}^{2+}$ ). The interlayer cations are fairly loosely attached to the phyllosilicate structure, and can, therefore, be exchanged for other cations; for this reason, they are called exchange cations. It is generally accepted that 80% of the exchange cations occupy sites within the clay interlayer and 20% are localised on the edges of the clay layers [1, 36]. The CEC of Mt is in the range 80-120 meq/100g.

Mt layers are about 7.5  $\text{\AA}$  thick and up to  $1\mu\text{m}$  in lateral dimensions. The regular distance between layers (d-spacing ( $d_{001}$ )) of Mt is 9.5  $\text{\AA}$  when dehydrated [38] (i.e. no water is present in the interlayer). This increases to 12.5  $\text{\AA}$  and 15.0  $\text{\AA}$ , respectively, [2, 38] when one and two layers of water are present in the interlayer.

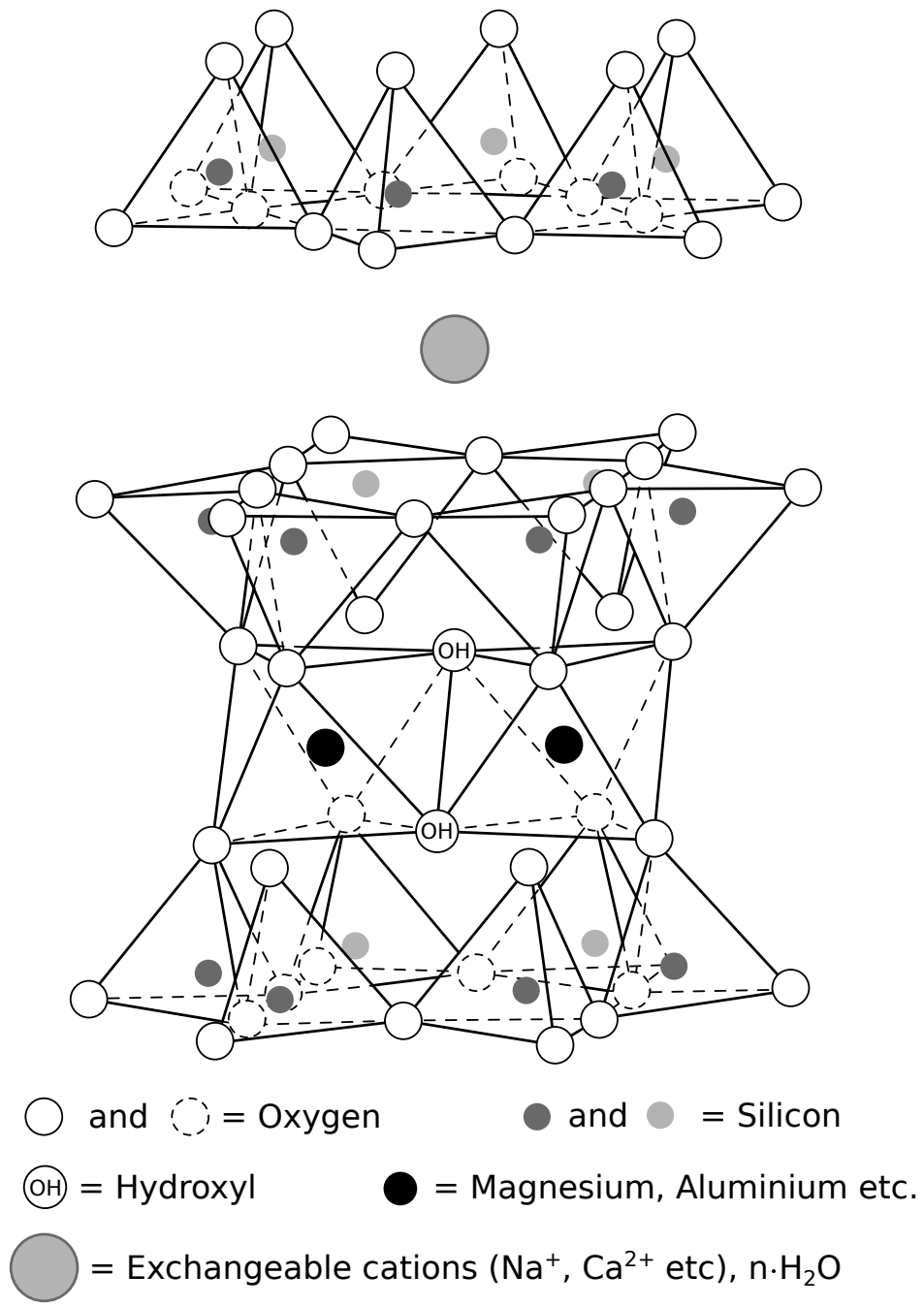


Figure 1.9: Diagrammatic sketch of the structure of smectite

### 1.1.3 The Swelling of the Clay Interlayer

Swelling is the process of expansion of clay layers due to increasing incorporation of polar molecules (e.g. water, polymers) in the interlayer region. This property is not characteristic for all clay minerals and is determined by many factors such as chemical composition of the clay mineral, nature of the surface atoms, exchangeable cations, and the magnitude and location of the layer charge. For example, if the layer charge is too high (micas, chlorites) or zero (kaolinite, pyrophyllite, talc), swelling of the layers does not occur. Therefore, studies of clay swelling are mostly focused upon 2:1 smectite clays due to their large swelling capacity [1, 12, 24, 38–43].

Swelling clays play significant roles in current industry. It has been observed [41] that smectite clays are candidate systems for the intercalation and capture of substances such as CO<sub>2</sub> and nuclear waste as well as for dehydration of laboratory samples. Furthermore, the process of interlayer swelling is directly related to the formation of polymer-clay nanocomposites. In order to enhance and control this formation, an understanding of the clay swelling mechanisms is required and, so, this will be described in the following sections.

#### Clay-Water Interactions

The phenomenon of swelling is associated with the hydration of clay. However, not all clays swell when hydrated. Clay minerals of the kaolinite group, due to the strong hydrogen bond interactions between their layers, display little or no swelling on hydration. Sodium montmorillonite, on the other hand, swells in water to many times its dry volume. Calcium montmorillonite and the hydrous micas fall between these two extremes but are, in general, much closer to kaolinite than to sodium montmorillonite in terms of their increase in volume on hydration [12, 42].

Comprehensive experimental investigations [1, 2, 12, 36–38, 42, 44] have revealed that the swelling of a clay interlayer occurs via two different regimes:

- ▷ Crystalline – characterised by the formation of one-, two-, three- and four- layer hydrates. Typical interlayer spacings documented in the crystalline swelling regime lie within the range 9 to 20 Å [12, 38, 39, 42].
- ▷ Osmotic – characterised by formation of wide interlayers up to 40 Å.

Osmotic swelling is not germane to the focus of this thesis, therefore it will not be discussed thoroughly.

The neutral siloxane surface, such as that found occurs on 2:1 phyllosilicates where no isomorphous substitution has occurred (e.g., talc and pyrophyllite) is hydrophobic under ambient conditions [1, Chapter 3]. The external oxygen atoms act as weak electron donors and are not capable of forming hydrogen bonds with water molecules. With this type of surface therefore, water molecules mainly interact with each other rather than with the clay surface. As a result, talc and pyrophyllite do not exhibit swelling properties.

Hydrophilicity of clay layers can, however, be introduced by isomorphous substitution in the octahedral or tetrahedral sheet inducing the presence of exchangeable cations. The chemical nature of these cations (e.g. ionic radius, charge, hydration energy) determines the swelling properties of the clay minerals. A common feature of these cations is that they have

appreciable enthalpies of hydration [1, Chapter 2]. These provide the options of achieving either complete or partial cation hydration shells, thereby forcing the clay layers apart.

### Swelling Isotherms

Adsorption of water in the clay interlayer proceeds by initial solvation of the exchangeable cations, followed by the occupation of the remaining interlayer space. Water molecules coordinated to the exchangeable cations are clustered around, and strongly polarised by, them [44]. These molecules, whose number increases with the water partial pressure, are organised into layers and promote an increase of the  $d_{001}$ -spacing (Fig. 1.10). Thus, for a  $\text{Na}^+$ -saturated Wyoming montmorillonite, the  $d_{001}$  spacing varies from 9.60 Å (0 water layer or 0W) to 12.5 Å (1 water layer – 1W), 15.5 Å (2 water layers – 2W) and 18.8 Å (3 water layers – 3W) when  $p/p_0$  increases from 0 to 1 (Fig. 1.10). When  $\text{Na}^+$ -Mt is dehydrated, the interlayer cations migrate from the centre of the interlayer space into the siloxane ditrigonal cavity and perturb the hydroxyl groups located at the base of that cavity [1, 2].

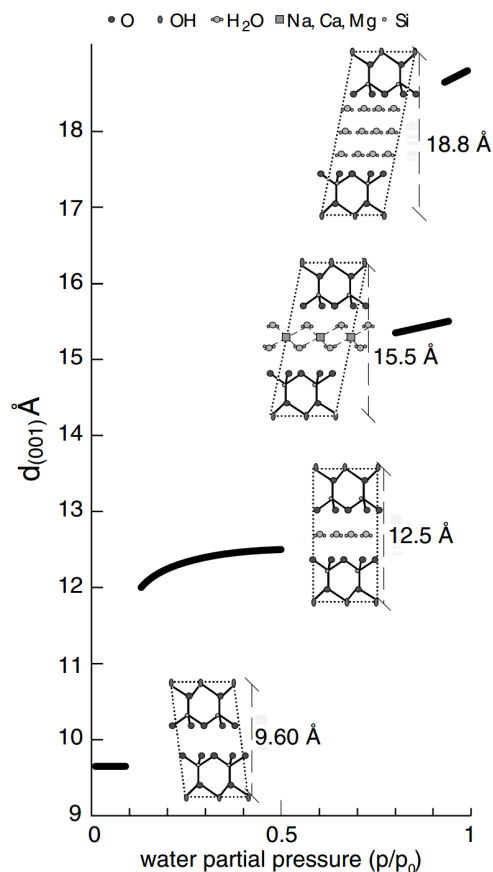


Figure 1.10: Variation in  $d$ -spacing of a Wyoming montmorillonite as a function of the water partial pressure ( $p/p_0$ ) [2]

Water is heterogeneously bound on the accessible surfaces of clays. As a result, the water layer in direct contact with the solid is not necessarily complete before additional layers start forming (Fig. 1.11(a)). The shapes of water adsorption isotherms (swelling curves), on the other hand, vary for a given clay as a function of the cations saturating the interlayer sites (Fig. 1.11(b)). The inflexion point of these curves depends on the affinity of the interlayer

cations for water. Thus,  $\text{Ca}^{2+}$ -saturated montmorillonite is more readily "hydrated" than  $\text{Ba}^{2+}$ - or  $\text{Cs}^+$ -saturated montmorillonite. The water content of  $0.1 \text{ g}_{\text{H}_2\text{O}}/\text{g}_{\text{clay}}$  is reached for a partial pressure of 0.1 compared with 0.2 and 0.5, respectively.

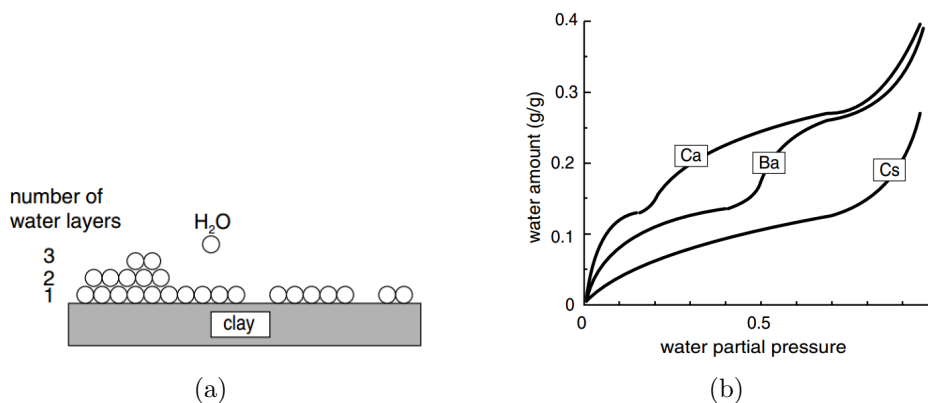


Figure 1.11: Adsorption of water by clays. a) Diagram showing that layers 2 and 3 can "nucleate" before completion of layer 1. b) Influence of saturation by different interlayer cations [2]

The swelling behaviour of montmorillonite has been extensively studied with various simulation techniques [7, 10, 18, 45–48]. A review of the outcomes from these simulations is presented in Chapter 3 of this thesis.

## 1.2 Polymer/Clay Nanocomposites

A composite is any material made of more than one component. Unlike alloys and blends, though, composite materials are solid multiphase substances formed through the combination of materials with different structural, physical and chemical properties. In a composite, one phase is continuous and is called the matrix, while the other is the filler material [49]. Many composite materials can be custom tailored to have specific properties that meet particular requirements.

Over the last three decades there has been interest in the use of composites consisting of clay platelets embedded within a polymer matrix. Such materials have been found to have similar properties to conventional composites, but to require substantially lower amounts of filler material. Furthermore, the resulting composites can be easily processed to form films with improved barrier properties to gases and water, and materials with improved fire-retardancy ability [30]. Owing to the nanoscale of both the clay platelets and the dimensions spacing between the clay layers, these compounds have become known as *nanocomposites* [30]. The first successful example of polymer-clay nanocomposites was developed by scientists at Toyota Central Research Laboratories in 1993 for nylon-6/clay nanocomposites which provided significant improvements on the mechanical properties of pure nylon-6 [50].

Adding as little as 5 wt% of clay filler with respect to the pristine polymer can be enough to achieve significant improvement in mechanical properties. This reduces the component weight since traditional fillers are added at 20-40 wt%. The reason for these improved properties is that the clay platelets have dimensions in the nanometre lengthscale range and, when dispersed, offer a much higher surface area for polymer-filler interactions than do

conventional composites [32]. Use of nanocomposites in packaging offers increased shelf life for many food products and benefits for food safety such as growth inhibition of bacteria and other organisms. In other words, the nature of the filler has a significant effect on the final structure and the macroscopic properties of the resultant polymer nanocomposite. Clays are one group of nano-fillers which have been extensively used for the preparation of polymer nanocomposites [1, 2, 30, 32].

### 1.2.1 Structure of Polymer/Clay Nanocomposites

The structures of polymer/clay nanocomposites are classified according to the level of intercalation and exfoliation of clays by the presence of the polymer, as shown in Fig. 1.12. Various parameters including clay nature, organic modifier, polymer matrix and preparation method influence the intercalation and exfoliation level. Therefore, depending on the nature and properties of the clay and the polymer as well as preparation methodology of nanocomposite, different composite micro-structures can be obtained.

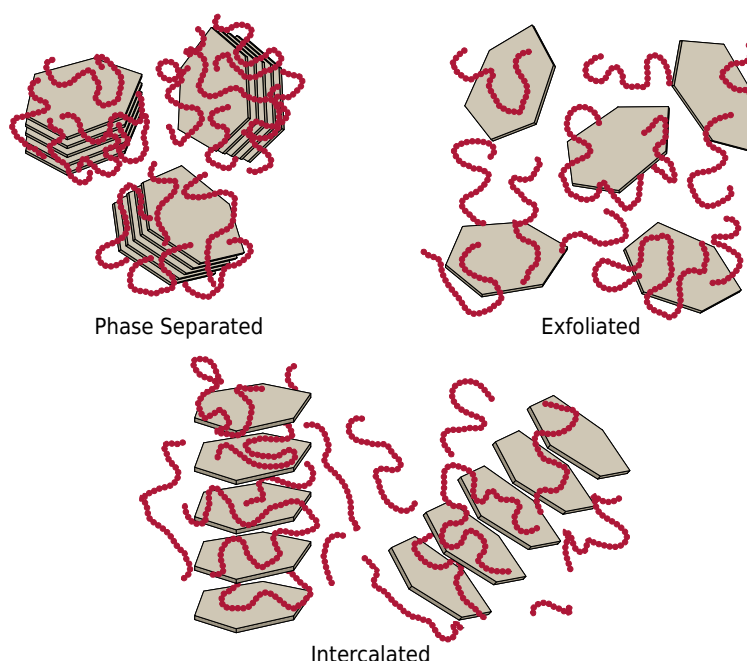


Figure 1.12: Different types of composites arising from interaction of polymer and clay

#### Phase Separated Structure

When an organic polymer is combined with an inorganic clay, the polymer cannot intercalate between the clay layers and the clay is dispersed as aggregates or particles with layers stacked together within the polymer matrix. The obtained composite structure is considered to be "phase separated". The properties of phase separated polymer/clay composites are in the range of traditional micro composites.

#### Intercalated Structure

When one or more polymer chains are inserted into the interlayer space leading to an increase in the interlayer spacing, while the periodic array of the clay layers is retained, an intercalated nanocomposite is formed. The presence of polymer chains in the galleries leads

to a decrease in electrostatic forces between the layers but it is not totally screened.

### Exfoliated Structure

Exfoliated structures are obtained when the insertion of polymer chains into the clay galleries causes separation of the layers, such that individual layers are dispersed within the polymer matrix. The exfoliated structure is considered to have developed when the interlayer spacing is more than 80-100 Å [32]. Due to the significant dispersion of individual clay layers, high aspect ratios are obtained and lower clay contents are more likely to produce exfoliated nanocomposites. As a result, the most significant improvements in polymer properties are obtained due to the large surface interactions between polymer and clay.

#### 1.2.2 Barrier Properties of Polymer/Clay Nanocomposites

One of the most considerable effects of clays on polymer matrix properties is the significant improvement they make to barrier properties. Clays increase the barrier properties of polymers by creating a sort of maze which imposes what is called a "tortuous path". This retards diffusion of gas molecules through the polymer matrix (Fig. 1.13).

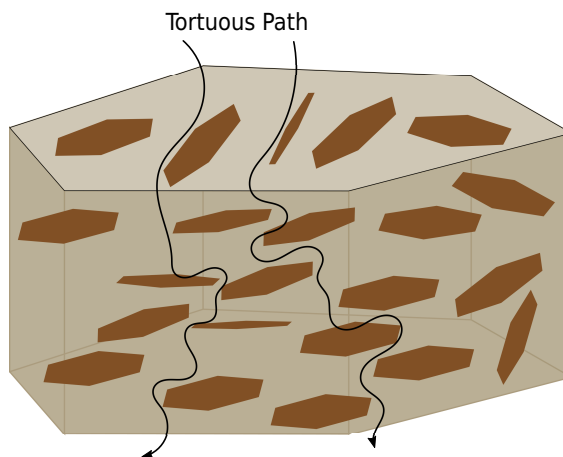


Figure 1.13: Schematic illustration of tortuosity for a diffusing penetrant introduced to exfoliated clay, layered in a polymer matrix

The degree of enhancement in the barrier properties depends on the degree of tortuosity created by clay layers (brown) and the diffusion way of molecules through the polymer film. Obviously, the best barrier properties of a given polymer/clay nanocomposite are achievable by exfoliated type arrangement. Many previous studies have reported enhanced barrier properties of polymer/clay nanocomposites against the diffusion of gases and vapours [1, 2, 19, 32, 51, 52].

#### 1.2.3 Preparation Techniques

Many efforts have been made to prepare intercalated and exfoliated polymer/clay nanocomposites with improved properties. A variety of polymer characteristics (including polarity, molecular weight, hydrophobicity, reactive groups) as well as clay characteristics (such as charge density and its modified structure and polarity influence the intercalation of polymer chains within the clay galleries) have been considered. Therefore, various different synthetic approaches have been used for the preparation of polymer/clay nanocomposites. Four dif-

ferent methods of preparation of polymer/clay nanocomposites have been identified [34, 49]:

- ▷ **Exfoliation-adsorption:** Through the means of a solvent in which the polymer is soluble, a layered silicate is exfoliated into layers. The polymer then adsorbs onto the delaminated sheets and, when the solvent is evaporated (or the mixture precipitated), the sheets reassemble. This sandwiches the polymer to yield, in the best case scenario, an ordered intercalated nanocomposite (Fig. 1.12).
- ▷ **In situ intercalative polymerization:** In order to encourage polymer formation in between the clay platelets, the layered silicate is swollen within the liquid monomer or a monomer solution. Initiation of the polymerization process is then achieved either by heating or by the diffusion of a suitable initiator.
- ▷ **Melt intercalation:** Polymer is mixed with the layered silicate in molten state conditions. If the chosen polymer is compatible with the layer surfaces, the polymer can diffuse into the interlayer space, leading to formation of either an intercalated or an exfoliated nanocomposite.
- ▷ **Template synthesis:** Double-layer hydroxide-based nanocomposites are synthesized using silicate building blocks. These silicates are formed in situ in an aqueous solution containing the polymer. In this technique, the polymer aids the nucleation and growth of the inorganic host crystals and gets trapped within the layers as they grow due to self-assembly forces.

### 1.3 Chapter Summary

In this chapter, the main aspects of the atomic structure and resulting properties of clay minerals and polymer/clay nanocomposites have been briefly reviewed. The elemental composition of clay minerals, in particular swelling clays, was reported in the earlier stages of the chapter. Although extensively investigated, the structure of clay minerals is very complex and possesses many variables (e.g. type of isomorphous substitution and exchangeable cation, charge and type of arrangement) which can drastically change the physical properties of any given clay mineral. This should be kept in mind when producing computational model of water/polymer/clay nanocomposites.

In addition, in this chapter, the interaction of clay surfaces with water was reported. The mechanism of water adsorption/swelling is influenced by both the clay charge location and the nature of the exchangeable cation that balances this charge. The particular sensitivity of this process to the structural composition of clay minerals means it represents a key apparatus for evaluating the computational models developed. For this reason, the swelling behaviour of clay mineral will be extensively investigated in the following chapters of this thesis.

In conclusion, this chapter has reported the formation mechanism of polymer/clay nanocomposites, their possible structures and properties. All the theoretical data gathered and presented in this chapter will be useful in evaluating the computer models which will be developed and used in the next chapters. In the next chapter the methods of molecular simulations are reviewed and an evaluation is made of previous atomistic-level modelling of clays. This includes an appraisal of the interaction potentials used in the system studied.

## 2 Methods and Computational Models

Experiment plays a central role in science. Experimental techniques, such as X-ray diffraction or nuclear magnetic resonance, allow determination of the structure and elucidation of the function of many large molecules of biological interest. However, full utility of experiment is only attainable when it is used in conjunction with models and theories [53].

Computer simulations have altered the interplay between experiment and theory. The principal aims of computational modelling are to complement and assist the interpretation of experimental data and to play a predictive role in, for example, the development of materials [54]. The calculations implied by a mathematical model are carried out by a machine and the results are interpreted in terms of physical properties. Since computer simulation deals with models, it may be classified as a theoretical method. On the other hand, various emergent physical quantities can (in a sense) be measured within these calculations, and this can justify use of the term "computer experiment" [6, 53].

Atomic-scale structural features can have a large influence on the properties of materials, so it is important to have a range of tools available to investigate materials at this scale. Various simulation techniques have been used successfully in a wide range of studies, showing good accord with experimental data and correctly predicting various material characteristics [6, 24, 30, 43, 55, 56]. Computer simulations vary from computer programs that run for just a few minutes on a PC to network-based clusters of high performance computing facilities running for hours or days. The scales of systems to be simulated also show great variation. In materials simulation, these methods spread from quantum chemistry, where simulation entities of size  $10^{-15}$  m are considered, through to finite element analysis, where the simulation box can be on the scale of metres (Fig. 2.1). The selection of an appropriate method, therefore, is essential to obtaining a meaningful solution for a proposed task.

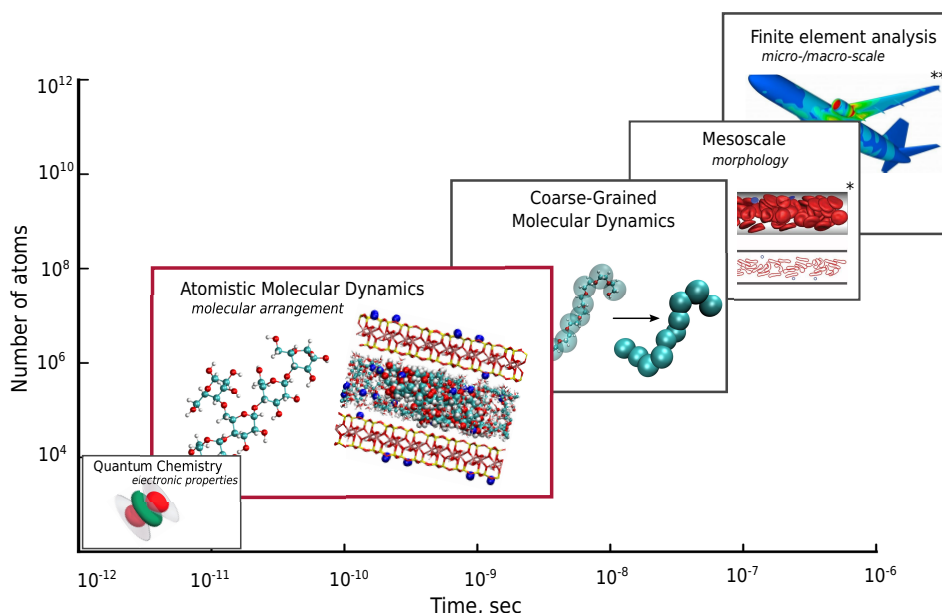


Figure 2.1: Simulation methods for materials systems, with associated time- and length scales. Pictures are taken from \* [4]; \*\* [5]

The large size and complexity of clay minerals and clay composites limits the information about molecular structure and arrangement of intercalants within the galleries that an

experimentalist can obtain. Computer simulation methods, particularly molecular dynamics (MD), have, over the past decade, therefore become an invaluable tool in the study of clay minerals. Physical and chemical properties may now be rationalised and even predicted. Atomistic simulations can also provide considerable insight into mechanisms within these layered materials, particularly given recent advances in high performance computing hardware and MD algorithms that have enabled large-scale simulations relatively free from major finite size effects [30,43]. The simulation of large systems is important if one is to accurately characterise complex and disordered clay minerals and, in particular, to predict materials properties.

The previous chapter was concerned with introducing the themes and material background of the thesis. This chapter focuses on the methodology of the work. Initially, this chapter contains a review of the different simulation techniques used to study clay minerals and polymer/clay nanocomposites with particular attention to the main method used in atomistic simulations, called MD. Following this, the history and the current state of potential models of various materials will be discussed.

## 2.1 Molecular Dynamics

One of the principal tools in the theoretical study of a vast variety of different physical systems is the method of MD simulation. MD simulation is a technique used to compute the equilibrium and transport properties of a classical many-body system by using essential information about a system's dynamics, usually resolved at atomistic detail. In this context, the term *classical* means that the motion of the constituent particles obeys the laws of classical mechanics [6] and that quantum effects are integrated out. Typically, the method's resolution is cut-off by the translational/rotational motion of light atoms or vibrations with a frequency  $\nu$  such that  $h\nu > k_B T$  [6,54].

In MD, successive configurations of the system are generated by integrating Newton's laws of motion. The result is a trajectory that specifies how the positions and velocities of the particles in the system vary with time. The trajectory is obtained by solving the differential equations embodied in Newton's second law of motion ( $F = ma$ ):

$$\frac{d^2 r_i}{dt^2} = \frac{F_{r_i}}{m_i} \quad (2.1)$$

These equations describe the motion of a particle  $i$  of mass  $m_i$  along coordinate  $r_i$  with  $F_{r_i}$  being the appropriate force component on the particle [54,55]. The forces are derived from the potential  $U$  that describes the interactions between the particles.

The MD approach has evolved in recent decades from a method used mainly for studying the dynamics of generic fluids, such as hard spheres and Lennard-Jones particles [55], to a comprehensive method for studying a vast range of system types with atomic resolution [24,30,43,54]. The development of this computational method was particularly stimulated in the late 1980s when several general purpose force-fields for water, proteins, polymers and DNA were generated and corresponding computer simulation codes (e.g. AMBER [57], LAMMPS [58], GROMACS [59], NAMD [60], DL\_POLY [61]) became generally available.

Interactions between atoms in MD are defined by the chosen force-field. The force-field

is a set of parameters that explicitly describe the behaviour of different kinds of atoms and bonds and, thus, give the total potential energy of the system [30, 54, 55]. This potential energy is naturally broken down into various energy terms, i.e. bond stretch, angle bend, torsion and non-bonded potentials:

$$U(\vec{r}) = U_{bond}(r) + U_{angle}(\Theta) + U_{torsion}(\tau) + U_{non-bonded}(r) \quad (2.2)$$

Many different kinds of force-field have been developed over the years. Some include additional energy terms that describe other kinds of deformations to improve the accuracy of the resultant mechanical model, but the basic structure stays the same. Force-field values are typically derived from various types of experimental data (e.g. spectral, calorimetric, crystallographic etc.) and quantum mechanical calculations [54]. The mathematical form of the potential terms also varies from force-field to force-field, but they ought to be differentiable for analytical calculation of forces. The more common forms will be described in following sections.

**Bond Stretching Potential.** The potential energy curve for a typical bond has the form shown in Figure 2.2. Of the many functional forms used to model this curve, most convenient is that suggested by Morse [54]:

$$U(\vec{r}) = D_e \{1 - \exp[-a(r - r_0)]\}^2, \quad (2.3)$$

where  $D_e$  is the depth of the potential energy minimum and  $a = \omega \sqrt{\mu/2D_e}$ , where  $\mu$  is the reduced mass and  $\omega$  is the frequency of the bond vibration. Although the Morse potential is very accurate, it is not usually used in force-fields [54]. Firstly, because it is not particularly well-suited for efficient computation and secondly because it is rare in MD calculations, for bonds to deviate considerably from their equilibrium values. As a result, a much simpler expression based on Hooke's law is usually used:

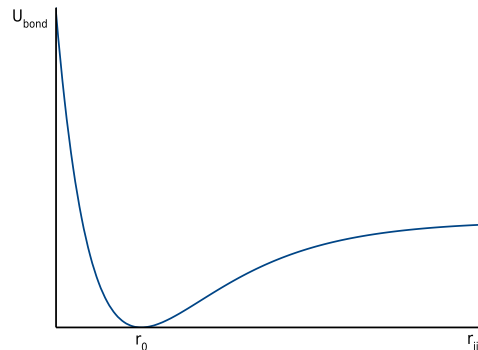


Figure 2.2: Variation in bond energy with interatomic separation

$$U_{bond}(r) = \frac{1}{2} \sum_{bonds} k_b (r - b_0)^2 \quad (2.4)$$

This is the equation of a parabola, as shown in Figure 2.3. The  $k_b$  parameter controls the stiffness of the bond spring, while  $b_0$  defines its equilibrium length. In each force-field, appropriate values of  $k_b$  and  $b_0$  are assigned to each pair of bonded atoms based on their types (e.g. C-O, C-H, C-C, etc.) so as to reproduce the optimum geometry and oscillatory frequencies of atom pairs. To model the Morse curve more accurately, cubic and higher terms can be included [54].

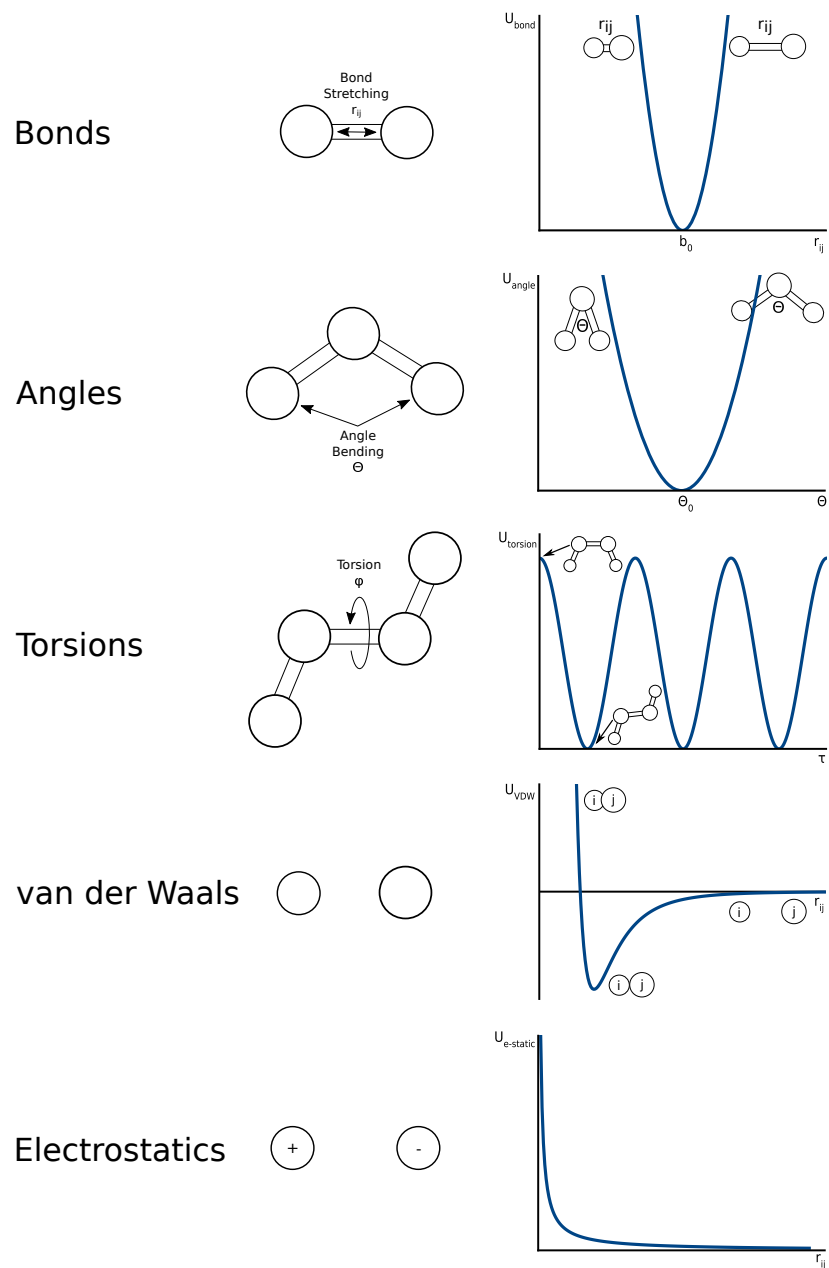


Figure 2.3: Empirical Potential Energy Functions

**Angle Bending Potential:**  $U_{angle} = \frac{1}{2} \sum_{angles} k_{\Theta}(\Theta - \Theta_0)^2$ . The bending energy is also frequently described using Hooke's law and a harmonic function (Fig. 2.3). Here, the  $k_{\Theta}$  parameter defines the angle stiffness and  $\Theta_0$  is the equilibrium angle. These parameters are based on the type of bonded triplet of atoms involved (e.g. C–O–C, H–C–C, C–C–C etc.) and are selected to achieve the equilibrium geometry and oscillation frequencies of the angle bend. As with the bond-stretching terms, the accuracy of the force-field can be improved by the incorporation of higher-order terms.

**Torsion Potential:**  $U_{torsion} = \frac{1}{2} \sum_{torsions} k_{\tau}[\cos(n\tau - \phi) + 1]$ . The existence of barriers to rotation about chemical bonds and the torsional energy have fundamental importance when considering the structural properties of molecules and performing conformational analysis [54,55]. Force-fields incorporate this behaviour by employing a torsional potential in modes of flexible molecules where conformational changes due to rotations about bonds are allowed. Within this, contributions are taken into account from each bonded quartet of atoms (e.g. C–C–O–C, H–C–C–H, C–C–C–H etc) in the system. The torsional energy is almost always expressed as a series of simple periodic functions (Fig. 2.3).  $n$  in the equation for the torsional potential is the *multiplicity* value which gives the number of minimum points in the function as the bond is rotated through  $360^\circ$ . The phase factor  $\phi$  then determines where the torsion angle passes through its minimum value. More sophisticated torsion potentials use a sum over several  $n$  values. Normally, these characteristic parameters are derived from *ab-initio* calculations and are able to ensure specific conformational structures of the molecule (e.g. *cis*- and *trans*- conformations corresponding to local maxima and local minima respectively (Fig. 2.3)).

**Non-bonded Potential:**  $U_{non-bonded} = \sum_i \sum_j \varepsilon \left[ \left( \frac{\sigma}{r_{ij}} \right)^{12} - \left( \frac{\sigma}{r_{ij}} \right)^6 \right] + \sum_i \sum_j \left( \frac{q_i q_j}{4\pi\epsilon_0 r_{ij}} \right)$ . Non-bonded potentials are usually expressed through Van der Waals (first term) and electrostatic interactions (latter term).

Van der Waals interactions are modelled using the best known potential function, the Lennard-Jones potential (L-J) (Fig. 2.4). In this,  $\varepsilon$  defines the strength of the interaction or the depth of the potential "well", and  $\sigma$  is the collision diameter – the separation for which the energy is zero and the potential becomes repulsive [54]. The repulsive part of the interaction is approximated by the  $\left( \frac{\sigma}{r_{ij}} \right)^{12}$  term, and the attractive longer-ranged tail is parametrised by the  $-\left( \frac{\sigma}{r_{ij}} \right)^6$  term (Fig. 2.4). Use of the inverse twelfth power in the repulsive term is a pragmatic approach, as it is the square of  $r^{-6}$  and, hence, leads to an efficient calculation of the potential. For the purpose of modelling complex molecules, several more advanced potentials can be linked together in order to obtain a high-performance model.

The attraction of electrons to atoms of electronegative elements results in an unequal distribution of charge across any molecule. The resultant charge distribution can be modelled using fractional point charges throughout the molecule, designed to reproduce the electrostatic properties of the molecule. The electrostatic interaction between two molecules is then calculated as a sum of the interactions between the pairs of point charges, using Coulomb's

law (Fig. 2.3). Here,  $q_{i,j}$  are the partial charges assigned to each point (usually, an atom) and  $\varepsilon_0$  is the relative permittivity of free space.

Simulations are, in many respects, very similar to real experiments [6] and the basic form of a MD algorithm is as follows:

step 1: set up the initial configuration, i.e. give all atoms a position and a velocity.

step 2: calculate the forces on all atoms using the chosen potential.

step 3: update positions/forces, i.e. move the atoms for a short timestep according to the calculated forces and the equations of motion.

Steps two and three are then repeated until the simulation is completed.

### 2.1.1 Initialisation

To start an MD simulation, one should assign initial positions and velocities to all particles in the system. The particle positions should be chosen to be compatible with the structure that one is aiming to simulate. In any event, the particles should not be located in such a way that there is any appreciable overlap of the atomic or molecular cores. Often this is achieved by initially placing the particles on a cubic lattice [6]. In most cases, this is a highly unstable structure and will melt quickly as the simulation runs. Alternatively, a preliminary simulation at 0 K can be used to enable a structure relaxation through which particles develop more stable configurations.

Secondly, the initial velocities of all the molecules must be specified. It is usual to choose random velocities, with magnitudes conforming to the required temperature and corrected so that there is no overall momentum:

$$P = \sum_{i=1}^N m_i v_i = 0. \quad (2.5)$$

Also velocities may be chosen randomly from a Gaussian distribution, in particular a Maxwell-Boltzmann distribution. Here, for particles with a mass  $m$  and a temperature  $T$ , velocities are assigned to the particles according to the aforementioned distribution function:

$$p(v_i) = \left( \frac{m_i}{2\pi k_B T} \right)^{1/2} \exp \left[ -\frac{1}{2} \frac{m_i v_i^2}{k_B T} \right] \quad (2.6)$$

## Equilibration

The equilibration period is the initial stage of each MD simulation. This period is designed to allow the starting configuration of the system, with its accompanying assigned velocities, to reach a state of equilibrium. During the equilibration time period, several properties of the system are monitored, including the total energy which is the sum of the potential energy terms from the atomic arrangement, and the kinetic energy due to atomistic motion. It is good practice to track these properties and take the point at which they become constant as a possible indication that an equilibrium state has been achieved. The length of the equilibration period depends on the size of the system or how dense is the initial configuration, and normally ranges from 100 ps to 10000 ps. Close to some phase transitions, a much greater equilibration period may be needed. Upon completion of the equilibration

period, the proper simulation can commence during which the desirable statistics of the calculation can be collated and extracted.

### 2.1.2 The Integration Algorithm

Having set up the system and assigned the initial velocities, the simulations can commence. An analytical solution of Eqn. 2.1 when a system consists of many particles is not possible. Therefore, the force that acts on each atom must be calculated by differentiating the overall potential function for each one. Many algorithms have been developed to tackle this problem, giving a vast selection of finite difference methods [54, 55]. Chosen finite difference techniques is then used to generate the MD trajectory. The main idea here is that the evolutionary integration is broken down into many small stages (i.e. time steps), each separated in time by a fixed increment portion  $\delta t$ . The total force that acts on each particle in the system at the given time  $t$  is calculated as the vector sum of its interactions with all nearby particles. Knowing this force, one can calculate the acceleration of each particle at time  $t$ , which, when combined with the corresponding positions and velocities, can be used to produce particle positions and velocities at time  $t + \delta t$ . Subsequently, the calculation algorithm can be repeated, resulting in a trajectory representing the "evolution" of the system.

*Verlet*, *velocity-Verlet*, *Leap-frog* and *predictor-corrector* methods are some examples of the finite difference algorithms widely used in MD [6, 54, 55]. All of these operate on the basis that the positions, velocities and accelerations using approximation based on a Taylor series expansion:

$$\begin{aligned} r(t + \delta t) &= r(t) + \dot{r}(t)\delta t + \frac{1}{2!}\ddot{r}(t)\delta t^2 + \frac{1}{3!}\dddot{r}(t)\delta t^3 + \frac{1}{4!}\dots \\ \dot{r}(t) &= v(t) \quad \text{- velocity} \\ \ddot{r}(t) &= a(t) \quad \text{- acceleration} \end{aligned} \tag{2.7}$$

Perhaps the most widely used method of integrating the equations of motion is *the Verlet algorithm* [62]. This method is based on positions  $r(t)$ , accelerations  $a(t)$  and the positions from the previous step  $r(t - \delta t)$  and calculates the new positions at  $t + \delta t$ ,  $r(t + \delta t)$ :

$$\begin{aligned} r(t + \delta t) &= r(t) + v(t)\delta t + \frac{1}{2}a(t)\delta t^2 + \dots \\ r(t - \delta t) &= r(t) - v(t)\delta t + \frac{1}{2}a(t)\delta t^2 - \dots \end{aligned} \tag{2.8}$$

Summing these two equations gives:

$$\begin{aligned} r(t + \delta t) + r(t - \delta t) &= 2r(t) + a(t)\delta t^2 + \dots \\ \text{or} \\ r(t + \delta t) &\approx 2r(t) - r(t - \delta t) + a(t)\delta t^2. \end{aligned} \tag{2.9}$$

As a result, the new position estimates contain an error that is of order  $\delta t^4$ . The Verlet algorithm does not explicitly define velocities, however they are useful for estimating the

kinetic energy (and hence, the total energy of the system). These can, though, be readily calculated from knowledge of the trajectory, using:

$$v(t) = \frac{[(r(t + \delta t) - r(t - \delta t))]}{2\delta t} \quad (2.10)$$

Once the new forces, accelerations and the new positions have been computed, those for time  $t - \delta t$  can be discarded. The current positions become the old positions and the new positions become the current positions. After each time step, the current temperature and the current potential energy are calculated in the force loop as well as the total energy, which should be conserved.

### Time Step

Choosing an appropriate value for the time-step ( $\delta t$ ) in an MD simulations is both highly important and non-trivial. If the value chosen for the time-step is too small, the simulations will take a very long time to achieve the required configurational evolution of the system. However, if too large a value is chosen, there is the possibility of instabilities arising which can lead to particles moving unphysical distances or having excessive forces acting on them and causing the simulation to fail. The ideal choice is for the time step value to be as large as possible, thus enabling the calculation to quickly simulate as much "real time" as possible, but without threatening any instability. In practice, values ranging between 0.001 and 0.01 picoseconds are found to be appropriate for such calculations.

### 2.1.3 Molecular Dynamics in Different Environments

The thermodynamic state of a simulation system is set by a small set of parameters such as the number of particles  $N$ , the temperature  $T$  and the pressure  $P$ . Other thermodynamic properties may then be derived through knowledge of the equations of state and the fundamental equation of thermodynamics. A collection of all possible systems which have different microscopic states but have an identical macroscopic or thermodynamic state is called an ensemble. Three main ensembles can be distinguished:

- ▷ Micro-canonical ensemble (**NVE**): The thermodynamic state characterised by a fixed number of atoms  $N$ , a fixed volume  $V$  and a fixed total energy  $E$ . Whilst the total energy  $E = K + U$  of the micro-canonical ensemble remains constant, the kinetic  $K$  and potential  $U$  contributions can fluctuate. Since the micro-canonical ensemble allows for large variations in temperature and pressure, the conditions produced are different from the "real" conditions under which most experimental investigations take place
- ▷ Canonical Ensemble (**NVT**): This is a collection of all systems whose thermodynamic state is characterised by a fixed number of atoms  $N$ , a fixed volume  $V$  and a fixed temperature  $T$ . The canonical ensemble allows the system under study to be probed as a function of temperature
- ▷ Isobaric-Isothermal Ensemble (**NPT**): This ensemble is characterised by a fixed number of atoms  $N$ , a fixed pressure  $P$  and a fixed temperature  $T$ . The isobaric-isothermal ensemble allows the system to be studied as a function of pressure.

## Thermostat and Barostat

It is important to control the temperature and pressure during the simulation of systems in NVT and NPT ensembles. This is made possible through use of mathematical thermostats and barostats, respectively. The instantaneous temperature of a system is proportional to its average kinetic energy and is, thus, directly related to the velocities of the constituent particles [54, 55]:

$$T \propto \frac{1}{2} \sum_{i=1}^N m_i v_i^2 \quad (2.11)$$

An easy way to ensure that the system maintains the required temperature, is to scale the velocities at each time-step. However, this approach would produce an unrealistic model, since no fluctuations in temperature would be allowed.

Berendsen et al. [56] proposed the use of an improved thermostat in which the simulation cell is weakly coupled<sup>1</sup> to a hypothetical external heat bath with a fixed temperature  $T_{bath}$ . At each step, the velocities are scaled thus, to keep the rate of change of temperature proportional to the temperature difference between the simulation cell and the heat bath:

$$\frac{dT(t)}{dt} = \frac{1}{\tau}(T_{bath} - T(t)), \quad (2.12)$$

This produces an exponential decay of the system temperature towards the desired temperature over time. The empirical parameter ( $\tau$ ), known as the *rise time*, allows the user to control the speed of this decay. Choosing an appropriate value of  $\tau$  is highly important. At small values of  $\tau$  the simulation cell and the bath are tightly coupled, so the fluctuations in the system temperature will be unrealistically small. As  $\tau \rightarrow \infty$  the effect of the Berendsen thermostat is removed, resulting in the simulation effectively sampling the micro-canonical ensemble. Typically, for MD simulations of condensed-phase systems, the value of  $\tau=0.1$  ps is used.

In order to scale simulation cell volume, rather than temperature, Berendsen et al. extended their thermostat in order to provide a barostat [56]. A similar approach applies when acting as a barostat, with the simulation cell now connected to a hypothetical external pressure bath. Using the Berendsen barostat, the rate of change of pressure can be calculated such that:

$$\frac{dP(t)}{dt} = \frac{1}{\tau}(P_{bath} - P(t)), \quad (2.13)$$

where, again,  $\tau$  represents an empirical coupling parameter (determining the strength of the coupling between the simulation cell and the pressure bath) with the pressure of the bath denoted  $P_{bath}$ . Depending on the pressure difference, the positions of the atoms are simply scaled so that the simulation cell is uniformly compressed or expanded as appropriate.

---

<sup>1</sup>A *coupling constant* describes the strength between an interaction between two systems. Systems are weakly coupled when the coupling constant is much smaller than one

### 2.1.4 Practical Aspects

#### Boundary Conditions and the Minimum Image Convention

The use of periodic boundary conditions is essential to modelling the bulk properties of atomistically described materials in large extended systems, since they reduce the amount of computational time required for the simulation. When periodic boundary conditions are imposed on the simulation cell, the super-cell is considered to be replicated infinitely in all three orthogonal space directions [30]. These super-cell images enable, in principle, the particles contained within the unit-cell to interact with each other, as well as the other particles contained within the images. Therefore, the periodic boundary conditions perform an essential role in making the simulation cell "feel" as if it is part of a large extended bulk system.

Even though periodic boundary conditions give representation of a bulk structure to small cells, the cell employed must be large enough to enable avoidance of artificial periodicity effects, where a molecule in one simulation cell is able to interact with its periodic replicas in adjacent cells [24,30]. This means that systems are computed according to the 'minimum image convention' where each particle interacts only with its nearest neighbours, including 'images' from the replicated boxes. In the course of the simulation, as a molecule moves in the original box, its periodic image in each of the neighbouring boxes moves in exactly the same way. Thus, as a molecule leaves the central box, one of its images will enter through the opposite face [55]. A two-dimensional version of such a periodic system is shown in Figure 2.5.

#### Cutoff and Verlet Neighbour List

The number of non-bonded terms in a force field increases as the square of the number of atoms in the system, whereas the number of bond-stretching, angle-bending and torsional terms is proportional to the number of atoms in the system. As a result, the most time-consuming part of MD simulation is the calculation of the non-bonded energies and forces. The Lennard-Jones potential diminishes very rapidly with distance (Fig. 2.4), therefore the most popular way to deal with its long-range component is to impose a non-bonded spherical *cutoff*. The dashed circle with radius  $r_{cut}$  in Figure 2.6 represents a cutoff, and in this case particles 1-7 contribute to the force acting on central particle, since their centres lie inside the cutoff. Particles 8-17, on the other hand, are further away than the cutoff value and so their interactions with the central particle are set to zero. Normally,  $r_{cut}$  is the separation at which the value of the potential is less than 1% of potential well depth or less than half the length of the shortest side of the simulation box when periodic boundary conditions are being applied. After imposing the cutoff radius, the potential curve itself is shifted up to avoid a jump in the potential.

The use of a cutoff on its own may not reduce computational time drastically, because one would still have to calculate the distance between all pairs of particles in the system to determine whether or not they lay within the cutoff radius. Calculating all the  $N(N - 1)$  distances would still take a lot of computational time. For further efficiency in the computation, a so-called Verlet neighbour list can be created for each particle [62]. When using this list, the potential cutoff sphere around a particular particle is surrounded by a 'skin',

to give a larger sphere of radius  $r_{list}$  as shown in Figure 2.6 [55]. The Verlet neighbour list is constructed of all neighbours of each particle, for which the pair separation is within  $r_{list}$ . This creates the list of atoms that are "potentially" ready for interaction and, during the force loop, only those particles appearing in the list are considered.

The most efficient way to implement the Verlet neighbour list would be through using a large neighbour array  $L$ , and a pointer array  $P$ . The pointer  $P[i]$  points to the position in the neighbour list where the first neighbour for particle  $i$  is located. The last neighbour of particle  $i$  is stored in element  $P[i + 1] - 1$  of the neighbour list. Thus, using  $P$ , one can readily identify the part of the large  $L$  array which contains neighbours of particle  $i$ .

The selection of the frequency at which the neighbour list is updated is very important. If skin ( $r_{list} - r_{cut}$ ) is too large, an unnecessarily large number of interactions will be taken into account and the force calculation will be inefficient; too low and particles might move within the non-bonded cutoff region, thus leading to an incorrect calculation of the energies and forces. Typically, an update frequency of between 10 and 20 steps and skin width ( $r_{list} - r_{cut}$ ) value of  $0.1r_{cut}$  is a good compromise between computational performance and the accuracy of derived values [54, 55, 62]. Allen and Tildesley [55, page 149] provided a table showing time saving using a Verlet neighbour list for MD simulations of Lennard-Jones atoms. Using the Verlet neighbour list provides a significant speed increase – like, twice as fast – especially for large systems (500 atoms in this example).

## Ewald Summation

Computation of non-bonded interactions can be a problem since their range is often greater than half the box length and are slow to converge. The Coulomb electrostatic interaction (Section 2.1, Non-bonded Potential) is particularly problematic in molecular dynamics, because even though the energy of each interaction decays as  $r^{-1}$ , the number of interactions increases as  $4\pi r^2$  (surface area of a sphere of radius  $r$ ). As a result, whilst one may expect that electrostatic interaction decays at larger separations, in reality the energy density of the interaction increases with particle separation. Spherical truncation cannot be used to solve this issue, because charged particles tend to migrate back and forth across the spherical surface, which inevitably would produce artificial effects at the cutoff [55, 63]. Fortunately, a variety of methods that can tackle the problem of slow convergence have been developed, one of which is widely used in three-dimensional simulations and called the Ewald summation method.

It was first introduced by Ewald in 1921 to study the energetics of ionic crystals [64]. The Ewald summation method divides the Coulomb series into summation of two convergent terms: a real and a reciprocal space summation [54, 55, 65, 66]. This separation can be mathematically expressed in the following simple equation [54, 64, 67]:

$$\frac{1}{r} = \frac{f(r)}{r} + \frac{1 - f(r)}{r} \quad (2.14)$$

Each charge in the system is surrounded by a screening charge of opposite sign but of equal magnitude. The functional form of the screening charge cloud  $f(r)$  is commonly assumed to be a Gaussian distribution (Fig. 2.7) [6, 54]. In that case the electrostatic potential is

constructed exclusively from the fraction of charges that are not screened. As a result, such a potential can be easily computed because this fraction rapidly goes to 0 at large separation and so the potential converges at the cutoff distance. However, to evaluate the electrostatic potential due to point charges but not screened by a cloud, a compensating charge distribution (negative screening charges,  $1 - f(r)$ ) of the same functional form is added. A smoothly varying periodic functional form of screening charges can be represented by a rapidly converging Fourier series resulting in an effective numerical implementation of this method.

A Gaussian charge distribution of the following functional form is commonly used [6]:

$$\rho_{Gauss}(r) = -q_i \left(\frac{\alpha}{\pi}\right)^{\frac{3}{2}} \exp(-\alpha r^2), \quad (2.15)$$

where  $\alpha$  is selected based on computational efficiency considerations.

### Partial Charges

Atomic charges are an integral part of any forcefield and cannot be assigned arbitrarily. A bonded potential assumes that the Coulomb energy associated with an atom is reduced by the transfer of the electron valency to the bond. Thus, molecular models relying on a bonded potentials will always use reduced partial charges. There are various methods available to calculate these partial charges, most convenient of which are based on quantum mechanical calculation, in particular, fitting to quantum mechanical molecular electrostatic potentials (ESP) [54, 63].

The electrostatic potential has contributions from both the nuclei and the electrons. The potential due to the  $N$  nuclei is calculated as the normalised sum of all atomic numbers  $Z_a$ , and that due to the electrons is obtained from the integral of the electron density:

$$U(r) = U_{nuc}(r) + U_{elec}(r) = \sum_a^N \frac{Z_a}{|r - R_a|} - \int \frac{dx' \rho(r)}{|r' - r|} \quad (2.16)$$

In order to implement this equation numerically, it is necessary to derive its discrete representation. For this purpose, a least-squares fitting procedure is employed and optimum atomic charges that reproduce the electrostatic potential are obtained.

#### 2.1.5 Measuring System Properties

Completed MD simulations can provide a lot of useful information on properties such as the diffusivity of ions and time averaged densities of particular particles. Various characteristic parameters can then be calculated directly through appropriate manipulation of the trajectories of simulated particles.

#### Pair Distribution Function

The radial pair distribution function or RDF ( $g(r)$ ) represents the probability of finding a pair of particles  $i$  and  $j$  with intermolecular separation  $r_{ij}$ . This function is particularly useful for giving insight into the average structure of the dynamic system under study. It can be

expressed as follows [55]:

$$g(r) = \left\langle \frac{V}{N^2} \sum_{i,j=1}^N \delta(r - r_{ij}) \right\rangle, \quad (2.17)$$

where this RDF is calculated as the mean value of all configurations;  $N$  is the total number of atoms,  $r_{ij}$  is the distance between the atoms ( $i, j$ );  $V$  is the volume of a spherical shell of inner radius  $r$  which accounts for the increasing number of atoms in shells of greater radius in an ideal gas. Lastly,  $\delta$  is a function that is non-zero only for small input values, thus, only pairs with separation close to the desired value of  $r$  are considered.

Practically, the RDF can be generated during a MD simulation by compiling a histogram, over discrete intervals of bins ( $r$ ), of the number of atom pairs with interatomic separations between  $r$  and  $r + \Delta r$ . At each timestep, the number of pairs of atoms that fall in each of these intervals is added on to the existing distribution. At the end of the simulation, the value for each interval of  $r$  is then divided by the number of timesteps and scaled according to the volume of the spherical shell.

### Coordination Number

The coordination number (CN) of a central particle is the number of its near neighbours. In relation to polymer/clay nanocomposites, CN is used for analysis of the first coordination spheres of interlayer cations and their hydration state. The CN can be defined through integration of the radial distribution function  $g(r)$ :

$$n = 4\pi \int_{r_0}^{r_1} r^2 g(r) \rho dr, \quad (2.18)$$

where  $[r_0, r_1]$  is the interval that includes the first peak of the RDF.

### Hydration Energy

The change in potential energy  $\Delta U(N)$  associated with adding water molecules to a dry clay was calculated as a function of increasing water content  $N$ :

$$\Delta U(N) = \frac{\langle U(N) \rangle - \langle U(0) \rangle}{N}, \quad (2.19)$$

where  $\langle U(0) \rangle$  is the average potential energy of dry Mt. All energy values were obtained from the production run after the equilibration process.

### Mean Square Displacement

Mean square displacement (MSD) measures the distances that atoms travel within the simulation cell in relation to their initial location. Therefore, through examination of MSDs, it is possible to gain valuable information regarding the diffusion rates of atoms within various systems. MSD is calculated by determining the square of the displacement of each atom from its initial position at time  $t$ , with the mean calculated over all the examined atoms:

$$MSD(t) = \frac{1}{N} \sum_{i=0}^N |r_i(t) - r_i(0)|^2, \quad (2.20)$$

where  $N$  is the total number of atoms, and  $r_i(0)$  and  $r_i(t)$  are the initial and current positions of atom  $i$  respectively (all periodic boundary conditions being removed).

The gradient of the MSD plot is directly related to the self-diffusion coefficient ( $D$ ) for the atomic species of interest:

$$MSD(t) = 2dDt, \quad (2.21)$$

where  $d$  denotes the dimension of the system.

### Radius of Gyration and Chain End-to-End Distance

The mean-square radius of gyration  $\langle R_g^2 \rangle$  and average square chain end-to-end distance  $\langle l^2 \rangle$  are defined in terms of chain configurations by:

$$\langle R_g^2 \rangle = \frac{1}{N} \left\langle \sum_{i=1}^N |r_i - r_{cm}|^2 \right\rangle \quad (2.22)$$

$$\langle l^2 \rangle = \langle |r_i - r_N|^2 \rangle \quad (2.23)$$

where  $\langle \dots \rangle$  denotes both a time average and an average over all polymer chains;  $r_i, r_N$  are the position vectors of the  $i$ th monomer unit;  $r_{cm}$  is the centre of mass of the polymer.

#### 2.1.6 The DL\_POLY Molecular Simulation Package

The DL\_POLY software package is considered as the most convenient for the applications discussed in the current work. DL\_POLY<sup>2</sup> is a general purpose parallel molecular dynamics code developed at STFC Daresbury Laboratory, Warrington, UK [61]. DL\_POLY is a package of subroutines, programs and data files, designed to facilitate MD simulations of macromolecules, polymers, ionic systems and solutions on a distributed memory parallel computer. It is available in two forms: DL\_POLY Classic [68] and DL\_POLY 4 [61]. The two forms differ primarily in their method of exploiting parallelism. DL\_POLY Classic uses a Replicated Data (RD) strategy [69] which works well on simulations of up to 30,000 atoms on up to 100 processors. DL\_POLY 4 is based on the Domain Decomposition (DD) strategy [70], and is best suited for large molecular simulations from  $10^3$  to  $10^9$  atoms on large processor counts. The two packages are reasonably compatible, so that it is possible to scale up from a DL\_POLY Classic to a DL\_POLY 4 simulation with little effort. DL\_POLY offers 14 MD integration algorithms, supports 13 different force fields and accommodates 5 different choices of boundary condition. Therefore the tasks that can be fulfilled within DL\_POLY and the nature of the explored systems can have vast variety.

For a typical simulation, DL\_POLY Classic requires three input files: a) The CONFIG file which includes all of the spatial coordinates of every atom in the system in a Cartesian form and the projection of the vectors defining the simulation box; b) the CONTROL file which contains the parameters defining the type and duration of the simulation and the thermodynamics state of the system; c) the FIELD file which contains the values of the parameters describing the force field(s) that define the simulation system. During a simulation, all of the observable variables are printed in the OUTPUT file. Simultaneously, the STATIS and HISTORY files collect statistical data and trajectory information, respectively. By the

<sup>2</sup><http://www.scd.stfc.ac.uk/SCD/research/app/44516.aspx>

end of the simulation, the new geometry of the system in Cartesian space, is summarised in the REVCON file.

In order to fully exploit the capabilities of the parallel MD DL\_POLY codes, a parallel computing facility is required. The modelling group at Sheffield Hallam University (SHU) has good access to a relatively powerful Beowolf cluster. A Beowolf cluster comprises a group of normally identical, commodity-grade computers that are networked into a small local area network with libraries and programs installed which allow processing to be shared among the compute nodes. The result is a high-performance parallel computing cluster derived from inexpensive personal computer hardware.

For the most of results presented in this thesis, the The Beowolf cluster at Sheffield Hallam University has contributed two types of nodes - 15 ‘Hal’ with 4 cores (processors) each and 16 ‘Viglen’ with 12 cores each - a total of 252 cores. The communication between the nodes has been fulfilled using a fast QDR Infiniband switch which allows transfer of data at high speeds (up to 36 Gbit/s). The estimated computer performance of the cluster in this configuration is approximately 1.8 TFLOPS (for **F**loating-point **O**perations **P**er **S**econd) – this allows simulation of large and complex systems over long time-scales whilst avoiding data storage / retrieval and queuing complications associated with use of national high performance computing facilities.

### 2.1.7 Visualisation

Visualisation provides crucial qualitative insight into the emergent properties of composite simulations. The dynamics of constituent particles is a key factor to the macro-scale behaviour of composite materials. Since the modelled systems consist of tens or hundreds of thousand of particles, it is necessary to use visualisation tools that can load a large amount of data, and be able to render particles’ representations effectively and smoothly. The Visual Molecular Dynamics (VMD)<sup>3</sup> software package is aimed at dealing with large MD simulation scenes of this sort. [71].

It is a cross-platform open source visualisation application that is created to model and visualise micro-biological systems such as proteins and enzymes. VMD can handle various file formats, including those that are produced by DL\_POLY, and render a scene efficiently by treating atoms and bonds as primitive spheres and cylinders. The main advantage of VMD over other MD visualisation packages is its embedded command line interpreter and various plugins and algorithms, such as z-buffering and volume-clipping, which, in turn, can accelerate the rendering process. With these multiple tools, one can create scripts to set up and render the visualisation of a scene such that the simulated system is presented in a most effective way.

---

<sup>3</sup><http://www.ks.uiuc.edu/Research/vmd/>

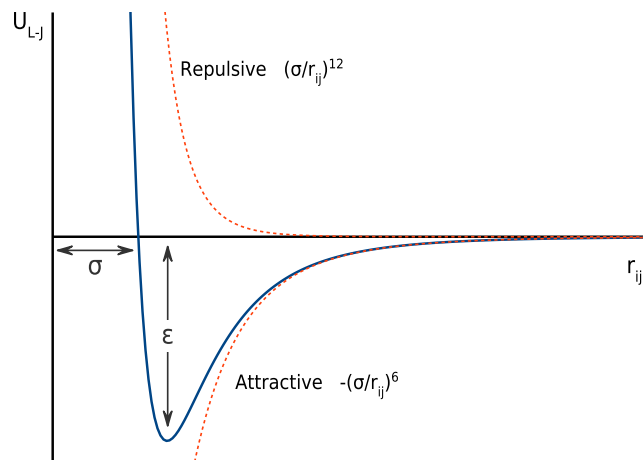


Figure 2.4: The Lennard-Jones potential and its repulsive ( $\alpha r^{-12}$ ) and attractive ( $\alpha r^{-6}$ ) component

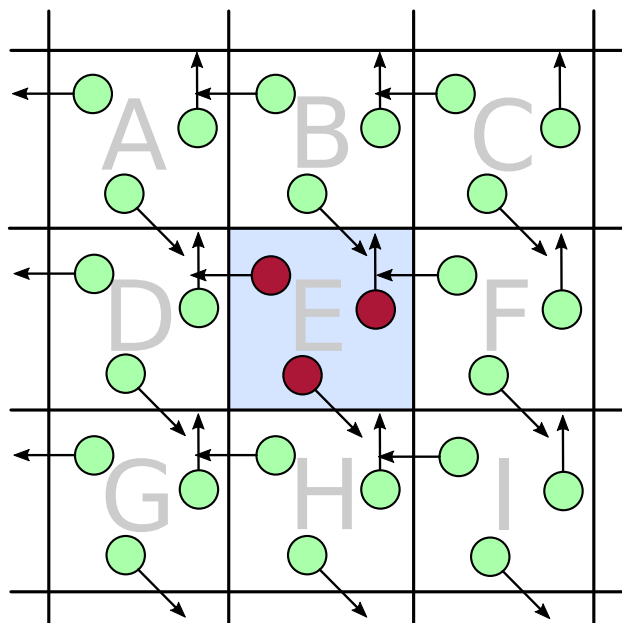


Figure 2.5: A schematic representation of periodic boundary conditions in two dimensions

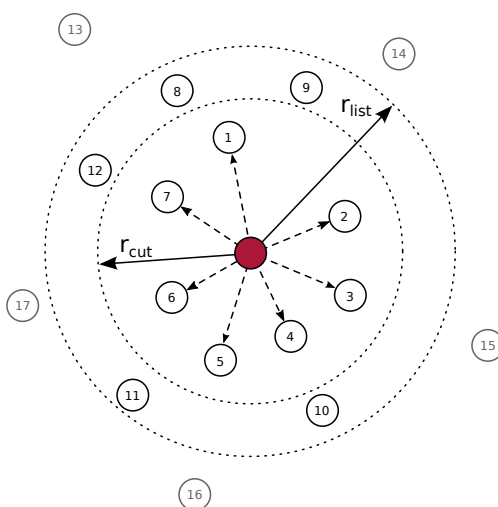


Figure 2.6: The cutoff sphere and the Verlet neighbour list skin around a central particle. Particles 1-12 are in the list of central particle. Only particles 1-7 are within the range of the potential

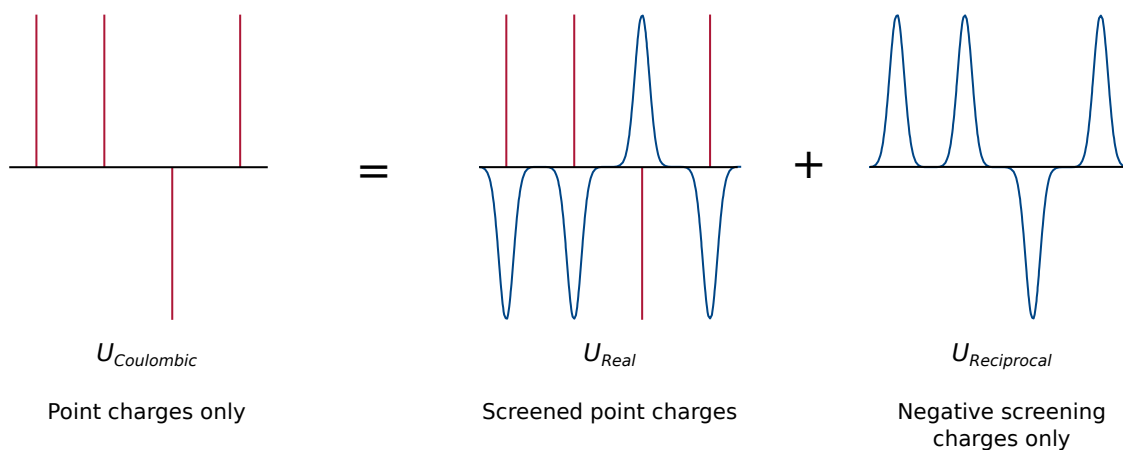


Figure 2.7: Schematic diagram of the series used in the Ewald summation method. The total Coulombic contribution to the non-bonded potential is calculated from two sums: the  $U_{real}$  sum consists of point and smoothly varying screening charges (performed in real space); and the  $U_{reciprocal}$  sum of smoothly varying screening background (adapted from [6])

## 2.2 Force fields

In the beginning of section 2.1, the concept of a force field was given in respect to computer simulations. The polymer/clay composites that are investigated in this thesis consist of organic polymers, clays and water. Thus, selecting an appropriate set of force fields for the corresponding components of this nanocomposite is essential to obtaining credible results. In the following sections, we will present some historical development, functional form and description of potentials used for simulation clays and their blends, with water and organic materials. Since clay potentials are less well established than those for water and organics, this is the key model selection for this thesis work. The compatibility of the water and organic models with the chosen clay model and capability to exhibit the classes of behaviour expected in the systems to be studied will be justified in section 2.2.5 of this thesis.

### 2.2.1 Force Field for Clays Minerals

While molecular simulations of organic materials is a well developed research area, only comparatively recently has simulation of clay minerals techniques developed to a state where it is able to reproduce the mechanical and chemical properties of all clay minerals. Importantly, in the context of this thesis, it has also proved able to produce robust results when the clay is interacting with other phases (e.g. water, organic molecules and exchangeable cations). The current section will address the history of clay force field development as well as architectural implementations and limitations of these computational models. Towards the end of the section, details of force field that has been used throughout this thesis will be given.

The very first computational model of montmorillonite was developed by Skipper, Refson and McConnel in 1991 [47]. It was used to simulate the structure of interlayer water in the presence of two exchangeable cations –  $\text{Na}^+$  and  $\text{Mg}^{2+}$ . The computational approach used considered only intermolecular potential interactions, and to model a clay-water-cation system, six different sets of interaction potentials were required (water-water, water-cation, clay-water etc.). The clay-water interactions were based on the discrete MCY water model [72]. Skipper et al. positioned a water molecule on each site where basal oxygen was found at the clay surface, and directed the hydrogen atoms towards the silicon sites. The potentials used were, therefore, based on the assumption that the electronic structure of an oxygen atom bonded to two silicon atoms is similar to that bonded to two hydrogen atoms in water. In order to avoid artificial "edge effects" being induced by a finite system size, the simulation cell was replicated periodically in space so to mimic the system in nature [47]. Due to the intermolecular potentials used, all atoms in the clay layer had to be immobile, the unit cell of montmorillonite being represented by an ideal crystallographic cell of pyrophyllite with some level of isomorphous substitution in the octahedral sheet to induce the layer charge. This approach showed reasonable accuracy in calculation of the water absorption isotherm. This model went on to be widely used for Monte Carlo and Molecular Dynamics calculations of the hydration dynamics [46, 73–75], structure of interlayer water in Mt [46–48, 73, 76, 77] and diffusion of water and various interlayer cations [74]. The model was also used to approximate the free energy, entropy of hydration and swelling isotherms of Mt with different exchangeable

cations in the interlayer [78–80].

A major advantage of Skipper’s model is its computational efficiency, which was largely achieved from the movement restrictions imposed on the atoms comprising the clay layer. However, it should be noted that, this approach may change the mobility of interlayer molecules, especially if their oscillation frequencies match those of the clay surface. Another limitation of the model is the fact that hydrogen bonds are not taken into account. This can introduce a significant change in the behaviour of absorbed material closest to the clay surface. Lastly, this Mt model cannot be used for thermomechanical analyses as it cannot reproduce thermal expansion of the clay layer. As a result, validation of the computational model can be difficult because comparing it to the experimental techniques such as IR-spectroscopy would not be possible.

In 1992 Kawamura introduced atom-atom potentials for computer simulation of multi-component oxides and, in particular, phyllosilicates [81]. The proposed force field was based on three pair-wise interaction potentials including electrostatic interactions, short range VDW interactions and bond stretch interactions described using the Morse potential (Section 2.1, Bond Stretching). A three body interaction or angle bend potential was introduced only for the H-O-H valence angle. Although the model was not extensively used, it was successfully applied for the investigation into the effects of various salts on the hydration process of Mt [82].

Five years later, Teppen et al. [7] demonstrated an alternative approach to the development of a clay force field. Unlike previous semi-empirical methods, it was based on an extensive analysis of experimental X-ray diffraction data and charge assignment from quantum mechanical calculations. In their approach, Teppen et al. chose to develop covalent-type potentials for all of the clay mineral atoms and also addressed the issue of octahedral coordination. In the clay minerals described in Chapter 2, aluminium atoms are octahedrally coordinated by oxygen which results in O–Al–O angles near both  $90^\circ$  and  $180^\circ$ . This is generally not easily modelled by computational techniques as it is difficult to find a function that can characterise these two states simultaneously [7]. The inclusion of cubic and quartic terms to the angle-bending potential (Section 2.1, Angle Bending Potential) was required to create the necessary anharmonicity of the potential function (Fig. 2.8). Most unique in this study, however, was the use of an O–Al–O angle bend potential to simultaneously treat both tetrahedrally and octahedrally coordinated aluminium. Prior to the Teppen et al. [7] study there was no published force field that could be used to properly evaluate this structural peculiarity of clay minerals. The developed set of bonded terms was successfully used to simulate several clay minerals and adsorption of organic materials in their interlayers [30, 83–85].

Despite the fact that the resultant force field showed good performance in simulating several clay structures including gibbsite, kaolinite, pyrophyllite and smectite, transferability proved a major problem in the practical implementation of this force field. Modelling of real polymer/water/clay composites involves the description of complex and poorly characterised crystal structures with low symmetries, large unit cells, variable interlayers and interfaces [18]. For such systems, utilisation of bonded force fields can lead to over-parametrisation due

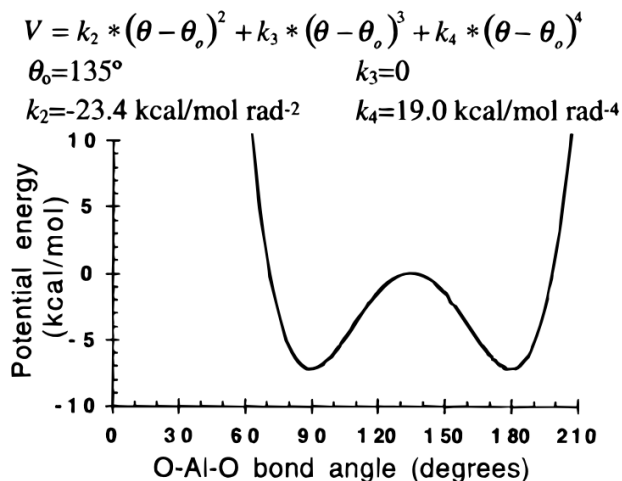


Figure 2.8: Octahedral O–Al–O angle-bending potential that allows multiple equivalent minima [7]

to a lack of relevant experimental data needed to meaningfully constrain the large number of force field parameters necessary to describe all bonded interactions.

Just over a decade ago Cygan, Liang and Kalinichev succeeded in overcoming these problems by designing an organic compatible force field called CLAYFF [18]. Unlike Teppen’s covalent approach, CLAYFF is based on an ionic (nonbonded) description of the metal–oxygen interactions. Also, it does not rely on quantum-mechanical calculations alone, but also incorporates a set of experimental crystal structure refinements in the parametrisation of the empirical force field. The functional form of the CLAYFF force field and its bonded and nonbonded parameters are listed in the Appendix A.

The CLAYFF force field uses bonded potential parameters from the SPC water model, by Berendsen et al. [86], to describe the hydroxyl and oxygen–oxygen interactions (Table A.6). Metal–oxygen interactions associated with hydrated phases are described by the conventional L-J (12-6) function with the Lorentz-Berthelot mixing rule applied. Parameters for the L-J function are optimised on the basis of known structures of simple oxides and hydroxides. For example, quartz ( $\alpha$ -SiO<sub>2</sub>), corundum ( $\alpha$ -Al<sub>2</sub>O<sub>3</sub>), boehmite ( $\gamma$ -AlO-(OH)) and gibbsite ( $\gamma$ -Al(OH)<sub>3</sub>) were used to derive optimum values for Si–O and Al–O interaction values [18]. These empirical nonbonded interaction parameters are provided in Table A.5 of Appendix A. An additional distinct feature of CLAYFF is the incorporation of three-body terms to describe metal adsorption on hydrated surfaces and to improve the vibrational behaviour of hydroxyl groups. This is described by a harmonic function, the optimal parameters for which were determined through an iterative process in which the results of MD simulations were compared with infrared spectra of gibbsite and portlandite (Table A.6).

As discussed in the Section 1.1.1 (The Layer Charge), delocalisation of layer charges occurs due to isomorphic substitution of metal species in the octahedral or tetrahedral clay sheet. This difficult to implement behaviour was another innovative feature of the CLAYFF force field. Partial charges for all atoms were initially assigned on the basis of the ESP method and were subsequently modified for nearest neighbour oxygens associated with substituting metal. The variation of partial charges was finally determined by density function

theory (DFT) calculations for structures derived from pyrophyllite clay with octahedral and tetrahedral substitutions. Atom charges corresponding to various positions in the clay layer are provided in the Table A.5.

Some authors, including developers of the CLAYFF model, performed tests to compare the CLAYFF potential model and DFT ab-initio method in predicting structural and vibrational properties of various phyllosilicates [8, 15]. This was done to probe the ability of CLAYFF to simulate realistic crystallographic parameters of clay minerals. Figure 2.9(a) suggests that the CLAYFF potential model over-idealises the hexagonal rings on the mineral’s surface. The structure derived from DFT (Figure 2.9(b)), on the other hand, is much more similar to the experimental structure of pyrophyllite discussed in Section 1.1.1.

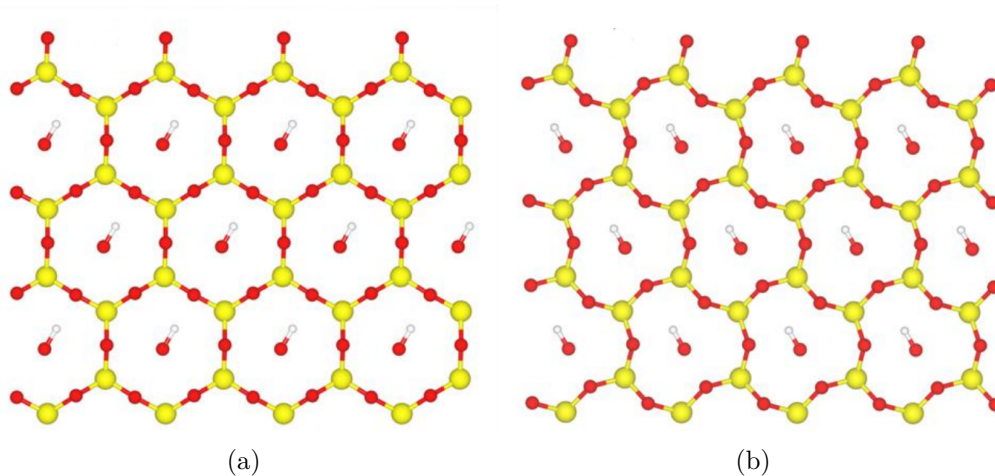


Figure 2.9: Structure of (001) surface of pyrophyllite minimised by (a) CLAYFF model and (b) DFT ab-initio method. Colours: O red; Si yellow; H white [8]

Simulated bond lengths of pyrophyllite are compared with experiment in Table 2.1. Each atom is classified by the atom type definitions reported in Table A.6. The average modelled bond lengths and angle bend distributions of the clay structure are all within 5% of experiment. The average orientation of the hydroxyl groups relative to the mineral surface plane predicted from DFT simulations is  $28\pm 16^\circ$ , while the mean CLAYFF angle is reduced down to  $15\pm 21^\circ$ . The experimentally measured muscovite (derivative of pyrophyllite structure) [87] OH angle distribution of  $16^\circ$  supports the CLAYFF results for pyrophyllite [15]. Therefore, CLAYFF yields a reasonably accurate description of the bulk structural properties of clay minerals.

Table 2.1: CLAYFF and DFT pyrophyllite bond lengths ( $\text{\AA}$ ) compared with experiment [15]

	ao-oba	ao-oh	ob-st	oba-st	oh-ho
CLAYFF	$1.98\pm 0.08$	$1.98\pm 0.08$	$1.56\pm 0.03$	$1.62\pm 0.04$	$1.03\pm 0.03$
DFT	$1.92\pm 0.06$	$1.89\pm 0.05$	$1.62\pm 0.03$	$1.63\pm 0.03$	$0.97\pm 0.01$
Experiment	1.90	1.92	1.61	1.63	

The relative simplicity, computational efficiency and performance of the CLAYFF force field makes it a very popular choice when simulating phyllosilicates of various types. It

has shown good performance in predicting the structure of kaolinite, pyrophyllite, montmorillonite and many other minerals [18] as well as in reproducing vibrational spectra of pyrophyllite and hydrotalcite under normal conditions [18] and under strain [88]. This force field has also been successfully used for mechanical characterisation of clay layers [89–93], simulation of clay/organic interfaces [94–98] and even in the study of electrical conductivity in montmorillonite layers [99]. Validation of the choice of potential models and clay–organic–water interactions will be discussed further in Section 2.2.5.

### 2.2.2 Force Field for Water

Discussion of the force fields available for computer simulation of water could be the topic of a separate thesis. Martin Chaplin of London South Bank University has constructed a database containing over 120 different water models [100], about 30 of which are routinely used by various research groups. Extensive reviews of different water models by the Vega group [101] and Bertrand Guillot [102] provide valuable insight into over 30 years of water simulation history, as well as model applicability and limitations.

For the purposes of this thesis, however, a water potential model, known as TIP3P/Fs was utilised [16]. This is a simple flexible three-point, non-polarisable model, intermolecular interaction of which includes harmonic bond-stretching and bond-bending potentials. Nonbonded interactions are described using the L-J function, two parameters of which were chosen to reproduce the density and pressure of water at room temperature [101]. It is quite often used to describe water interactions in systems including organic molecules. Bonded and nonbonded parameters of TIP3P/Fs model can be found in Appendix A.

### 2.2.3 Force Field for Organic Materials

The organic molecules are parameterised using the so called GAFF force field [17] which started off as part of the (AMBER) Assisted Model Building with Energy Refinement) project [103].

The GAFF force field is widely used for simulation of proteins, nucleic acids and simple chain polymers. In reality, there is very little difference between the GAFF and AMBER potentials and they can be used interchangeably. GAFF is designed specifically for smaller molecules. Here, bond stretch and angle bend potentials are represented by a harmonic expression, the VDW interactions are represented by a L-J potential and electrostatic interactions modelled by a Coulombic form which assumes that the influence of the protons and electrons in a given atom can be represented by a single point charge (Appendix A).

The potential used for polymeric materials was set up using the AmberTools package [57]. This is a powerful software suite that contains a set of programs for biomolecular simulation and analysis which are designed to work well together. In particular, energy minimisations (geometry optimisations) and partial charges of organic molecules were derived using a quantum chemistry program called *sgm*. Then the potential set was converted from AMBER to DL\_POLY energy units and the FIELD file was generated.

The functional form, along with the bonded and nonbonded parameters of the resultant AMBER potential are given in Appendix A.

#### 2.2.4 Deriving Cross Terms

Description of the non-bonded interactions between organic and inorganic systems can be challenging in MD as one often has to deal with different types of force field used to model the two systems. A system containing  $N$  different types of atom would require  $N(N - 1)/2$  sets of parameters for the interaction between unlike atoms [54]. As calculation of the van der Waals parameters may be a time consuming process, it is common to assume that parameters for the cross interactions can be obtained from the parameters of the pure atoms using *mixing rules*. In this work, the Lorentz-Berthelot [104, 105] mixing rules were used in order to generate the required potentials, as it has previously shown good performance for the combination of CLAYFF and AMBER force fields. The collision diameter  $\sigma_{AB}$  for the A–B interaction is represented as the arithmetic mean of the values for the two pure atoms, and the well depth  $\varepsilon_{AB}$  is given as the geometric mean [6, 54, 55]:

$$\sigma_{AB} = \frac{1}{2}(\sigma_{AA} + \sigma_{BB}) \quad (2.24)$$

$$\varepsilon_{AB} = \sqrt{\varepsilon_{AA}\varepsilon_{BB}} \quad (2.25)$$

A table with calculated parameters for the intermolecular interactions can be found in Appendix B.

#### 2.2.5 Validating the Potential Models

As noted in previous section, incorporation of organic interactions within the CLAYFF force field may be challenging, especially when dealing with hydrated mineral surfaces. Freeman et al. [9] provided a systematic approach of combining water-organic-mineral interactions in their model. This utilised a model developed by Pavese et al. [106] to parametrise a calcite surface, the AMBER potential to represent the organic interactions and the TIP3P water model. This choice of water model eliminated any requirement to refit water-organic interactions, as TIP3P is incorporated within the AMBER potential. Firstly, their method involved using Schröder’s equation [107] to refit existing potentials to mineral structures so as to achieve consistency with the Coulombic interactions between the mineral and non-mineral atoms. Secondly, all of the surface interactions were generated by fitting a L-J potential to the Buckingham surface oxygen-oxygen potential and mixing with Lorentz-Berthelot rules. This approach showed great success in parametrising water-organic-mineral interactions, leading to it being adopted, by other researchers [8, 94–96]. With this in mind, it was decided to follow a similar strategy in constructing the water-organic-mineral interactions used in this work.

In terms of mixing between the models, the interactions between the TIP3P/Fs and AMBER potential sets are justified as they are designed to work together. The parameters required to combine TIP3P/Fs and CLAYFF force fields are established as well, because the adsorption energy of a water molecule on the (001) surface of pyrophyllite TIP3P was calculated to be -0.14 eV, which is identical to the value when CLAYFF’s own SPC/E water model is used [108]. Whilst organic-clay systems are less well studied than water-clay there is some recent literature. In particular, Shapley and Parker have performed a significant

number of DFT calculations to assess the mixing rules between CLAYFF and AMBER, and found them to be acceptable. [8].

Motivated by this, various organic molecules were selected and their adsorption energies on the pyrophyllite and NaMt surfaces were calculated and are presented in Table 2.2. In broad view, a good agreement between the potential model and DFT calculations was observed. The adsorption energies of pyridine and thiophene and, more importantly for the purpose of this thesis, ethylene glycol on either mineral surface show excellent agreement.

Table 2.2: Comparison of adsorption energies of organic molecules onto pyrophyllite and Na-montmorillonite using both the potential model and DFT methods [8]

Molecule	Adsorption Energy (eV)					
	Pyrophyllite			Na-Montmorillonite		
	Model	DFT	Deviation (%)	Model	DFT	Deviation (%)
ethylene glycol	-0.48	-0.50	4.0	-0.63	-0.61	3.3
benzene	-0.29	-0.28	3.5	-0.62	-0.86	27.9
pyridine	-0.31	-0.32	3.1	-0.88	-0.86	2.3
thiophene	-0.26	-0.29	10.3	-0.71	-0.76	6.5

Similarly, Freeman et al. performed a computational experiment of adsorbing dimethylether onto a calcite surface (Figure 2.10) [9]. Here, the absorption well depths were found to be within 0.02 eV and the process of decaying to zero at larger separations showed very good consistency. The main difference between the potential model and ab-initio calculations was found in the range of very small separations where DFT calculation predicted a steeper well than those seen in the potential model. All aforementioned differences may come from the difficulty with optimising the position of the organic molecules on the complex mineral surfaces.

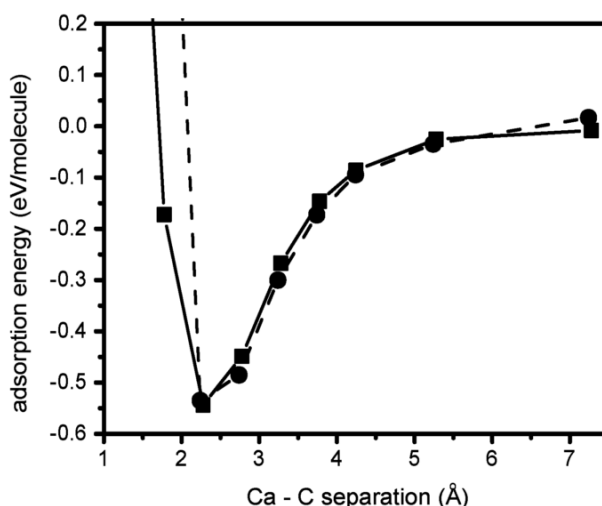


Figure 2.10: Comparison of adsorption energies for a dimethylether with a calcite surface calculated with potential model (squares) and DFT method (circles) [9]. The Ca-C separation is the distance between molecular carbon and the calcite surface

The CLAYFF force field displays reasonable agreement with DFT calculations for the

adsorption of organic materials onto mineral surfaces and, therefore, it appears to be fit for purpose in terms of this thesis. Hence, the following chapters will be focusing on the use of the CLAYFF force field to probe the dynamics of polymer/clay nanocomposites.

## 2.3 Experimental Techniques

Part of this PhD study was based on experimental results that were acquired by the candidate. These were obtained to validate computational models and inform on the interplay of experimental and simulation techniques. The broader aim here was to gain better understanding of the processes involved in real polymer/clay composite formations.

### 2.3.1 X-ray Diffraction Analysis

Possibly the most extensively used technique in the study of clay minerals and associated swelling behaviour of polymer/clay nanocomposites is X-ray diffraction (XRD) [36]. It is a non-destructive analytical technique used for identification of various crystalline forms of powders or solid samples. As a result, the XRD method is widely used to monitor the interlayer spacing (basal  $d_{001}$ -spacing) of clay mineral layers. The swelling profile can be obtained by measuring X-ray diffraction curves of the clay at increasing relative humidity or water content [38, 109]. Whilst it is effective for determination of interlayer spacings, the main limitation of XRD analysis is lack of information it yields regarding the arrangement of interlayer species or interactions of these species with the clay layers. Therefore, significant care should be taken when interpreting the XRD results.

X-rays are a form of high energy electromagnetic radiation with wavelength ranging from 0.1 to 100 Å. Figure 2.11(a) schematically describes an X-ray diffractometer. It is generally consists of an X-ray tube which generates radiation by targeting electrons onto a metal target, a detector which is rotated to receive the signal from X-rays reflected from a sample, which is supported so that its rotation through an angle  $\Theta$  is accompanied by a  $2\Theta$  rotation of the detector.

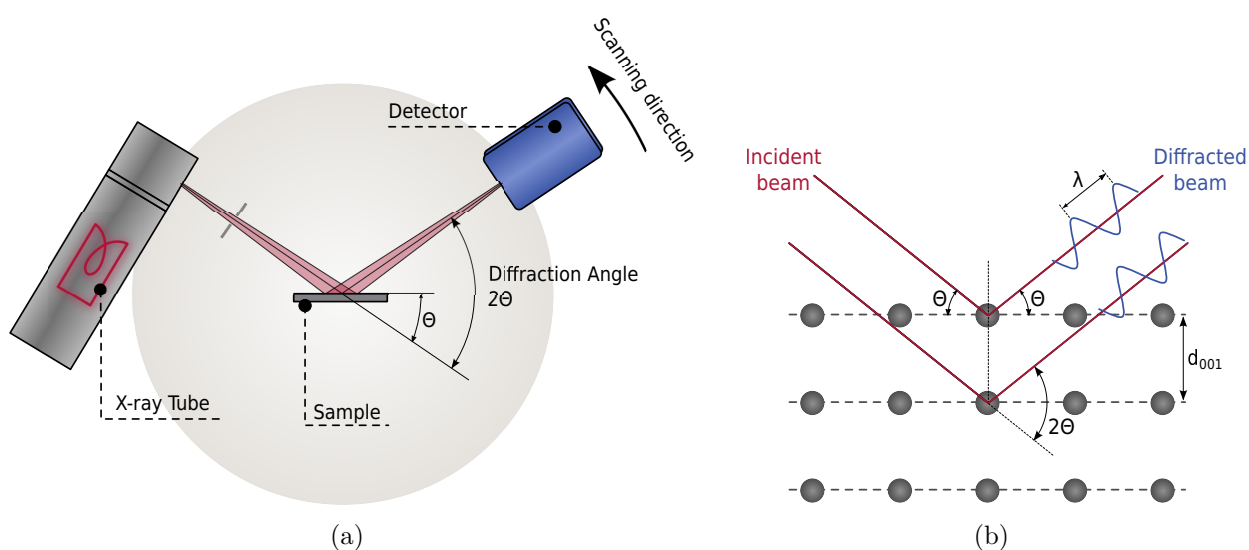


Figure 2.11: (a) Schematic diagram of an X-ray diffractometer; (b) Bragg's condition

Systems that have a certain level of order or a regular three dimensional array of atoms,

molecules or layers, scatter X-rays such that diffracted beams from two adjacent arrays positively interfere with each other giving a strong signal on the detector (Fig. 2.11(b)) [35]. Diffraction only occurs if the Bragg equation is satisfied for a particular family of planes:

$$n\lambda = 2d \sin \Theta, \quad (2.26)$$

where  $n$  is the order of diffraction,  $\lambda$  is the X-ray wavelength,  $d$  is the distance between reflecting planes and  $\Theta$  is the diffraction angle.

The interplanar distance, or in the case of this study, the interlayer spacing of the clay is then calculated from the position of the 001 peak using Bragg's law as follows:

$$d_{001} = \frac{n\lambda}{2 \sin \Theta} \quad (2.27)$$

In this study, all XRD measurements were undertaken on a X'Pert Pro Diffractometer, Philips. A copper tube  $\text{CuK}_\alpha$  (1.54186 Å) as the source of X-rays was used with current and voltage of 40 mA and 40 kV applied to it respectively. A divergent slit of  $0.5^\circ$  and anti scatter slit of  $1^\circ$  were used. Data was collected in the  $2\Theta$  range of  $2\text{--}45^\circ$  with step size of  $0.02^\circ$  and a scan time of 1 second per step.

### 2.3.2 Thermogravimetric Analysis

Thermogravimetric analysis (TGA) is a technique used to measure the weight change of a sample as a function of increasing temperature or isothermally as a function of time. Most TG curves display weight losses due to the evaporation of volatile products (Fig. 2.12). Additionally, useful information on the rate of weight loss provides a negative first derivative curve of weight loss  $W$  with respect to temperature  $T$  or  $-dW/dT$ . Thermogravimetric analysis can reveal the distribution and the amount of water or organic material in a polymer/clay composite sample which, in turn, can be used to understand the swelling process.

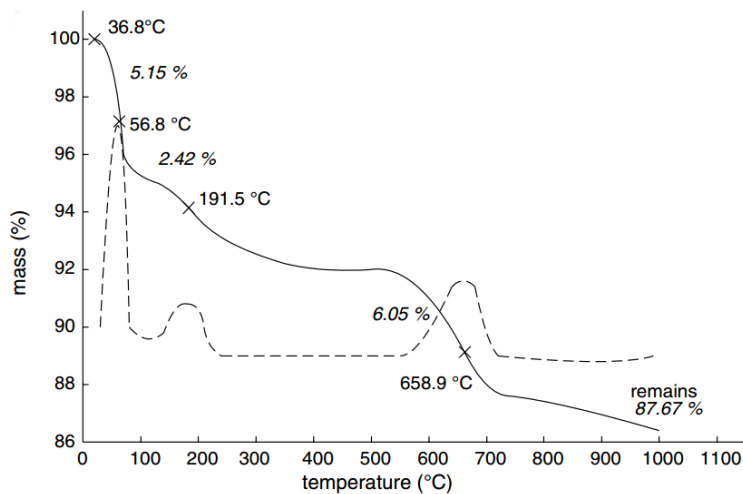


Figure 2.12: Thermogravimetric analysis (direct curve and derivative) of a saturated Na-montmorillonite showing two low temperature dehydration stages and the dehydroxylation stage [2]

TGA relies on a high degree of precision in three measurements: mass change, temperature and temperature change. Therefore, it consists of several basic components including a precision balance, a crucible loaded with the sample and a programmable furnace.

In this study, a Mettler Toledo TG50 Thermogravimetric analyser was used with crucibles made of alumina. Samples with mass of  $5 \pm 0.1$  mg were heated from 30 to 800 °C at a rate of 20 °C/min. Nitrogen was constantly purged through the furnace chamber with a flow rate of 40 mL/min. To minimise the amount of water vapour on the crucible, a "normalisation process" was utilised. In this, samples were kept at 35 °C for 15 minutes prior to measurements being undertaken.

### 2.3.3 Thermogravimetry Mass Spectrometry Analysis

Thermogravimetry Mass Spectrometry (TGMS) is a technique which is used to determine the elemental composition of a measured sample. It involves ionisation of chemical compounds, to produce charged molecules or molecular fragments, and then measurement of their mass to charge ratio. TGMS instruments are partially similar to TGA instruments. Additionally to a TG furnace, a TGMS instrument comprises an ion source, a mass analyser and a detector. The furnace is used to heat the sample in the same manner as that described in the previous section and results in the desorption of species or the creation of volatile products. The ion source is used to convert the evolved gas phase molecules into ions. The mass analyser separates ions by their mass to charge ratio by applying electromagnetic fields. Finally, the detector is used to count the number of ions hitting the detector over a period of time.

## 2.4 Chapter Summary

In this chapter, the main simulation techniques applied to model polymer/clay composite behaviour have been briefly reviewed. The main focus on the MD simulation method with particular attention being paid to the variety of potential models, their performance and functional forms. Careful selection of simulation parameters is crucial to obtaining trustworthy results in simulation.

The culmination of the chapter is the section Validating the Potential Models, where a justification of model choice was presented. The creation of a reliable and flexible model that can be applied to a range of interfaces has been presented. Arguably, this can be considered as proof of concept and that the potential model could be applied to almost any water-organic-mineral interface.

In conclusion brief details of experimental work performed on polymer/clay systems has been given. In the following chapters, potential model of polymer/clay nanocomposite will be used to probe more complex and realistic bilayer systems.

### 3 Hydration of Clay Layers

The most important surface interactions in phyllosilicate minerals occur when liquid water is in contact with clay surfaces [37]. An understating of these interactions requires not only information about the structural chemistry of the mineral but also energetic characterisation of the constituent particles, the exchangeable cations, for instance. The formation of polymer/clay nanocomposites always involves hydration of the mineral’s surface or the polymer itself to some extent. Taking into account the fact that hydration of interlayer cations is the main driving force in the process of adsorption of water by clays [1], the importance of understanding this phenomenon at a molecular level becomes evident. In particular, the influence of the clay’s structure on the thermodynamics of this hydration process is a key factor.

Previously reported simulation data investigating the effect of layer charge location and magnitude on hydration is limited, and some of the conclusions drawn are contradictory. For instance, Skipper et al. reported that the basal spacing of tetrahedrally charged NaMt increase more than that of octahedrally charged clay [48]. Liu et al., however, reported that the basal spacings of tetrahedrally and octahedrally charged CaMts were indistinguishable within the reported error [110]. The more recent investigation of Greathouse et al. [11] further extended this result to NaMt, where it was reported that clay charge location has an influence on the interlayer structure of montmorillonite hydrates.

The previous chapters have been concerned with introducing the themes and methods of this thesis. In this and the two succeeding chapters the results of the thesis are addressed. Here we use the atomistic MD approach to investigate the effect of the layer charge location and magnitude on the hydration properties of a range of clay minerals. One aim of this work is to establish a set of simulation and analysis protocols for such systems, based on utilisation of the DL\_POLY package. A more scientific aim is to relate simulation and experimental results for swelling–deswelling behaviour of clay, and gain a molecular level understanding of such behaviour. The specific objectives are to characterize the structure and energetics of  $\text{Na}^+$  and  $\text{Ca}^{2+}$  adsorption as functions of water content; the relationships between the coordination environments of clay surface–interlayer water–exchangeable cations; the influence of cation hydration energy on the dynamics and swelling mechanism of clays; and the influence of charge distribution on all of the above. Finally, establishing an understanding of these clay/water systems is viewed as a sensible foundation for the more complex systems considered later in this thesis.

#### 3.1 Simulation Details

Montmorillonite (Mt) was selected for this study, the model framework being generated from a pyrophyllite crystal structure based on that from Zhu et al. [95]. A total of eighteen Mt models were investigated with a selection of layer charge magnitudes, charge locations and two exchange cations ( $\text{Na}^+$ ,  $\text{Ca}^{2+}$ ). The network of negative layer charge was created by substituting  $\text{Mg}^{2+}$  for  $\text{Al}^{3+}$  in the octahedral sheet, giving rise to octahedral charge (Oh), or  $\text{Al}^{3+}$  for  $\text{Si}^{4+}$  in the tetrahedral sheet (Th charge). Mixed substitutions in octahedral and tetrahedral sheets (Oh/Th) were also considered. Charge sites were randomly distributed, but subject to the constraints of Lowenstein’s substitution rule whereby substitution sites cannot be adjacent to each other [111]. To balance the negative layer charge, an appropriate

number of  $\text{Na}^+$  cations were initially placed in the gallery between clay layers. To generate a CaMt structural model, every pair of  $\text{Na}^+$  cations in the initial model was replaced by a single  $\text{Ca}^{2+}$  cation. The structural formulas and net negative structural charges of the developed clay models are given in Table 3.1.

Table 3.1: Cation exchange capacity, charge location and chemical composition of clay models used in this work

CEC	Tetrahedral layer charge	$\text{Na}^+$	$\text{Ca}^{2+}$
87.0 meq (-0.625) <sup>a</sup>	0	$\text{Na}_{0.625}[\text{Al}_{3.375}\text{Mg}_{0.625}]\text{Si}_8\text{O}_{20}(\text{OH})_4^b$	$\text{Ca}_{0.312}[\text{Al}_{3.375}\text{Mg}_{0.625}]\text{Si}_8\text{O}_{20}(\text{OH})_4$
	0.312	$\text{Na}_{0.625}[\text{Al}_{3.688}\text{Mg}_{0.312}][\text{Si}_{7.688}\text{Al}_{0.312}]\text{O}_{20}(\text{OH})_4$	$\text{Ca}_{0.312}[\text{Al}_{3.688}\text{Mg}_{0.312}][\text{Si}_{7.688}\text{Al}_{0.312}]\text{O}_{20}(\text{OH})_4$
	0.625	$\text{Na}_{0.625}\text{Al}_4[\text{Si}_{7.375}\text{Al}_{0.625}]\text{O}_{20}(\text{OH})_4$	$\text{Ca}_{0.312}\text{Al}_4[\text{Si}_{7.375}\text{Al}_{0.625}]\text{O}_{20}(\text{OH})_4$
104.4 meq (-0.750)	0	$\text{Na}_{0.75}[\text{Al}_{3.25}\text{Mg}_{0.75}]\text{Si}_8\text{O}_{20}(\text{OH})_4$	$\text{Ca}_{0.375}[\text{Al}_{3.25}\text{Mg}_{0.75}]\text{Si}_8\text{O}_{20}(\text{OH})_4$
	0.375	$\text{Na}_{0.75}[\text{Al}_{3.625}\text{Mg}_{0.375}][\text{Si}_{7.625}\text{Al}_{0.375}]\text{O}_{20}(\text{OH})_4$	$\text{Ca}_{0.375}[\text{Al}_{3.625}\text{Mg}_{0.375}][\text{Si}_{7.625}\text{Al}_{0.375}]\text{O}_{20}(\text{OH})_4$
	0.750	$\text{Na}_{0.75}\text{Al}_4[\text{Si}_{7.25}\text{Al}_{0.75}]\text{O}_{20}(\text{OH})_4$	$\text{Ca}_{0.375}\text{Al}_4[\text{Si}_{7.25}\text{Al}_{0.75}]\text{O}_{20}(\text{OH})_4$
113.1 meq (-0.812)	0	$\text{Na}_{0.812}[\text{Al}_{3.188}\text{Mg}_{0.812}]\text{Si}_8\text{O}_{20}(\text{OH})_4$	$\text{Ca}_{0.406}[\text{Al}_{3.188}\text{Mg}_{0.812}]\text{Si}_8\text{O}_{20}(\text{OH})_4$
	0.438	$\text{Na}_{0.812}[\text{Al}_{3.625}\text{Mg}_{0.375}][\text{Si}_{7.562}\text{Al}_{0.438}]\text{O}_{20}(\text{OH})_4$	$\text{Ca}_{0.406}[\text{Al}_{3.625}\text{Mg}_{0.375}][\text{Si}_{7.562}\text{Al}_{0.438}]\text{O}_{20}(\text{OH})_4$
	0.812	$\text{Na}_{0.812}\text{Al}_4[\text{Si}_{7.188}\text{Al}_{0.812}]\text{O}_{20}(\text{OH})_4$	$\text{Ca}_{0.406}\text{Al}_4[\text{Si}_{7.188}\text{Al}_{0.812}]\text{O}_{20}(\text{OH})_4$

<sup>a</sup>Values in parentheses correspond to a layer charge expressed in  $e \cdot uc^{-1}$  ( $e$  is the elementary charge,  $uc$  is the  $\text{O}_{20}(\text{OH})_4$  based unit cell)

<sup>b</sup>Brackets denote atoms in octahedral and tetrahedral sheets for Mt respectively

The simulation supercell was constructed from two orthogonal clay layers each containing 32 unit cells in an  $8 \times 4$  expansion. The lateral dimensions ( $x, y$ ) for all simulated systems were approximately  $41.5 \times 36.0 \text{ \AA}^2$ , which was large enough to fit all the required water and organic molecules in the interlayer and avoid any gross finite size effects. The selected cell dimensions also allowed for a disordered distribution of substitution sites, such that the nearest distances between them were in the range 8 to 18  $\text{\AA}$ , to comply with experimental observations [1, 3]. A broad range of water concentrations, ranging from 0 to 0.41  $\text{g}_{\text{H}_2\text{O}}/\text{g}_{\text{clay}}$  (0 to  $\sim 33.74 \text{ H}_2\text{O} \cdot uc^{-1}$ ), were introduced between the clay layers (interlayer) to study the effect of the interlayer expansion and the hydration processes associated with same. The final supercell configuration with the lowest potential energy at each water content was chosen for subsequent equilibration and production runs.

Initially, each required interlayer water concentration was obtained by filling two interlayers with pre-equilibrated multiple replicas of water boxes containing 125 water molecules and equilibrated by NPT MD simulation without imposed periodic boundary conditions for 0.5 ns (Fig. 3.1, left). For each clay model, NPT simulations were performed under ambient conditions ( $T = 300 \text{ K}$ ,  $P = 1 \text{ atm}$ ) for 1 ns to achieve equilibration (Fig. 3.1, middle). Equilibration was identified through monitoring of the interlayer water density, basal spacing ( $d_{001}$ -spacing) and potential energy of the system (Fig. 3.2).

The density of pure TIP3P/Fs water simulated at ambient conditions with the NPT ensemble was calculated as  $0.998 \text{ g} \cdot \text{cm}^{-3}$ , which is identical to the value calculated by Vega et al. [101] and denoted as the blue dashed line in Figure 3.2. This water density can be considered as the target value for the diffuse central region in the interlayer space of clay – it represents a further indicator of equilibration of a system [112]. As shown by (Fig 3.2), other observables also reached statistical equilibrium within 250 ps simulation. Equilibration was

followed by a 0.5 ns NPT production run where a range of thermodynamic properties and cell dimensions were calculated to obtain the basal spacing of the clay interlayer.

Structural and dynamic properties were later determined from subsequent NVT simulations of a single interlayer, which was performed for another 1 ns. The initial atomic positions for the NVT simulations were taken from the previous NPT simulation but with 25 Å of vacuum added above the clay surfaces to eliminate the interaction between them through the periodic boundary condition (Fig. 3.1, right). The water density and basal spacing were monitored during the NVT simulations to make sure that they matched those obtained from the NPT simulations. One water interlayer region was removed from the simulation box in this way as this significantly improved the computational efficiency of the simulation without losing in the accuracy of obtained observables. This selection of thermodynamic ensembles and simulation approach was motivated by the success of previous authors in determining corresponding observables when simulating clay-water and clay-organic interactions [112].

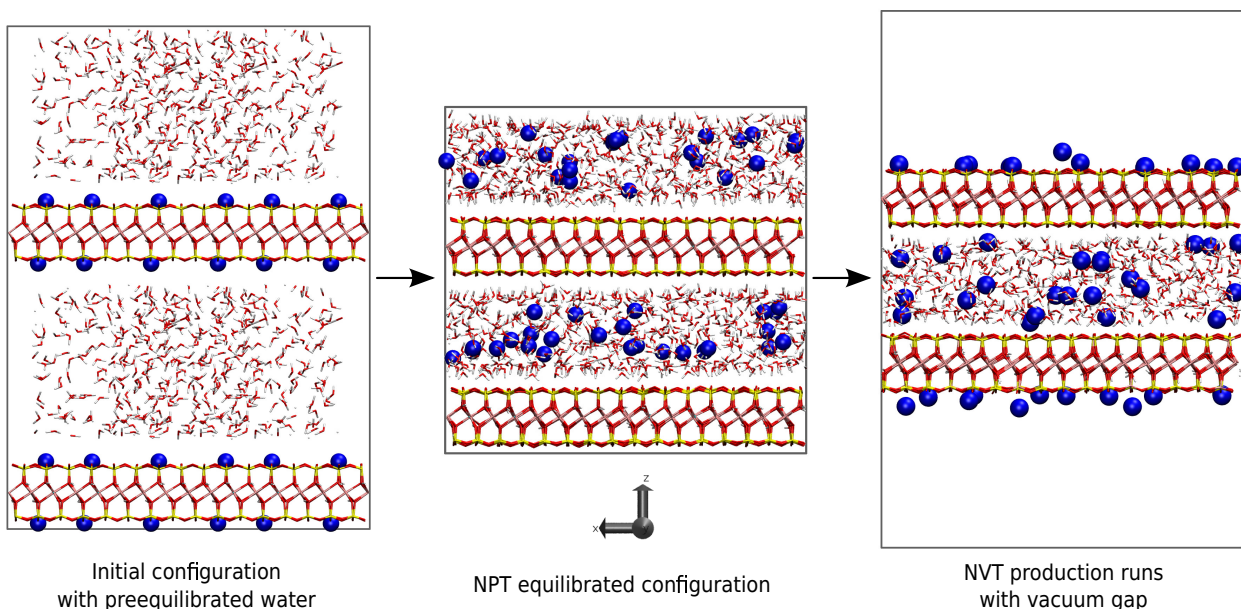


Figure 3.1: Construction and simulation flow of studied systems. Here a NaMt cell containing  $30.5 \text{ H}_2\text{O} \cdot \text{uc}^{-1}$  in the interlayers (460 water molecules in each interlayer) is shown. Colours: Na blue; Si, yellow; Mg cyan; Al pink; O red; H white

Molecular dynamics simulations were performed using the Nosé-Hoover thermostat and DL\_POLY simulation package with a 1.0 ps relaxation time. For the NPT simulations, a Nosé-Hoover barostat was utilised to control the pressure with a barostatic relaxation time of 1.0 ps. Interatomic interactions were evaluated using a time step of 0.001 ps, and three-dimensional periodic boundary conditions were employed with a cutoff of 15 Å for short-range interactions. Long-range electrostatic interactions were calculated using the Ewald summation (Sec. 2.1, Ewald Summation) with an accuracy of  $1 \times 10^{-6}$ . All MD simulations were performed at 300 K and at 1 atm for the NPT ensemble. Statistical and atomic position data were collected over 1 ns and stored every 25 ps to obtain thermodynamic and structural properties. The basal spacing was calculated by averaging the distance between planes formed by basal oxygen atoms at the top surface of each clay layer and reducing the interlayer

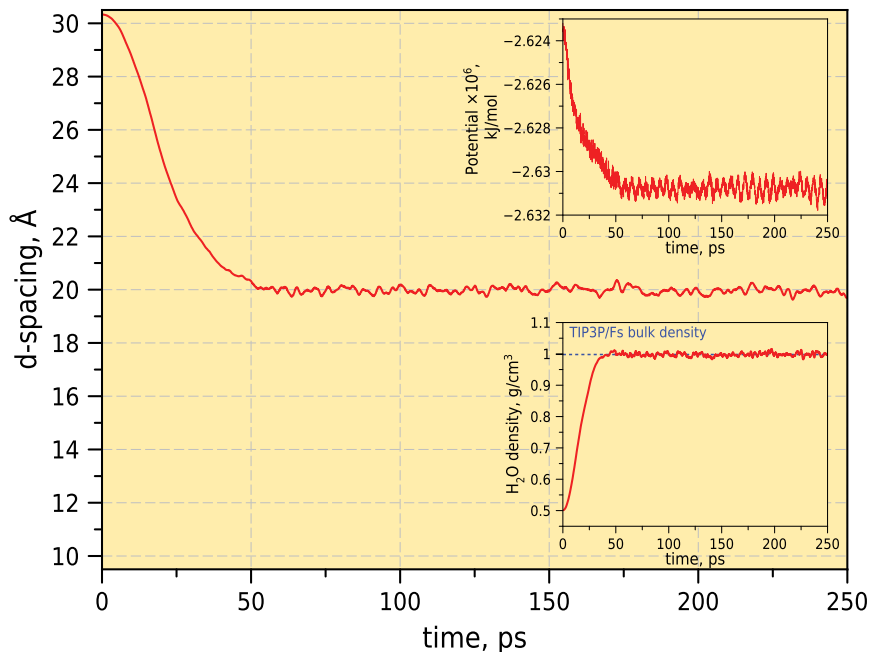


Figure 3.2: Basal spacing evolution of 104.4 meq NaMt clay model containing  $30.5 \text{ H}_2\text{O}\cdot\text{uc}^{-1}$  in the interlayers as a function of simulation time. First 250 ps of the equilibration process are shown

water content in decrement of 20 water molecules starting from an initial configuration with 540 water molecules ( $33.74 \text{ H}_2\text{O}\cdot\text{uc}^{-1}$ ) in the interlayer region. A number of swelling simulations (achieved by incrementally introducing water into the interlayer region) were then performed on the NaMt and CaMt systems. These gave identical montmorillonite structures and  $d_{001}$ -spacings as those observed for the series of de-swelling simulations. This lack of hydration-dehydration hysteresis provides reasonable reassurance that the examined final configurations were fully equilibrated. Therefore, due to the relative simplicity of the system configuration, further simulations were performed using the de-swelling approach.

### 3.2 Results and Discussion

The crystalline swelling, structure, thermodynamics and dynamics of the interlayer of montmorillonite at various water contents with respect to the type of exchangeable cation and clay layer charge configuration was studied using the MD simulation approach. In the following, comparison with previous theoretical and experimental results is presented. Novel results of the effect of layer charge on swelling and hydration properties of NaMt and CaMt are discussed later.

For a long time the clay mineral montmorillonite has attracted interest and found many applications because of its ability to absorb large amounts of water [38]. Mt expands when water is introduced into the interlayer region, thus reducing the electrostatic interactions between the negatively charged layers, while simultaneously, solvating the free interlayer cations and the clay surface. Increasing the quantity of interlayer water also leads to the development of a hydrogen-bonded network of water within the interlayer. This intrinsic behaviour of, in particular NaMt, clay was extensively studied both experimentally [10, 12,

38,44,113,114] and theoretically [7,11,18,47,115].

Figure 3.3(a) presents the results of the current series of simulations for the hydration of NaMt. The calculated basal spacing of clay is plotted as a function of water content along with experimental data. The results are in very good agreement, both qualitatively and quantitatively, and indicate that the swelling of clay layers occurs in a stepwise manner, with formation of plateaux around water contents of 0.1 and 0.2  $\text{g}_{\text{H}_2\text{O}}/\text{g}_{\text{clay}}$ .

For CaMt, comparison with experimental swelling curves is challenging due to a dearth of data on swelling behaviour with reported interlayer water content. Therefore, our simulated data for basal spacing of CaMt is presented in Figure 3.3(b) along with recent results obtained from MD simulation [11]. The inset axes show the experimental swelling behaviour of CaMt with predominantly octahedral charge [12] as a function of relative humidity (RH). Analogous to the NaMt simulations, CaMt demonstrates a non-linear increase in d-spacing with increasing water content, although this reveals only a single plateau at around 0.15  $\text{g}_{\text{H}_2\text{O}}/\text{g}_{\text{clay}}$ . Despite the fact that direct correlation between RH and the actual amount of water in the interlayer is not possible, the experimental swelling trend is in good agreement with simulation, showing similar d-spacings of  $\sim 15 \text{ \AA}$  starting from lower RH. Discrepancies between the expansion behaviours of NaMt and CaMt upon hydration have been previously noted through multiple experimental [12,37,109,114,116,117] and theoretical [11,97] studies.

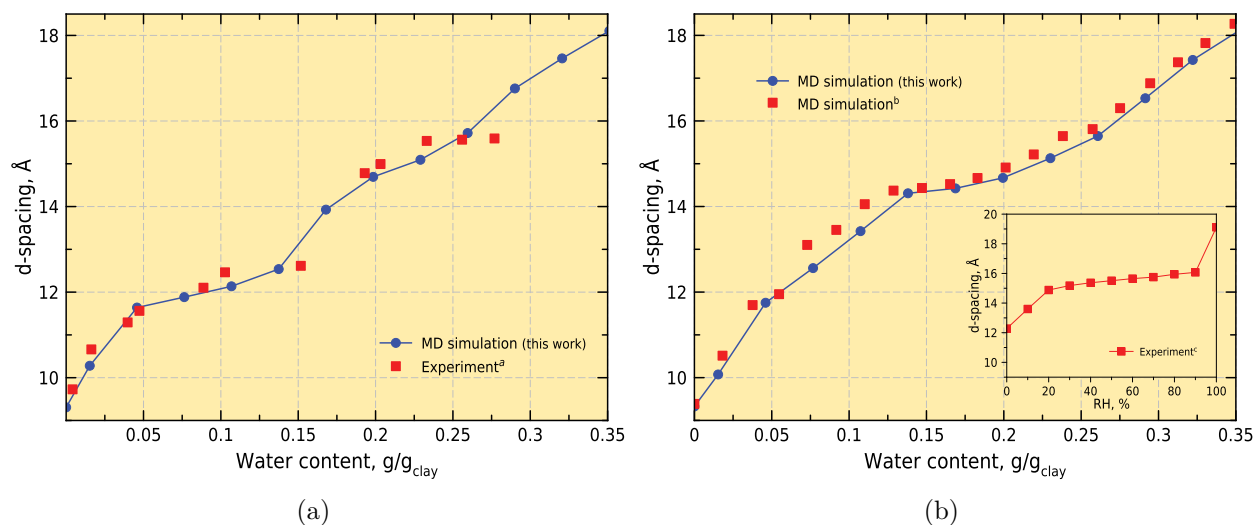
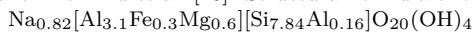


Figure 3.3: Simulated and experimental basal spacing of (a) 113 meq NaMt with octahedral charge and (b) 104 meq CaMt with octahedral charge as a function of increasing water content

<sup>a</sup>Experimental data for NaMt taken from Fu et al. [10]. Structural formula of the clay used in the experiment is



<sup>b</sup>MD simulation data for CaMt taken from Teich-McGoldrick et al. [11]

<sup>c</sup>Experimental data for octahedrally charged CaMt with net layer charge of  $0.86 e \cdot \text{uc}^{-1}$  is taken from Sato et al. [12]

This good agreement with experimental findings and previous simulations ensured the appropriateness of potential model selection and allows us to focus on the main topic of the thesis. Therefore, the following sections will concentrate on investigating the effects of clay layer charge distribution on the hydration and adsorption properties of montmorillonite clay minerals.

### 3.2.1 Swelling and Hydration Energetics

Nine simulated swelling and hydration energy curves for NaMt and CaMt models with a range of layer charges are shown in Figures 3.4 and 3.5, respectively. Standard deviations for all presented data were calculated from block averaging over the last 1 ns of simulation. Resultant error bars are less than a curve symbol size and, therefore, are not visible on the plots.

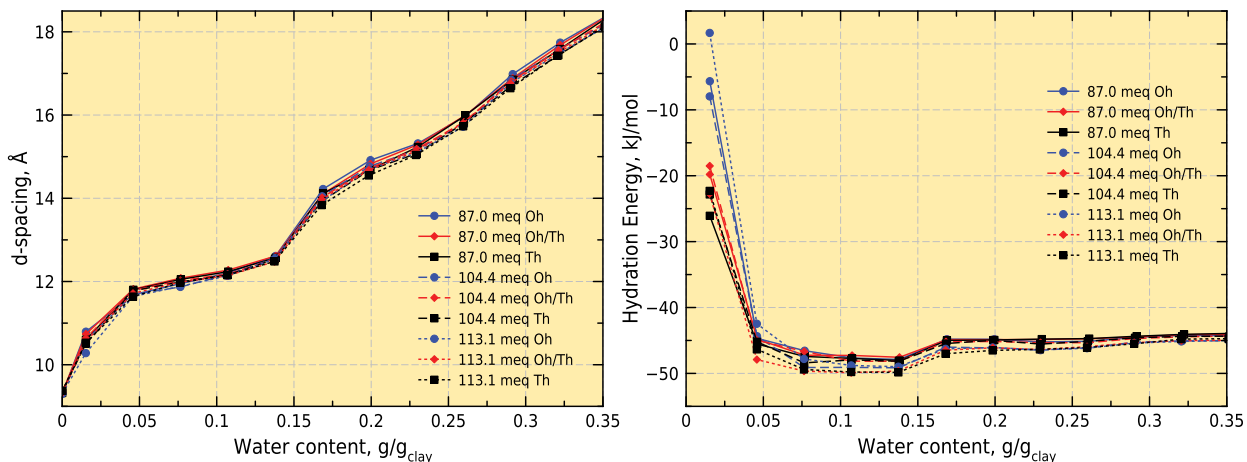


Figure 3.4: Na<sup>+</sup>-montmorillonite swelling curves (left) and hydration energies (right) as a function of water content from MD simulations at 300 K and 1 atm

The overall stepwise swelling behaviour of NaMt suggests the potential for formation of a well-defined monolayer hydrate (1W) with partially and fully filled interlayers, a bilayer hydrate (2W), and three layer hydrate, which will be further evidenced from the atomic density profiles discussed in Section 3.2.2. The observed values of basal spacings of 9.3–9.7 Å for the anhydrous interlayer, 12.15–12.27 Å for the monolayer hydrate and 14.55–14.92 Å for the bilayer hydrate are in very good agreement with reported values from experimental observations (Table 3.2). Formation of a third water layer in the interlayer is identified by a narrow shoulder at  $\sim 0.3$  g<sub>H<sub>2</sub>O</sub>/g<sub>clay</sub> on the simulated swelling curves but is not supported by some experimental observations [10, 109]. These studies suggested that the bilayer hydrate was the expansion limit of NaMt under most ambient conditions found in nature. However, if NaMt is exposed to a highly humid environment, basal spacings of  $\sim 18$  Å have been found, indicating the formation of a three layer hydrate at corresponding water contents [12, 74]. It also should be noted that these experimental studies comprise a range of clay layer charge states and that these can induce variation in the hydration dynamics of clay mineral. Our simulated NaMt swelling curves show distinct 0W–1W (0.05–0.15 g<sub>H<sub>2</sub>O</sub>/g<sub>clay</sub>) and 1W–2W (0.17–0.23 g<sub>H<sub>2</sub>O</sub>/g<sub>clay</sub>) transitions (Fig. 3.4), although the 2W state is less stable than 1W and does not exhibit a flat plateau as the d-spacing grows slightly as the water content increases.

Trends in basal spacing for NaMt with the selected charge locations and magnitudes are virtually identical (Fig. 3.4). The d-spacing for 113.1 meq clay with tetrahedral charge is smaller than 87.0 meq clay with octahedral charge by as little as 0.1 Å at monolayer hydrate and 0.3 Å at bilayer hydrate water content. This indicates that neither clay layer charge

Table 3.2: Values of basal d-spacing ( $\text{\AA}$ ) from MD simulations at 300 K and 1 atm for Montmorillonite with various layer charge as a function of interlayer cation compared with previous experiments

Layer charge	dry				monolayer				bilayer			
	Na <sup>+</sup>		Ca <sup>2+</sup>		Na <sup>+</sup>		Ca <sup>2+</sup>		Na <sup>+</sup>		Ca <sup>2+</sup>	
Total Tetrahedral	this work <sup>b,c</sup>	exp	this work	exp	this work	exp	this work	exp	this work	exp	this work	exp
0	9.30	9.7-9.8 <sup>12,109,116</sup>	9.31	11.6-12.0 <sup>12,116</sup>	12.21	12.4-12.5 <sup>12,109</sup>	12.70	12.6 <sup>12</sup>	14.92	14.8-15.3 <sup>12,109,116,118</sup>	14.84	14.5-15.6 <sup>12,109,116</sup>
-0.625 (87.0) <sup>a</sup>	9.32	11.6 <sup>12</sup>	9.49	11.1 <sup>12</sup>	12.27	12.6 <sup>12</sup>	12.53	12.3 <sup>12</sup>	14.83	14.5-15.6 <sup>12</sup>	14.77	13.8 <sup>12</sup>
0.625	9.32	9.8 <sup>12</sup>	9.30		12.24		12.54		14.69		14.66	
0	9.30	9.5-9.8 <sup>12,119</sup>	9.33		12.16	12.0-12.6 <sup>10,12,119</sup>	12.56		14.76	14.8-15.6 <sup>10,12,119,120</sup>	14.67	15.2-16.0 <sup>12,109</sup>
-0.750 (104.4)	9.33	9.5-10.0 <sup>12,45</sup>	9.31		12.17	12.5 <sup>12,45</sup>	12.23		14.72	14.8-15.5 <sup>12,45,118</sup>	14.66	
0.750	9.37	9.5-9.8 <sup>12,109</sup>	9.26		12.16	12.2-12.5 <sup>12</sup>	12.25		14.67	14.9-15.4 <sup>12</sup>	14.40	15.1 <sup>12</sup>
0	9.31	9.7 <sup>116</sup>	9.31	12.7 <sup>116</sup>	12.14		12.04		14.69	14.8-14.9 <sup>116,118</sup>	14.67	15.5 <sup>116</sup>
-0.812 (113.1)	9.33	9.9 <sup>12</sup>	9.32	11.8 <sup>12</sup>	12.14	12.2 <sup>12</sup>	12.21		14.68	15.1 <sup>12</sup>	14.68	14.6-15.1 <sup>12</sup>
0.812	9.37		9.26		12.15		12.05		14.55		14.39	

<sup>a</sup> Values in parenthesis correspond to layer charge expressed in meq

<sup>b</sup> Results obtained in this work are in correspondence with previous simulation and experimental investigations [7, 10-12, 18, 38, 39, 44, 45, 109, 113-116, 118-120]

<sup>c</sup> Standard deviation for d-spacing measurement does not exceed  $\pm 0.05 \text{ \AA}$

magnitude nor its location appear to have a significant influence on the swelling behaviour of  $\text{Na}^+$ -montmorillonite clay. This corresponds well with corresponding values of 1W and 2W hydrates obtained experimentally (Table 3.2). As discussed in Section 1.1.3, siloxane surface of smectites are predominantly hydrophobic, especially in locations where no isomorphous substitutions in octahedral or tetrahedral sheet have occurred [1]. Therefore, the main mechanism by which montmorillonites adsorb water is through hydration of exchangeable cations. The hydration enthalpy of monovalent sodium is comparatively low (Table 3.3); the hydration shell that is formed around it is relatively weak, especially at low water content. As a result, a uniform distribution of water is achieved in the interlayer of NaMt with various charge networks.

Table 3.3: Experimental ion radii and hydration enthalpies, and water contents for 1W and 2W states in montmorillonite from MD simulations at 300 K and 1 atm

	radius <sup>a</sup> Å	$-\Delta H_{hyd}$ (kJ·mol <sup>-1</sup> )	monolayer <sup>b</sup>	bilayer <sup>b</sup>
$\text{Na}^+$	1.16	406	0.1068 (5.38)	0.1995 (13.00)
$\text{Ca}^{2+}$	1.14	1577	0.0462 (6.00)	0.1693 (22.00)

<sup>a</sup>Ionic radii and hydration enthalpies are taken from ref [121]

<sup>b</sup>Values in parentheses correspond to water content in  $\text{H}_2\text{O}\cdot\text{cation}^{-1}$

In our calculations, the hydration energies denote the potential energy change of the hydrated interlayer as a water molecule is introduced (Fig. 3.4 (right)). They show minima at  $\text{H}_2\text{O}/\text{Na}^+$  ratios of 2.5–7.5 (0.05–0.15  $\text{g}_{\text{H}_2\text{O}}/\text{g}_{\text{clay}}$ ) which correspond to partial and full monolayer hydrates. As hydration continues,  $\Delta U(N)$  rises before levelling off. The hydration energies of all studied NaMts at all water contents are lower than thereof the bulk TIP3P/Fs water model ( $-41.1 \text{ kJ}\cdot\text{mol}^{-1}$  [122]), which may indicate the potential of expansion to larger basal spacings. The increase in hydration energy at very low water contents indicates that such states are energetically unfavourable. In the first phase of the hydration at lower water content  $\Delta U(N)$  for tetrahedrally charged clays show more negative hydration enthalpies (up to  $\sim 15 \text{ kJ}\cdot\text{mol}^{-1}$ ) compared to those for NaMt with octahedral charge. Therefore, it is slightly more energetically favourable to add water molecules to tetrahedral charge sites of NaMt.

Since the ionic radii of  $\text{Na}^+$  and  $\text{Ca}^{2+}$  cations are similar ( $\sim 1.15 \text{ \AA}$ , Table 3.3), the simulated basal spacings of dehydrated NaMt and CaMt are also very similar (Fig. 3.5) and equal to  $9.3 \pm 0.05 \text{ \AA}$  for all studied types of clay. Experimentally, however, it is very difficult to obtain completely dry CaMt at room temperature due to the high hydration enthalpy of the divalent cation (Table 3.2) [11, 109]. Consequently, even under extremely dry conditions, the basal spacing of CaMt is  $\sim 12.0 \text{ \AA}$  (Table 3.2) [12, 114]. This difference of about  $3 \text{ \AA}$  approximately equal to the diameter of a water molecule. In normal conditions, the interlayer of CaMt with octahedral charge contains two water layers [1, 114] which is consistent with the simulated swelling behaviour of this mineral. There is no stable plateau corresponding to a monolayer hydrate on swelling curves of octahedrally charged CaMt (Fig. 3.5); swelling to the bilayer hydrate with basal spacing of  $14.5 \text{ \AA}$  occurs at  $\sim 0.12 \text{ H}_2\text{O}/\text{g}_{\text{clay}}$ , much lower

that that for NaMt. This difference relates to the hydration energies of the exchangeable cations [109].

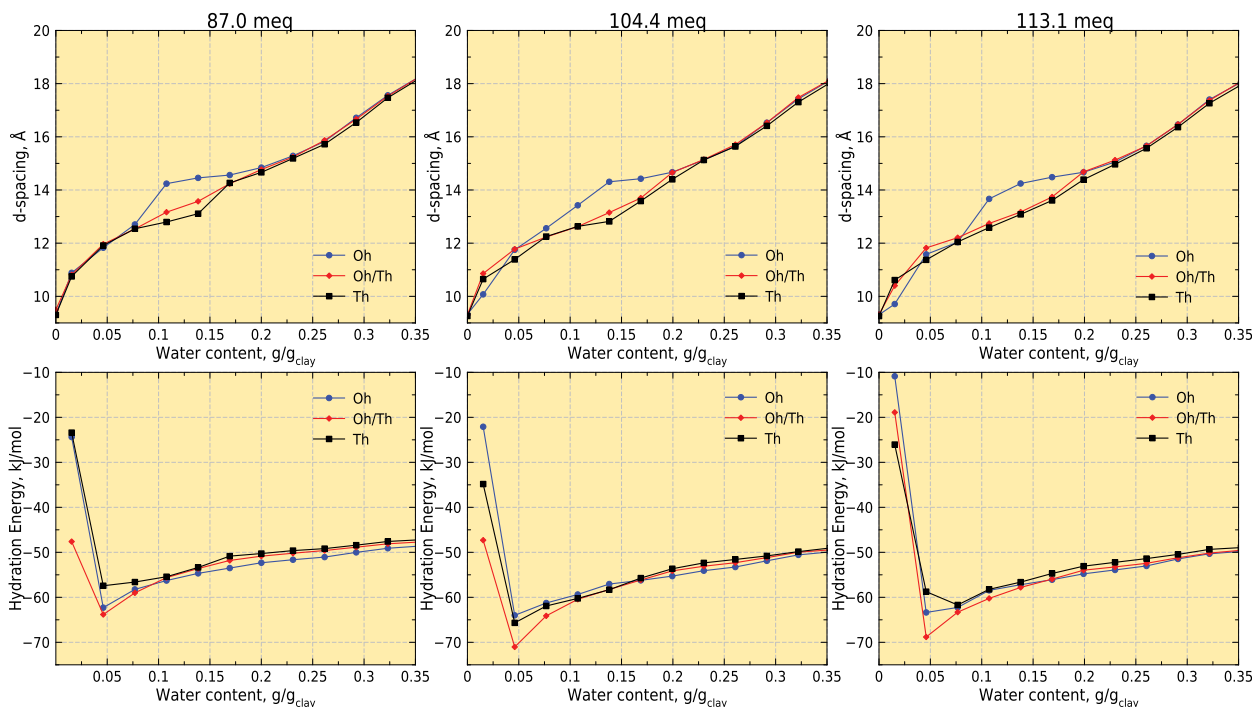


Figure 3.5:  $\text{Ca}^{2+}$ -montmorillonite swelling curves (top) and hydration energies (bottom) as a function of water content from MD simulations at 300 K and 1 atm

Upon introducing tetrahedral charge to CaMt systems, the basal spacing reduces down to 12.5 Å corresponding to a monolayer hydrate (Figure 3.11). This will be further evident from the atomic density profiles illustrated in Section 3.2.2, for the first time by the present study. The high hydration energy of divalent calcium, results in a strong interaction with substitution sites in the tetrahedral sheet close to the clay surface, breaking up the hydration shell of the cation and constraining the d-spacing. Comparison with experimental observations is particularly challenging here, as there is little data on the swelling behaviour of tetrahedrally charged CaMt. The few spacings presented in Table 3.2 are insufficient for a statistically valid assessment.

The computed interlayer hydration energy of CaMt is always more negative than that of NaMt due to the greater affinity of  $\text{Ca}^{2+}$  for water molecules (Fig. 3.5 (bottom)). It shows minima at an  $\text{H}_2\text{O}/\text{Na}^+$  ratio of 5 (0.05  $\text{g}_{\text{H}_2\text{O}}/\text{g}_{\text{clay}}$ ), associated with hydration energies of  $-65 - 70 \text{ kJ}\cdot\text{mol}^{-1}$ . Similar energies, much lower than that of bulk TIP3P/Fs water, were observed in previous MD simulation studies of  $\text{Ca}^{2+}$ -montmorillonite and  $\text{Ca}^{2+}$ -hectorite [11, 97, 123]. The sharp increase in hydration energy on approaching the dry interlayer limit, indicates that such a hydration state is energetically unfavourable, in good agreement with the experimental observations that basal spacing at very low RH correspond to the monolayer hydrate (Fig. 3.3(b) (inset)).

Together, these observations clearly confirm that the affinity of the cations for water molecules plays an important role in determining the interlayer spacing in humid environments.

### 3.2.2 Interlayer Structure of Hydrated Montmorillonites Atomic Density Profiles

For every studied system, the distribution of interlayer cations and water molecules in the interlayer was calculated for each water content, as shown in Figures 3.6 and 3.11 for NaMt and CaMt respectively. The distributions are represented as one-dimensional atomic density profiles (ADPs) along the  $c$ -axis normal to the basal surface of clay. These profiles represent the average positioned probabilities for molecules across the interlayer with respect to the simulation cell, where 0 Å corresponds to the midplane of the interlayer. Systems with a water content corresponding to the monolayer hydrate ( $\sim 0.1 \text{ g}_{\text{H}_2\text{O}}/\text{g}_{\text{clay}}$ ), bilayer hydrate ( $\sim 0.2 \text{ g}_{\text{H}_2\text{O}}/\text{g}_{\text{clay}}$ ) and three layer hydrate ( $\sim 0.3 \text{ g}_{\text{H}_2\text{O}}/\text{g}_{\text{clay}}$ ) were selected as most representative. The obtained data confirm the water interlayer structures identified from the swelling curves. However, the ADPs provide additional detailed structural information, in particular, various cation adsorption configurations related to their hydration state (Fig. 3.7). These configurations can be identified from their respective cation-surface distances and correspond to anhydrous cation, inner-sphere (IS) and outer-sphere (OS) configurations. An IS surface complex has no water molecules interposed between the interlayer cation and the clay surface, whereas an OS adsorption complex has at least one such interposed water molecule [46]. Similar hydration conformations were identified for mono and divalent cations in previous theoretical [46, 124] and experimental studies [44].

The ADPs of the partial and full monolayer hydrate with a  $\text{H}_2\text{O}/\text{Na}^+$  ratio of 2.5–7.8 ( $0.05\text{--}0.14 \text{ g}_{\text{H}_2\text{O}}/\text{g}_{\text{clay}}$ ) consist of a single peak for  $\text{O}_{\text{H}_2\text{O}}$  located in the centre of the interlayer. This peak is not influenced in any way by the clay layer charge location or its magnitude. The distribution of sodium cations, on the other hand, depends significantly on the clay layer charge arrangement. Thus, octahedrally charged clay possess a single peak for  $\text{Na}^+$  cations located in the centre of the interlayer,  $\sim 2.9 \text{ Å}$  from both basal surfaces. This distance indicates that the  $\text{Na}^+$  cation occurs in IS coordination (Fig.3.7(b)), where it is associated with both basal oxygens ( $\text{O}_{\text{basal}}$ ) from the clay surfaces and water oxygens in  $xy$  plane (parallel to the basal surface). Increasing the tetrahedral charge contribution to the net layer charge, results in a splitting of the  $\text{Na}^+$  peak into two positioned at  $\pm 1.0 \text{ Å}$ . This configuration corresponds to IS coordination as well, although in this case one side of each cation is completely coordinated by  $\text{O}_{\text{basal}}$  and the other by  $\text{O}_{\text{H}_2\text{O}}$  (as depicted in Fig.3.7(b)). This occurs due to the localised tetrahedral charge which attracts the exchangeable cations much more strongly than the delocalised octahedral charge.

The three peaks for water hydrogen atoms ( $\text{H}_{\text{H}_2\text{O}}$ ) (Fig. 3.8 top left) demonstrate the different orientations of water molecules and their H-bonding configurations. The ratio of integral intensities of the  $\text{O}_{\text{H}_2\text{O}}$  peak and the  $\text{H}_{\text{H}_2\text{O}}$  peaks at  $\pm 1.2 \text{ Å}$  ( $\sim 1.7 \text{ Å}$  off the basal surface) suggests that one of the H-bonds is oriented towards the nearest montmorillonite surface, with the other pointing approximately parallel to the basal surface. Considering the single layer of water in the interlayer, it appears that nearly every water molecule donates, on average, one H-bond to the  $\text{O}_{\text{basal}}$ . The nuclear magnetic resonance (NMR) spectroscopic studies on hydrated  $\text{Li}^+$ -hectorite support this picture of water molecule configurations [44]. DFT calculations of water loading on a pyrophyllite surface also indicate that this water configuration is the most favourable for a partial monolayer hydrate [108].

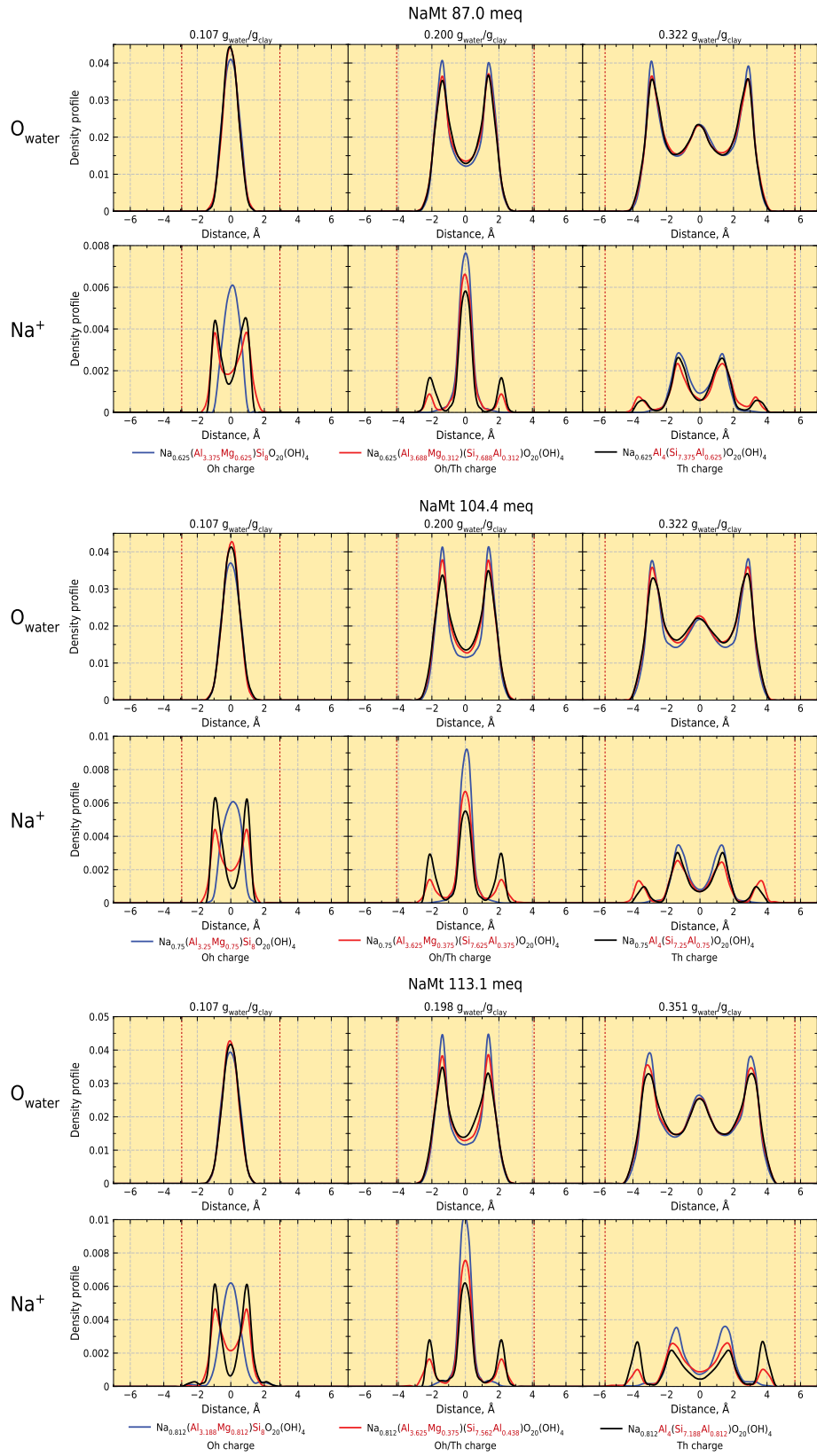


Figure 3.6: Atomic density profiles from MD simulations at 300 K and 1 atm for NaMt of water ( $O_{\text{water}}$ ) and sodium ( $Na^+$ ). Left to right increases the water contents in the interlayer space of clay. Vertical dashed lines designate the planes of basal oxygens; 0 Å corresponds to the centre of the interlayer

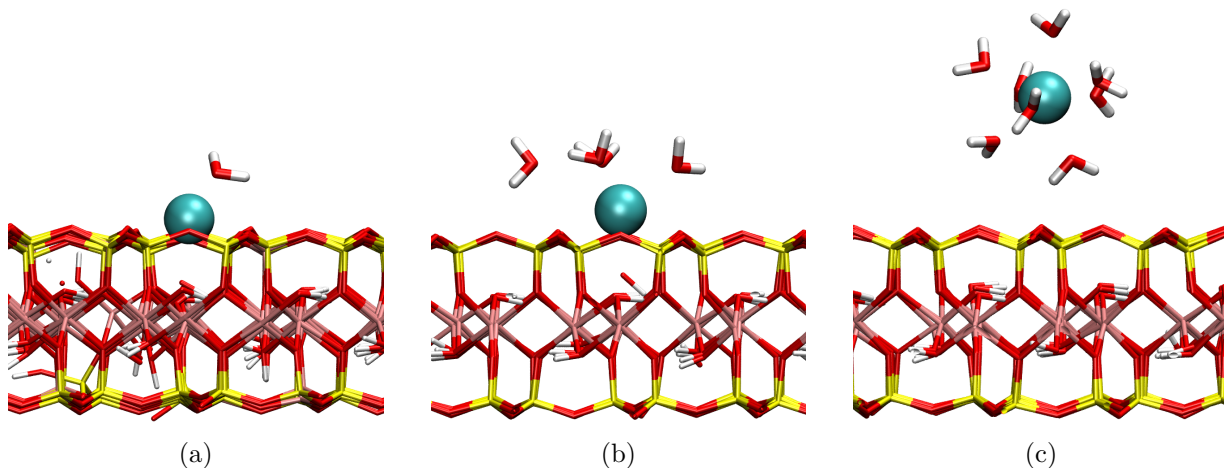


Figure 3.7: Snapshots of clay surface ( $yz$  plane) showing configurations of adsorbed calcium cations in (a) anhydrous, (b) inner-sphere (IS), and (c) outer-sphere (OS) water complexes on the  $\text{Ca}^{2+}$ -montmorillonite. Colours as in Figure 3.1

The bilayer hydrate corresponds to a  $\text{H}_2\text{O}/\text{Na}^+$  ratio of 10.8 and is characterised by two nearly discrete water peaks in the ADP at  $2.7 \text{ \AA}$  from each basal surface ( $\pm 1.36 \text{ \AA}$ ) (Fig 3.6 middle). The  $\text{Na}^+$  cation distribution is characterised by a single peak positioned in the centre of the interlayer at  $4.1 \text{ \AA}$  from octahedrally charged Mt, and three peaks located at  $\sim 2.0 \text{ \AA}$  from both basal surfaces ( $\pm 2.1 \text{ \AA}$ ), and  $4.1 \text{ \AA}$  ( $0 \text{ \AA}$  peak) for Mt with tetrahedral charge. Cations positioned in the centre of the interlayer occur in fully hydrated OS water complexes (Fig. 3.7(c)) whereas cations located closer to the clay surface correspond to IS coordination (Fig. 3.7(b)).

From the MD simulations it can be clearly seen that, if charge deficit occurs in the tetrahedral sheet, adsorption of cations is favoured near to the tetrahedral sheet and presumably to the sites of isomorphous substitution. To determine the relative fraction of each cation–water complex type in the bilayer hydrate interlayer, the sodium peaks in the ADP were integrated as presented in Table 3.4. Due to the relatively low hydration enthalpy of  $\text{Na}^+$  cations they can be easily solvated by water molecules. Therefore,  $\text{Na}^+$  cations are not present in the dodecahedral cavities at the clay surface i.e. anhydrous complexes. Moving away from the surfaces, inner-sphere cations constitute only a small fraction (2–4%) of sodium cations when the charge deficit is in the octahedral sheet, but this fraction increases significantly up to 36–42% when there is charge deficit in the tetrahedral sheet. The rest of the cations in the systems are coordinated within OS hydration shells.

The bilayer hydrate is characterised by four layers of water hydrogens located at  $1.7 \text{ \AA}$  (peaks at  $\pm 1.3 \text{ \AA}$ ) and  $2.4 \text{ \AA}$  (peaks at  $\pm 1.7 \text{ \AA}$ ) from both basal surfaces. As in the monolayer hydrate, some hydrogen atoms point toward the basal surface, but, due to the larger space available and the full hydration of the cation, the orientations of the water dipole moment are more diverse (Fig. 3.9). To quantify this, the distribution of dipole moments of the water molecules forming the hydration shell of each cation as a function of the angle between the dipole moment vector and the  $c$ -axis is presented in Figure 3.10. Water orientations in which one of the  $\text{OH}_{\text{H}_2\text{O}}$  bonds point toward the clay surface and other being nearly parallel to it

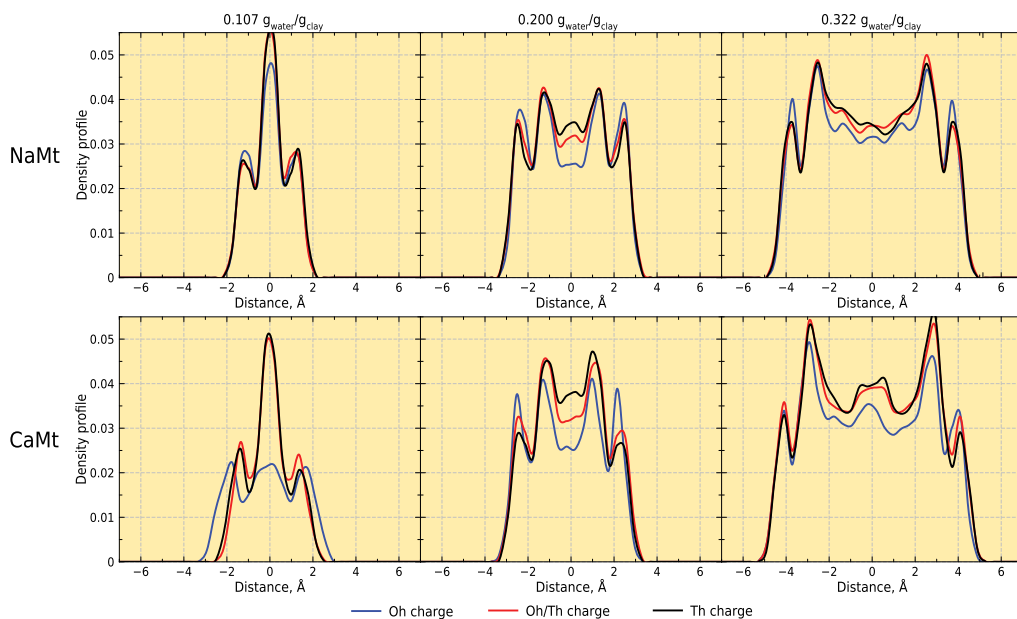


Figure 3.8: Atomic density profiles of water hydrogen ( $H_{\text{water}}$ ) for NaMt (top) and CaMt (bottom). Left to right increases the water contents in the interlayer space of clay

were the most frequent. These are followed up by the configuration in which both hydrogen atoms are oriented toward the basal surface of clay. A NMR spectroscopy investigation into the water dynamics at the smectite/water interface suggested similar water orientations in bilayer hydrates [125].

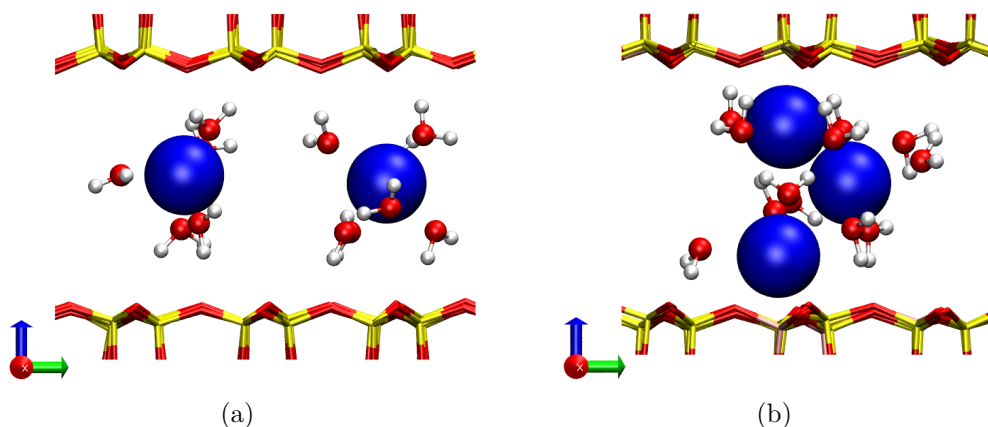


Figure 3.9: Spatial arrangements of cation and water molecules in the bilayer hydrate on the example of NaMt with a) octahedral charge (OS configuration) and b) tetrahedral charge (combination of IS and OS configuration)

Increasing the water content in the interlayer results in the formation of three  $\text{O}_{\text{H}_2\text{O}}$  peaks (Fig. 3.6, right), two of which are positioned at  $2.7 \text{ \AA}$  (peaks at  $\pm 2.9 \text{ \AA}$ ) from both clay surfaces and one in the middle of interlayer at  $5.6 \text{ \AA}$ . The cations, in this case, occupy two layers in octahedrally charged NaMt and four layers in montmorillonite with a tetrahedral charge component. The cations responsible for peaks at  $\pm 3.7 \text{ \AA}$  ( $1.9 \text{ \AA}$  above both basal surfaces) in the interlayer of tetrahedrally charged Mt correspond to IS coordination (Fig. 3.7(b)).

Table 3.4: Percentage of exchangeable cations in each adsorption layer of bilayer hydrate interlayers ( $\sim 0.2 \text{ g}_{\text{water}}/\text{g}_{\text{clay}}$ )

	104.4 meq			
	Na <sup>+</sup>		Ca <sup>2+</sup>	
	Oh	Th	Oh	Th
anhydrous	0	0	0	0
inner-sphere	2.3	42.1	1.2	84.3
outer-sphere	97.7	58.9	98.8	15.7
	113.1 meq			
	Na <sup>+</sup>		Ca <sup>2+</sup>	
	Oh	Th	Oh	Th
anhydrous	0	0	16.2	0
inner-sphere	3.7	36.4	0.7	66.6
outer-sphere	96.3	63.6	83.1	33.4

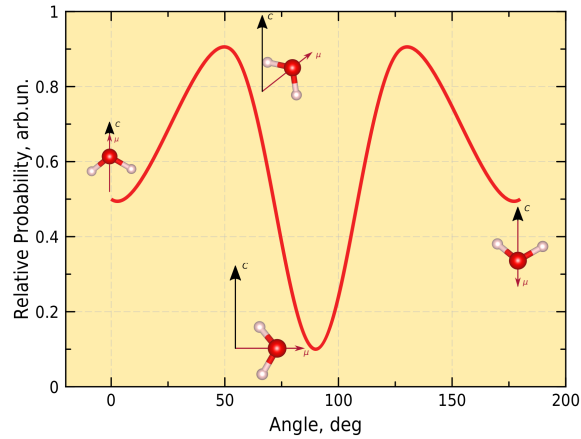


Figure 3.10: Distribution of water dipole showing major orientations of water molecules in the bilayer hydrate interlayer. Note that angle is with respect to the  $c$ -axis vector which is perpendicular to clay layer

Cations positioned deeper in the interlayer, at  $4.3 \text{ \AA}$  from both surfaces (peaks at  $\pm 1.36 \text{ \AA}$ ), occur in the fully hydrated OS water complexes (Fig. 3.7(c)). The interlayer structure, in the form of the ADPs for NaMt with various charges, is in a good agreement with previous theoretical observations [11, 78, 97].

The ADPs of Ca<sup>2+</sup> cations and H<sub>2</sub>O molecules (Fig 3.11) provide the more detailed structural information required to interpret the thermodynamic results. The distinct swelling behaviour of CaMt, discussed in previous sections, becomes evident from these profiles. Here, at low water content ( $0.107 \text{ g}_{\text{H}_2\text{O}}$ ) (which corresponds to a monolayer hydrate for NaMt), a bilayer of water is observed for octahedrally charged CaMt (Fig. 3.11, blue line). Just a single peak for Ca<sup>2+</sup>, positioned in the centre of the interlayer, suggests the formation of an OS coordination sphere at low water content (Fig. 3.7(c)). This was previously attributed to the much higher enthalpy of Ca<sup>2+</sup> in contrast to Na<sup>+</sup> [109]. The single cation peak becomes

broader as the layer charge magnitude increases. Eventually, for 113.1 meq clay, this splits into three peaks, two of which are located at  $\pm 2.5 \text{ \AA}$  with the third peak at the midplane of interlayer. At this point, the cation is "locked" in the siloxane rings on the clay surface due to the high layer charge and hydration energy of the divalent cation, and an anhydrous adsorption conformation is formed (Fig. 3.7(a)).

Shifting the clay layer charge into the tetrahedral sheet reduces the basal spacing, leading to a much narrower distribution of water in the interlayer (Fig. 3.11, black line). As pointed out in the previous section, this configuration corresponds to  $d_{001}$ -spacing of  $12.5 \text{ \AA}$  or a monolayer hydrate. Similar to  $\text{Na}^+$  in NaMt, two, much sharper layers of  $\text{Ca}^{2+}$  are formed at  $0.107 \text{ g}_{\text{H}_2\text{O}}/\text{g}_{\text{clay}}$  water content. This hydration state is characterised by cations adsorbed in IS configuration associated with the substitution sites in the tetrahedral sheets. The ADPs presented here provide direct confirmation of the tendency of CaMt to form a bilayer hydrate even at very low water concentrations, as observed by experimentalists over last half of century [12, 37, 38, 109, 114].

The full bilayer hydrate formed at  $0.2 \text{ g}_{\text{H}_2\text{O}}/\text{g}_{\text{clay}}$  ( $\text{H}_2\text{O}/\text{Ca}^{2+} \sim 21.6$ ) is consistently observed for CaMt for all charge distributions within the layer (Fig. 3.11 middle). The distribution of calcium, however, varies depending on where the deficit of positive charge occurs. Tetrahedrally charged CaMt is characterised by three layers of exchangeable cations ( $\pm 1.75$  and  $0 \text{ \AA}$ ) corresponding to IS and OS complexes, respectively. Interlayers formed by low charge clays with octahedral substitutions are composed by a single layer of  $\text{Ca}^{2+}$  positioned in the centre. For high charge clays, three  $\text{Ca}^{2+}$  peaks are observed at  $\pm 2.9$  and  $0 \text{ \AA}$  indicating anhydrous and OS cation complexes. This sharp change in the fraction of anhydrous cations for low and high charge clays (Table 3.4) may be accentuated by the relatively small simulated system size available (compared to length scale of real Mt). Nonetheless, the higher probability of exchangeable cation being trapped in the dodecahedral cavities of highly charged clay surfaces is a clear qualitative observation.

To summarise the interlayer structures discussed in this section, density profiles during swelling are collated in Figure 3.12 where the ordinate corresponds to the  $d_{001}$ -spacing and the abscissa to the respective density profiles of water and exchangeable cation. This shows the evolution of interlayer structure during the swelling process. The lowest interlayer separation of NaMt comprises a monolayer hydrate with sodium cations forming IS surface complexes (Fig. 3.12(a)). This configuration is retained for a range of water contents from dry to  $\text{H}_2\text{O}/\text{Na}^+ \approx 4.1$ . A transformation occurs at a layer spacing close to  $12.0 \text{ \AA}$ , when the exchangeable cation migrates towards the midplane of the interlayer. Subsequently, the bilayer hydrate forms with  $d$ -spacing of  $\sim 13.5 \text{ \AA}$ . When it is fully formed, the  $\text{H}_2\text{O}/\text{Na}^+$  ratio is approximately 5.8 which agrees well with the sodium coordination number in concentrated NaCl aqueous solutions [99] and corresponds to the OS cation complex. CaMt, on the other hand, does not form a distinct monolayer hydrate, only bilayers with a starting separation of  $14.2 \text{ \AA}$ . The driving force for this is the energy associated with full hydration of these cations.

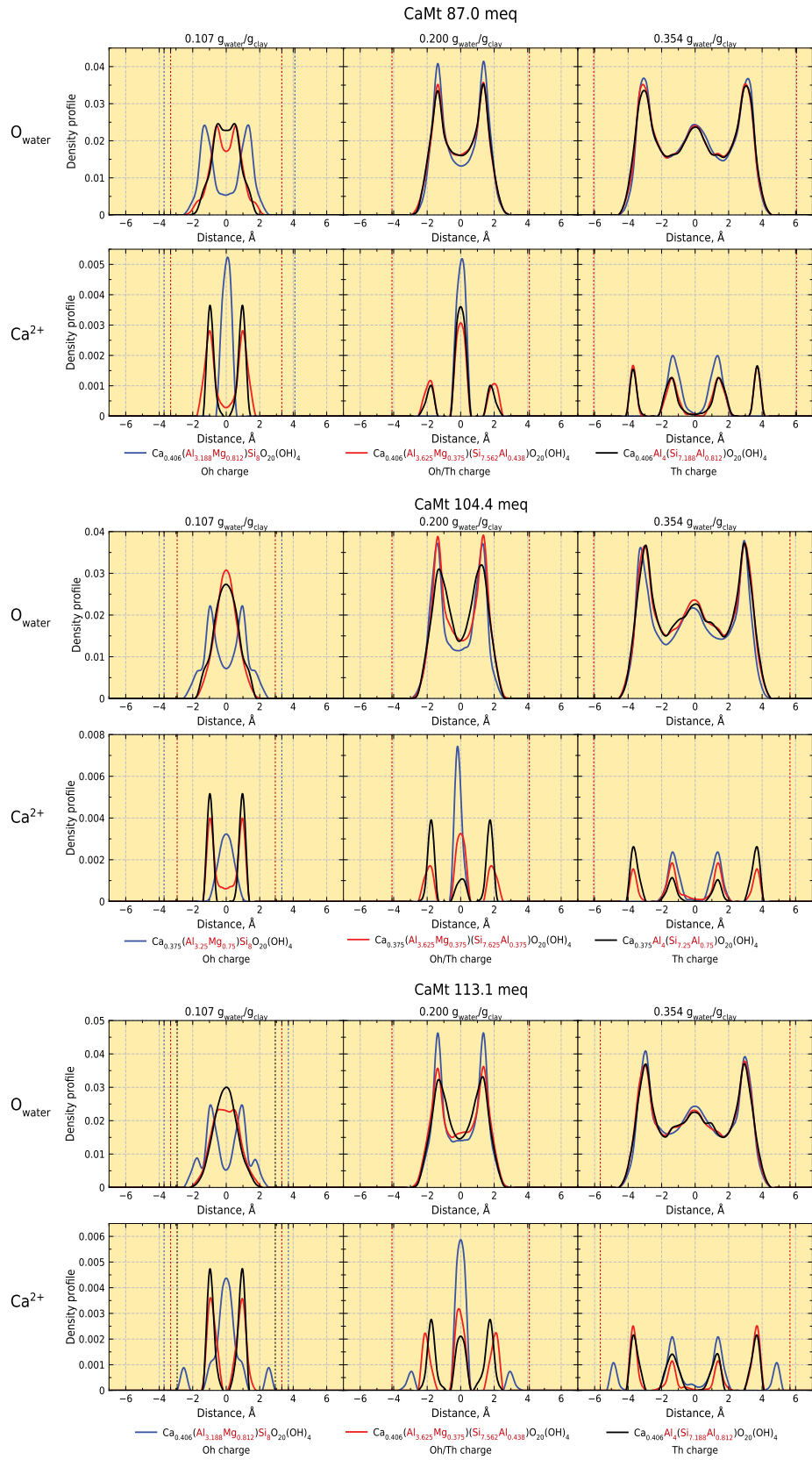
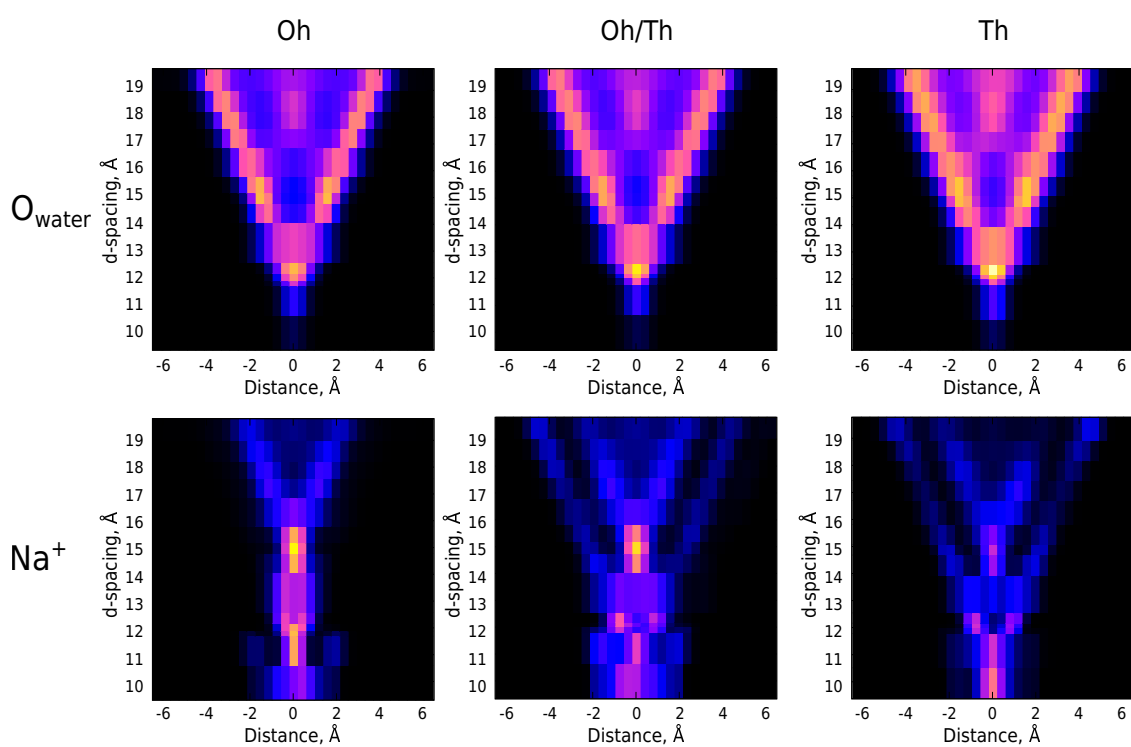
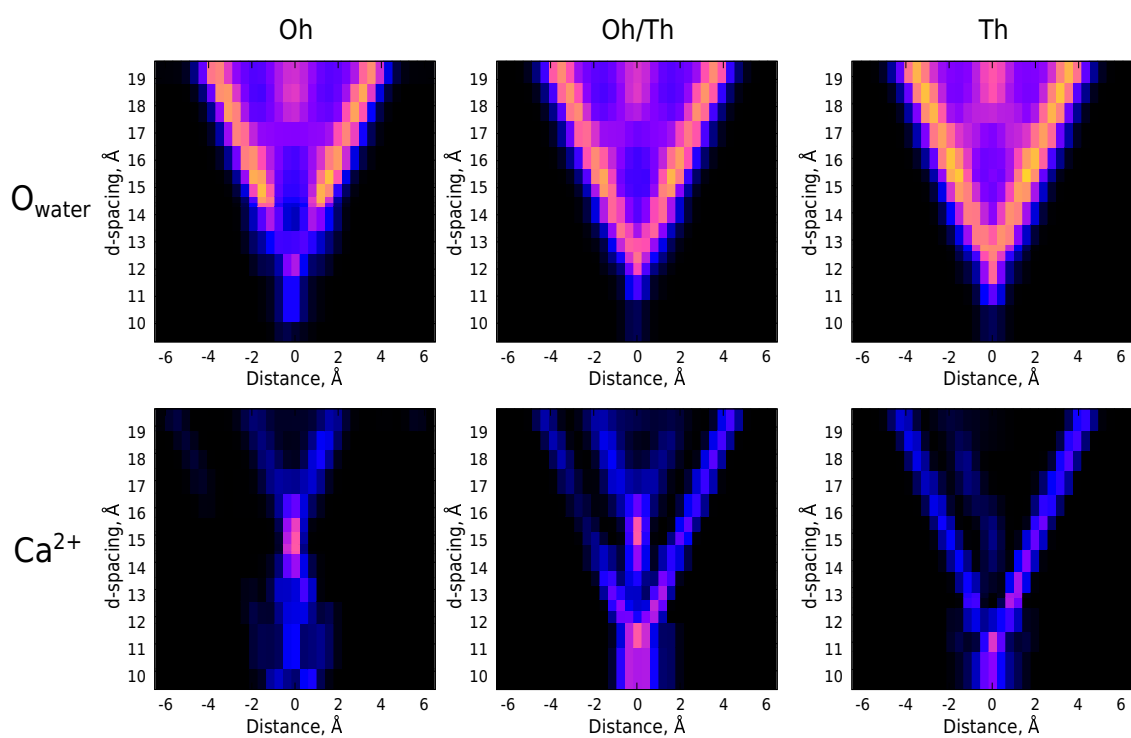


Figure 3.11: Atomic density profiles from MD simulations at 300 K and 1 atm for CaMt of water ( $\text{O}_{\text{water}}$ ) and calcium ( $\text{Ca}^{2+}$ ). Left to right increases the water contents in the interlayer space of clay. Vertical dashed lines designate the planes of basal oxygens; 0 Å corresponds to the centre of the interlayer



(a)



(b)

Figure 3.12: Evolution of the water and interlayer cation distribution in the 104.4 meq (a) NaMt and (b) CaMt clay interlayer during the swelling process. The graphs represent corresponding atomic density as a function of the layer spacing. Colour scheme: black–blue–red–yellow from lowest to highest density

## Radial Distribution Functions

The relationship between the interlayer cations and water was probed further by the calculation of a radial distribution function (RDF) and a coordination number (CN) of  $\text{Na}^+ - \text{O}_{\text{H}_2\text{O}} / \text{O}_{\text{basal}}$  and  $\text{Ca}^{2+} - \text{O}_{\text{H}_2\text{O}} / \text{O}_{\text{basal}}$  at various water contents (Fig. 3.13 and Fig. 3.14 respectively).

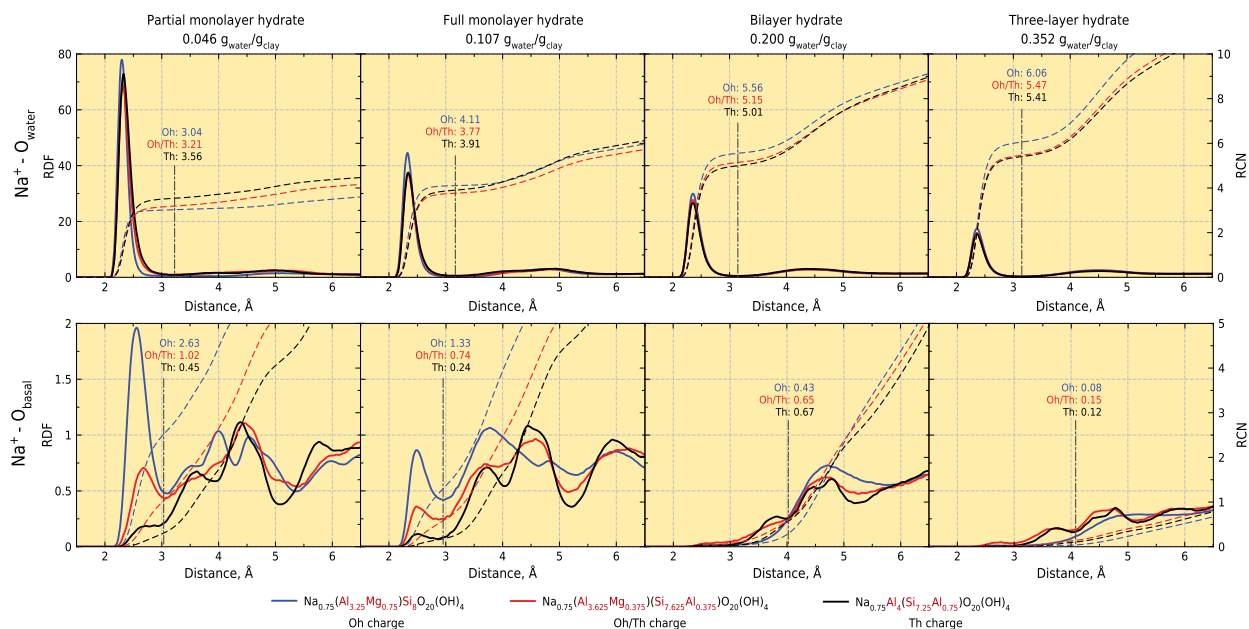


Figure 3.13: Radial distribution functions (solid lines) and the corresponding coordination numbers (dashed lines) for atomic pairs in the interlayer of 104.4 meq NaMt at different water content:  $\text{Na}^+ - \text{O}_{\text{H}_2\text{O}}$  (top) and  $\text{Na}^+ - \text{O}_{\text{basal}}$  (bottom)

In all  $\text{Na}^+ - \text{O}_{\text{H}_2\text{O}}$  RDFs, the main peak represents the first hydration shell and is located at about 2.35 Å (Fig. 3.13), which agrees well with theoretical DFT and MD simulations [97,126] (2.35–2.37 Å) and experimental observations [127] (2.32 Å). The first coordination shell of  $\text{Na}^+ - \text{O}_{\text{basal}}$  is located at  $\sim 2.5$  Å and diminishes as water content is increased, completely disappearing at 0.2  $\text{g}_{\text{H}_2\text{O}} / \text{g}_{\text{clay}}$  water content which corresponds to bilayer hydrate. As was evident from Table 3.4, the bilayer hydrate is characterised by a very small number of cations adsorbed as anhydrous and IS configurations. Here, most  $\text{Na}^+$  cations are fully hydrated (OS configuration) and do not interact with oxygens located in the basal plane of clay.

For NaMt the total oxygen CN of  $\text{Na}^+$  is always in the range 5.5–6.0. However, the distribution between  $\text{H}_2\text{O}$  and  $\text{O}_{\text{basal}}$  sites is strongly dependent on the hydration state of the interlayer. When the layer charge is shifted from the octahedral to the tetrahedral sheet, the coordination number of  $\text{Na}^+ - \text{O}_{\text{basal}}$  decreases. This can be explained by the mechanism of cation adsorption on the clay surface. When tetrahedral charge is dominant in the layer, exchangeable cations tend to adsorb adjacent to the substitution site in the tetrahedral sheet [127] where only three neighbour basal oxygens are available. In contrast, the cation adsorbs at the dodecahedral cavity of octahedrally charged clays where a total of six oxygens are available (Fig. 1.6).

For  $\text{Ca}^{2+} - \text{O}_{\text{H}_2\text{O}}$  pairs, the average neighbour distance calculated is 2.43 Å (Fig. 3.14). The mean interatomic distance between  $\text{Ca}^{2+}$  and first shell  $\text{O}_{\text{basal}}$  is 2.52 Å. Both of these values

are very similar to the value found in bulk solution and reported in the simulation of hydrated Ca-hectorite (2.5 Å and 2.7 Å) [123] and Ca-montmorillonite (2.43 Å and 2.52 Å) [97].

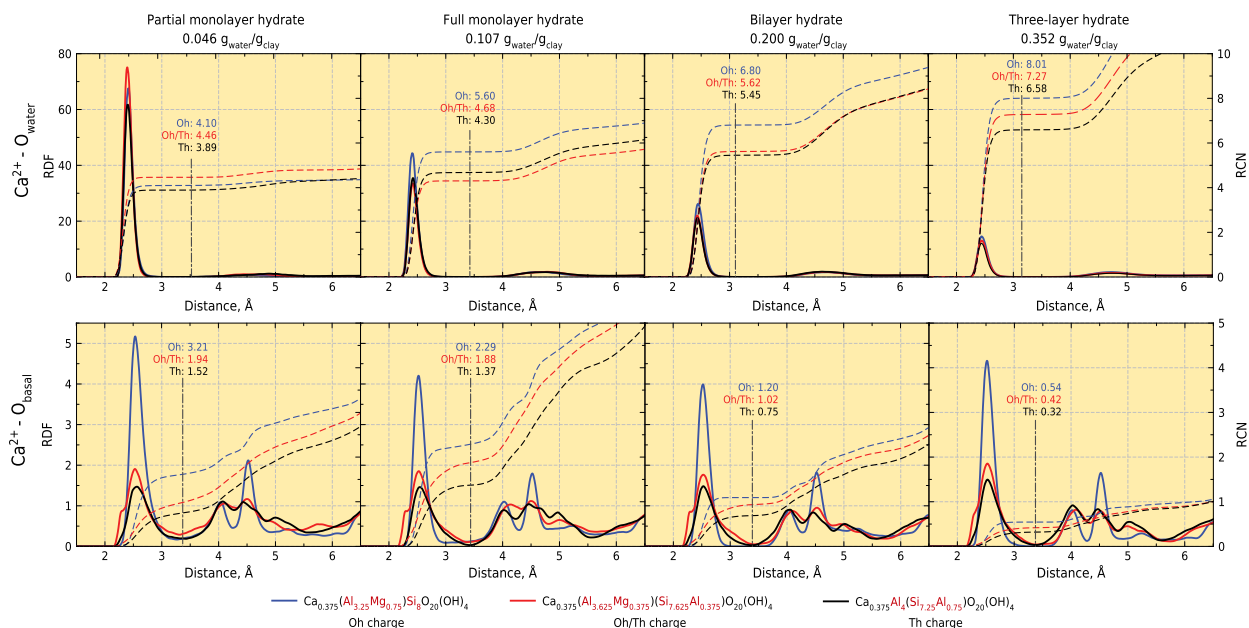


Figure 3.14: Radial distribution functions (solid lines) and the corresponding coordination numbers (dashed lines) for atomic pairs in the interlayer of 104.4 meq CaMt at different water content: Ca<sup>2+</sup>-O<sub>H<sub>2</sub>O</sub> (top) and Ca<sup>2+</sup>-O<sub>basal</sub> (bottom)

Similar to Na<sup>+</sup>, the CN of Ca<sup>2+</sup> is strongly dependent on the hydration state of the interlayer and, thus, the distribution between H<sub>2</sub>O and O<sub>basal</sub> coordination spheres. The total CN of Ca<sup>2+</sup>, however, is always in the range of 7.0–8.0 Å. For the partial monolayer hydrate structure, the coordination of cations consists of ~4.0 H<sub>2</sub>O and ~3.0 O<sub>basal</sub>, whereas it is 6.0 H<sub>2</sub>O and 2.0 O<sub>basal</sub> for the complete monolayer structure. For the bilayer hydrate of CaMt and on its external surface, Ca<sup>2+</sup> is coordinated by 7.0 H<sub>2</sub>O molecules and ~1.0 O<sub>basal</sub> atoms. This differs from the equivalent results for bilayer hydrate of NaMt because a substantial amount of calcium in octahedrally charged CaMt is adsorbed in the dodecahedral cavity of the clay surface (anhydrous conformation seen in Table 3.4).

### 3.2.3 Dynamics of the Interlayer

The dynamics of the interlayer species is a key process in the hydration of clay and it is, therefore useful to explore the mechanisms involved in this. To this end, 500 ps overlapped trajectory maps of NaMt and CaMt with various water contents in the interlayer are presented in Figure 3.15. These illustrate both the mobility and the hydration of exchangeable cations and water in the interlayer.

The obtained patterns clearly indicate that adsorption of water by montmorillonite clays occurs in two stages. Firstly, solvation of the exchangeable cations by either three (Na<sup>+</sup> monovalent cations) or more (Ca<sup>2+</sup> divalent cations) water molecules takes place (Fig. 3.15, 0.046 g<sub>H<sub>2</sub>O</sub>/g<sub>clay</sub>). At this stage, the water is located predominantly around the cations or close to substitution sites that are the focus of the net negative charge of the clay layers. This latter phenomenon is closely related to hydrophobic behaviour of neutral siloxane sur-

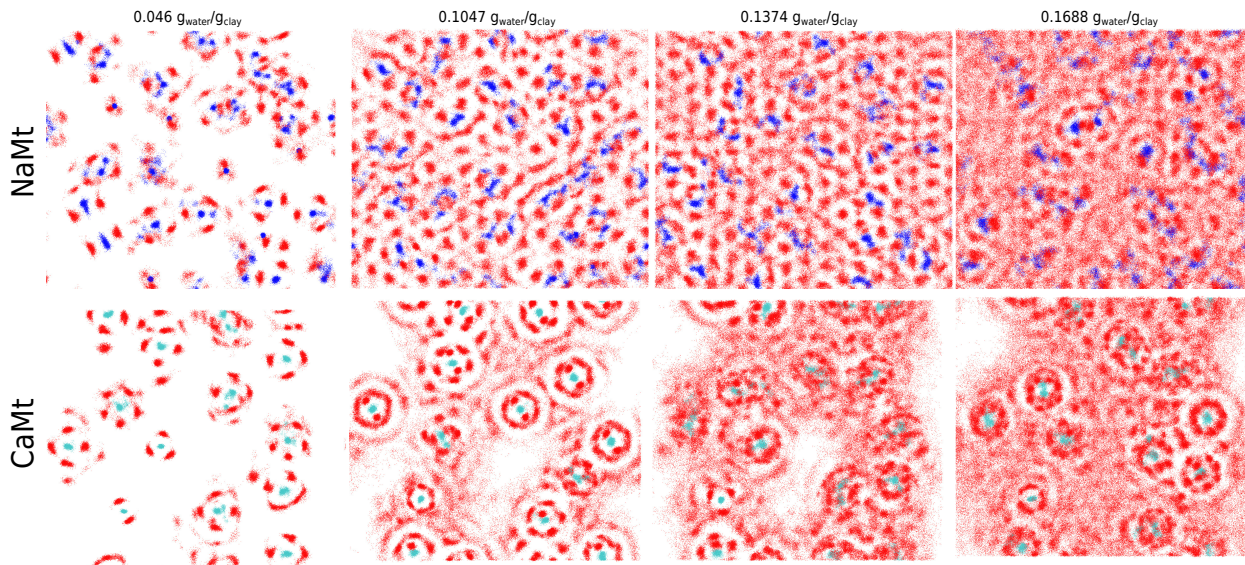


Figure 3.15: Overlapped final 500 ps snapshots from MD simulations at 300 K and 1 atm of 113.1 meq octahedrally charged NaMt and CaMt at different water contents. It can be observed that the overlapped trajectories of  $\text{Ca}^{2+}$  and their accompanying coordinated water molecules are much denser than is the case for  $\text{Na}^+$ . Colours are as follows:  $\text{Na}^+$  blue,  $\text{Ca}^{2+}$  cyan,  $\text{O}_{\text{water}}$  red

faces of clay minerals [1]. Secondly, as the amount of water in the interlayer increases, full hydration shells around the cations are formed [44]. Monovalent sodium cations develop an octahedral solvation complex, whereas divalent calciums form a second solvation shell (Fig 3.15, 0.1047  $\text{g}_{\text{H}_2\text{O}}/\text{g}_{\text{clay}}$ ). Since this hydration process depends only on the hydration ability of the exchangeable cations, the formation of complete monolayers of water is not necessary as indicated by the "non-occupied" region between the hydrated  $\text{Ca}^{2+}$  cations. At water content values that are too low for a full monolayer to form, molecules that are involved in the formation of any cation's hydration shell tend to condense in the siloxane rings of the montmorillonite's surface. This results in the "dot" pattern – localised areas with high water concentration visible in Figure 3.15 at 0.1047  $\text{g}_{\text{H}_2\text{O}}/\text{g}_{\text{clay}}$ . This simulated water arrangement is in good agreement with IR spectroscopy analysis of adsorbed water in Li-hectorite performed by Prost [44].

The more negative hydration enthalpy of  $\text{Ca}^{2+}$ , produces a water coordination sphere around it is much more stable than that of  $\text{Na}^+$  (Fig. 3.15). The mobility of  $\text{Ca}^{2+}$  is constrained because of this, in contrast to  $\text{Na}^+$  cations which remain mobile, even at low water contents. Diffusion of  $\text{Ca}^{2+}$  is further inhibited by a second coordination water shell, which can either be complete or share some parts with those of neighbouring cations. Calculated three dimensional diffusion coefficients derived from MD simulations of NaMt and CaMt are presented in Figure 3.16 as a function of exchangeable cation concentration (M). Here, data points from right to left correspond to 1W hydrate, 2W hydrate and 3W hydrate. Overall, five trends are distinguished: (i) diffusion coefficients for exchangeable cations ( $D_{\text{cation}}$ ) and water ( $D_{\text{OW}}$ ) decrease as the clay layer charge increases; (ii)  $D_{\text{cation}}$  and  $D_{\text{OW}}$  decrease when clay layer charge is shifted to the tetrahedral sheet; (iii) diffusion of interlayer water is sig-

nificantly higher than that of the exchangeable cations; (iv) diffusion of water in NaMt is higher than that in CaMt; (v) diffusion of sodium ( $D_{\text{Na}}$ ) is higher than diffusion of calcium ( $D_{\text{Ca}}$ ). The values of the diffusion coefficients obtained for water and exchangeable cations in Mt with 104.4 meq are summarised in Table 3.5.

The results are quantitatively consistent with the recently reported self-diffusion coefficients of  $\text{Na}^+$  in clay nanopores [124, 128]. For NaMt,  $D_{\text{Na}}$  sharply increases by a factor of 1.5–2, when the interlayer swells from monolayer to bilayer hydrate. This process is associated with the formation of full hydration shells around the cations, thus moving the cations away from the mineral surface. This leads to a conclusion that OS adsorption complexes are much more mobile than IS complexes. The corresponding increase in diffusion of  $\text{Ca}^{2+}$  cations in CaMt is much smaller as most calcium cations are already fully hydrated at low water content (Fig. 3.15). The smaller  $D_{\text{cation}}$  in tetrahedrally charged montmorillonite can be explained similarly, as the probability of forming IS cation adsorption complexes is greater in clays with charge deficit in the tetrahedral sheet (Table 3.4). Further increase in the diffusion coefficients  $D_{\text{Na}}$  and  $D_{\text{Ca}}$  is shallower at 2W–3W transitions, indicating that only the increase in accessible volume rather than enhancements in the cation coordination environments. This observation is further confirmed by the RDF analysis discussed in the previous section, which noted formation of full hydration shells at water content corresponding to the bilayer hydrate (Fig. 3.13 and Fig. 3.14).

The trends obtained here are confirmed by experimental investigations into interlayer dynamics available from quasi-elastic neutron scattering [129, 130]. Our simulated  $D_{\text{OW}}$  values for NaMt are well in the range of previously reported values (Table 3.5). It should further be noted, that the mobility of interlayer water molecules is much lower than the  $D_{\text{OW}}$  value of  $(3.45 \pm 0.05) \times 10^{-9} \text{ m}^2\text{s}^{-1}$  in bulk TIP3P/Fs water ( $3.53 \times 10^{-9} \text{ m}^2\text{s}^{-1}$  reported in [131]). Their mobility is restricted due to the close proximity of the water molecules to the metal cations, which significantly alter their physical and chemical properties from those of bulk water [1]. Simulation was able to reproduce this behaviour and conclude that polarisation effects due to the cation are sensitive to its nature. Also, experiment inferred an extremely low  $D_{\text{Ca}}$  coefficient for octahedrally charged CaMt at 1W hydrate. As is clear from the interlayer structures presented in this chapter, this is due to confinement of  $\text{Ca}^{2+}$  in the ditrigonal cavity of clay surface.

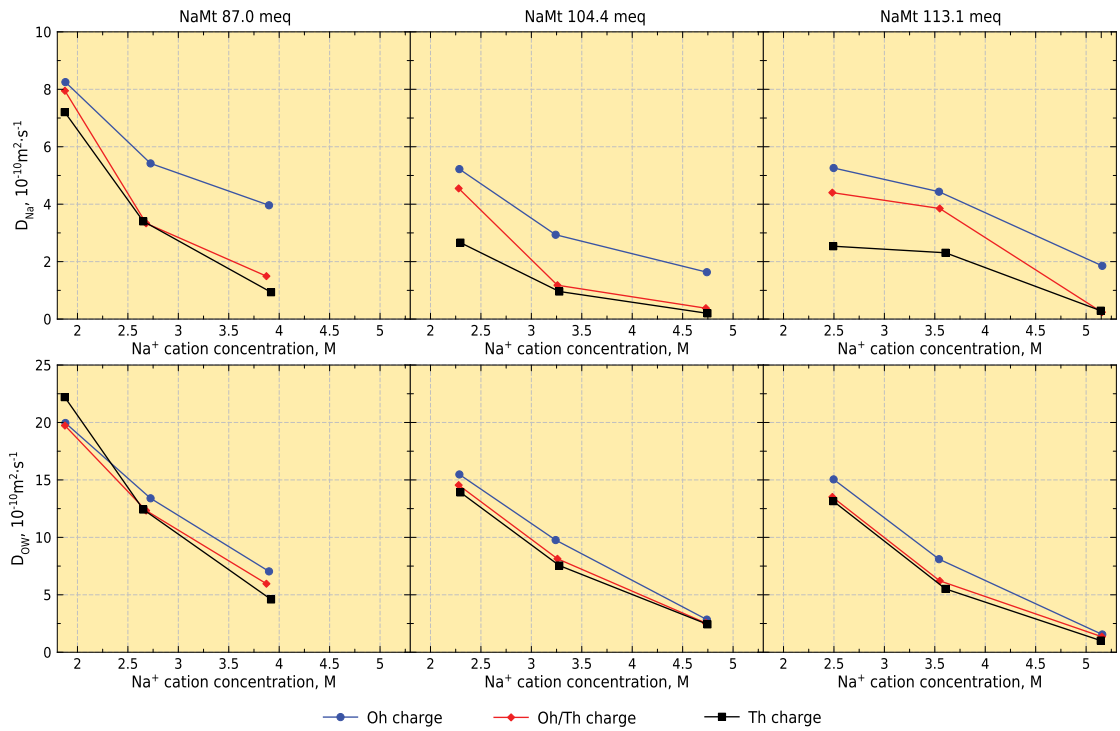
Table 3.5: Cation and water diffusion coefficients ( $10^{-10} \text{ m}^2\text{s}^{-1}$ ) from MD simulations and experiment for a CEC of 104 meq

	$D_{\text{OW}}$ (NaMt)		$D_{\text{OW}}$ (CaMt)		$D_{\text{Na}^+}$		$D_{\text{Ca}^{2+}}$	
	this work	exp <sup>a</sup>	this work	exp	this work	exp <sup>a</sup>	this work	exp <sup>b</sup>
1W	2.4-2.8	1-3	1.7-4.2		0.2-1.6	0.1	0.02-0.03	0.06-0.2
2W	7.5-9.7	5-10	3.5-6.7		0.9-2.9	1	0.02-0.5	
3W	13.9-15.4		7.6-9.5		2.6-5.2	2	0.2-1.2	

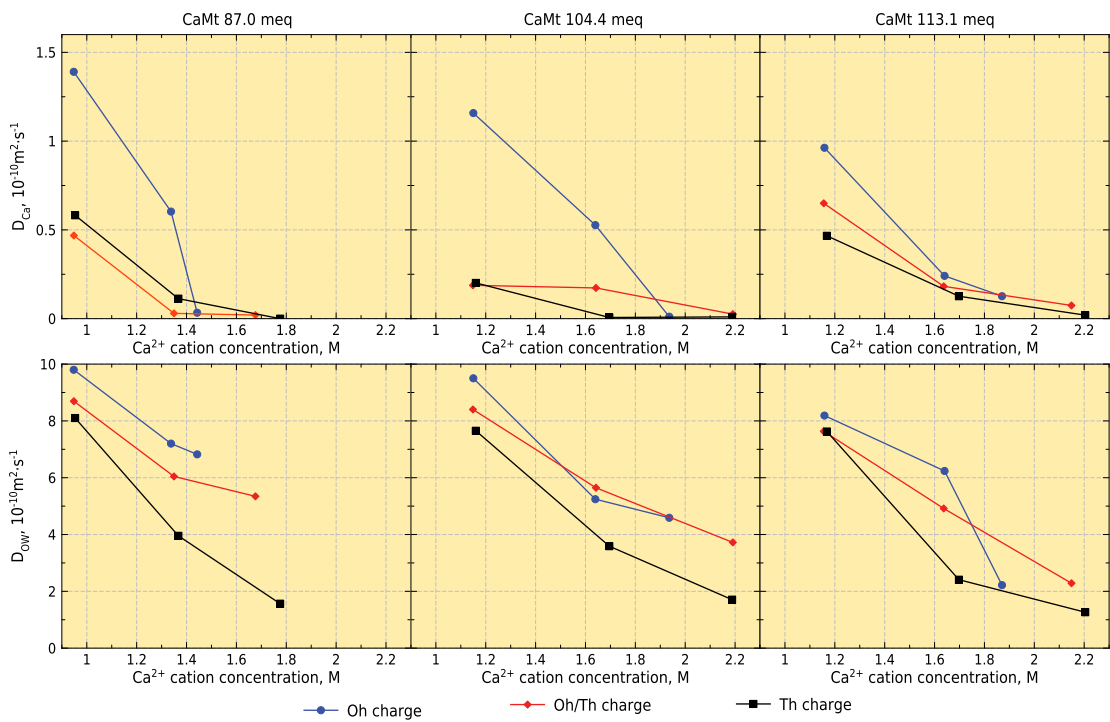
<sup>a</sup>Experimental results from Malikova et al. [129]

<sup>b</sup>Experimental results from Kozaki et al. [130, 132]

<sup>c</sup>Standard deviation for diffusion coefficients did not exceed  $\pm 0.005 \cdot 10^{-10} \text{ m}^2\text{s}^{-1}$



(a)



(b)

Figure 3.16: Diffusion as a function of cation concentration of cation (top) and  $O_{water}$  (bottom) for a) NaMt; b) CaMt

### 3.3 Conclusions and Chapter Summary

In this chapter MD simulation has been used to study hydration structures and dynamics of clay minerals. Initially, the work has focused on validating the carefully chosen potential models from the literature (CLAYFF and TIP3P/Fs) by comparing simulated thermodynamic characteristics of swelling clays with experiment. Later, simulation protocols that allowed a range of clay minerals to be simulated with a range of structural and energetic characteristics were developed. These showed that it is feasible to produce results that are comparable with experimental observations and to replicate distinctive features of clay hydration. This, along with the agreement with experimental observations, provided reassurance regarding the validity of the selected potential models.

A total of eighteen montmorillonite configurations with selected charge distributions and cation choices were investigated. The simulations predicted the swelling behaviours of negatively charged clay layers balanced with sodium and calcium cations with high accuracy. This included prediction of a step-wise mechanism of water absorption by NaMt and swelling from dry to bilayer hydrate of CaMt previously discussed in experimental studies. Additionally, the mechanism of water absorption by CaMt with predominantly tetrahedral charge was shown for the first time in this work.

Particular attention was paid to the interlayer structure and dynamics of water and exchangeable cations. This information will be crucial in subsequent chapters of this thesis where competitive intercalation of water and polymers will be probed. It was shown that cation coordination complexes are significantly influenced by clay charge location and magnitude. For example,  $\text{Ca}^{2+}$  adsorbed on the surface of clay with high octahedral charge forms an anhydrous complex and resides in the dodecahedral cavity of clay surface, reducing separation of clay layers as a result. CaMt interlayers with low water content are characterised by the presence of two layers of water with a layer of cations between them as most of the divalent cations are fully hydrated due to their high hydration affinity. However, introducing as little as  $-0.3 e \cdot uc^{-1}$  of tetrahedral charge into the clay model, rearranges the cations into two distinct layers sandwiching one single layer of water. This leads to significant reduction in the basal spacing of clay. The driving force of this process is considered to be the interaction between the exchangeable cation and the charged sites associated with isomorphous substitution in the tetrahedral sheet of clay. Water adopts its final structure accordingly.

In conclusion, this chapter has reported investigation into the dynamics of interlayer species as a function of clay layer charge distribution. The diffusion calculations allow identification of five major trends: (i) diffusion coefficients for exchangeable cations ( $D_{\text{cation}}$ ) and water ( $D_{\text{OW}}$ ) decrease as the clay layer charge increases; (ii)  $D_{\text{cation}}$  and  $D_{\text{OW}}$  decrease when clay layer charge is shifted to tetrahedral sheet; (iii) diffusion of interlayer water is significantly higher than that of exchangeable cations; (iv) diffusion of water in NaMt is higher than that in CaMt; (v) diffusion of sodium ( $D_{\text{Na}}$ ) is higher than diffusion of calcium ( $D_{\text{Ca}}$ ).

The work in this chapter can be considered as proof of concept and evidence that the potential model used for clay minerals is transferable to a range of other scenarios. In the following chapter the model is extended to probe the competitive intercalation of water and poly(ethylene glycol) by a variety of clay minerals.

## 4 Adsorption of Poly(ethylene) Glycol onto Montmorillonite

In the previous chapter, a detailed study of processes involved in the hydration of clay minerals was presented as these processes play a major role in the formation of polymer/clay nanocomposites. This chapter will firstly focus on a molecular simulation study of the dynamics and structure of a polymer/clay system that approximates an exfoliated nanocomposite, the definition of which was given in Chapter 1.2. The influence of the clay layer charge distribution on the dynamics of this nanocomposite obtained using MD simulations will thus be reported for the first time.

Later, the intercalated polymer/clay nanocomposite will be studied both experimentally and theoretically. Structural and thermodynamic properties of formulated nanocomposites will be probed using XRD, TGA and TG-MS techniques and then compared with corresponding values derived from a series of MD simulations of intercalated polymer/clay nanocomposites. The swelling dynamics, energetics and structure of the clay interlayers will be examined. Particular attention will be paid to the behaviour of polymer and water when they coexist in the clay interlayer. The experimental results will help in setting the criteria for the construction of the simulation cells in order that they relate to real systems as accurately as possible. Finally, the effect of the clay layer charge distribution on the polymer conformations in the interlayer of polymer/clay nanocomposites will be presented.

### 4.1 Introduction

Poly(ethylene glycol) (PEG, formula:  $\text{H}-(\text{O}-\text{CH}_2-\text{CH}_2)_n-\text{OH}$ ) has the molecular structure shown in Figure 4.1 and is also known as poly(ethylene oxide) (PEO) or polyoxyethylene (POE) [133]. The two names are chemically synonymous, but historically PEG refers to oligomers and polymers with a molecular mass below  $20\,000\text{ g}\cdot\text{mol}^{-1}$ , and PEO to polymers with a molecular mass above  $20\,000\text{ g}\cdot\text{mol}^{-1}$ . It is commercially available over a wide range of molecular weights from  $100\text{ g}\cdot\text{mol}^{-1}$  to  $10\,000\,000\text{ g}\cdot\text{mol}^{-1}$ . Pure PEG has been characterised as a clear viscous liquid ( $\text{MW} \leq 200\text{ g}\cdot\text{mol}^{-1}$ ), a wax-like substance ( $\text{MW} = 200 - 2000\text{ g}\cdot\text{mol}^{-1}$ ), or as an opaque white crystalline solid ( $\text{MW} > 2000\text{ g}\cdot\text{mol}^{-1}$ ). The methylene groups are hydrophobic, whereas the ether oxygen is hydrophilic [134]. Thus, PEG is readily soluble in water, but the solubility decreases with increasing molecular weight. Being a non-toxic compound, it is one of the most important polymers widely used in biotechnology, pharmaceutical compositions and as a food additive [135]. In recent years, however, it has found popularity in biodegradable food packaging applications [19, 136] where it can be used as plasticiser for polymer/clay-containing films which are otherwise notoriously brittle [137, 138].

To construct a PEG structural model for simulation, the unit cell of crystalline PEG ( $\text{C}_2\text{H}_4\text{O}$ ) was replicated to create the chain segment which was then terminated with hydroxyl groups. The resultant composition of a single PEG chain is  $\text{HO}[\text{C}_2\text{H}_4\text{O}]_4\text{H}$  which corresponds to a molecular weight of  $194.2\text{ g}\cdot\text{mol}^{-1}$  and end-to-end length of  $\sim 19.4\text{ \AA}$ . This poly(ethylene glycol) chain is denoted as PEG200. The polymer with this particular molecular weight was selected for the majority of the runs performed due to restrictions imposed by the size of the clay model and evidence that it readily intercalates into smectite minerals (shown later from experimental observations in Section 4.3.2). PEG chains with different MW were also utilised to probe the dependence of molecular weight on the swelling behaviour of clays.

The interaction between clay and polymer, i.e. PEG, is influenced by many factors, such

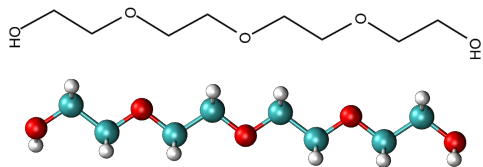


Figure 4.1: Graphical representation of poly(ethylene glycol) of  $MW = 194.2 \text{ g}\cdot\text{mol}^{-1}$  (PEG200). Colours: C cyan; O red; H white

as the nature of the clay, length and nature of the polymer chain and any solvent present. There are different accounts of the intercalation of PEG in layered silicates in the available literature [32, 41, 139, 140]. Studies based on X-ray diffraction propose a highly ordered polymer arrangement within the clay galleries. One proposed structure of the intercalated PEG is a helix (Fig. 4.2(a)). In this model, the axis of the polymer chain is oriented parallel to the basal surface and exchangeable cations reside in the centre of interlayer. It was first proposed by Ruiz-Hitzky et al. [13] and was believed to be plausible because only one plateau was observed in the adsorption isotherms, corresponding to basal spacing of  $18 \text{ \AA}$ . A second possible interlayer structure considers PEG chains to be organised in two extended chains parallel to clay surface layers (Fig. 4.2(b)). Here, exchangeable cations are also positioned in the middle of interlayer [14, 32, 41]. Unlike the helix conformation, this model contemplates two stages of swelling depending on the amount of PEG available – a monolayer with  $d_{001}$ -spacing of  $14 \text{ \AA}$  and a planar bilayer with  $d_{001}$ -spacing of  $18 \text{ \AA}$  [19].

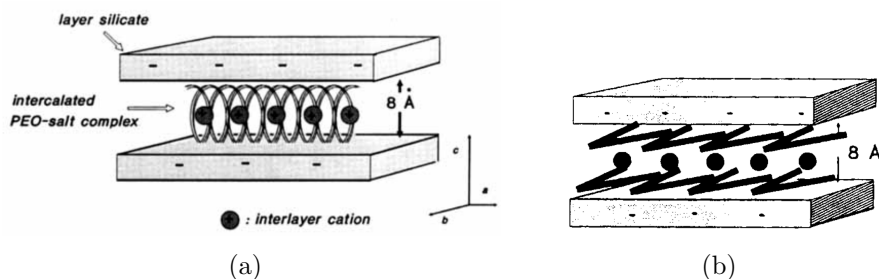


Figure 4.2: Schematic representation of models of PEG intercalation in smectites: a) helical conformation of PEG chains [13]; b) double layer planar conformation [14]

It was also proposed [41] that fully replacing the water molecules in the coordination environment of the exchangeable cation with the less polar PEG oxygen atoms was unlikely. Therefore, there is always interlayer water present to some extent. This assertion is confirmed via thermogravimetric analysis of formulated polymer/clay nanocomposites, and discussed later in this chapter.

Using MD and MC simulations, Hackett et al. [141] showed that the intercalated PEG chains in clay-based nanocomposites were arranged parallel to the basal surface of the hecatorite galleries. This structure agreed well with results of neutron scattering experiments, a review of which was given by Ray [142]. Further simulations of PEG/clay nanocomposites also suggested layered PEG structures [32, 92, 93, 134, 143, 144].

Therefore, it is reasonable to take, from the literature, that PEG may adopt various

conformations in the galleries of different clays. However, obtaining detailed molecular-scale insight into the structure and dynamics in the interlayer is difficult because of static and dynamic disorder of these systems. Here, computational approaches, e.g. MD, can be highly informative especially when considering both hydration and polymer intercalation processes simultaneously.

For the work presented in this Chapter, eighteen montmorillonite models with a selection of layer charge distribution and exchangeable cations (as described in Chapter 3) were utilised (Table 3.1) to simulate various PEG/Mt nanocomposites. Clay layers of similar size containing 32 unit cells were used to provide a disordered distribution of substitution sites and achieve sufficient statistics of the processes associated with adsorption of polymer on clay surfaces.

This chapter presents, therefore, a study undertaken to investigate the structure of exfoliated and intercalated PEG/Mt nanocomposites on a molecular level using the MD technique. It will focus on important questions such as: (i) is the structure derived from experiment confirmed in the MD simulations; (ii) how much water is co-adsorbed with PEG; (iii) how this water is distributed in the interlayer space; (iv) should the magnitude of clay mineral basal spacing be attributable purely to the varying amounts of PEG and water in the interlayer, or does the varying thickness of the PEG/water complex also play a role; (v) what is the influence of the layer charge and its location; and (vi) what is the influence of the nature of the exchange cation.

## 4.2 The Exfoliated System

### 4.2.1 Simulation Details

In the study of exfoliated PEG200/Mt system we consider a case with no water which corresponds to the situation when PEG has replaced all the water from the clay surfaces [145]. Each simulation of PEG200/Mt exfoliated nanocomposite involved the following stages:

1. The initial structure of bulk molten PEG200, was constructed using a random distribution of 130 molecules in a box with dimensions of  $39 \times 33 \times 50 \text{ \AA}^3$ , such that the system's density was close to the experimental value of  $1.120 \text{ g/cm}^3$  [146]. Then, an MD simulation in the NPT ensemble on this system was performed. Initially, the system was heated to a molten state at 700 K over 0.5 ns and then run for 1 ns at 700 K and quenched to 300 K over 0.5 ns. Thermodynamic and structural parameters were observed to ensure that the system had no memory of the initial set-up configuration (Fig. 4.3, inset).
2. The next step involved the addition of PEG chains on the clay mineral surface. For this, copies of the equilibrated PEG200 box were positioned on either side of the selected clay layer, with a  $45 \text{ \AA}$  of vacuum gap imposed, to eliminate the interaction of polymer chains through the periodic boundaries in a direction perpendicular to the clay layer.
3. Energy minimisation of the obtained PEG200/Mt supercell was followed by an annealing process at 500 K for 0.5 ns and then cooling to 300 K over the next 0.5 ns in the NVT ensemble. This was followed by a MD production run for 2 ns in the NVT ensemble. A snapshot of an exfoliated system after such a production run is shown in Fig. 4.4.

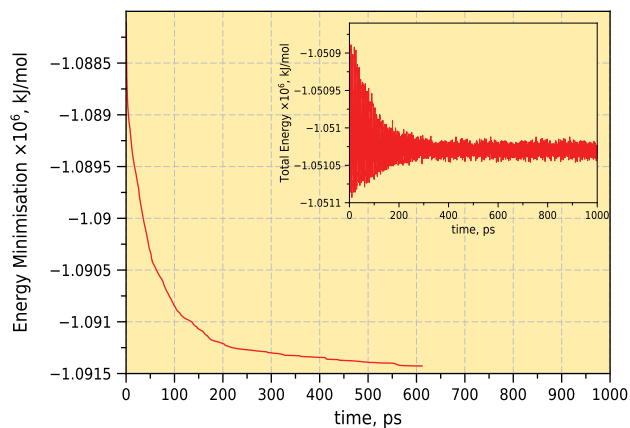


Figure 4.3: Energy minimisation of PEG200/Mt exfoliated system; After  $\sim 600$  ps the structure is minimised. The total energy during equilibration of the bulk PEG200 system is shown in the inset

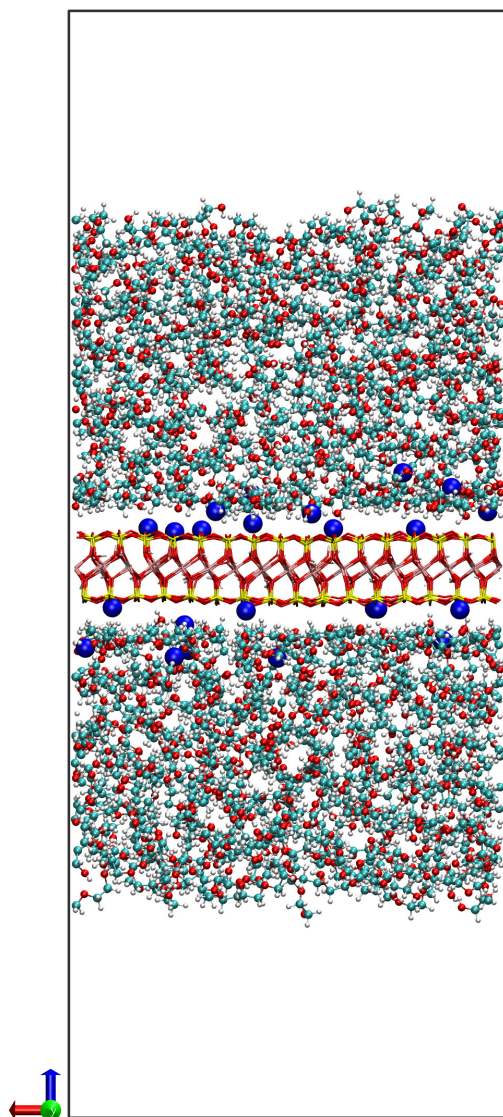


Figure 4.4: Snapshot obtained after 1 ns of MD simulation at 300K following the annealing cycle for an exfoliated PEG/NaMt system. Colours: Na blue; Si yellow; Mg cyan; Al pink; C cyan; O red; H white

For comparative purposes, a bulk PEG200 system was also considered. The initial structure contained 300 randomly distributed PEG200 molecules, and an annealing process was performed by MD simulation at 700 K for 1 ns followed by cooling to 300 K over 0.5 ns. The production MD run after that lasted for 2 ns at 300 K in the NPT ensemble. The experimentally obtained glass transition temperature of bulk PEG200 is  $\sim 223$  K [146]. It is therefore expected that the simulated systems will contain PEG200 in an amorphous state, as found experimentally at room temperature.

MD simulations were performed using the Nosé-Hoover thermostat with a 1.0 ps relaxation time. For the NPT simulations, a Nosé-Hoover barostat was utilised to control the pressure with a barostatic relaxation time of 1.0 ps. Interatomic interactions were evaluated using a time step of 0.001 ps, and three-dimensional periodic boundary conditions were employed with a cutoff at 12 Å for short-range interactions. Long-range electrostatic interactions were calculated using the Ewald summation with an accuracy of  $1 \times 10^{-6}$ . All MD production runs were performed at 300 K and at 1 atm for the NPT ensemble. Statistical and atomic position data were collected over the last 1 ns and stored every 25 ps to obtain the thermodynamic and structural properties of the simulated systems.

#### 4.2.2 Results and Discussion

##### Structure at the Interface

For all simulated exfoliated PEG200/Mt systems, at least five distinct layers of PEG chains were observable above the clay layers. This is apparent from atomic density profile measured normal to the clay surface (Fig. 4.5). The profiles shown here are for 104 meq NaMt with isomorphous substitutions in octahedral sheet only. The other investigated clays with various charge distributions show very little difference in the ordering structure of formulated PEG200/Mt nanocomposites. The ordering of PEG molecules persists up to 25 Å above the clay surface forming layers of thickness  $\sim 4$  Å. The highest density peak is found close to the clay surface, at 6.4 Å from the basal surface, which indicates a strong affinity between the polymer and the clay. A slight shoulder on the PEG oxygen atom density peak closest to the clay surface (Fig. 4.5, red line) is due to the participation of ether oxygens in the coordination of exchangeable cations.

The  $\text{Na}^+$  profile has three distinct peaks, one of which is very close to the surface, e.g. indicating the presence of a cation in the ditrigonal cavity of the clay surface and the formation of an anhydrous adsorption complex (Fig. 3.7(a)). The other two layers of sodium reside within the first peak of the PEG chains, leaving the opportunity to only form complexes with the first layer of PEG oxygen atoms. The limited mobility of the exchange cations is due to the development of a more complex coordination environment than that found for hydrated cations in Chapter 3. The mobility of these complexes will be addressed later in this chapter.

There is clear ordering of the PEG atoms in the direction perpendicular to the clay slab. This does not mean, however, that individual PEG polymer chains cannot span more than one polymer layer. To understand the PEG layer disorder, the calculation technique described by Suter et.al. [144] was employed. Here, the polymer domain is divided into layers 4 Å thick, with the origin at the minima of the atomic density profile (Fig. 4.5). The layer closest to the clay surface is denoted by Layer 1 and the farthest by Layer 5. In each layer,

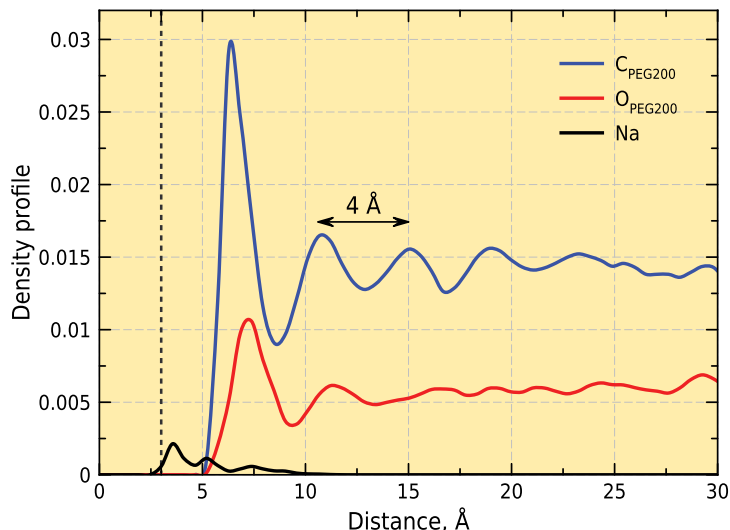


Figure 4.5: Atomic density profiles of the exfoliated PEG/NaMt nanocomposite species from MD simulation at 300 K. Vertical dashed line designate the plane of basal oxygens

the position of the centre of mass of every PEG molecule was calculated and the PEG layer to which it belonged to was ascertained. The relative proportion of each PEG chain’s carbon atom in each layer was then calculated, as given in Table 4.1. This shows that the PEG in the inner-most layer (Layer 1) does not mix much with polymer in the layers further from the clay surface. In contrast, the further away the centre of mass is from the clay surface, the more likely the PEG chain is to span several layers. The very planar arrangement of the layer closest to the basal surface is another indication of the strong interaction between the polymer and the clay.

Table 4.1: Distribution of carbon PEG200 atoms as a function of centre of mass location of polymer chain. The results presented for Mt with 104.4 meq layer charge in the octahedral sheet

PEG layer	Percentage of PEG carbon atoms				
	Layer 1	Layer 2	Layer 3	Layer 4	Layer 5
1	89	11			
2	20	70	10		
3	1	25	60	12	2
4		2	32	54	12
5		14	24	34	28

The differences in the structural conformations of PEG chains in the various layers are further evidenced by end-to-end distance distribution analysis. Figure 4.6 illustrates these distributions for PEG molecules in each layer of the PEG/Mt exfoliated system and with those found in the bulk polymer system. Initial end-to-end distance histograms were generated with a bin size of 0.5 Å and were subsequently fitted with a Gaussian function. These data show that the closer a PEG is to the basal surface (Fig. 4.6, Layer 1) the more extended or linear conformations are. Also, moving away from the clay layer the full width at half maximum of the distribution increases, indicating prevalence of more diverse coiled conformations in distant layers. In the layer farthest above the clay surface it is expected that the

end-to-end distance distribution of polymer molecules would approximate that in the molten bulk system where the polymer conformations approach that of an expanded coil [144].

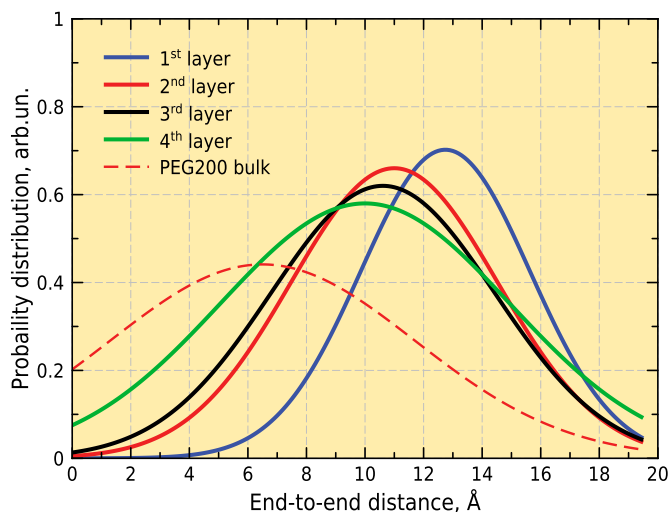


Figure 4.6: Gaussian fits to end-to-end distributions of PEG200 chains forming different layers above the clay surface of 104 meq NaMt and in molten bulk (dashed line)

The root mean square end-to-end distances of PEG200 molecules as a function of the layer position and type of clay are listed in Table 4.2. For the bulk PEG system, the polymer chains exhibit an average end-to-end distance of  $6.5 \pm 1.7$  Å. The PEG chains in the exfoliated PEG/NaMt system, however, have an average end-to-end distance of  $11.1 \pm 0.5$  Å, again indicating a more extended linear conformation of the PEG chains.

Whilst density profiles were indistinguishable for all systems simulated, a significant difference was observed in the end-to-end distances and radii of gyration of the PEG chains as the exchange cation and surface charge were varied. As shown in Table 4.2, for example changing the cation gives a difference of  $\sim 2.5$  Å (with respective values of  $11.9 \pm 0.5$  and  $9.5 \pm 0.3$  Å) in Layer 1 end-to-end distance. This phenomenon is due to the nature of exchangeable cation and the conformation that the PEG chains adopt with them (Fig. 4.7). The extended linear conformations of the adsorbed PEG chains (Fig. 4.7(a)) are found more often on NaMt than is the case of CaMt where the polymer tends to adopt bent conformations around the exchangeable cations (Fig. 4.7(b)). This is, in part, due to more negative hydration enthalpy of  $\text{Ca}^{2+}$  which requires the polymer chains to form cation coordination spheres in a more effective manner. The significantly closer relative proximity of  $\text{Na}^+$  cations, there are twice as many interlayer cations in NaMt than there are  $\text{Ca}^{2+}$  in CaMt, also plays a role – it increases the likelihood of extended linking configuration between two neighbouring  $\text{Na}^+$  cations. Analysis of simulation can also be used to interpret the prevalence of cis- and trans- orientations of the polymer chains and compare these with those proposed from experimental observations [41]. Thus, a high number of cis- orientation of H-C-C-H dihedrals can be understood in terms of a cation which is coordinated by a single PEG chain, whereas all trans- indicates that a chain lies flat on the clay surface (Fig. 4.7). A more detailed qualitative and quantitative overview of the PEG – exchangeable cation conformations will be provided in Section 4.3.3.

The average root mean square radius of gyration ( $R_g$ ) for the PEG chains in each layer

Table 4.2: Root mean end-to-end distance and radius of gyration of PEG200 chains in different layers of exfoliated PEG/Mt systems. Values for montmorillonites with CEC of 104.4 meq are presented

System	PEG200 Layer	End-to-end distance, Å			
		NaMt		CaMt	
		Oh	Th	Oh	Th
Exfoliated PEG/Mt	1	11.9 ± 0.5	12.3 ± 0.4	9.5 ± 0.3	9.3 ± 0.3
	2	11.2 ± 0.4	12.1 ± 0.4	10.4 ± 0.7	10.4 ± 0.7
	3	11.3 ± 0.6	11.9 ± 0.6	10.5 ± 0.8	10.1 ± 0.6
	4	10.8 ± 0.8	12.0 ± 0.5	10.6 ± 0.9	9.8 ± 0.5
	5	10.3 ± 0.9	11.8 ± 0.8	10.8 ± 1.0	9.5 ± 0.8
PEG200 bulk		6.5 ± 1.7			
		Radius of gyration, Å			
		NaMt		CaMt	
		Oh	Th	Oh	Th
Exfoliated PEG/Mt	1	5.3 ± 0.1	5.4 ± 0.2	4.0 ± 0.1	3.8 ± 0.5
	2	5.1 ± 0.2	5.3 ± 0.1	4.7 ± 0.4	4.8 ± 0.2
	3	5.0 ± 0.1	5.1 ± 0.3	4.8 ± 0.2	4.6 ± 0.3
	4	4.7 ± 0.3	5.0 ± 0.2	4.9 ± 0.2	4.5 ± 0.1
	5	4.9 ± 0.4	5.1 ± 0.3	4.6 ± 0.1	4.6 ± 0.9
PEG200 bulk		2.5 ± 1.1			

above the basal surface of different clays are also listed in Table 4.2. The radius of gyration is an indication of the distribution of the components of a polymer chain around an axis and calculated as root mean square distances between a molecule's centre of mass and all its constituent atoms (Section 4.3.2). We find  $R_g$  in every PEG layer to be between 4.9–5.4 Å for NaMt and 3.8–4.9 Å for CaMt. Values for both exchanged forms are much larger than in the bulk polymer system with its  $R_g = 2.5 \pm 1.1$  Å. This indicates, again, that the ordered and aligned PEG chains in the exfoliated nanocomposites are significantly expanded compared to those in the bulk system.

### Mobility at the Interface

Transport properties of PEG molecules were examined through calculation of the mean-square displacements (MSD) of polymer backbone atoms in each layer and comparison with those found in the bulk PEG200 system (Fig. 4.8). The slopes of these curves give a quantitative measure of the diffusion coefficients, according to Equation 2.21.

The previously evidenced strong interaction between the first polymer layer, basal surface and exchangeable cations exerts a significant effect on the mobility of PEG backbone atoms (Fig. 4.8, Layer 1). The dynamics of the PEG chains near the silicate surface is retarded compared to that in the remaining polymer layers. In the polymer layer farthest from the clay surface, the polymer chains are more mobile, however the MSDs for all the PEG molecules in system are still much lower than those of the bulk PEG system (Fig. 4.8). Similar behaviours were observed previously in theoretical investigations of exfoliated PEG/Mt nanocomposites [144].

All the MSD curves were fitted with linear functions resulting in coefficient of determination  $R^2$  found to be not less than 0.9970. The values of the diffusion coefficients obtained

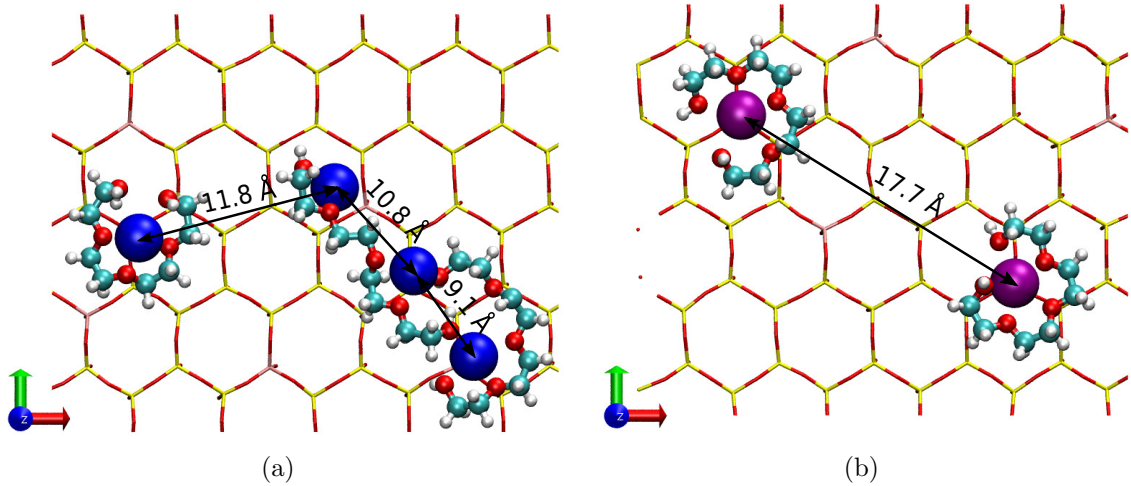


Figure 4.7: Fragments of clay surface of exfoliated a) PEG200/NaMt and b) PEG200/CaMt systems showing structural conformations of PEG molecules in complexes with exchangeable cations in the 1<sup>st</sup> layer. Distortion in measured and visual distances are due to 2D orthographic projection; cations can be positioned at different distances from the clay surfaces. Colours: Na blue; Ca purple; Si yellow; Mg cyan; Al pink; C cyan; O red; H white

for the backbone atoms of the polymer  $D_{\text{C}_{\text{PEG}}}$  and cations  $D_{\text{N}^{n+}}$  are summarised in Tables 4.3 and 4.4 respectively. In general, the diffusion coefficients for the PEG carbon atoms increase with distance from the clay surface. Atoms from first and fifth polymer layers of PEG/NaMt system diffuse with a rate of  $(1.02 \pm 0.01) \times 10^{-10} \text{ m}^2\text{s}^{-1}$  and  $(1.53 \pm 0.01) \times 10^{-10} \text{ m}^2\text{s}^{-1}$  respectively. In a similar manner to the end-to-end length distribution and the radius of gyration of farthestmost polymer layer, these carbon atom diffusion coefficients approach, but do not reach those of the bulk PEG200 system. The obtained diffusion coefficient value for the bulk PEG200 system ( $(2.91 \pm 0.01) \times 10^{-10} \text{ m}^2\text{s}^{-1}$ , Table 4.3) is very close to that computationally derived by Lee et al.  $(3.09 \pm 0.15) \times 10^{-10} \text{ m}^2\text{s}^{-1}$  for a 9-mer PEG with  $\text{MW} \sim 300 \text{ g}\cdot\text{mol}^{-1}$  [147] and experimentally obtained by Waggoner et al.  $2.76 \times 10^{-10} \text{ m}^2\text{s}^{-1}$  for PEG194 [148]. The type of exchangeable cation only appears to influence the dynamics of PEG chains in the first polymer layer. This is consistent with the conclusion made in previous section that exchangeable cations are always located within first polymer layer (Fig. 4.5).

Due to the large fraction of exchangeable cations in close contact with the clay surfaces and, thus, only partially complexed by PEG (Fig. 4.5), one may expect the existence of a large fraction of immobilised confined cations. The diffusion of exchangeable cations is inhibited by the complexes formed with polymer chains (Fig. 4.7) and is also sensitive to the magnitude of the clay layer charge (Table 4.4). Overall, diffusion of both exchangeable cations is smaller in tetrahedrally charged clays.  $D_{\text{Na}^+}$  in octahedrally charged clay significantly decreases when clay layer charge reaches CEC of 113 meq. This corresponds to a scenario where the cations are trapped in the dodecahedral cavity of the mineral surface. Divalent calcium, on other hand, is positioned in these cavities even in a low clay-charge environments. Similar trends were observed when the hydration dynamics of different montmorillonite clays were investigated (refer to Chapter 3).

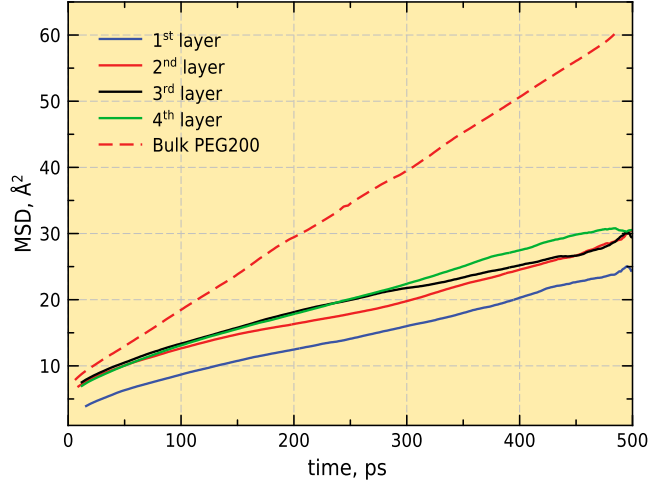


Figure 4.8: The mean square displacement (MSD) of the PEG carbon atoms as a function of time for exfoliated PEG/NaMt nanocomposite. MSD for PEG carbon atoms in the bulk system has been added for comparison purposes

Table 4.3: Diffusion coefficients ( $(10^{-10} \text{ m}^2\text{s}^{-1})$ ) of PEG200 chains carbons in each layer as a function of clay layer charge location and exchangeable cation. Values for clay with CEC of 104.4 meq are shown

System	PEG200 Layer	$D_{\text{C}_{\text{PEG}}}^a$ (PEG/NaMt)		$D_{\text{C}_{\text{PEG}}}$ (PEG/CaMt)	
		Oh	Th	Oh	Th
Exfoliated PEG/Mt	1	1.02	0.98	0.94	0.95
	2	1.35	1.33	1.34	1.30
	3	1.39	1.37	1.40	1.42
	4	1.48	1.40	1.44	1.45
	5	1.53	1.52	1.50	1.55
PEG200 bulk		2.91			

<sup>a</sup>Standard deviation of all calculated diffusion coefficients did not exceed  $\pm 0.01 \times 10^{-10} \text{ m}^2\text{s}^{-1}$

Table 4.4: Diffusion coefficients ( $(10^{-10} \text{ m}^2\text{s}^{-1})$ ) of exchangeable cations located in the first polymer layer of the exfoliated PEG/Mt system. Values for clays with different charge distribution are presented

CEC	$D_{\text{Na}^+}$		$D_{\text{Ca}^{2+}}$	
	Oh	Th	Oh	Th
87.0 meq	0.61	0.50	0.34	0.33
104.4 meq	0.48	0.38	0.29	0.33
113.1 meq	0.28	0.23	0.25	0.31

### 4.2.3 Conclusions

MD simulations of a range of PEG200/Mt systems containing full atomistic detail to approximate the exfoliated nanocomposite case were performed to determine the structural and the transport properties of polymer chains in the vicinity of the clay layer. Investigations into the effect of clay charge distribution on the structure and dynamics of formulated nanocomposites were also performed.

At least five layers of PEG chains were identifiable, these being 4 Å thick and parallel with the clay surface. The inner-most layer (closest to clay surface) was most stable due to presence of the exchangeable cations and the charges within the clay surface. With increasing distance from the clay surface, individual polymer chains showed a tendency to be distributed over several layers. End-to-end distance distributions and radius of gyration analyses indicated that PEG200 polymer chains were much more extended than in the molten bulk PEG200 system and arranged parallel to the clay surface. This was apparent even at distances more than 25 Å away from the mineral surface due to the effective confinement imposed by adjacent PEG layers.

Also, an interesting difference was found between polymer conformations in the NaMt, and the CaMt based nanocomposites. Extended linear conformations of PEG chains were found more often on the NaMt surface than in the case of CaMt, where polymer tended to adopt coiled conformations around the divalent  $\text{Ca}^{2+}$  cations. This is due to more negative hydration enthalpy of the  $\text{Ca}^{2+}$  cation, and the significantly higher concentration of monovalent  $\text{Na}^+$  cations in the nanocomposite which increased the opportunity for polymer chains to "bridge" two or more cations.

The polymer layer closest to the basal surface also showed the lowest diffusional motion. This effect was particularly evident in nanocomposites formed with high charge clays with charge predominantly located in the octahedral sheet. Similar to the clay-water systems, presented in Chapter 3, cations were found to adsorb onto the dodecahedral cavity of the mineral surface, thus, constricting their transport as well as that of the polymer chains that have formed complexes with them. One may speculate that this immobilisation of adsorbed polymer may contribute to the low permeability of gasses and vapours in clay nanocomposite materials by making any diffusional path more tortuous.

It appears that MD is a useful tool for determining the structural and transport properties of polymer/clay nanocomposites. In the next section, intercalated clay polymer nanocomposites will be investigated, and further extended by introducing water in the system.

### 4.3 The Intercalated Systems

One of the reasons that clay minerals are efficient adsorbents is that the interlayer spaces are potentially accessible not only for water molecules, but for organic materials as well. Thus, it is necessary to investigate the adsorption between the layers by applying the techniques employed to study single clay minerals to new bilayer systems. To this end, here we present experimental and molecular simulation investigations of different combinations of PEG and water in a range of montmorillonites.

#### 4.3.1 Details of Experimental and Simulated Systems

##### Preparation of PEG200/Clay Films

In order to assess the ability of chosen models to simulate the swelling behaviour of PEG/Mt composite and rationalise the simulation observations, some experimental work on the swelling of various montmorillonite clays, when loaded with different amounts of PEG200, was performed by the candidate. The broader aim here was to gain a better understanding of the processes involved in real polymer/clay composite formations.

All experimental PEG/clay nanocomposites presented in this thesis were prepared using the solvent casting method. The bentonite clay samples, Cloisite<sup>®</sup> Na<sup>+</sup> (NaMt) and Cloisite<sup>®</sup> Ca<sup>2+</sup> (CaMt), were supplied by Southern Clay Products and used as received. The bentonite is predominantly composed of montmorillonite with CEC value of 92.5 meq/100g. PEG of molecular weight of 200 g·mol<sup>-1</sup> was used as supplied by Aldrich.

For the nanocomposite preparation, the concentration of each component used was based on the total solid content.  $3 \pm 0.001$  g of clay was initially mixed with 60 ml of distilled water in a beaker and agitated for 2 hours using a magnetic stirrer. The desired amount of PEG200 (PEG200:clay=0, 3, 9, 12, 18, 27 wt%) was mixed in 20 ml of distilled water and added to the clay suspension. The PEG200/clay solution was then stirred for a further 6 hours at room temperature before being cast onto a glass slide and placed into a Petri dish. All of the suspensions were dried in an oven at 40 °C for 3 h and then left at room temperature for 12 h before being analysed by XRD, TG and TG-MS. XRD, in particular, provides evidence for the formation of intercalated systems by allowing measurement of the interlayer spacing. The Petri dishes containing the dispersions were used for general characterisation after grinding.

##### Simulation Details

The set up of the intercalated PEG/water/Mt nanocomposite model is similar to that described in Chapter 3. A broad range of PEG200 and H<sub>2</sub>O concentrations, ranging from 0 to 0.35 g<sub>PEG200</sub>/g<sub>clay</sub> (0 to  $\sim 7.1$  PEG200·uc<sup>-1</sup>) and 0 to 0.2 g<sub>H<sub>2</sub>O</sub>/g<sub>clay</sub> (0 to  $\sim 16.5$  H<sub>2</sub>O·uc<sup>-1</sup>) respectively were used. Range of clay models utilised to simulate PEG/water/Mt intercalated nanocomposite comprised of eighteen montmorillonite models described in Chapter 3 (Table 3.1). The preparation of each simulation cell consisted of the following steps:

1. The initial structure of the PEG/H<sub>2</sub>O blend was constructed using randomly distributed PEG200 molecules with pre-equilibrated water molecules at the desired ratios. Then, a 2 ns MD simulation in the NPT ensemble of the formulated system was performed. Initially, the system was heated to a molten state at 700 K over 0.5 ns and

then run for 1 ns at 700 K and quenched back to 300 K over 0.5 ns.

- Two clay layers were then separated to create two interlayers wide enough to accommodate the PEG/H<sub>2</sub>O blend. Energy minimisation of the obtained PEG/Mt supercell was then followed by an annealing process at 500 K for 0.5 ns and, then, cooling to 300 K over a further 0.5 ns in NPT ensemble. This was followed by a production run for 2 ns in the NPT ensemble; the cell dimensions being monitored to allow the basal spacing of the clay interlayer to be measured (Fig 4.9). A snapshot of the intercalated PEG/Mt nanocomposite model after a production run is shown in Figure 4.10, left. Subsequently, the d-spacing curves were calculated by decrementally removing a number of polymer molecules from the interlayers, and the aforementioned annealing process was performed at each reduced PEG content followed by a MD production run. As for the clay + water systems presented in Chapter 3, for some systems, an incremental increase of PEG200 interlayer loading was also performed. This provided identical montmorillonite structures and d-spacings to those observed in the series of deswelling simulations. This demonstrated conformity between the swelling and deswelling behaviour (i.e. reversibility) for these systems and indicated that the examined configurations were fully equilibrated.
- The structural and dynamic properties of constructed models were later determined from subsequent NVT simulations of a single interlayer, which were performed for another 2 ns. The initial atomic positions for the NVT simulations were taken from the previous NPT simulation and 25 Å of vacuum was added between one pair of clay surfaces to eliminate the interaction between them through periodic boundary condition (Fig. 4.10, right). The basal spacing was controlled during the NVT simulations to make sure that they matched those obtained from the NPT simulations. One interlayer region was removed from the simulation box because this significantly improved the computational efficiency of the simulation without losing in the accuracy of obtained observables.

Molecular dynamics simulations were performed using the Nosé-Hoover thermostat and DL\_POLY simulation package with 1.0 ps of relaxation time. For the NPT simulations, a Nosé-Hoover barostat was utilised to control the pressure with a barostatic relaxation time of 1.0 ps. Interatomic interactions were evaluated using a time step of 0.001 ps, and three-dimensional periodic boundary conditions were employed with a cutoff at 10 Å for short-range interactions. Long-range electrostatic interactions were calculated using the Ewald summation with an accuracy of  $1 \times 10^{-6}$ . All MD simulations were performed at 300 K and at 1 atm for the NPT ensemble. Statistical and atomic position data were collected over the last 1 ns of the simulation and stored every 25 ps to obtain the thermodynamic and structural properties of the simulated systems.

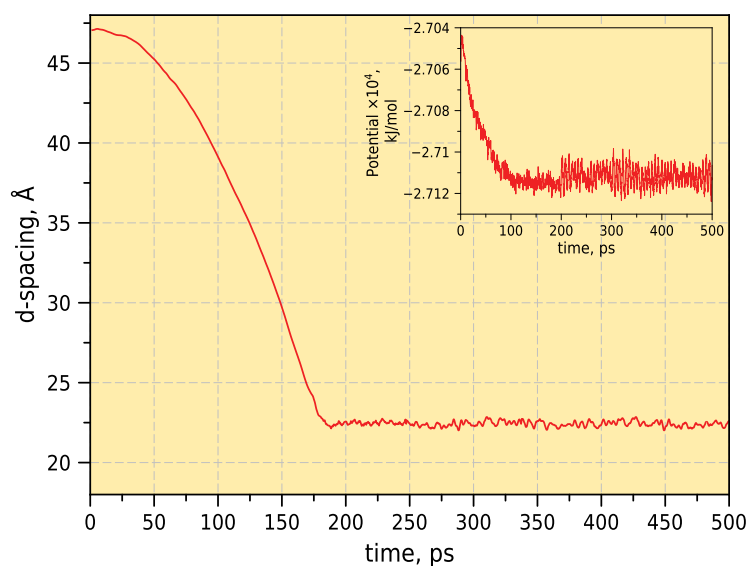


Figure 4.9: Basal spacing evolution of 104.4 meq NaMt clay with Oh charge containing 34 PEG200 and 180 H<sub>2</sub>O molecules in the interlayer as a function of simulation time. First 500 ps of the equilibration process are shown

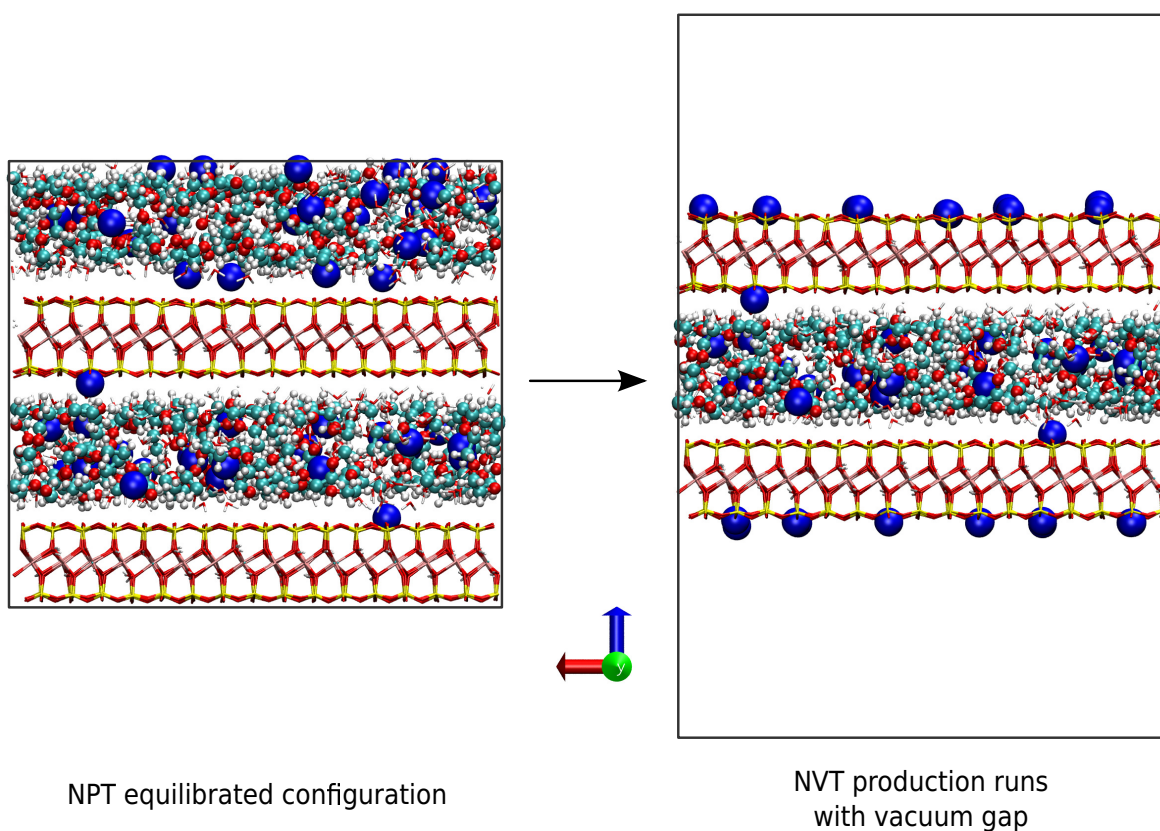


Figure 4.10: Simulation flow of the intercalated PEG200/Mt systems. Here a NaMt cell containing 34 PEG200 molecules (0.28 g<sub>PEG</sub>/g<sub>clay</sub>) and 180 H<sub>2</sub>O molecules in each interlayer are shown. Colours as in Figure 4.4

### 4.3.2 Experimental Characterisation of PEG/water/Mt Intercalated Films

The XRD patterns for PEG/NaMt and PEG/CaMt with a range of PEG200 loadings are presented in Figure 4.11 and the corresponding calculated  $d_{001}$ -spacings are plotted in Figure 4.12. The diffraction profiles obtained are in a very good agreement with numerous previous investigations of PEG intercalation into NaMt [41, 139, 140]. The shift of the XRD peak positions for Na<sup>+</sup> exchanged clay (Fig. 4.11(a)) indicate the presence of intercalated structures for the whole range of PEG loadings. Even a very small amount of PEG200 (3 wt%) forces the clay layers to expand from 12.7 Å to 13.6 Å ( $6.98^\circ 2\Theta$  and  $6.46^\circ 2\Theta$  respectively). This continues with higher loadings of PEG which gradually fills the interlayer until a complete PEG200 monolayer in the interlayer is apparently formed at 12 wt% ( $6.22^\circ 2\Theta$ ) with a d-spacing of  $\sim 14.4$  Å (Fig. 4.12(a)). Further loading of PEG200 (18 wt%) results in the formation of two coexisting structures – monolayer (14.4 Å) and bilayer (16.7 Å) which are apparent from the two peaks in the XRD trace at  $6.1^\circ 2\Theta$  and  $5.1^\circ 2\Theta$  respectively. The bilayer polymer structure is completely formed when the PEG200 loading reaches 27 wt%, as evidenced by the narrow distribution of d-spacings and the high intensity of the XRD peak, corresponding to a d-spacing of 18.5 Å.

XRD traces suggest completely different behaviour for the Ca<sup>2+</sup> exchanged clay upon intercalation of PEG200 (Fig. 4.11(b)). The XRD peak for the sample with 0 wt% PEG200 is located at  $5.68^\circ 2\Theta$  which corresponds to d-spacing of 15.1 Å (Fig. 4.12(b)). At this point, only water and hydrated Ca<sup>2+</sup> cations are present in the interlayer. The calculated d-spacing agrees with that of the simulated clay + water systems presented in Chapter 3 where it was concluded that CaMt always forms a bilayer hydrate interlayer at ambient conditions, due to the high hydration capability of bivalent the exchange cation. Upon introducing PEG200 into this system, the d-spacing of PEG/CaMt increases nearly linear until it reaches a spacing of 18.8 Å at 18 wt%. It then levels off, presumably showing the limit of intercalation capability of Ca<sup>2+</sup>-cloisite<sup>®</sup> at room temperature and normal pressure.

Although there is strong agreement between these observations and previously published data [41, 139, 140], it should be noted, that clays with a range of layer charge distributions and purity were used by different research groups. Also, the preparation methods and measurement conditions in the different laboratories can induce discrepancies in calculated basal spacings of PEG/Mt intercalated nanocomposites.

### Thermal Decomposition of PEG in Nanocomposites

The thermal stability of the formulated samples was investigated using the TGA technique. The thermograms (TG) and corresponding negative derivatives (dTG) for PEG/Mt nanocomposites are presented in Figures 4.13 and 4.14 and were utilised to quantify the amount of intercalated PEG and water present in the nanocomposites. Thermal decomposition of the PEG/Mt nanocomposites proceeds as a multiple-step process: (i) weight loss due to the release of water at temperature less than 225°C; (ii) decomposition of polymer at 250–400°C forming monomers, small oligomers, and other decomposition products [41]; (iii) dehydroxylation of the Mt layer at  $\sim 700^\circ\text{C}$ . These three processes are intrinsic for both Na<sup>+</sup> exchanged and Ca<sup>2+</sup> exchanged montmorillonites, as revealed by the TG curves shown in Figures 4.13(a) and 4.13(b) respectively.

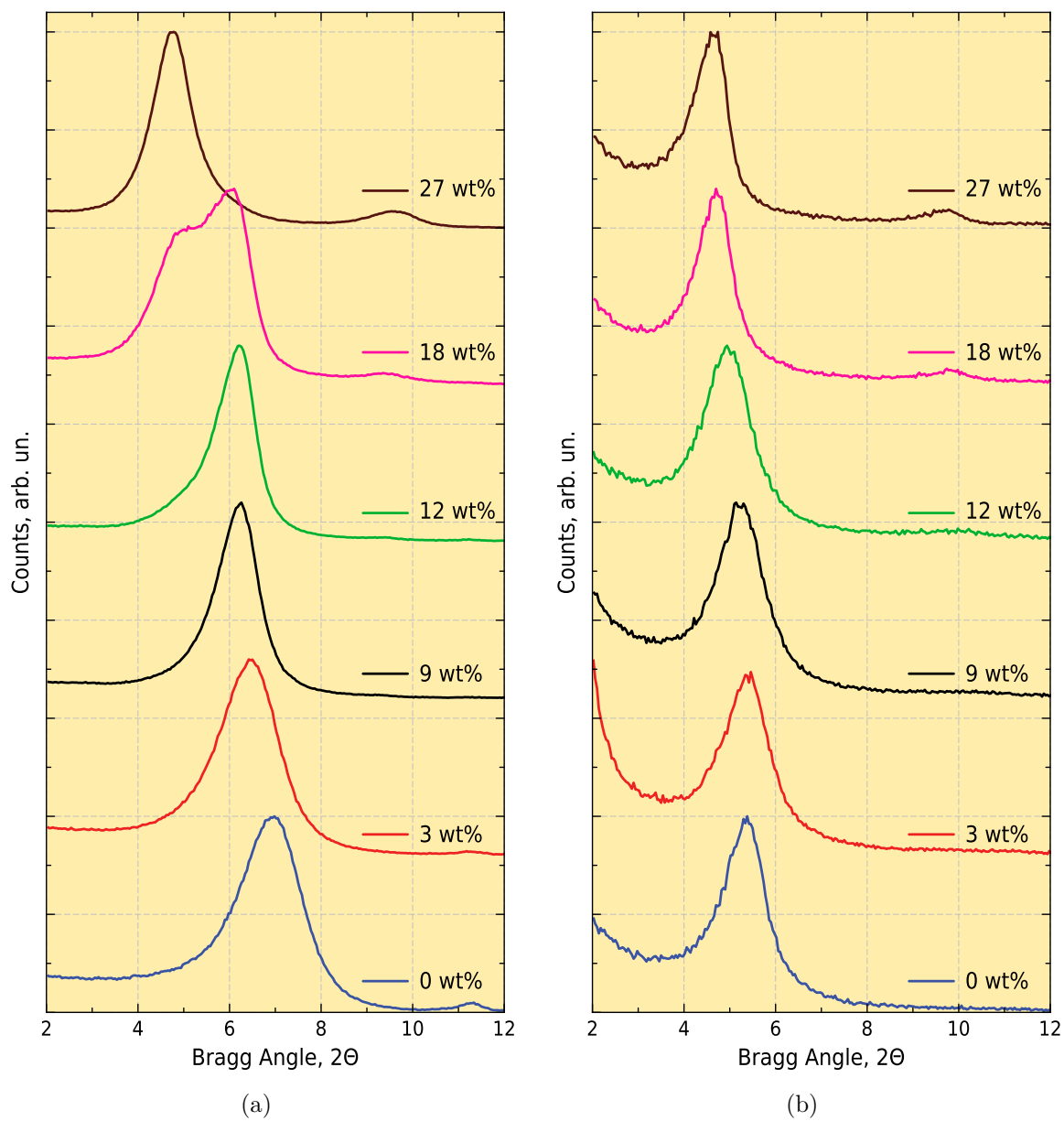


Figure 4.11: XRD patterns of PEG/Mt with 0–27 wt% PEG200 for a) Na<sup>+</sup>-cloisite<sup>®</sup> and b) Ca<sup>2+</sup>-cloisite<sup>®</sup>

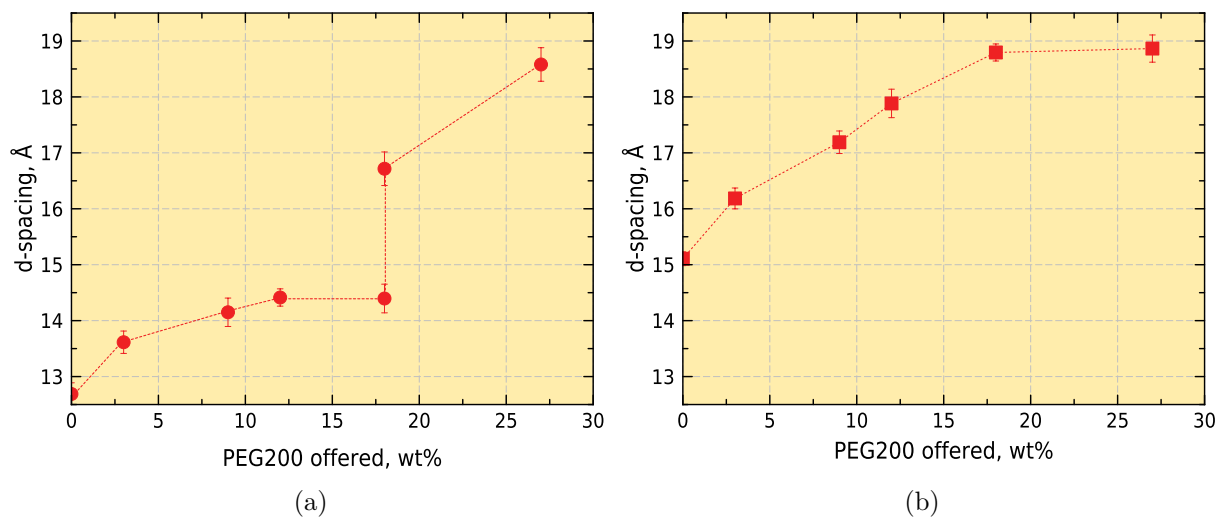


Figure 4.12: Summary of d-spacing observed in the XRD traces of PEG200/Mt for a) Na<sup>+</sup>-cloisite<sup>®</sup> and b) Ca<sup>2+</sup>-cloisite<sup>®</sup>

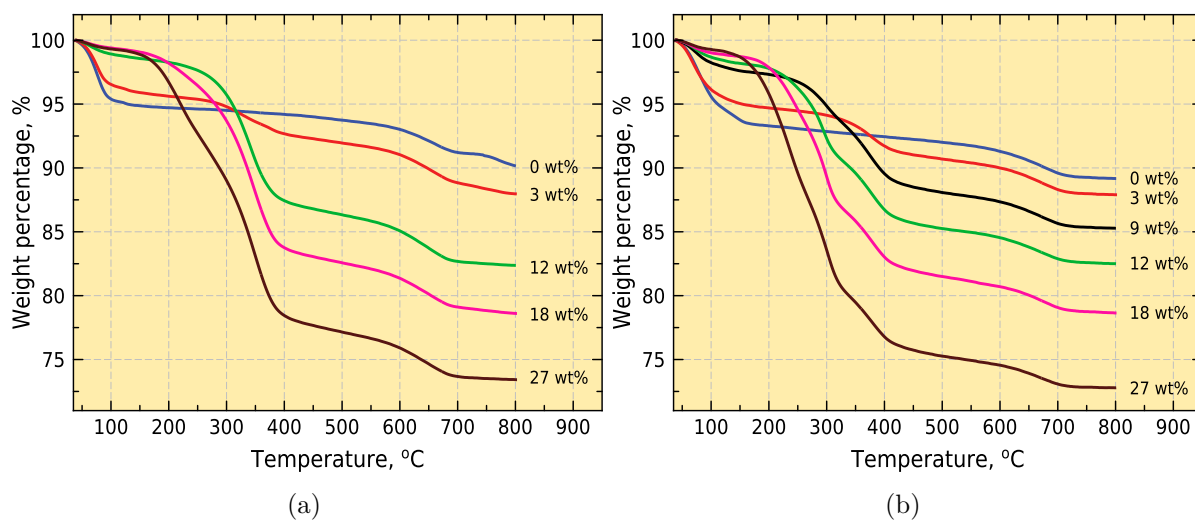


Figure 4.13: Thermograms of PEG200/Mt with different wt% PEG200 for a) Na<sup>+</sup>-cloisite<sup>®</sup> and b) Ca<sup>2+</sup>-cloisite<sup>®</sup>

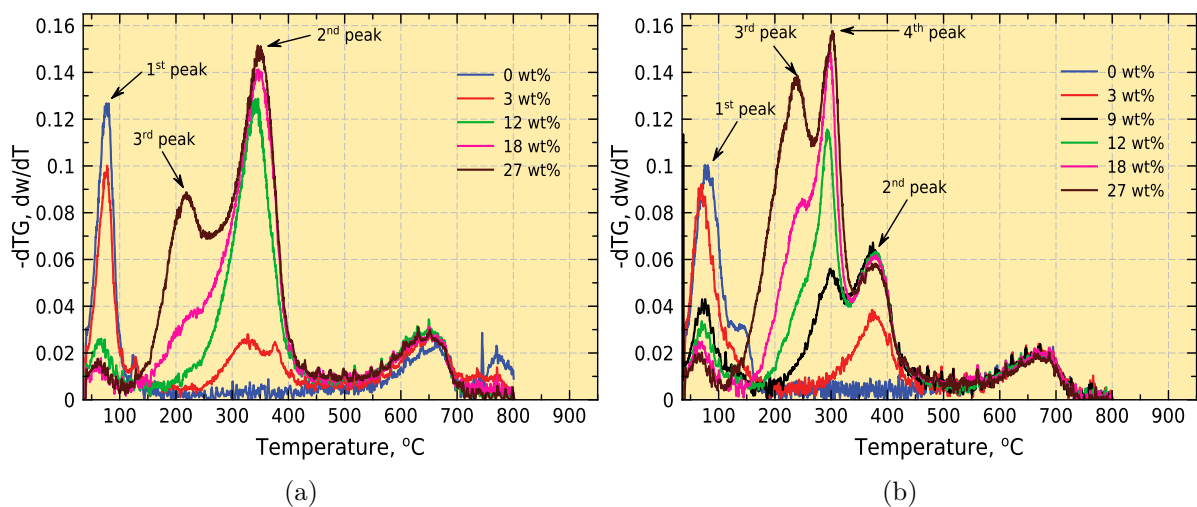


Figure 4.14: TGA negative derivatives of PEG200/Mt with different wt% PEG200 for a) Na<sup>+</sup>-cloisite<sup>®</sup> and b) Ca<sup>2+</sup>-cloisite<sup>®</sup>

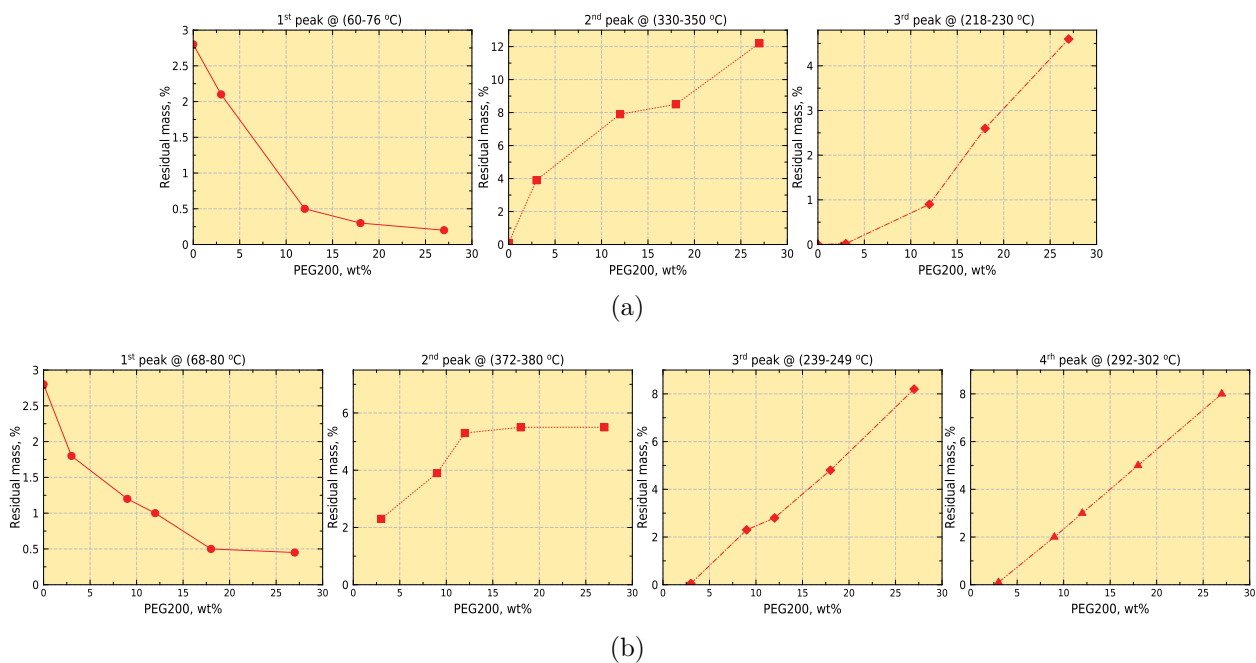


Figure 4.15: Weight losses associated with peaks 1–4 defined in Figure 4.14 for a) Na<sup>+</sup>-cloisite<sup>®</sup> and b) Ca<sup>2+</sup>-cloisite<sup>®</sup>

The first major weight loss occurs between 35 and 150°C. The reciprocal dTG peak, denoted as 1<sup>st</sup> peak in Figures 4.14(a) and 4.14(b), corresponds to the removal of water from the samples. The amount of released water decreases as the PEG concentration increases from 0 to 27 wt% (Fig. 4.15(a) and 4.15(b), 1<sup>st</sup> peak). This indicates that either some of the water present in clay is being replaced by PEG200 [139] or that more compact water aggregates are created which remain in place up to ~ 150°C [140]. A shoulder at ~ 140°C in dTG curve of pure Ca<sup>2+</sup>-cloisite<sup>®</sup> (Fig. 4.14(b)) is due to the decomposition of the relatively strong Ca<sup>2+</sup> hydration shells [41].

Adding as little as 3 wt% of PEG200 to both clays reveals a 2<sup>nd</sup> weight loss peak between 300°C and 400°C (Fig. 4.14). The intensity of this peak increases as the amount of PEG in the nanocomposite increases – significantly, up to 7x for NaMt but to a much smaller extent for CaMt (up to 1.5x). The weight loss curves associated with the 2<sup>nd</sup> dTG peak (Fig. 4.15) correlate clearly to the shapes and progression of the corresponding XRD swelling curves (Fig. 4.12). In particular, the weight loss curves of PEG/NaMt nanocomposites level off between 12 and 18 wt% PEG200 content, which corresponds to a monolayer polymer organisation within the interlayer. Further increase in PEG content results in a significant increase in the weight loss associated with this. The corresponding weight loss of the CaMt based nanocomposites, on the other hand, reaches a plateau at a lower PEG200 content which corresponds to the formation of a PEG200 bilayer in the interlayer. Similar to the swelling curve, further increase in PEG200 content does not influence the observed weight loss.

Selected m/z chromatograms from the TG-MS data obtained from PEG/NaMt (27 wt%) are presented in Figure 4.16. These indicate, that the 2<sup>nd</sup> peak is due to decomposition of water (m/z = 17) and PEG200 (m/z = 43,44,45). The large amount of water could be due to strong association with PEG200 (in gallery or bulk) or exchangeable cations. It should be noted, however, that the intensity of the m/z chromatograms does not necessarily relate to the amount of species present in the sample, since various levels of responses can be observed from different m/z ions. Therefore, taking into account all above said (particularly the correspondence of the weight loss and d-spacing data), it can be concluded that the appearance of a 2<sup>nd</sup> peak is due to the decomposition of intercalated water and polymer.

The third peak (Fig. 4.14(a)) becomes sizeable at PEG200 contents of 18 wt% for NaMt and 12 wt% for CaMt. These loadings correspond to the formation of the bilayer interlayer structure for clays in both exchanged forms (Fig. 4.12(a)). The weight losses at these corresponding temperatures are nearly linear, especially at high PEG content (Fig. 4.15, 3<sup>rd</sup> peak). In mass chromatograms at temperatures corresponding to the 3<sup>rd</sup> peak on Figure 4.15, substantial amounts of water (m/z = 17) and products of PEG decomposition (m/z = 43,44,45) are detected. One explanation of the 3<sup>rd</sup> weight loss peak could be not fully intercalated PEG, in which only a few polymer chain segments are occluded by the gallery and the bulk of each molecule remains in solution [32].

A 4<sup>th</sup> weight loss peak is visible only for calcium exchanged montmorillonite (Fig. 4.14(b)) and becomes sizeable at 9 wt% PEG200 content, which corresponds to a partially complete bilayer interlayer structure ( $d_{001} = 17.2 \text{ \AA}$ ) and increases with an increase in PEG200 content.

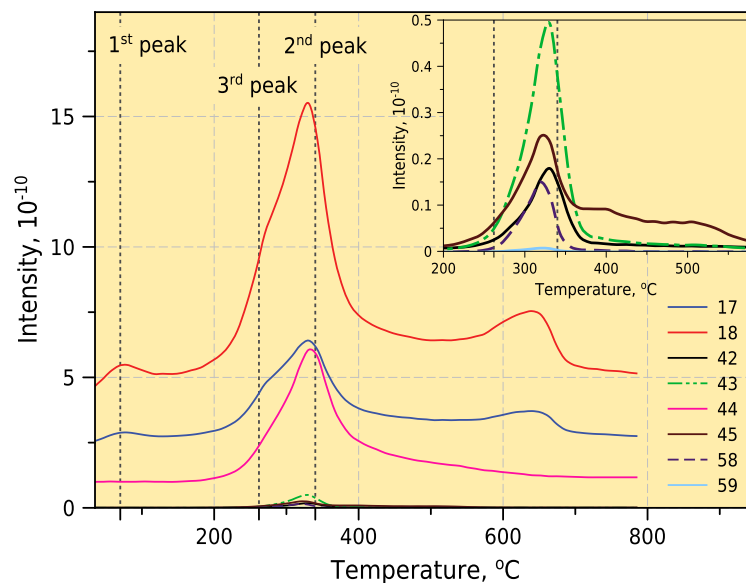


Figure 4.16: Mass chromatograms obtained from volatile degradation products during the thermal degradation of a PEG200/NaMt mixture (27 wt%)

The change in weight loss with increase in the amount of polymer gives a good linear fit with formula  $0.3301x - 0.9355$  and  $R^2 = 0.9998$ . The position of this weight loss peak also coincides well with the temperature of PEG200 decomposition ( $300^{\circ}\text{C}$ ). Taking into account the linear weight loss behaviour at this temperature, it is fair to conclude that the 4<sup>th</sup> weight loss peak corresponds to bulk PEG200 that reside outside of the clay galleries (supernatant configuration). This configuration is specific for  $\text{Ca}^{2+}$ -montmorillonite only and correlates with previous experiment which showed that NaMt uptakes of PEG is greater than than of CaMt [149]

The amounts of water and PEG200 for all studied samples, calculated on the basis of TG curves and TGMS analysis, are presented in Table 4.5. Only the 1<sup>st</sup>, 2<sup>nd</sup> and 3<sup>rd</sup> weight loss peaks (Fig. 4.14) were taken into account here. It is rather important to recognise that these values do not relate exclusively to intercalated media, as there is no direct way to distinguish intercalated from supernatant adsorption configurations. CaMt retained a higher amount of water for all studied samples, as expected from hydration analysis presented in Chapter 3. For example, pure NaMt and CaMt contained 5.0% and 7.3% of water respectively. NaMt, on the other hand, adsorbed higher amounts of polymer, giving adsorbed PEG loadings very close to the percentages of offered polymer. As the PEG content in the nanocomposite increased the amount of water decreased for both exchanged clay forms. This suggests that PEG intercalates by replacing the free water molecules in the gallery as well as some water that is directly coordinated to the exchangeable cations.

Table 4.5: Amounts of PEG and water adsorbed from water solution on NaMt and CaMt, as determined by thermogravimetry

PEG200 offered (wt%)	NaMt		CaMt	
	H <sub>2</sub> O amount (%)	PEG amount (%)	H <sub>2</sub> O amount (%)	PEG amount (%)
0	5.0	-	7.3	-
3	4.1	3.8	5.4	2.7
12	1.2	10.2	2.2	9.1
18	0.5	17.3	1.5	15.8
27	0.4	23.6	1.1	21.0

## Conclusions

Two types of commercially available bentonite clay were used to produce intercalated polymer/clay nanocomposites with a wide range of PEG and water concentrations. This was done to provide an evidence base for direct comparison with computer simulations of similar systems that will be presented in the next section of this chapter. Also, additional information on the processes involved in the collaborative intercalation of water and PEG into clay minerals was required. Through the use of XRD analysis, particular attention was paid to the interlayer structure of the formulated samples. Thermal stability and quantitative analysis of adsorbed organic material was assessed by TG and TGMS analysis.

XRD analysis indicated significant expansion of both clays studied upon increase of polymer content. Two stable polymer structures within the interlayer of NaMt were identified – a monolayer and a bilayer. The exchangeable cation has a significant effect on the expansion properties of montmorillonite. CaMt did not produce a stable monolayer, showing a linear increase of basal spacing as the polymer content in the system increased, until a stable bilayer polymer structure was created. The value of the d-spacing at 0 wt% of PEG200 was on par with that found in the simulations of the hydration process of clay layers presented in Chapter 3, indicating the presence of a bilayer hydrate in the CaMt interlayer even at low relative humidity.

Experimental measurements of intercalated PEG/Mt nanocomposites showed that polymer chains replace some of the adsorbed water, filling the space between hydrated exchangeable cations. The amount of polymer adsorbed is influenced by the hydration enthalpy of the exchangeable cation, indicating possible associations between those exchangeable cation and the ether oxygen atoms of PEG chains. The uptake of PEG200 by NaMt is higher than that by CaMt.

Finally, it should be noted that XRD analysis does not readily tell one the amount of water or organic material in the interlayer of a clay mineral. Therefore, computer simulation of similar nanocomposites can be useful in assessing these values. This will be discussed in the following sections of this Chapter.

### 4.3.3 Molecular Simulation of PEG/clay Intercalated System

Intercalated PEG/clay nanocomposites are well studied both experimentally and theoretically. The aim of the following section is to probe the applicability of developed potential models to predict structural features of these materials. Morphological characterisation of the polymer chains, competitive adsorption of water and polymer in the interlayer and dependence of this process on the clay net layer charge and location will be discussed in detail as well.

#### Swelling Energetics and Interlayer Structures

Figure 4.17 presents the results of a series of simulations for the intercalation of PEG200 in the montmorillonite exchanged by  $\text{Na}^+$  and  $\text{Ca}^{2+}$  cations. The calculated basal spacing of the clay complex is plotted as a function of polymer content along with experimental data presented previously in this chapter. Carefully selected variable amounts of water in the interlayer were based on experimental data obtained from TGA and TGMS calculations (Table 4.5), but a whole range of PEG and water interlayer concentrations were simulated to probe the dynamics of the intercalation process. The simulations correctly predict a step-wise swelling behaviour for NaMt. Two plateaux around PEG200 contents of 0.10 and 0.25  $\text{g}_{\text{PEG200}}/\text{g}_{\text{clay}}$  are observed (Fig. 4.17(a)), which supports interlayer polymer organisation in two extended layers parallel to the clay surfaces – monolayer and bilayer (Fig 4.2(b)). More importantly, for the first time we have achieved realistic basal spacings from simulation for these two polymer arrangements. The first plateau on the swelling curve corresponds to a monolayer organisation of polymer with a d-spacing of 14.5 Å. This is an excellent match to the experimental observations presented in the previous section as well as previous experimental investigations. [32, 41, 138, 140, 150]. The simulated spacing that corresponds to the bilayer polymer structure is approximately 0.5 Å smaller than that obtained experimentally.

Similar to the clay hydration process, the exchangeable cation affects intercalation of PEG significantly (Fig. 4.17(b)). CaMt exhibits a nearly linear increase in d-spacing with uptake of PEG200 until reaching a plateau at around 0.2–0.25  $\text{g}_{\text{PEG200}}/\text{g}_{\text{clay}}$  with a spacing of 18.8 Å. This plateau corresponds to formation of a bilayer polymer structure and again matches experimental observations. At lower polymer content, the swelling curve for CaMt is less accurate than for NaMt, however, the nearly linear swelling trend is similar to that observed experimentally. The absence of a stable monolayer polymer structure in the interlayer suggests that level of uptake of PEG200 by CaMt is smaller when compared to that by NaMt. Similar behaviour was observed experimentally, where the ratio of the uptake of PEG1500 by NaMt to that by CaMt has been found to be about 2.3 [140, 149].

All previous simulation investigations of intercalated PEG/clay nanocomposites [32, 33, 92, 98, 134, 141, 144, 151] have underestimated the basal spacing values for monomer and bilayer structures, obtaining 13.5 Å and 16–16.5 Å respectively. It should be noted, however, that those did not consider water in the interlayer. Achieving realistic basal spacings for a range of polymer loadings in the interlayer gives additional assurance that combination of AMBER and TIP3P/Fs potentials used here provides effective performance in simulation of hydrated polymer/clay nanocomposites. It is also noteworthy that a structural model of relatively small size is able to replicate macro properties of studied systems.

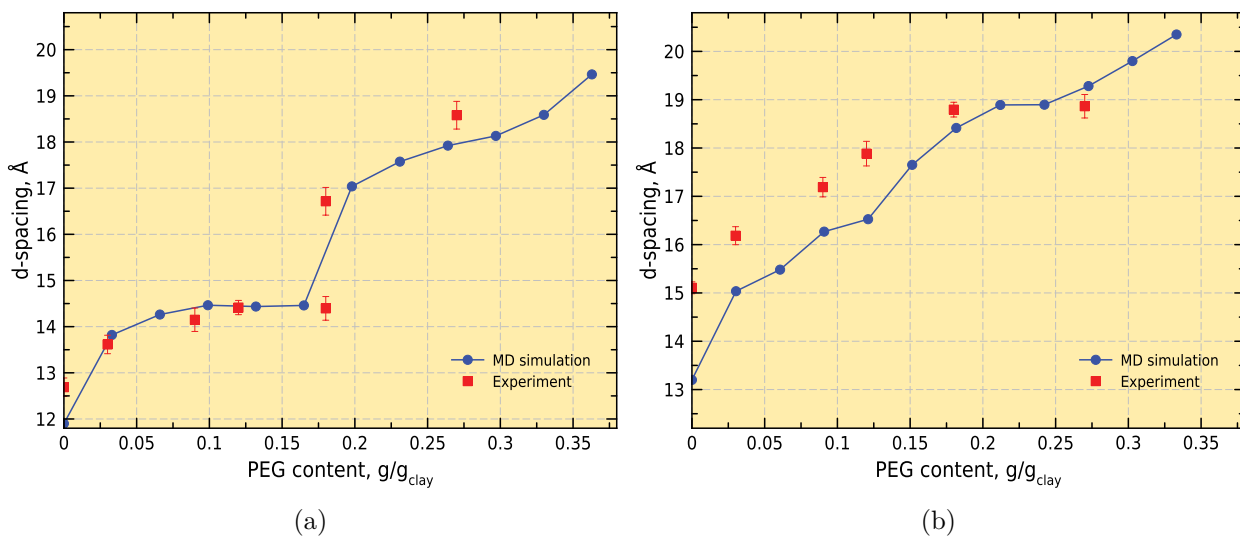


Figure 4.17: Simulated and experimental basal spacing of (a) NaMt and (b) CaMt as a function of increasing poly(ethylene glycol) (PEG200) content in the interlayer. Amount of water in the interlayer was selected according to experimental findings presented in Table 4.5

### Preferential Intercalation of Poly(ethylene glycol) and its Morphologies

The effect of polymer molecular on the process of intercalation has also been studied. Figure 4.18 shows the simulated swelling curves of anhydrous NaMt upon intercalation of PEG chains of various molecular weights – from 100 to 450  $\text{g}\cdot\text{mol}^{-1}$ . PEG450 here represents the limit of the chain length that can be used in conjunction with the developed clay model. The extended chain length of this polymer is  $\sim 37 \text{ \AA}$ , which is very close to the lateral dimensions of the clay model. In order to avoid artificial "edge effects" through periodic boundary conditions, this is the highest MW of PEG that has been used.

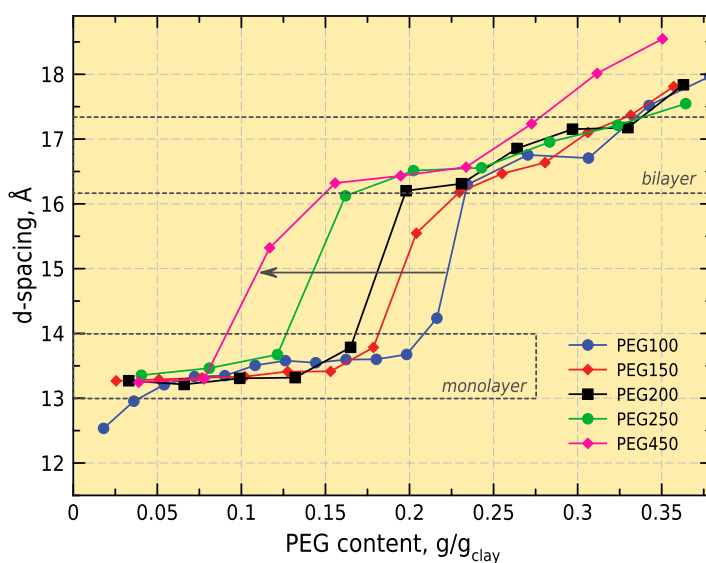


Figure 4.18: Dehydrated NaMt with PEG of different MW

Swelling curves of all nanocomposites are characterised by step wise expansion similarly

to that discussed in the previous section. Due to lack of water in the interlayer, d-spacings for monolayer ( $\sim 13.5$  Å) and bilayer ( $\sim 16.5$  Å) polymer structures are smaller than those obtained experimentally (Figure 4.17) [14, 138, 140]. Nonetheless, they are in a very good agreement with these from previous simulations of PEG/Mt intercalated nanocomposites [30, 32, 92, 98, 134, 141, 144, 151]. Surprisingly, these intrinsic basal spacings are identical across the full range of studied intercalated polymers. This was previously observed experimentally [41, 140], where montmorillonite clays with intercalated PEG with MW of 600 and  $6 \times 10^5$  g·mol<sup>-1</sup> showed identical  $d_{001}$ -spacings. Likewise, Vaia et al. [152] showed that the MW of the polymer only affected the rate of polymer intercalation but not the final layer spacing of the nanocomposite. It was positive to see that simulation techniques are able to replicate this behaviour. From a simulation point of view, the number of polymer chain monomers in the clay gallery remains constant regardless the polymer MW. At a given polymer content in the interlayer, the higher MW<sub>PEG</sub> has fewer intercalated molecular chains, which results in the same total energy of the system and, subsequently, similar basal spacings for the full range of PEGs.

Simulation has also suggested preferential intercalation of higher MW<sub>PEG</sub> polymer chains. This is indicated as a shift to lower PEG content values of the monolayer to bilayer transition with increase of MW<sub>PEG</sub> (Fig. 4.18). A similar effect was recently observed by Chen who investigated the intercalation dynamics of PEGs with MW of 4000 and 35000 g·mol<sup>-1</sup> in montmorillonite [140]. The author attributed this behaviour to specific conformations that PEG chains form with the exchangeable cations and clay surface. Although, montmorillonite is generally hydrophilic (Chapter 1.1.3), the basal Si-O groups in the spaces between hydrated cations in clay interlayers are relatively hydrophobic and PEG is preferentially adsorbed on these sites [41]. The low molecular weight polymer has a larger number of hydrophilic (OH<sup>-</sup>) end groups than the high one, and this was thought to facilitate the energetically preferential intercalation of high molecular weight polymer. Additionally, longer polymer chains can form bridges linking the silicate layers and spreading them apart, thus forming a bilayer structure even at low PEG content.

This conclusion was supported by our morphological investigation of intercalated polymer chains as a function of clay type and clay layer charge structure. The root mean square end-to-end distances of intercalated PEG200 molecules as a function of layer position and type of clay are listed in Table 4.6. The limited number of interlayer PEG chains in these systems mean it is not possible to plot appropriate end-to-end distribution functions similar to those presented for exfoliated polymer/clay nanocomposite system because of statistical inaccuracy (Fig. 4.6). As shown in Table 4.6, there is a strong correlation between the layer charge distribution and the root mean square end-to-end distance of polymer chains. Overall, it increases with clay layer charge, indicating the transformation from coiled or "Saturn ring" like polymer/cation conformation (Fig. 4.19(a)) to extended linear conformation (Fig. 4.19(b)). Obviously, higher clay layer charge requires higher number of exchangeable cations in the interlayer which, in turn, reduces the average distance between neighbour cations. Consequently, PEG200's chain length is ultimately sufficient to link two neighbouring cations, and this mechanism promotes more linear extended conformations. This interpretation is

further supported by the fact that polymer end-to-end distances in CaMt are significantly lower than those in NaMt due to the number of  $\text{Ca}^{2+}$  cations in the interlayer. Therefore, a coiled polymer/cation conformation is preferable in the interlayer of CaMt. Smaller polymer end-to-end distances in the interlayer of tetrahedrally charged clay indicate prevalence of "crown" like conformations, wherein a cation is coordinated by coiled polymer chains from one side and by basal oxygens from another (Fig. 4.20).

Table 4.6: Root mean end-to-end distance of PEG200 chains intercalated in various clays

CEC	NaMt		CaMt	
	Oh	Th	Oh	Th
87 meq	$8.2 \pm 0.2$	$6.5 \pm 0.1$	$8.3 \pm 0.5$	$8.2 \pm 0.2$
104 meq	$12.9 \pm 0.4$	$12.4 \pm 0.4$	$9.5 \pm 0.4$	$7.9 \pm 0.5$
113 meq	$14.1 \pm 0.3$	$15.0 \pm 0.6$	$10.5 \pm 0.2$	$9.8 \pm 0.6$

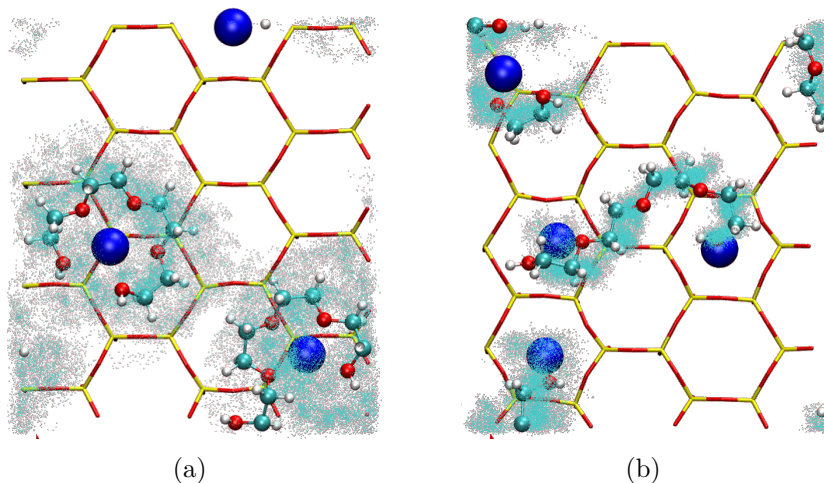


Figure 4.19: Fragments of NaMt surface (110) of intercalated PEG200/Mt system showing predominant polymer conformations in (a) low charge clay – "crown" conformation and (b) high charge clay – "planar extended" conformation. Overlapped trajectories are shown over last 500 ps. Colours as in Figure 4.4

To quantify correlation between the polymer conformation and the clay layer charge, we have developed a code that calculates the fraction of each polymer–cation conformation on the basis of the root square end-to-end distance of the PEG chain, the nature of the polymer–cation linkage (ether oxygens or  $\text{OH}^-$  end groups) and the relative position of their centres of mass. Four individual polymer conformations were distinguished: (i) "Saturn ring"; (ii) "Crown"; (iii) Planar extended and (iv) Non-planar extended. These conformations are illustrated in Figure 4.20 and their fractions in each PEG200/Mt nanocomposite are given in Table 4.7. It should be noted that, due to limited statistics, these values can change when the size of simulated model is increased and more polymer chains are present in the interlayer of the clay. Nonetheless, the values in Table 4.7 indicate a clear trend of polymer conformation dependence on the type of clay.

As shown in Figure 4.19, polymer/clay nanocomposites based on low charge clay is characterised by predominant polymer conformations in form of "Saturn ring" and "Crown" with

Table 4.7: Percentage of characteristic polymer conformations in bilayer polymer structure  
(  $0.25 \text{ g}_{\text{PEG200}}/\text{g}_{\text{clay}}$  )

Polymer conformation type	87.0 meq		104.4 meq		113.1 meq	
	Oh	Th	Oh	Th	Oh	Th
"Saturn ring"	69.5	32.9	19.1	12.7	5.0	14.6
"Crown"	24.1	67.1	10.0	13.0	13.7	10.2
Planar ext.	6.4	0	55.6	33.4	62.2	49.9
Non-planar ext.	0	0	15.3	40.9	19.1	25.3

latter more often occurring in tetrahedrally charged clays, due to their partial coordination of the exchangeable cation by the oxygens of mineral surface (Fig 4.20). Increase of layer charge, however, increases the fraction of linear extended conformation, both planar and non-planar. Here, "planar polymer conformation" refers to polymer chains absorbed parallel to the basal surface, and "non-planar conformation" to chains which bridge the silicate layers (Fig. 4.20). When a polymer creates a "bridge" between adjacent clay layers, the resultant basal spacing is larger for the given PEG content in the interlayer as shown in Figure 4.20. This illustrates the mechanisms of preferential adsorption of a high molecular weight polymer discussed earlier, that is when it is easier to bridge clay layers for a longer polymer chain, thus enabling the layer to spread apart sooner. The small fraction of "Saturn ring" conformations in high charge clays with positive charge deficit in the octahedral sheet is due to the position of the exchangeable cations in the dodecahedral cavities of the mineral surface, similar to that described in Chapter 3 of this thesis.

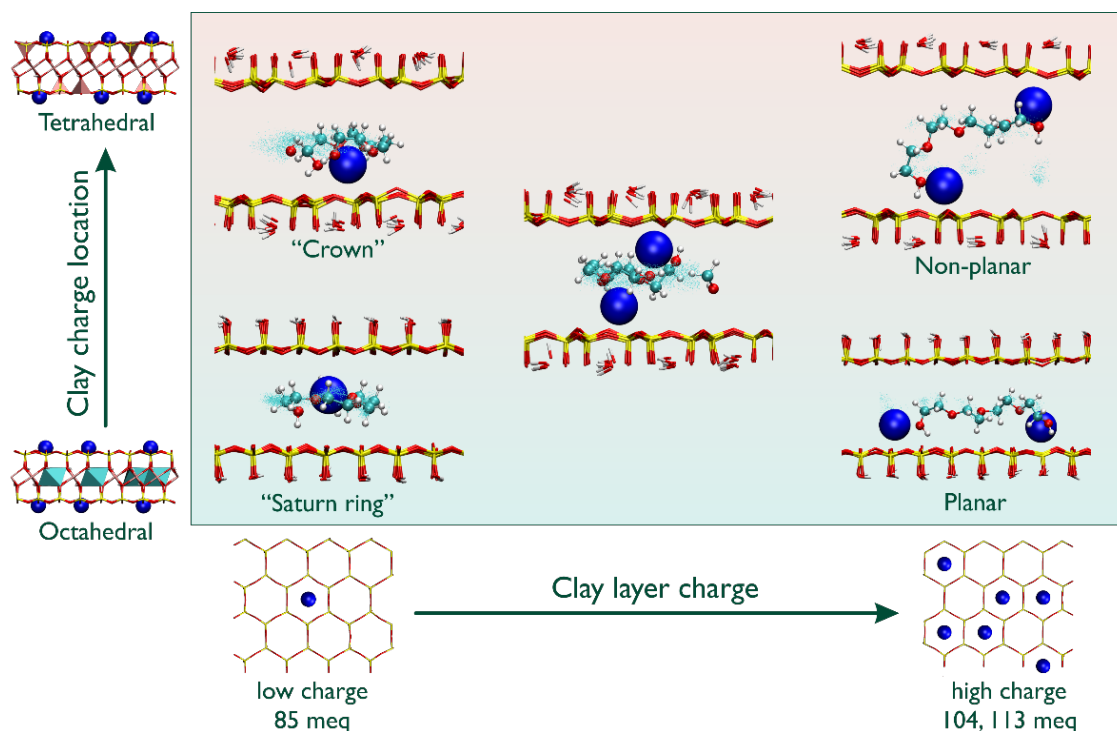


Figure 4.20: Influence of magnitude and location of clay layer charge on the interlayer conformations of PEG200

#### 4.4 Conclusions and Chapter Summary

In this chapter, computational and experimental techniques were applied to investigate exfoliated and intercalated polymer/clay nanocomposites. For much of this work, PEG200 was utilised because of the restrictions imposed by the size of the clay model and experimental evidence that it is readily intercalated into the smectite minerals. Moreover, PEG200 showed great plastification properties - the reason to use it when creating paper coatings. Particular attention was paid to the structure of the formulated nanocomposites, and the influence of clay layer charge on the polymer morphologies adopted. The model of PEG200/Mt nanocomposites has proved both experimentally and theoretically to be successful at reproducing the structural and thermodynamic properties of all studied nanocomposites. Therefore, the simulation methods can be considered an asset in investigating structurally realistic polymer/clay nanocomposites.

An ordered structure of PEG polymer chains parallel to the clay surface was observed in the computational model of PEG/Mt system that approximates the exfoliated nanocomposite. At least five successive PEG chains layers were seen, indicating the strong influence of the clay mineral surface on the polymer interface. The polymer layer closest to the basal surface of the clay exhibits the least translational motion and shows a tendency to increase the surface area in contact with the clay surface. This is especially evident in nanocomposites based on NaMt and with charge deficit in the octahedral sheet. Immobilisation of adsorbed polymer chains and formation of strong complexes with exchangeable cations very probably contributes to the reduced permeability of gasses and vapours in clay nanocomposites, by creating a more tortuous path for permeating molecules.

Experimentally obtained intercalated PEG200/Mt nanocomposites provide evidence of having increasing basal spacing with increased PEG200 content. Two stable polymer structures within the interlayer were identified – a monolayer and a bilayer. The exchangeable cation, however, has a significant effect on the dynamics of polymer intercalation – the uptake of PEG200 by Na<sup>+</sup> exchanged montmorillonite is noticeably higher than that of Ca<sup>2+</sup> exchanged montmorillonite. It was also shown that polymer chains replace some of the adsorbed water, filling the space between hydrated exchangeable cations. The amount of polymer adsorbed is controlled by the hydration enthalpy of the exchangeable cation, indicating possible associations between the exchangeable cation and the ether oxygen atoms of the PEG chains.

PEG/Mt nanocomposites spanning a range of molecular weights (100 to 450 g·mol<sup>-1</sup>) and a range of loadings (0 to 40 wt%) were simulated. In each case d<sub>001</sub>-spacing of the clay increased, regardless of molecular weight, to 13.5 Å and 16.5 Å for monolayer and bilayer structure respectively. The clay containing higher molecular weight PEG was more stable in water. It was also found that montmorillonite mineral preferentially absorbs the high molecular weight fractions of PEG. From an engineering point of view, these results are significant because they suggest that nanocomposites with better barrier and mechanical properties could be obtained by controlling molecular weight distribution to avoid low polymer fractions.

## 5 Synergistic Adsorption of Poly(ethylene glycol) and Amylose onto Montmorillonite

In the previous chapter, a detailed study of one-component polymer/clay nanocomposites was presented. It was recently reported [19] that synergistic coexistence of two organic materials in the interlayer of smectites, in particular poly(ethylene glycol) and starch significantly enhances the water and oxygen barrier properties of this polymer/clay nanocomposite. Structural investigation of polymer/clay intercalated nanocomposites containing more than one organic compound is very difficult, if at all possible experimentally. It is, therefore, both interesting and relevant to investigate the energetics and dynamics of adsorption of binary mixture of poly(ethylene glycol) and starch onto hydrated montmorillonite clays. Conventionally, poly(ethylene glycol) acts as a plasticiser for otherwise very brittle starch/clay nanocomposite.

This chapter presents results of simulations series of starch/clay nanocomposite with and without presence of poly(ethylene glycol) in the interlayer with relation to the barrier properties of formulated composite. Particular attention was paid to the structural confinement of PEG and starch in the interlayer and investigation into the effect of clay layer charge environment on them.

In the beginning, structure of PEG/starch blend from MD simulation will be presented. Later, swelling dynamics and energetics of binary starch/clay system will be shown.

### 5.1 Introduction

The applications of disposable oil-based plastic materials are increasing significantly and have led to serious ecological problems as being non-biodegradable and non-renewable. The search for renewable materials to replace these materials is an intense search field. In the domain of packaging applications, for instance, thermoplastic starch is one of the promising biopolymer materials, because it is renewable, low in price, fully biodegradable and rather importantly, approved for food contact [20–23, 153–159]. The incorporation of clay minerals into different polymeric matrices has drawn a particular interest due to their potential to improve the barrier properties of formulated coatings. When montmorillonite clay was added to starch polymer matrix, the barrier properties were significantly improved [159].

The clay type and, in particular, layer charge distribution, however, has significant effect on the barrier properties of formulated coatings. In some studies addition of Mt sometimes had no effect or even a slight negative effect on the resultant barrier properties [160–162]. One explanation of that has been difference in the polymer intercalation dynamics for various Mts [19, 23]. It was concluded that starch-PEG/clay based coatings would have good barrier properties only when both starch and plasticiser coexist in the interlayer of clay. Adsorbed PEG onto the Mt surfaces forms a strongly constrained layer with very low oxygen permeability [23]. The organisation of plasticiser and bio-polymer in the clay interlayer, however, is not accessible through experimental techniques. Therefore, molecular simulation of PEG-starch/clay nanocomposites may provide insight on the nanocomposite interlayer structure in relation to the clay type, and, as a result on the mechanism of the formation of coatings with high barrier properties.

Starch is one popular natural polymer material due to the fact that it can be easily produced from plants, e.g. potato, corn, cassava etc. [163]. Starch consists of two types

of molecules: amylose (denoted as AML) and amylopectin. It is generally accepted that amylose is amorphous polymer whereas amylopectin has semi-crystalline structure [163]. Through analysis of the XRD traces of the thermoplastic starch plasticised with urea, it was shown that freshly prepared nanocomposite contained starch in its amorphous form [164]. Therefore, for our computer simulations we created a model of amorphous amylose, which will be used throughout of this Chapter to represent starch/clay interactions. Amylose is a spiral polymer made up of D-glucose units, the DFT-optimised structure of which is shown in Figure 5.1. Each molecule of amylose in the developed model consisted of five D-glucose units resulting in total molecular weight of  $828.7 \text{ g}\cdot\text{mol}^{-1}$ . It is rather unrealistically small fraction of the amylose molecule found in nature, however for the sake of better statistics (as more AML molecules will be present in the interlayer at the given AML/clay weight ratio) and due to scale of clay model, we accept this approximation. Later we will provide evidence of appropriateness of selecting such a small molecule. Computational model of AML was parametrised by the same potential set as PEG.

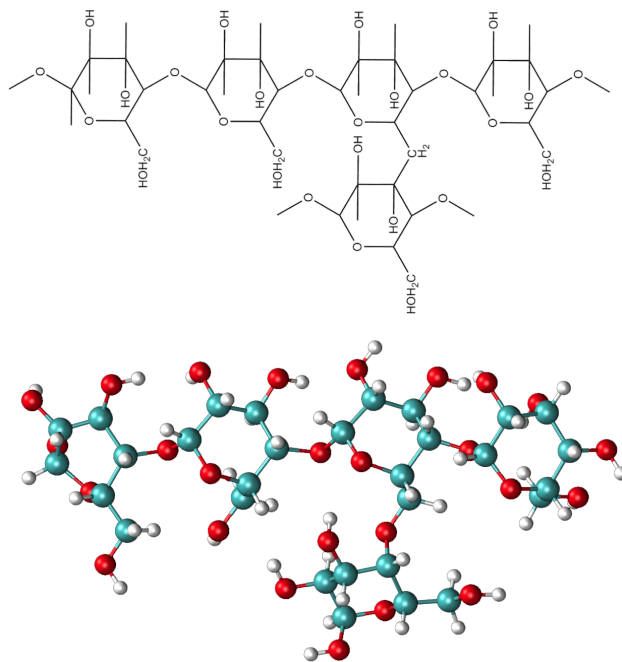


Figure 5.1: Graphical representation of amylose of  $\text{MW} = 828.7 \text{ g}\cdot\text{mol}^{-1}$  (PEG200).  
Colours: C cyan; O red; H white

## 5.2 Simulation Details

The construction of simulation cells for AML/Mt and AML-PEG/Mt nanocomposites is identical to that described in Chapter 5. The initial binary and tri-systems were constructed by randomly distributed AML or AML and PEG200 molecules with pre-equilibrated water molecules at desired ratios. Starting amylose and water content for AML/Mt system was  $0.7 \text{ g}_{\text{AML}}/\text{g}_{\text{clay}}$  and  $0.07 \text{ g}_{\text{H}_2\text{O}}/\text{g}_{\text{clay}}$  respectively. Water content of 7 wt% is reported from experimental observation of starch based clay nanocomposites [165]. For AML-PEG/Mt system, a broad range of PEG200 and  $\text{H}_2\text{O}$  concentrations, ranging from 0 to  $0.35 \text{ g}_{\text{PEG200}}/\text{g}_{\text{clay}}$  (0 to  $\sim 7.1 \text{ PEG200}\cdot\text{uc}^{-1}$ ) and 0 to  $0.2 \text{ g}_{\text{H}_2\text{O}}/\text{g}_{\text{clay}}$  (0 to  $\sim 16.5 \text{ H}_2\text{O}\cdot\text{uc}^{-1}$ ) respectively were

used.

The procedure of simulation cell construction, energy minimisation and annealing simulations, production runs and selection of equilibration points are identical to that described in Chapter 4 (Section 4.3.1), so we will not repeat the description of this workflow here again. Constructed equilibrated simulation cells for binary AML/Mt and tri-system AML-PEG/Mt are presented in Figures 5.2 and 5.3 respectively.

To study the thermodynamics of the intercalation of amylose in the clay, the potential energy of bulk AML is required. The procedure to obtain equilibrium configurations of the pure amylose material is described as follows: (i) the material chains were randomly distributed in a large simulation box; (ii) After energy minimisation, the system was quenched from 1000 K to 300 K with a cooling rate of 50 K per ps at 1 atm in the NPT ensemble; (iii) finally, the MD simulation was performed at 300 K and 1 atm for 500 ps to obtain the equilibrium state; (iv) structures which reached the equilibrium state were then used to calculate the potential energy of the bulk AML system.

Adsorption of Clays with various charge distributions and exchange cations were The adsorption analysis employs a simple model of montmorillonite – amylose interface, containing one layer of Mt and one single chain of AML. MD simulations were used in order to investigate the adsorption process of AML on hydrated clays and influence of clay charge location on this process. The simulation cell of this model is shown in Figure 5.4. The free energy of adsorption was calculated from potentials of mean force (PMF).

Each AML was placed parallel to the selected Mt surface with its centre of mass at a distance of 3.5 Å above the surface. Two main orientations of amylose molecule were considered – parallel to [100] direction (Fig. 5.5(a)) and parallel to [010] direction (Fig. 5.5(b)). Thereafter, into each system 2400 of pre-equilibrated H<sub>2</sub>O molecules were added (Fig. 5.4).

All simulations were performed in NPT ensemble at 300 K and 1 atm. The timestep was 1 fs. Simulation lasted for 10 ns. The data from final 5 ns was used for analysis. All bonds were constrained.

The equilibration was established through monitoring two parameters – structural and energetical stability. Structural stability of a molecule was assessed by calculating the root-mean-square deviation (RMSD) of AML molecule.

Energy stability was judged by the total instantaneous interaction energy between the AML and Mt, which is defined as:

$$E_{int}(t) = E_{AML+Mt}(t) - E_{AML}(t) - E_{Mt}(t), \quad (5.1)$$

where  $E_{int}$  refers to the interaction energy between the AML and Mt,  $E_{AML+Mt}$  is the total energy of the AML and Mt, and  $E_{AML}$  and  $E_{Mt}$  are the internal energies of AML and Mt, respectively. The instantaneous RMSD of the AML and interaction energy between the AML and Mt are presented in Figures 5.6(a) and 5.6(b), respectively. Here, data for 104.4 meq NaMt with octahedral charge is shown. All twelve studied models reached equilibration at around 4 ns of the MD simulation. Therefore, the data from final 5 ns was used for analyses.

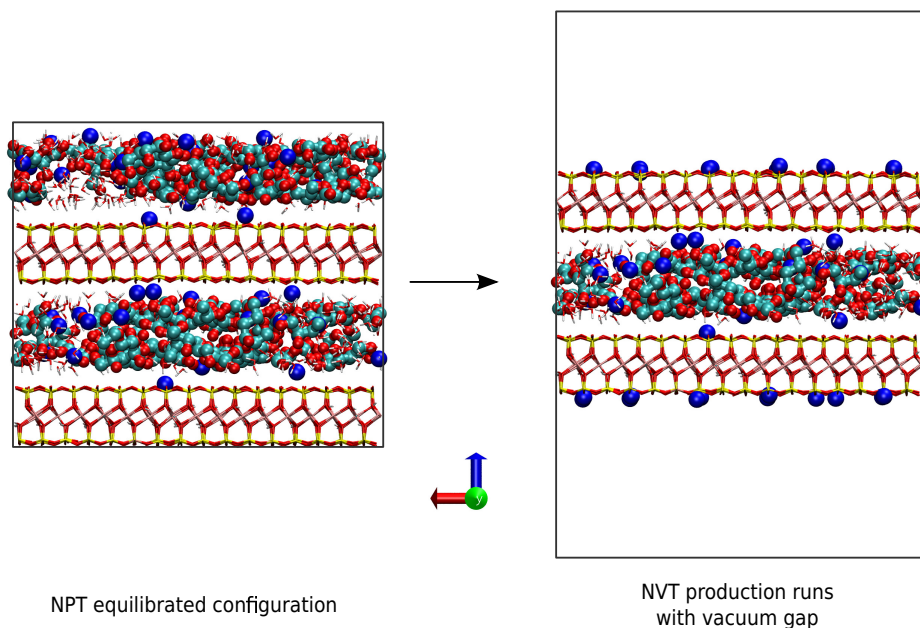


Figure 5.2: Snapshots of equilibrated configurations of AML/clay intercalated nanocomposite obtained in NPT and NVT MD simulations. NaMt interlayer consists of 8 AML molecules ( $0.28 \text{ g}_{\text{AML}}/\text{g}_{\text{clay}}$ ) and 100  $\text{H}_2\text{O}$  molecules ( $0.07 \text{ g}_{\text{H}_2\text{O}}/\text{g}_{\text{clay}}$ ). Colours: Na blue; Si yellow; Mg cyan; Al pink; C cyan; O red; H white

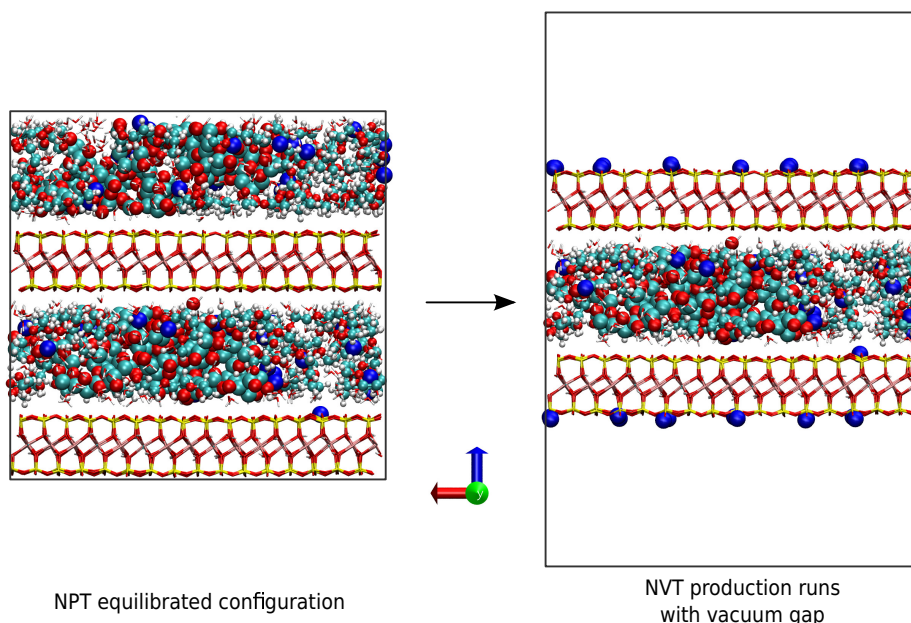


Figure 5.3: Snapshots of equilibrated configurations of AML-PEG/clay intercalated nanocomposite obtained in NPT and NVT MD simulations. NaMt interlayer consists of 4 AML molecules ( $0.14 \text{ g}_{\text{AML}}/\text{g}_{\text{clay}}$ ), 26 PEG200 molecules ( $0.21 \text{ g}_{\text{PEG200}}/\text{g}_{\text{clay}}$ ) and 100  $\text{H}_2\text{O}$  molecules ( $0.07 \text{ g}_{\text{H}_2\text{O}}/\text{g}_{\text{clay}}$ ). Colours as in Figure 5.2

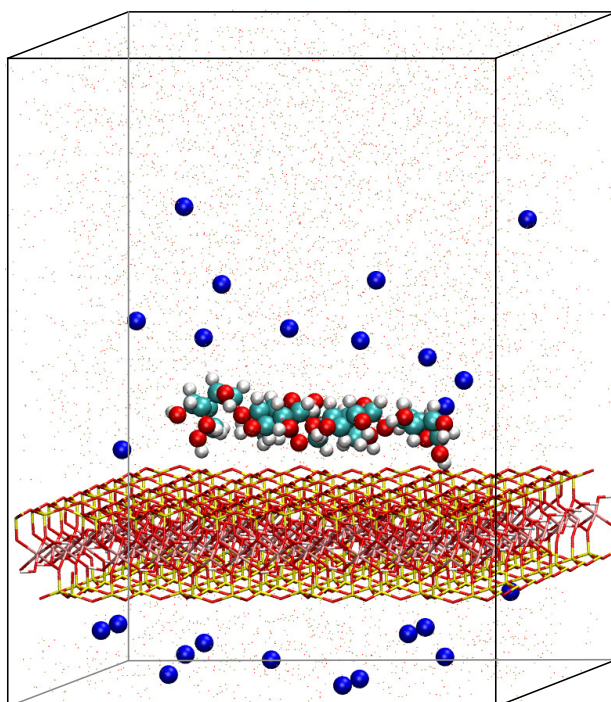


Figure 5.4: Starting structure of the AML/Mt adsorption model. The centre of mass of single amylose molecule in aqueous environment is positioned at 3.5 Å above the clay surface. Colours as in the Figure 5.2

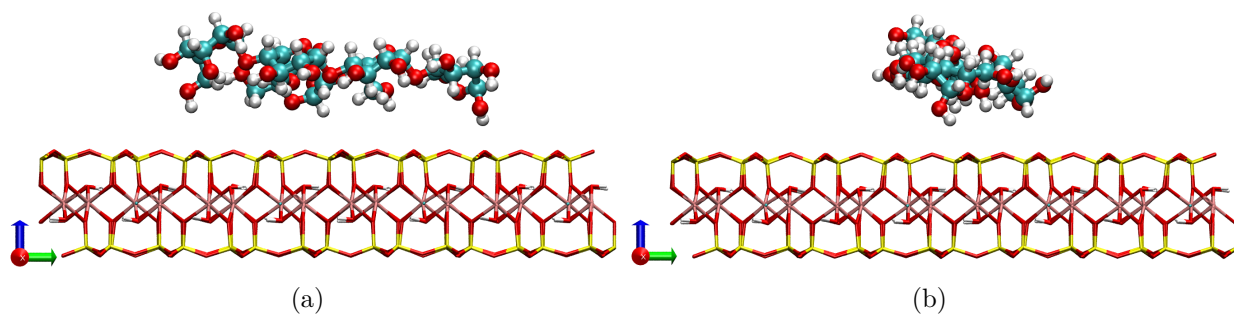


Figure 5.5: Definition of the AML orientations of the AML/Mt adsorption model. The amylose molecule is oriented along (a) [010] and (b) [100]. Colours as in Figure 5.3

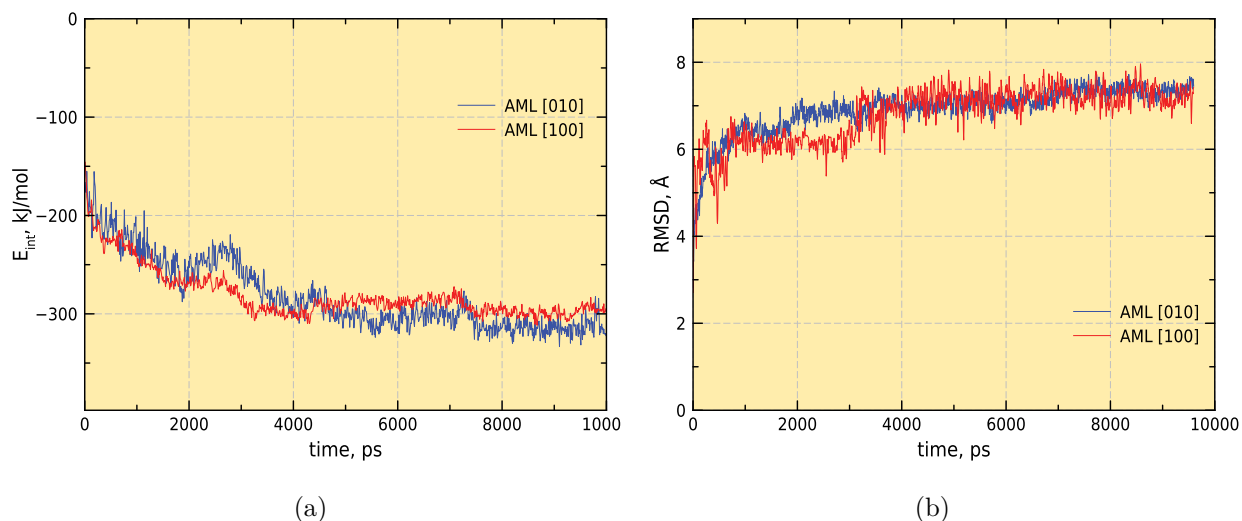


Figure 5.6: Variation of (a)  $E_{\text{int}}$  and (b) RMSD of amylose molecules adsorbed onto 104.4 meq NaMt with octahedral charge in different adsorption configurations with simulation time

### 5.3 Results and Discussion

Unfortunately, to date, there are no research papers investigating interaction of starch or its constituents with aluminosilicate minerals using computational techniques. Therefore, obtained results will be compared with experimental investigations of PEG-AML/clay systems where possible.

#### 5.3.1 AML/Mt binary system

##### Thermodynamics of the Intercalation

In order to study the thermodynamics of the intercalation of amylose in the clay, the change of potential energy during this process was calculated. Being multicomponent system, the relation of reactants and products of AML/Mt- $H_2O$  nanocomposite intercalation can be expressed by following equation:



Where hydrated montmorillonite (Mt- $H_2O$ ) and Amylose (AML) are reactants, and intercalated nanocomposite (AML/Mt- $H_2O$ ) is the product. The change of energy during the reaction of intercalation can be calculated as follows:

$$\Delta E = \sum E_{\text{products}} - \sum E_{\text{reactants}} \quad (5.3)$$

or

$$\Delta E = E_{\text{AML/Mt-H}_2\text{O}} - E_{\text{Mt-H}_2\text{O}} - E_{\text{AML}} \quad (5.4)$$

The calculation of  $\Delta E$  for this reaction requires computation of the potential energy of all reactants. The potential energy of hydrated montmorillonite was taken from simulations presented in Chapter 3 of this thesis. To obtain the potential energy of bulk AML, a simula-

tion cell consisting of randomly distributed 100 AML molecules was constructed, equilibrated and simulated in NPT ensemble at 300 K and 1 atm (Fig. 5.7). The resultant density of the pure AML was calculated as  $1.41 \text{ g/cm}^3$ , which is very close to the experimental value of  $1.43 \text{ g/cm}^3$  [166] and exactly matches simulated density of bulk AML parametrised by COMPASS force field [163]. This gave us reassurance, that selected MW of AML in this work is able to reproduce at least structural parameters of real amylose system.

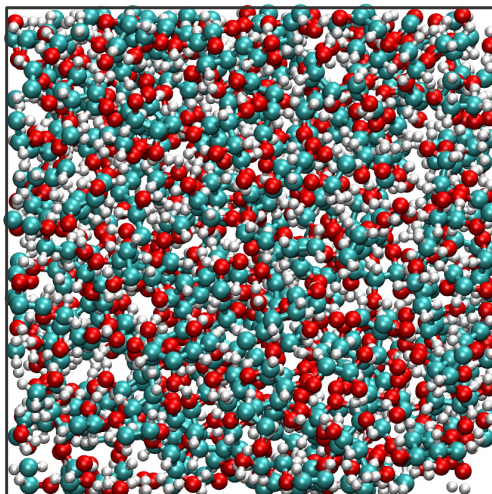


Figure 5.7: Simulation cell for molecular dynamics simulations of amorphous AML containing 100 molecules. Simulation was equilibrated at 300 K and 1 atm

### Swelling Dynamics and Interlayer Structure

Similar to simulation series presented in Chapter 4 and 5, investigation into the effect of clay layer charge on the amylose intercalation process is presented here. A total of 12 simulated swelling curves for NaMt and CaMt models are shown in Figures 5.8 and 5.9, respectively. Error bars based on standard deviation calculated from block averaging over the last 1 ns of simulations are less than data symbol, therefore are not visible on the plots.

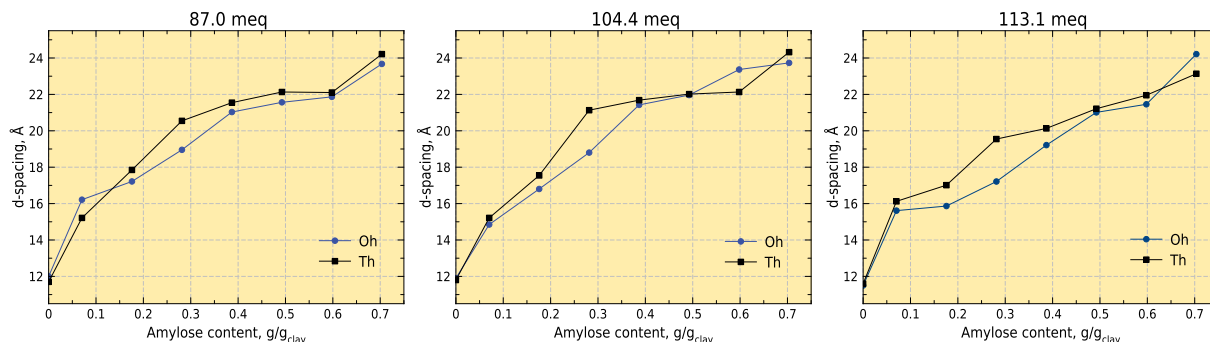


Figure 5.8: Swelling curves of NaMt as a function of amylose content in the interlayer from MD simulations at 300 K and 1 atm. Swelling curves are shown for clays with various net charge distribution

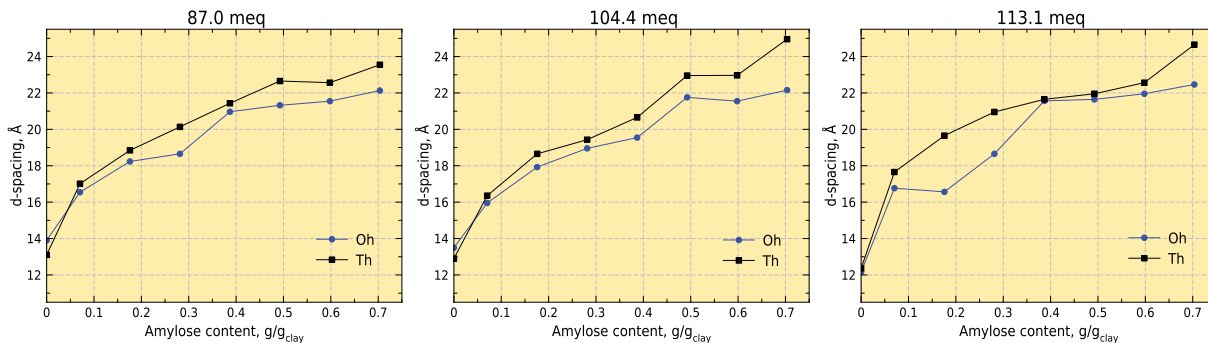


Figure 5.9: Swelling curves of CaMt as a function of amylose content in the interlayer from MD simulations at 300 K and 1 atm. Swelling curves are shown for clays with various net charge distribution

Unlike swelling curves of hydrated montmorillonite or PEG/Mt systems, intercalation of amylose in the Mt do not suggest formation of highly ordered polymer structures within the interlayer. Most simulated clays swell gradually with increase of polymer content in the interlayer until reaching an "equilibrated" basal spacing of  $\sim 21\text{-}22$  Å. Similar d-spacings were observed by many experimentalists who were investigating intercalation of starch in montmorillonites under ambient conditions [19, 22, 160, 161]. This is revealed as a plateau at higher AML content on all simulated swelling curves (Fig. 5.8 and 5.9). It is very important result obtained from simulation and indicates the preferable interlayer organisation of amylose, evidences of which will be provided during the course of this chapter.

Another peculiar conclusion that can be drawn from the simulated swelling curves is that spacings of AML/Mt nanocomposites based on the low charge clays are overall higher by approximately  $0.9\text{-}1.2$  Å in the region of  $0.3$  g<sub>AML</sub>/g<sub>clay</sub> than those that are based on the high charge clays. Similar conclusion was drawn from investigation of barrier properties of starch-clay nanocomposites based on various clay types [22, 140, 157]. There are evidences that high charge clay do not uptake starch in the interlayer at all [160]. It is, however impossible to investigate directly by the methods presented here, as content of organic material in the interlayer is fixed and cannot escape from the clay gallery.

Clays with isomorphous substitutions occurring in tetrahedral sheet (Th charge) produce higher basal spacing compared to those with charge deficit in the octahedral sheet (Oh charge). The reason for that is primarily due to the distribution of exchangeable cation within the interlayer of AML/Mt nanocomposite which is illustrated in Figure 5.10 as atomic density profile along the *c*-axis normal to the basal surface of clay. Strong association between exchangeable cations and substitution sites in the tetrahedral sheet of clay, and low diffusivity of cations and amylose, results in most of them being located between the clay layer and amylose molecules. Additionally, exchangeable cations in the high charge clay with charge deficit in the octahedral sheet form anhydrous adsorption complex more readily, similar to that described in Chapter 4 and shown in Figure 3.7(a). This opens up space for organic material, leading to overall smaller basal spacing.

Distribution of carbon atoms for all studied systems suggests formation of pseudo bilayer

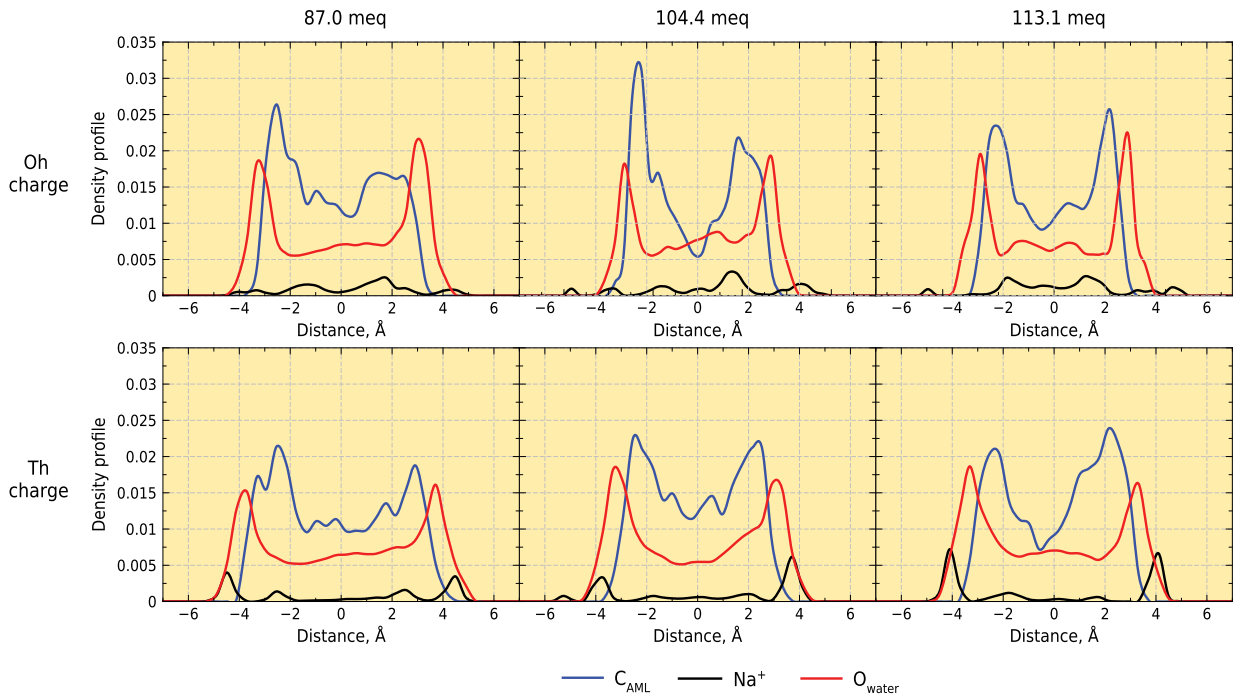


Figure 5.10: Atomic density profiles from MD simulations at 300 K and 1 atm for AML/NaMt nanocomposite. Amylose backbone carbon atom ( $C_{AML}$  - blue curve), sodium ( $Na^+$  - black curve) and water ( $O_{water}$  - red curve). Left to right increases clay layer charge

of starch in the interlayer. Amylose can produce larger number of conformations than PEG, therefore its ADPs are so distorted (Fig. 5.10). Interestingly, even at relatively low water concentration ( $\sim 0.07 \text{ g}_{H_2O}/\text{g}_{clay}$ ), a water bilayer is found in the interlayers of all samples. It is expelled from the middle of the interlayer and distinct, sharp OW peaks are positioned between the basal surface of clay and layer of AML indicating hydrophilic nature of amylose and formation of a network of hydrogen bonds. Similar behaviour is right for the divalent exchangeable cations.

## General Conclusions

The theoretical and experimental research carried out in the PhD thesis led to the following considerations:

1. New scientific results of theoretical and applied importance in the field of biopolymer technology for food packaging have been obtained. Potential biopolymer models based on polyethylene glycol, amylose and Na<sup>+</sup>- and Ca<sup>2+</sup>-montmorillonite clays were developed and optimised. The research carried out allowed to describe the molecular structure of the composites in order to improve the barrier properties of the layers deposited on the basis of these biodegradable bio-composites, subchapters 3.2.1-3.2.2 (SIMINEL N. et al., 2022).
2. Based on the analysis of the main simulation techniques applied to the polymer/clay composites model, the molecular simulation method of the intermediate layer was selected, which is justified by creating a reliable barrier that can be applied to a wide range of interfaces. Model validation was performed by applying the experimental techniques of conventional X-ray diffraction (XRD), thermogravimetric analysis (TGA) and thermogravimetry coupled with mass spectrometry (TGMS), subsections 2.1-2.3 (GURIEVA G. et al, 2022).
3. Experimental and computational investigations of polyethylene glycol/clay nanocomposites allowed to describe the swelling behavior of selected clay minerals in the presence of plasticizer and the relative affinity of water and polymer for different cations. The experimental results corresponded to the model both qualitatively and quantitatively, demonstrating that the swelling of the clay layers occurs gradually, with the formation of plateaus around water contents of 0.1 and 0.2 g<sub>H<sub>2</sub>O</sub>/clay<sub>NaMt</sub>. For CaMt only one plateau was found at 0.15 g<sub>H<sub>2</sub>O</sub>/clay<sub>CaMt</sub>, subchapters 4.2.1-4.2.2 (SIMINEL N., no.1, 2023).
4. It was found, that rotational disorder influences both the internal energy of the clay layers and the basal distance. Hydrated clay and clay with water and PEG intercalated showed rotational resistance by increasing potential energy and extending basal distance (0.1-0.2 Å ). Disorder was energetically favorable in the case of dry clay, but involved decreasing internal energy and interlayer distance (about 0.1 Å ). Mutual rotation of basal surfaces generates a configurational pattern. The distribution of interlayer molecules (water and PEG) and counterions corresponds to the Moire model, subsection 4.3.1 (SIMINEL N. et al., 2018).
5. It was found that the Mg<sup>2+</sup>/Al<sup>3+</sup> substitution occurs in the octahedral substrate of the clay and the Al<sup>3+</sup>/Si<sup>4+</sup> substitution occurs in the tetrahedral substrate, leading to two different swelling profiles. The substitution site influences the distribution of intercalated water and polymer molecules as well as counterions. In the Na-MMT system the PEG conglomerates are disordered in the interlayer space. In the ternary Ca-MMT system, they are organised and PEG conglomerates avoid isomorphous substitution centres, while cation-water complexes are positioned near these centres. Phyllosilicates with a higher number of tetrahedral substitutions have a higher capacity to retain PEG molecules, subsection 4.3.3 (SIMINEL N. et al., 2017).
6. The polymer layer adjacent to the basal clay surface shows minimal translational motion and tendency to concretization with the clay surface, especially NaMt-based nanocomposites with charge deficit in the octahedral substrate. Immobilization of

adsorbed polymer chains and formation of complexes with exchangeable cations contribute to reduced gas and vapour permeability by creating a more convoluted pathway for permeable molecules. PEG/Mt nanocomposites with a molecular mass of 100-450 g·mol<sup>-1</sup> and intercalated PEG content from 0 to 40% are bistratal, with  $d_{001}$  distances of 16.5 Å, subsection 3.2.3 (SIMINEL N., 2019).

7. It was found, that the mineral montmorillonite preferentially adsorbs PEG fractions with high molecular mass. Clay with higher molecular weight PEG content also showed higher stability towards water. From an engineering point of view, these results suggest, that nanocomposites with better barrier and mechanical properties could be obtained by controlling the molecular mass distribution to avoid small polymer fractions, subsection 4.3.2 ( L ASCOVA-BACIU R et al, 2018)
8. It has been shown, that phyllosilicates with a layer charge < 0.4 electrons per stoichiometric unit can intercalate starch into the interlayer space, forming a barrier for water vapour in the coating layer. Phyllosilicates with a layer charge of > 0.4 electrons per stoichiometric unit were not able to intercalate starch. The water vapour transfer rate (WVTR) for similar coatings prepared from higher charge bentonites was 3-4 times higher ( $35 \pm 7 \text{ g}\cdot\text{m}^2\cdot\text{day}^{-1}$ ) than for phyllosilicates with a layer charge < 0.4 electrons per stoichiometric unit. Thus, a dry food packaging material has been proposed, which provides limited water vapour transfer rates of  $8 \pm 2 \text{ g}\cdot\text{m}^2\cdot\text{day}^{-1}$ , subsections 5.2-5.3 (SIMINEL N., 2022; SIMINEL N., no.2, 2023).

### Recommendations

The research carried out in the framework of the PhD thesis allowed to recommend the optimal methodology for planning and obtaining nanocomposites based on polyethylene glycol, amylose and Na<sup>+</sup>- and Ca<sup>2+</sup>-montmorillonite clays for the manufacture of coatings for food packaging. Recommended:

#### **1. Coarse-grained model. Model for clay minerals and polymer molecules.**

A big problem in modeling physical material processes is the time scale and length scale. In this context, simulations of PEG molecule interaction using Coarse-Grained potentials are recommended, which are more than 5 times faster than when using fully atomistic potential models. This can provide a significant performance gain in simulating large-scale systems. To parameterize the CG model of the clay, the use of the VOTCA potential is recommended. In this model, the interface clay layer fragments do not differ from the internal ones. This is the point where the model is to be improved and the wetting properties of the interfaces should be analysed.

#### **2. Starch intercalation and open surface enhancement in water and carbon dioxide adsorption.**

In experiments it was found that smectite layers are not purely continuous, but naturally include discontinuities and breaks due to cracks and defects. Therefore, it is also recommended to investigate surfaces in other geometrical directions, such as 010 and 100, which include reactive sites. In the case of exposure to interbedded species, these may have an impact on the behavioural response of the clay. Therefore, in future research edges of layers should be considered to study different reactive clay surfaces and how they can enhance swelling.

## Concluzii Generale

Cercetările teoretice și experimentale realizate în cadrul tezei de doctorat au condus la formularea următoarelor considerații:

1. Au fost obținute rezultate științifice noi de importanță teoretică și aplicativă în domeniul tehnologiei biopolimerilor, destinați fabricării ambalajelor pentru alimente. Au fost dezvoltate și optimizate modele potențiale de biopolimeri pe bază de polietilenglicol, amiloză și argile  $\text{Na}^+$ - și  $\text{Ca}^{2+}$ -montmorillonit. Cercetările efectuate au permis de a descrie structura moleculară a compozitelor în vederea îmbunătățirii proprietăților de barieră ale straturilor depuse pe baza acestor materiale bio-compozite biodegradabile, subcapitole 3.2.1-3.2.2 (SIMINEL N. et al., 2022).
2. În baza analizei principalelor tehnici de simulare aplicate modelului de materiale compozite polimer/argilă a fost selectată metoda de simulare moleculară a stratului intermediar (SM), care este justificată prin crearea unei bariere de încredere, ce poate fi aplicată unei game largi de interfețe. Validarea modelului a fost realizată prin aplicarea tehnicilor experimentale de difracție convențională de raze X (XRD), analiza termogravimetrică (TGA) și termogravimetria cuplată cu spectrometria de masă (TGMS), subcapitole 2.1-2.3 (GURIEVA G. et al, 2022).
3. Investigațiile experimentale și computaționale ale nanocompozitelor polietilenglicol/argilă au permis descrierea comportamentului de gonflare a mineralelor argiloase selectate în prezența plastifiantului și afinitatea relativă a apei și polimerului pentru diferiți cationi. Rezultatele experimentale au corespuns modelului atât calitativ, cât și cantitativ, demonstrând că gonflarea straturilor de argilă are loc în mod treptat, cu formarea de platouri în jurul conținutului de apă de 0,1 și 0,2  $\text{g}_{\text{H}_2\text{O}}/\text{clay}_{\text{NaMt}}$ . Pentru CaMt s-a constatat doar un singur platou la 0,15  $\text{H}_2\text{O}/\text{clay}_{\text{CaMt}}$ , subcapitole 4.2.1-4.2.2 (SIMINEL N., no.1, 2023).
4. S-a constatat, că dezordinea rotațională influențează atât energia internă a straturilor de argilă, cât și distanța bazală. Argila hidratată și argila cu apă și PEG intercalate au prezentat rezistență la rotație prin creșterea energiei potențiale și extinderea distanței bazale (0,1-0,2 Å). Dezordinea a fost favorabilă din punct de vedere energetic în cazul argilei uscate, dar implică scăderea energiei interne și a distanței dintre straturi (aproximativ 0,1 Å). Rotația reciprocă a suprafețelor bazale generează un model configurațional. Distribuția moleculelor interstrat (apă și PEG) și a contraionilor corespunde modelului Moire, subcapitol 4.3.1 (SIMINEL N. et al., 2018).
5. S-a constatat, că substituția  $\text{Mg}^{2+}/\text{Al}^{3+}$  are loc în substratul octaedric al argilei, iar substituția  $\text{Al}^{3+}/\text{Si}^{4+}$  are loc în substratul tetraedric, ceea ce conduce la două profiluri de gonflare diferite. Locul de substituție influențează distribuția moleculelor de apă și de polimer intercalate, precum și a contraionilor. În sistemul Na-MMT conglomeratele de PEG se află dezordonate în spațiul interstrat. În sistemul ternar Ca-MMT, acestea sunt organizate, iar conglomeratele de PEG evită centrele de substituție izomorfe, în timp ce complexe cation-apă se poziționează în apropierea acestor centre. Filosilicatele cu un număr mai mare de substituții tetraedrice au o capacitate mai mare de a reține moleculele de PEG, subcapitolul 4.3.3 (SIMINEL N. et al., 2017).
6. Stratul de polimer învecinat cu suprafața bazală a argilei prezintă mișcare de translație minimă și tendința de concreștere cu suprafața argilei, în special nanocompozitele pe bază de NaMt, cu deficit de sarcină în substratul octaedric. Imobilizarea lanțurilor de polimeri adsorbiți și formarea de complecși cu cationi schimbabili contribuie la

reducerea permeabilității gazelor și vaporilor, prin crearea unui traseu mai întortocheat pentru moleculele permeabile. Nanocompozite PEG/Mt cu o masa moleculară 100–450 g·mol<sup>-1</sup> și conținutul de PEG intercalat de la 0 la 40% sunt bistratale, cu distanțe  $d_{001}$  de 16,5 Å , subcapitolul 3.2.3 (SIMINEL N., 2019).

7. S-a constatat, că mineralul montmorilonit absoarbe preferențial fracțiunile de PEG cu masa moleculară mare. Argila cu un conținut PEG cu masă moleculară mai mare a prezentat și o stabilitate mai înaltă față de apă. Din punct de vedere ingineresc, aceste rezultate sugerează, că nanocompozitele cu proprietăți de barieră și mecanice mai bune ar putea fi obținute prin controlul distribuției masei moleculare pentru a evita fracțiunile mici de polimeri, subcapitol 4.3.2 ( Lascova-Baciu R et al, 2018).
8. S-a demonstrat, că filosilicații cu o sarcină de strat  $< 0,4$  electroni pe unitate stoechiometrică pot să intercaleze amidonul în spațiul interstrat, formând o barieră pentru vaporii de apă în stratul de acoperire. Filosilicații cu o sarcină de strat de  $> 0,4$  electroni pe unitate stoechiometrică nu au fost capabili să intercaleze amidonul. Viteza de transfer a vaporilor de apă (WVTR) pentru acoperiri similare, preparate pe bază de bentonite cu încărcătură mai mare a fost de 3-4 ori mai mare ( $35 \pm 7$  g·m<sup>2</sup>·zi<sup>-1</sup>) decât în cazul filosilicaților cu o sarcină de strat  $< 0,4$  electroni pe unitate stoechiometrică. Astfel, a fost propus materialul pentru ambalaj a produselor alimentare uscate, care asigură viteze limitate de transfer a vaporilor de apă  $8 \pm 2$  g·m<sup>2</sup>·zi<sup>-1</sup>, subcapitole 5.2-5.3 (SIMINEL N., 2022; SIMINEL N., no.2, 2023).

### Recomandări

Cercetările realizate în cadrul tezei de doctorat au permis de a recomanda metodologia optimală pentru planificarea și obținerea nanocompozitelor pe bază de polietilenglicol, amiloză și argile Na<sup>+</sup>- și Ca<sup>2+</sup>-montmorillonit, destinate fabricării acoperirilor pentru ambalaje alimentare. Se recomandă:

#### **1. Modelul cu granulație grosieră. Model pentru minerale de argilă și molecule de polimeri.**

O mare problemă în modelarea proceselor fizice materiale este scara de timp și scara de lungime. În acest context, se recomandă simulările interacțiunii moleculelor de PEG folosind potențialele Coarse-Grained, care sunt de peste 5 ori mai rapide decât atunci când se utilizează modele de potențial complet atomistice. Acest lucru poate oferi un câștig semnificativ de performanță în simularea sistemelor la scară mare. Pentru a parametriza modelul CG al argilei, se recomandă utilizarea potențialului VOTCA. În acest model, fragmentele stratului de argilă de interfață nu diferă de cele interne. Acesta este punctul în care modelul urmează să fie îmbunătățit și analizat proprietățile de umectare ale interfețelor.

#### **2. Starch intercalation and open surface enhancement in water and carbon dioxide adsorption.**

În experimentele realizate s-a constatat, că straturile de smectită nu sunt pur continue, ci includ în mod natural discontinuități și rupturi datorate fisurilor și defectelor. Prin urmare, se recomandă și cercetarea suprafețelor în alte direcții geometrice; cum ar fi 010 și 100; care includ situsuri reactive. În cazul expunerii la speciile interstratificate, acestea pot avea un impact asupra răspunsului comportamental al argilei. Prin urmare, în cercetările de viitor trebuie luate în considerare straturile discontinue pentru a studia diferite suprafețe reactive ale argilei.

## Bibliography

- [1] F. Bergaya, B.K.G. Theng, and G. Lagaly, editors. *Handbook of clay science*. Elsevier Ltd, first edition, 2006.
- [2] A. Meunier. *Clays*. Springer Science and Business Media, 2005.
- [3] B.L. Sawhney, editor. *Organic pollutants in the environment*. The Clay minerals Society, 1996.
- [4] K. Müller, D. Fedosov, and G. Gompper. Margination of micro- and nano-particles in blood flow and its effect on drug delivery. *Scientific Reports*, 4:4871, 5 2014.
- [5] <http://www.stressebook.com/finite-element-analysis-in-a-nut-shell/>. finite element analysis in a nut shell.
- [6] D. Frenkel and B. Smit. *Understanding molecular simulation*, 1996.
- [7] B.J. Teppen, K. Rasmussen, P.M. Bertsch, D.M. Miller, and L. Schäfer. Molecular dynamics modeling of clay minerals. 1. gibbsite, kaolinite, pyrophyllite, and beidellite. *The Journal of Physical Chemistry B*, 101:1579–1587, 1997.
- [8] T.V. Shapley. *Molecular adsorption and templating at the solid-water interface*, 2013.
- [9] C.L. Freeman, J.H. Harding, D.J. Cooke, J.A. Elliott, J.S. Lardge, and D.M. Duffy. New forcefields for modeling biomineralization processes. *The Journal of Physical Chemistry C*, 111:11943–11951, 2007.
- [10] M.H. Fu, Z.Z. Zhang, and P.F. Low. Changes in the properties of a montmorillonite-water system during the adsorption and desorption of water: hysteresis. *Clays and Clay Minerals*, 38:485–492, 1990.
- [11] S.L. Teich-McGoldrick, J.A. Greathouse, C.F. Jove-Colon, and R.T. Cygan. Swelling properties of montmorillonite and beidellite clay minerals from molecular simulation: comparison of temperature, interlayer cation, and charge location effects. *The Journal of Physical Chemistry C*, 119:20880–20891, 2015.
- [12] T. Sato, T. Watanabe, and R. Otsuka. Effect of layer charge, charge location, and energy change on expansion properties of dioctahedral smectites. *Clays and Clay Minerals*, 40:103–113, 1992.
- [13] E. Ruiz-Hitzky and P. Aranda. Polymer-salt intercalation complexes in layer silicates. *Advanced Materials*, 2:545–547, 1990.
- [14] B. Chen. Polymer-clay nanocomposites: an overview with emphasis on interaction mechanisms. *British Ceramic Transactions*, 103:241–249, 2004.
- [15] J.P. Larentzos, J.A. Greathouse, and R.T. Cygan. An ab initio and classical molecular dynamics investigation of the structural and vibrational properties of talc and pyrophyllite. *The Journal of Physical Chemistry C*, 111:12752–12759, 2007.
- [16] Y. Wu, H.L. Tepper, and G.A. Voth. Flexible simple point-charge water model with improved liquid-state properties. *The Journal of Chemical Physics*, 124:024503, 2006.

- [17] J. Wang, R.M. Wolf, J.W. Caldwell, P.A. Kollman, and D.A. Case. Development and testing of a general amber force field. *Journal of Computational Chemistry*, 25:1157–1174, 2004.
- [18] R. Cygan, J.J. Liang, and A.G. Kalinichev. Molecular models of hydroxide, oxyhydroxide, and clay phases and the development of a general force field. *The Journal of Physical Chemistry B*, 108:1255–1266, 2004.
- [19] C. Johansson, J. Bras, I. Mondragon, P. Nechita, D. Plackett, P. Simon, D.G. Svetec, S. Virtanen, M.G. Baschetti, C. Breen, F. Clegg, and S. Aucejo. Renewable fibers and bio-based materials for packaging applications - a review of recent developments. *Bioresources*, 7:2506–2552, 2012.
- [20] M.F. Huang, J.G. Yu, and X.F. Ma. Studies on the properties of montmorillonite-reinforced thermoplastic starch composites. *Polymer*, 45:7017–7023, 2004.
- [21] M. Avella, J.J. De Vlieger, M.E. Errico, S. Fischer, P. Vacca, and M.G. Volpe. Biodegradable starch/clay nanocomposite films for food packaging applications. *Food Chemistry*, 93:467–474, 2005.
- [22] W. Gao, H. Dong, H. Hou, and H. Zhang. Effects of clays with various hydrophilicities on properties of starch-clay nanocomposites by film blowing. *Carbohydrate Polymers*, 88:321–328, 2012.
- [23] E. Olsson, C. Johansson, and L. Järnström. Montmorillonite for starch-based barrier dispersion coating - part 1: the influence of citric acid and poly(ethylene glycol) on viscosity and barrier properties. *Applied Clay Science*, 97-98:160–166, 2014.
- [24] J.L. Suter, R.L. Anderson, C.H. Greenwell, and P.V. Coveney. Recent advances in large-scale atomistic and coarse-grained molecular dynamics simulation of clay minerals. *Journal of Materials Chemistry*, 19:2482, 2009.
- [25] Yining Xia, Maria Rubino, and Rafael Auras. Interaction of nanoclay-reinforced packaging nanocomposites with food simulants and compost environments. *Food Applications of Nanotechnology*, 88:275–298, 2019.
- [26] Kalpani Y Perera, Maille Hopkins, Amit K Jaiswal, and Swarna Jaiswal. Nanoclays-containing bio-based packaging materials: properties, applications, safety, and regulatory issues. *Journal of Nanostructure in Chemistry*, 2023.
- [27] C.H. Greenwell, M.J. Harvey, P. Boulet, A.A. Bowden, P.V. Coveney, and A. Whiting. Inter-layer structure and bonding in nonswelling primary amine intercalated clays. *Macromolecules*, 38:6189–6200, 2005.
- [28] Eliezer Velásquez, Sebastián Espinoza, Ximena Valenzuela, Luan Garrido, María José Galotto, Abel Guarda, and Carol de Dicastillo. Effect of organic modifier types on the physical-mechanical properties and overall migration of post-consumer polypropylene/clay nanocomposites for food packaging. *Polymers*, 13, 2021.
- [29] Asif Ali, Yi Wai Chiang, and Rafael M Santos. X-ray diffraction techniques for mineral characterization: A review for engineers of the fundamentals, applications, and research directions. *Minerals*, 12, 2022.

- [30] C.H. Greenwell, W. Jones, P.V. Coveney, and S. Stackhouse. On the application of computer simulation techniques to anionic and cationic clays: a materials chemistry perspective. *Journal of Materials Chemistry*, 16:708, 2006.
- [31] Stefanos Mourdikoudis, Roger M Pallares, and Nguyen T K Thanh. Characterization techniques for nanoparticles: comparison and complementarity upon studying nanoparticle properties. *Nanoscale*, 10:12871–12934, 2018.
- [32] B. Chen, J.R.G. Evans, C.H. Greenwell, P. Boulet, P.V. Coveney, A.I.A. Bowden, and A. Whiting. A critical appraisal of polymer-clay nanocomposites. *Chemical Society reviews*, 37:568–94, 3 2008.
- [33] C.H. Greenwell, A.A. Bowden, B. Chen, P. Boulet, J.R.G. Evans, P.V. Coveney, and A. Whiting. Intercalation and in situ polymerization of poly(alkylene oxide) derivatives within montmorillonite ( $m = \text{li, na, k}$ ). *Journal of Materials Chemistry*, 16:1082, 2006.
- [34] S. Sinha Ray. *Clay-containing polymer nanocomposites*. Elsevier, 2013.
- [35] D.M. Moore and R.C. Jr Reynolds. *X-ray diffraction and the identification and analysis of clay minerals*. Oxford University Press, 1997.
- [36] G.W. Brindley and G. Brown. *Crystal structures of clay minerals and their X-ray identification*. Mineralogical Society, 1980.
- [37] G. Sposito. *The surface chemistry of soils*. Oxford University Press, 1984.
- [38] K. Norrish. The swelling of montmorillonite. *Discussions of the Faraday Society*, 18:120–134, 1954.
- [39] B. Dazas, B. Lanson, A. Delville, J.L. Robert, S. Komarneni, L.J. Michot, and E. Ferrage. Influence of tetrahedral layer charge on the organization of interlayer water and ions in synthetic na-saturated smectites. *The Journal of Physical Chemistry C*, 2015.
- [40] Richard L. Anderson, I. Ratcliffe, Christopher H. Greenwell, P.A. Williams, S. Cliffe, and Peter V. Coveney. Clay swelling - a challenge in the oilfield. *Earth-Science Reviews*, 98:201–216, 2 2010.
- [41] J. Bujdák, E. Hackett, and E.P. Giannelis. Effect of layer charge on the intercalation of poly(ethylene oxide) in layered silicates: implications on nanocomposite polymer electrolytes. *Chemistry of Materials*, 12:2168–2174, 2000.
- [42] Margaret D Foster. The relation between composition swelling in clays. *U.S. Geological Survey*, pages 205–220, 1960.
- [43] J.L. Suter, P.V. Coveney, R.L. Anderson, C.H. Greenwell, and S. Cliffe. Rule based design of clay-swelling inhibitors. *Energy and Environmental Science*, 4:4572, 2011.
- [44] G. Sposito and R. Prost. Structure of water adsorbed on smectites. *Chemical Reviews*, 82:553–573, 1982.

- [45] I. Bérend, J.M. Cases, M. François, J.P. Uriot, L. Michot, A. Masion, and F. Thomas. Mechanism of adsorption and desorption of water vapor by homoionic montmorillonites. *Clays and Clay Minerals*, 43:324–336, 1995.
- [46] E.S. Boek, P.V. Coveney, and N.T. Skipper. Monte carlo molecular modeling studies of hydrated li, na, and k smectites: understanding the role of potassium as a clay swelling inhibitor. *Journal of the American Chemical Society*, 117:12608–12617, 1995.
- [47] N T Skipper, K Refson, and J D C McConnell. Computer simulation of interlayer water in 2:1 clays. *The Journal of Chemical Physics*, 94:7434–7445, 6 1991.
- [48] N.T. Skipper, F.C. Chang, and G. Sposito. Monte carlo simulation of interlayer molecular structure in swelling clay minerals. 1. methodology. *Clays and Clay Minerals*, 43:285–293, 1995.
- [49] G.W. Beall and C.E. Powel. *Fundamentals of polymer-clay nanocomposites*. Cambridge University Press, 1 edition, 8 2011.
- [50] Y. Kojima, A. Usuki, M. Kawasumi, A. Okada, T. Kurauchi, and O. Kamigaito. Sorption of water in nylon-6 clay hybrid. *Journal of Applied Polymer Science*, 49:1259–1264, 1993.
- [51] J. Rhim, H. Park, and C. Ha. Bio-nanocomposites for food packaging applications. *Progress in Polymer Science*, 38:1629–1652, 10 2013.
- [52] G. Findenig, S. Leimgruber, R. Kargl, S. Spirk, K. Stana-Kleinschek, and V. Ribitsch. Creating water vapor barrier coatings from hydrophilic components. *Applied Materials and Interfaces*, 4:3199–3206, 2012.
- [53] R. Petrenko and J. Meller. *Molecular dynamics*. John Wiley and Sons, Ltd, 2001.
- [54] A.R. Leach. *Molecular modelling. Principles and applications*. Longman, 2001.
- [55] M.P. Allen and D.J. Tildesley. *Computer simulation of liquids*. Clarendon, Oxford, 1987.
- [56] H.J.C. Berendsen, J.P.M. Postma, W.F. van Gunsteren, A. DiNola, and J.R. Haak. Molecular dynamics with coupling to an external bath. *The Journal of Chemical Physics*, 81:3684–3690, 1984.
- [57] D.A. Case, J.T. Berryman, R.M. Betz, D.S. Cerutti, T.E. Cheatham, T.A. Darden, R.E. Duke, T.J. Giese, H. Gohlke, A.W. Goetz, N. Homeyer, S. Izadi, P. Janowski, A. Kovalenko, T.S. Lee, S. LeGrand, T. Luchko, P. Li, and R. Luo. Amber2015. *University of California, San Francisco*, 2015.
- [58] S. Plimpton. Fast parallel algorithms for short-range molecular dynamics. *Journal of Computational Physics*, 117:1–19, 1995.
- [59] H.J.C. Berendsen, D. van der Spoel, and R. van Drunen. Gromacs: a message-passing parallel molecular dynamics implementation. *Computer Physics Communications*, 91:43–56, 1995.
- [60] J.C. Phillips, R. Braun, W. Wang, J. Gumbart, E. Tajkhorshid, E. Villa, C. Chipot, R.D. Skeel, L. Kalé, and K. Schulten. Scalable molecular dynamics with namd. *Journal of Computational Chemistry*, 26:1781–1802, 2005.

- [61] I.T. Todorov, W. Smith, K. Trachenko, and M.T. Dove. Dl-poly-3: new dimensions in molecular dynamics simulations via massive parallelism. *Journal of Materials Chemistry*, 16:1911–1918, 2006.
- [62] L. Verlet. Computer 'experiments' on classical fluids. i. thermodynamical properties of lennard-jones molecules. *Physical Review*, pages 98–103, 1967.
- [63] R.T. Cygan. Molecular modeling in mineralogy and geochemistry. *Reviews in Mineralogy and Geochemistry*, 42:1–35, 2001.
- [64] P Ewald. Die berechnung optischer und elektrostatischer gitterpotentiale. *Annalen der Physik*, 64:253–287, 1921.
- [65] M.P. Tosi. Cohesion of ionic solids in the born model. *Solid State Physics - Advances in Research and Applications*, 16:1–120, 1964.
- [66] S.W. de Leeuw, J.W. Perram, and E.R. Smith. Simulation of electrostatic systems in periodic boundary vonditions. i. lattice sums and dielectric constants. *Proceedings of the Royal Society of London A: Mathematical, Physical and Engineering Sciences*, 373:27–56, 10 1980.
- [67] J.P. Hansen. Molecular-dynamics simulations of coulomb systems in two and three dimensions. *Molecular Dynamics Simulations of Statistical Mechanics Systems*, 97:89–129, 1986.
- [68] W Smith and T R Forester. Dl-poly-2.0: A general-purpose parallel molecular dynamics simulation package. *Journal of Molecular Graphics*, 14:136–141, 1996.
- [69] W. Smith, T.R. Forester, and I.T. Todorov. The dl-poly classic user manual. *STFC Daresbury Laboratory*, 1.9, 2012.
- [70] I.T. Todorov and W. Smith. The dl-poly-4 user manual. *STFC Daresbury Laboratory*, 4.07, 2015.
- [71] W. Humphrey, A. Dalke, and K. Schulten. Vmd: visual molecular dynamics. *Journal of Molecular Graphics*, 14:33–38, 1996.
- [72] O. Matsuoka, E. Clementi, and M. Yoshimine. Ci study of the water dimer potential surface. *The Journal of Chemical Physics*, 64:1351, 1976.
- [73] A. Delville. Monte carlo simulations of surface hydration: an application to clay wetting. *The Journal of Physical Chemistry*, 99:2033–2037, 1995.
- [74] F.C. Chang, N.T. Skipper, and G. Sposito. Monte carlo and molecular dynamics simulations of interfacial structure in lithium-montmorillonite hydrates. *Langmuir*, 13:2074–2082, 1997.
- [75] N.T. Skipper. Computer simulation of aqueous pore fluids in 2:1 clay minerals. *Mineralogical Magazine*, 62:657–667, 1998.
- [76] V.C. DeSiqueira, N.T. Skipper, P.V. Coveney, and E.S. Boek. Computer simulation evidence for enthalpy driven dehydration of smectite clays at elevated pressures and temperatures. *Molecular Physics*, 92:1–6, 1997.

- [77] M. Pintore, S. Deiana, P. Demontis, B. Manunza, G.B. Suffritti, and C. Gessa. Simulations of interlayer methanol in ca- and na-saturated montmorillonite using molecular dynamics. *Clays and Clay Minerals*, 49:255–262, 2001.
- [78] E.J. Hensen, T.J. Tambach, A. Blik, and B. Smit. Adsorption isotherms of water in li-, na-, and k-montmorillonite by molecular simulation. *The Journal of Chemical Physics*, 115:3322–3329, 2001.
- [79] H.D. Whitley and D.E. Smith. Free energy, energy, and entropy of swelling in cs-, na-, and sr-montmorillonite clays. *The Journal of Chemical Physics*, 120:5387–5395, 2004.
- [80] D.E. Smith, Yu Wang, A. Chaturvedi, and H.D. Whitley. Molecular simulations of the pressure, temperature, and chemical potential dependencies of clay swelling. *The Journal of Physical Chemistry B*, 110:20046–20054, 2006.
- [81] K. Kawamura. Interatomic potential models for molecular dynamics simulations of multi-component oxides, 1992.
- [82] Y. Ichikawa, K. Kawamura, M. Nakano, K. Kitayama, T. Seiki, and N. Theramast. Seepage and consolidation of bentonite saturated with pure- or salt-water by the method of unified molecular dynamics and homogenization analysis. *Engineering Geology*, 60:127–138, 2001.
- [83] B.J. Teppen, C. Yu, D.M. Miller, and L. Schäfer. Molecular dynamics simulations of sorption of organic compounds at the clay mineral / aqueous solution interface. *Journal of Computational Chemistry*, 19:144–153, 1998.
- [84] C. Yu, S.Q. Newton, M.A. Norman, D.M. Miller, L. Schafer, B.J. Teppen, and B J Teppen. Molecular dynamics simulations of the adsorption of methylene blue at clay mineral surfaces. *Clays and Clay Minerals*, 48:665–681, 2000.
- [85] M. Pospíšil, P. Capková, D. Merínská, Z. Malác, and J. Simoník. Structure analysis of montmorillonite intercalated with cetylpyridinium and cetyltrimethylammonium: molecular simulations and xrd analysis. *Journal of Colloid and Interface Science*, 236:127–131, 2001.
- [86] H.J.C. Berendsen, J.P.M. Postma, W.F. van Gunsteren, and J. Hermans. Interaction models for water in relation to protein hydration, 1981.
- [87] A. Beran. Infrared spectroscopy of micas. *Reviews in Mineralogy and Geochemistry*, 46:351–369, 1 2002.
- [88] A. Kalra, D.M. Parks, and G.C. Rutledge. Molecular simulation of strain dependence of vibrational frequencies for montmorillonite clay and analysis of strain transfer in a polymer-clay nanocomposite. *Macromolecules*, 40:140–144, 2007.
- [89] J.L. Suter, P.V. Coveney, C.H. Greenwell, and M. Thyveetil. Large-scale molecular dynamics study of montmorillonite clay: emergence of undulatory fluctuations and determination of material properties. *The Journal of Physical Chemistry C*, 111:8248–8259, 2007.
- [90] M. Thyveetil, P.V. Coveney, J.L. Suter, and C.H. Greenwell. Emergence of undulations and determination of materials properties in large-scale molecular dynamics simulation of layered double hydroxides. *Chemistry of Materials*, 19:5510–5523, 2007.

- [91] B. Carrier, M. Vandamme, R.J.M. Pellenq, and H. Van Damme. Elastic properties of swelling clay particles at finite temperature upon hydration. *The Journal of Physical Chemistry C*, 118:8933–8943, 2014.
- [92] M.A. Mazo, L.I. Manevitch, E.B. Gusarova, M.Yu. Shamaev, A.A. Berlin, N.K. Balabaev, and G.C. Rutledge. Molecular dynamics simulation of thermomechanical properties of montmorillonite crystal. 3. montmorillonite crystals with peo oligomer intercalates. *The Journal of Physical Chemistry B*, 112:3597–3604, 2008.
- [93] M.A. Mazo, L.I. Manevitch, E.B. Gusarova, A.A. Berlin, N.K. Balabaev, and G.C. Rutledge. Molecular dynamics simulation of thermomechanical properties of montmorillonite crystal. ii. hydrated montmorillonite crystal. *The Journal of Physical Chemistry C*, 112:17056–17062, 2008.
- [94] R. Zhu, W. Chen, T.V. Shapley, M. Molinari, F. Ge, and S.C. Parker. Sorptive characteristics of organomontmorillonite toward organic compounds: a combined molecular dynamics simulation study. *Environmental Science Technology*, 45:6504–6510, 2011.
- [95] T.V. Shapley, M. Molinari, R. Zhu, and S.C. Parker. Atomistic modeling of the sorption free energy of dioxins at clay-water interfaces. *The Journal of Physical Chemistry C*, 117:24975–24984, 2013.
- [96] R. Zhu, M. Molinari, T.V. Shapley, and S.C. Parker. Modeling the interaction of nanoparticles with mineral surfaces: adsorbed c60 on pyrophyllite. *The Journal of Physical Chemistry A*, 117:6602–6611, 2013.
- [97] L. Zhang, X. Lu, X. Liu, J. Zhou, and H. Zhou. Hydration and mobility of interlayer ions of (na, ca)-montmorillonite: a molecular dynamics study. *The Journal of Physical Chemistry C*, 118:29811–29821, 2014.
- [98] M. Szczerba, Z. Klapyta, and A. Kalinichev. Ethylene glycol intercalation in smectites. molecular dynamics simulation studies. *Applied Clay Science*, 91:87–97, 2014.
- [99] J.A. Greathouse, R.T. Cygan, J.T. Fredrich, and G.R. Jerauld. Molecular dynamics simulation of diffusion and electrical conductivity in montmorillonite interlayers. *The Journal of Physical Chemistry C*, page acs.jpcc.5b10851, 2016.
- [100] M. Chaplin. Water models.
- [101] C. Vega and J.L.F. Abascal. Simulating water with rigid non-polarizable models: a general perspective. *Physical Chemistry Chemical Physics*, 13:19663–88, 11 2011.
- [102] B. Guillot. A reappraisal of what we have learnt during three decades of computer simulations on water. *Journal of Molecular Liquids*, 101:219–260, 2002.
- [103] W.D. Cornell, P. Cieplak, C.I. Bayly, I.R. Gould, K.M. Merz, D.M. Ferguson, D.C. Spellmeyer, T. Fox, J.W. Caldwell, and P.A. Kollman. A second generation force field for the simulation of proteins, nucleic acids, and organic molecules. *Journal of the American Chemical Society*, 117:5179–5197, 1995.

- [104] H.A. Lorentz. Ueber die anwendung des satzes vom virial in der kinetischen theorie der gase. *Annalen der Physik*, 248:127–136, 1881.
- [105] D. Berthelot. Sur le mélange des gaz. *Comptes rendus hebdomadaires des séances de l'Académie des Sciences*, 126:1703–1855, 1898.
- [106] A. Pavese, M. Catti, S.C. Parker, and A. Wall. Modelling of the thermal dependence of structural and elastic properties of calcite, caco<sub>3</sub>. *Physics and Chemistry of Minerals*, 23:89–93, 1996.
- [107] K.P. Schröder, J. Sauer, M. Leslie, C. Richard, A. Catlow, and J.M. Thomas. Bridging hydroxyl groups in zeolitic catalysts: a computer simulation of their structure, vibrational properties and acidity in protonated faujasites. *Chemical Physics Letters*, 188:320–325, 1 1992.
- [108] G. Zhang, E.M. Myshakin, and K.D. Jordan. Dispersion-corrected density functional theory and classical force field calculations of water loading on a pyrophyllite(001) surface. *The Journal of Physical Chemistry C*, pages 17134–17141, 2012.
- [109] R.W. Mooney, A.G. Keenan, and L.A. Wood. Adsorption of water vapor by montmorillonite. ii. effect of exchangeable ions and lattice swelling as measured by x-ray diffraction. *Journal of the American Chemical Society*, 74:1371–1374, 1952.
- [110] X. Liu, X. Lu, R. Wang, and H. Zhou. Effects of layer-charge distribution on the thermodynamic and microscopic properties of cs-smectite. *Geochimica et Cosmochimica Acta*, 72:1837–1847, 2008.
- [111] W. Loewenstein. The distribution of aluminum in the tetrahedra of silicates and aluminates. *American Mineralogist*, 39:92–96, 1954.
- [112] T.R. Zeitler, J.A. Greathouse, and R.T. Cygan. Effects of thermodynamic ensembles and mineral surfaces on interfacial water structure. *Physical Chemistry Chemical Physics*, 14:1728–34, 2 2012.
- [113] C.T. Johnston, G. Sposito, and C. Erickson. Vibrational probe studies of water interactions with montmorillonite. *Clays and Clay Minerals*, 40:722–730, 1992.
- [114] S. Morodome and K. Kawamura. Swelling behavior of na- and ca-montmorillonite up to 150c by in situ x-ray diffraction experiments. *Clays and Clay Minerals*, 57:150–160, 2009.
- [115] E.J.M. Hensen and B. Smit. Why clays swell. *The Journal of Physical Chemistry B*, 106:12664–12667, 2002.
- [116] C.T. Chiou and D.W. Rutherford. Effects of exchanged cation and layer charge on the sorption of water and egme vapors on montmorillonite clays. *Clay Minerals*, 45:867–880, 1997.
- [117] G.M. Bowers, J.W. Singer, D.L. Bish, and R.J. Kirkpatrick. Structural and dynamical relationships of ca and h<sub>2</sub>o in smectite/h<sub>2</sub>o systems. *American Mineralogist*, 99:318–331, 2014.
- [118] D.A. Laird. Layer charge influences on the hydration of expandable 2:1 phyllosilicates. *Clays and Clay Minerals*, 47:630–636, 1999.

- [119] J. M. Cases, I. Berend, M. Francois, J. P. Uriot, L. J. Michot, and F. Thomas. Mechanism of adsorption and desorption of water vapor by homoionic montmorillonite. *Clays and Clay Minerals*, 45:8–22, 1997.
- [120] A.M. Posner and J.P. Quirk. Changes in basal spacing of montmorillonite in electrolyte solutions. *Journal of Colloid Science*, 19:798–812, 1964.
- [121] C.T. Jognston. *CRC Handbook of Chemistry and Physics, 94th Edition, 2013-2014*, volume 53. CRC Press, 2013.
- [122] U.W. Schmitt and G.A. Voth. The computer simulation of proton transport in water. *The Journal of Chemical Physics*, 111:9361–9381, 1999.
- [123] N. Loganathan, A.O. Yazaydin, G.M. Bowers, A.G. Kalinichev, and R.J. Kirkpatrick. Cation and water structure, dynamics, and energetics in smectite clays: a molecular dynamics study of ca–hectorite. *The Journal of Physical Chemistry C*, page acs.jpcc.6b00230, 2016.
- [124] J.A. Greathouse, D.B. Hart, G.M. Bowers, R.J. Kirkpatrick, and R.T. Cygan. Molecular simulation of structure and diffusion at smectite-water interfaces: using expanded clay interlayers as model nanopores. *The Journal of Physical Chemistry C*, 119:17126–17136, 2015.
- [125] G.M. Bowers, J.W. Singer, D.L. Bish, and R.J. Kirkpatrick. Alkali metal and h2o dynamics at the smectite/water interface. *The Journal of Physical Chemistry C*, 115:23395–23407, 2011.
- [126] E.S. Boek and M. Sprik. Ab initio molecular dynamics study of the hydration of a sodium smectite clay. *The Journal of Physical Chemistry B*, 107:3251–3256, 2003.
- [127] N.T. Skipper and G.W. Neilson. X-ray and neutron diffraction studies on concentrated aqueous solutions of sodium nitrate and silver nitrate. *Journal of Physics: Condensed Matter*, 1:4141–4154, 1999.
- [128] M. Holmboe and I.C. Bourg. Molecular dynamics simulations of water and sodium diffusion in smectite interlayer nanopores as a function of pore size and temperature. *The Journal of Physical Chemistry C*, 118:1001–1013, 2014.
- [129] N. Malikova, A. Cadene, V. Marry, E. Dubois, and P. Turq. Diffusion of water in clays on the microscopic scale: modeling and experiment. *The Journal of Physical Chemistry B*, 110:3206–3214, 2006.
- [130] T. Kozaki, Y. Adachi, K. Inada, S. Sato, and H. Ohashi. Diffusion behavior of ca ions in compacted na-montmorillonite. *MRS Online Proceeding*, 663, 2011.
- [131] G. Raabe and R.J. Sadus. Molecular dynamics simulation of the effect of bond flexibility on the transport properties of water. *The Journal of Chemical Physics*, 137:104512, 2012.
- [132] Y. Zheng and A. Zaoui. How water and counterions diffuse into the hydrated montmorillonite. *Solid State Ionics*, 203:80–85, 2011.
- [133] Q. Wang, D.J. Keffer, and D.M. Nicholson. A coarse-grained model for polyethylene glycol polymer. *The Journal of Chemical Physics*, 135:214903, 12 2011.

- [134] M. Krishnan, M. Saharay, and J.R. Kirkpatrick. Molecular dynamics modeling of co<sub>2</sub> and poly(ethylene glycol) in montmorillonite: the structure of clay-polymer composites and the incorporation of co<sub>2</sub>. *The Journal of Physical Chemistry C*, 117:20592–20609, 2013.
- [135] M.L. Adams, A. Lavasanifar, and G.S. Kwon. Amphiphilic block copolymers for drug delivery. *The Journal of Pharmaceutical Sciences*, 92:1343–1355, 2003.
- [136] J.A. Barish and J.M. Goddard. Polyethylene glycol grafted polyethylene: a versatile platform for nonmigratory active packaging applications. *Journal of food science*, 76:E586–91, 2011.
- [137] S. Rodriguez-Llamazares, B. L. Rivas, M. Perez, and F. Perrin-Sarazin. Poly(ethylene glycol) as a compatibilizer and plasticizer of poly(lactic acid)/clay nanocomposites. *High Performance Polymers*, 24:254–261, 2012.
- [138] F. Clegg, C. Breen, and Khairuddin. Synergistic and competitive aspects of the adsorption of poly(ethylene glycol) and poly(vinyl alcohol) onto na-bentonite. *The Journal of Physical Chemistry B*, 118:13268–13278, 2014.
- [139] Khairuddin. Clay-polyvinylalcohol nanocomposites: competitive adsorption of polyvinylalcohol and plasticiser onto na-bentonite, 2012.
- [140] B. Chen. Polymer-clay nanocomposites, 2004.
- [141] E. Hackett, E. Manias, and E.P. Giannelis. Computer simulation studies of peo/layer silicate. *Chemistry of Materials*, 12:2161–2167, 2000.
- [142] S. Sinha Ray and M. Okamoto. Polymer/layered silicate nanocomposites: a review from preparation to processing. *Progress in Polymer Science*, 28:1539–1641, 2003.
- [143] L.J.A. Siqueira and M.C.C. Ribeiro. Molecular dynamics simulation of the polymer electrolyte poly(ethylene oxide)/liclo(4). ii. dynamical properties. *The Journal of Chemical Physics*, 125:214903, 12 2006.
- [144] J.L. Suter and P.V. Coveney. Computer simulation study of the materials properties of intercalated and exfoliated poly(ethylene)glycol clay nanocomposites. *Soft Matter*, 5:2239, 2009.
- [145] B. Chen and J.R.G. Evans. Preferential intercalation in polymer-clay nanocomposites. *The Journal of Physical Chemistry B*, 108:14986–14990, 2004.
- [146] S. Ottani, D. Vitalini, F. Comelli, and C. Castellari. Densities, viscosities, and refractive indices of poly(ethylene glycol) 200 and 400 + cyclic ethers at 303.15k. *Journal of Chemical and Engineering Data*, 47:1197–1204, 2002.
- [147] H. Lee, R.M. Venable, A.D. Mackerell, and R.W. Pastor. Molecular dynamics studies of polyethylene oxide and polyethylene glycol: hydrodynamic radius and shape anisotropy. *Biophysical journal*, 95:1590–1599, 8 2008.
- [148] R.A. Waggoner, F.D. Blum, and J.C. Lang. Diffusion in aqueous solutions of poly(ethylene glycol) at low concentrations. *Macromolecules*, 28:2658–2664, 1995.

- [149] R.L. Parfitt and D.J. Greenland. Adsorption of water by montmorillonite-poly(ethylene glycol) adsorption products. *Clay Minerals*, page 317, 1970.
- [150] R.W.A. Franco, C.A. Brasil, G.L. Mantovani, E.R. de Azevedo, and T.J. Bonagamba. Molecular dynamics of poly(ethylene glycol) intercalated in clay, studied using  $^{13}\text{C}$  solid-state nmr. *Materials*, 6:47–64, 2013.
- [151] R. Toth, D. Voorn, J. Handgraaf, J.G.E.M. Fraaije, M. Fermeglia, S. Pricl, and P. Posocco. Multiscale computer simulation studies of water-based montmorillonite/poly(ethylene oxide) nanocomposites. *Macromolecules*, 42:8260–8270, 11 2009.
- [152] R.A. Vaia and E.P. Giannelis. Lattice model of polymer melt intercalation in organically -modified layered silicates. *Macromolecules*, 30:7990–7999, 1997.
- [153] A. Sorrentino, G. Gorrasi, and V. Vittoria. Potential perspectives of bio-nanocomposites for food packaging applications. *Trends in Food Science and Technology*, 18:84–95, 2007.
- [154] H.M.C. de Azeredo. Nanocomposites for food packaging applications. *Food Research International*, 42:1240–1253, 2009.
- [155] M.T. Taghizadeh, N. Sabouri, and B. Ghanbarzadeh. Polyvinyl alcohol:starch:carboxymethyl cellulose containing sodium montmorillonite clay blends; mechanical properties and biodegradation behavior. *SpringerPlus*, 2:376–1–376–8, 2013.
- [156] A.C. Souza, R. Benze, E.S. Ferrão, C. Ditchfield, A.C.V. Coelho, and C.C. Tadini. Cassava starch biodegradable films: influence of glycerol and clay nanoparticles content on tensile and barrier properties and glass transition temperature. *LWT - Food Science and Technology*, 46:110–117, 2012.
- [157] J.A. Mbey, S. Hoppe, and F. Thomas. Cassava starch-kaolinite composite film. effect of clay content and clay modification on film properties. *Carbohydrate Polymers*, 88:213–222, 2012.
- [158] E. Olsson, C. Menzel, C. Johansson, R. Andersson, K. Koch, and L. Jarnstrom. The effect of ph on hydrolysis, cross-linking and barrier properties of starch barriers containing citric acid. *Carbohydrate Polymers*, 98:1505–1513, 2013.
- [159] E. Olsson, C. Johansson, J. Larsson, and L. Järnström. Montmorillonite for starch-based barrier dispersion coating - part 2: pilot trials and pe-lamination. *Applied Clay Science*, 97-98:167–173, 2014.
- [160] H.M. Park, X. Li, C.Z. Jin, C.Y. Park, W.J. Cho, and C.S. Ha. Preparation and properties of biodegradable thermoplastic starch/clay hybrids. *Macromolecular Materials and Engineering*, 287:553–558, 2002.
- [161] H. Park, W. Lee, C. Park, W. Cho, and C. Ha. Environmentally friendly polymer hybrids. *Journal of Materials Science*, 38:909 – 915, 2003.
- [162] C. Masclaux, F. Gouanve, and E. Espuche. Experimental and modelling studies of transport in starch nanocomposite films as affected by relative humidity. *Journal of Membrane Science*, 363:221–231, 2010.

- [163] Y. Wang, S. Ju, C. Chen, H. Chen, and J. Hsieh. Mechanical property prediction of starch/polymer composites by molecular dynamics simulation. *RSC Advances*, 4:11475, 2014.
- [164] X. Ma and J. Yu. The effects of plasticizers containing amide groups on the properties of thermoplastic starch. *Starch/Staerke*, 56:545–551, 2004.
- [165] A.S. Giroto, A. de Campos, E.I. Pereira, C.C.T. Cruz, J.M. Marconcini, and C. Ribeiro. Study of a nanocomposite starch-clay for slow-release of herbicides: evidence of synergistic effects between the biodegradable matrix and exfoliated clay on herbicide release control. *Journal of Applied Polymer Science*, 41188:1–9, 2014.
- [166] O. Lyckfeldt and J.M.F. Ferreira. Processing of porous ceramics by 'starch consolidation'. *Journal of the European Ceramic Society*, 18:131–140, 1998.

## A Force Field Parameters

### A.1 TIP3P/Fs

Table A.1: Nonbond Parameters for the TIP3P/Fs Force Field [16]

atom symbol	charge (e)	$\epsilon_0$ (kcal/mol)	$\sigma_0$ (Å)
OW	-0.834	0.152	3.150
HW	0.417		

Table A.2: Bond Parameters for the TIP3P/Fs Force Field [16]

bond stretch		$k_1$ (kcal/mol Å <sup>2</sup> )	$r_o$ (Å)	
species $i$	species $j$			
OW	HW	1059.162	0.96	
angle bend				
species $i$	species $j$	species $k$	$k_2$ (kcal/mol rad <sup>2</sup> )	$\Theta_o$ (deg)
HW	OW	HW	68.087	104.5

### A.2 AMBER

The AMBER force field function has contributions from bond stretch, angle bend and torsion potentials in the form of a cosine function. Nonbonded interaction are represented by VDW and Coulomb functions:

$$\begin{aligned}
 E_{pair} = & \sum_{bonds} K_r (r - r_0)^2 \\
 & + \sum_{angles} K_{\Theta} (\Theta - \Theta_0)^2 \\
 & + \sum_{dihedrals} \frac{V_n}{2} [1 + \cos(n\phi - \gamma)] \\
 & + \sum_{i,j} \left[ \left( \frac{A_{ij}}{r_{ij}} \right)^{12} - \left( \frac{B_{ij}}{r_{ij}} \right)^6 + \frac{q_i q_j}{\epsilon r_{ij}} \right]
 \end{aligned} \tag{A.1}$$

Table A.3: Nonbond Parameters for AMBER Force Field [17]

atom type	symbol	$A_{ij}$ (eV)	$B_{ij}$ (Å)
sp <sup>3</sup> carbon	c3	$4.743 \times 10^{-3}$	3.816
sp <sup>3</sup> oxygen in ethers and esters	os	$7.371 \times 10^{-3}$	3.367
sp <sup>3</sup> oxygen in hydroxyl group	oh	$9.123 \times 10^{-3}$	3.442
hydrogen on oxygen	ho	$6.504 \times 10^{-4}$	2.918
hydrogen on aliphatic carbon	h1	$6.807 \times 10^{-4}$	2.774

Table A.4: Bond Parameters for the AMBER Force Field [17]

bond stretch				
species $i$	species $j$			
oh	ho	$K_r$ (eV Å <sup>2</sup> )	$r_o$ (Å)	
oh	c3	32.052	0.974	
c3	c3	27.239	1.426	
c3	h1	26.285	1.535	
c3	os	29.129	1.093	
c3	os	26.146	1.439	
angle bend				
species $i$	species $j$	species $k$	$K_\Theta$ (eV rad <sup>2</sup> )	$\Theta_o$ (deg)
c3	oh	ho	4.084	108.160
c3	c3	oh	5.873	109.430
c3	c3	h1	4.020	110.070
c3	os	c3	5.410	112.450
c3	c3	os	5.878	108.420
os	c3	h1	4.409	108.820
oh	c3	h1	4.420	109.880
h1	c3	h1	3.398	109.550

### A.3 CLAYFF

The functional form of CLAYFF force field is in many ways similar to that described in the section 2.1. However, for the reference, form of CLAYFF constituent potentials will be presented bellow. Nonbond and bond parameters that have been used in this thesis will be given in tables A.5 and A.6 respectively.

Total energy of the CLAYFF force field have contributions from Coulombic interactions, short-range interactions (van der Waals) and the boned interactions:

$$E_{total} = E_{Coul} + E_{VDW} + E_{bond\ stretch} + E_{angle\ bend} \quad (\text{A.2})$$

Coulombic energy is inversely proportional to the distance of separation  $r_{ij}$  of two charges  $q_{i,j}$ :

$$E_{Coul} = \frac{e^2}{4\pi\epsilon_0} \sum_{i \neq j} \frac{q_i q_j}{r_{ij}} \quad (\text{A.3})$$

The van der Waals term is represented by the Lennard-Jones (12-6) potential:

$$E_{VDW} = \sum_{i \neq j} D_{o,ij} \left[ \left( \frac{R_{o,ij}}{r_{ij}} \right)^{12} - 2 \left( \frac{R_{o,ij}}{r_{ij}} \right)^6 \right] \quad (\text{A.4})$$

The Lorentz-Berthelot mixing rule between the unlike atoms is used throughout the CLAYFF force field. Details on these rules are given in section 2.2.4.

$$R_{o,ij} = \frac{1}{2} (R_{o,i} + R_{o,j}) \quad (\text{A.5})$$

$$D_{o,ij} = \sqrt{D_{o,i} D_{o,j}} \quad (\text{A.6})$$

The bond stretch and angle bend energies are described by harmonic terms:

$$E_{bondstretchij} = k_1 (r_{ij} - r_0)^2 \quad (\text{A.7})$$

$$E_{anglebendijk} = k_2 (\Theta_{ijk} - \Theta_0)^2 \quad (\text{A.8})$$

Table A.5: Nonbond Parameters for the CLAYFF Force Field [18]

atom type	symbol	charge (e)	D <sub>0</sub> (kcal/mol)	R <sub>0</sub> (Å)
hydroxyl hydrogen	ho	0.4250		
hydroxyl oxygen	oh	-0.9500	0.1554	3.5532
bridging oxygen	ob	-1.0500	0.1554	3.5532
bridging oxygen with octahedral substitution	obos	-1.1808	0.1554	3.5532
bridging oxygen with tetrahedral substitution	obts	-1.1688	0.1554	3.5532
bridging oxygen with double substitution	obss	-1.2996	0.1554	3.5532
hydroxyl with substitution	ohs	-1.0808	0.1554	3.5532
tetrahedral silicon	st	2.1000	1.8405·10 <sup>-6</sup>	3.7064
octahedral aluminium	ao	1.5750	1.3298·10 <sup>-6</sup>	4.7943
tetrahedral aluminium	at	1.5750	1.8405·10 <sup>-6</sup>	3.7064
octahedral magnesium	mgo	1.3600	9.0298·10 <sup>-7</sup>	5.9090
sodium cation	Na	1.0	0.1301	2.6378
calcium cation	Ca	2.0	0.1000	3.2237

Table A.6: Bond Parameters for the CLAYFF Force Field [18]

bond stretch				
species <i>i</i>	species <i>j</i>	<i>k</i> <sub>1</sub> (kcal/mol Å <sup>2</sup> )	<i>r</i> <sub>0</sub> (Å)	
o	h	554.1349	1.0000	
oh	ho	554.1349	1.0000	
ohs	ho	554.1349	1.0000	
angle bend				
species <i>i</i>	species <i>j</i>	species <i>k</i>	<i>k</i> <sub>2</sub> (kcal/mol rad <sup>2</sup> )	Θ <sub>0</sub> (deg)
h	o	h	45.7696	109.47
Metal	oh	ho	30.0	109.47
Metal	ohs	ho	30.0	109.47

## B Cross Terms

Table B.1: Nonbonded Cross Terms for water–organic, water–mineral and organic–mineral interactions

<b>water–organic</b>			
ion pair ( <i>ij</i> )		$A_{ij}$ (eV Å <sup>12</sup> )	$B_{ij}$ (eV Å <sup>6</sup> )
OW	c3	34085.216	27.614
OW	os	19961.812	23.594
OW	oh	25264.352	27.997
OW	h1	2063.305	4.182
<b>water–mineral</b>			
ion pair ( <i>ij</i> )		$A_{ij}$ (eV Å <sup>12</sup> )	$B_{ij}$ (eV Å <sup>6</sup> )
OW	st	116.752	0.103
OW	ob, obos, oh, ohs	26249.418	26.456
OW	ao	532.059	0.203
OW	mgo	1978.605	0.357
OW	Na	4571.319	10.560
<b>organic–mineral</b>			
ion pair ( <i>ij</i> )		$A_{ij}$ (eV Å <sup>12</sup> )	$B_{ij}$ (eV Å <sup>6</sup> )
c3	st	155.955	0.110
c3	ob, obos, oh, ohs	35402.054	28.295
c3	ao	670.429	0.211
c3	mgo	2380.970	0.360
c3	Na	6594.209	11.681
os	st	92.952	0.095
os	ob, obos, oh, ohs	20769.439	24.197
os	ao	439.752	0.190
os	mgo	1684.016	0.338
os	Na	3462.760	9.451
oh	st	117.282	0.112
oh	ob, obos, oh, ohs	26278.456	28.708
oh	ao	545.666	0.224
oh	mgo	2062.467	0.395
oh	Na	4467.480	11.322
h1	st	9.870	0.017
h1	ob, obos, oh, ohs	2152.602	4.294
h1	ao	54.017	0.037
h1	mgo	231.502	0.069
h1	Na	301.939	1.538



MD 4776 B1 2021.11.30

## REPUBLICA MOLDOVA

(19) Agenția de Stat  
pentru Proprietatea Intelectuală(11) **4776** (13) **B1**  
(51) Int.Cl: *C07F 3/08* (2006.01)  
*C07D 213/53* (2006.01)  
*C07D 213/90* (2006.01)  
*C07C 229/52* (2006.01)  
*C09K 11/06* (2006.01)  
*C09K 11/54* (2006.01)

## (12) BREVET DE INVENȚIE

<b>In termen de 6 luni de la data publicării mențiunii privind hotărârea de acordare a brevetului de invenție, orice persoană poate face opoziție la acordarea brevetului</b>	
<p>(21) Nr. depozit: a 2020 0076 (22) Data depozit: 2020.10.16</p>	<p>(45) Data publicării hotărârii de acordare a brevetului: 2021.11.30, BOPI nr. 11/2021</p>
<p>(71) Solicitanți: INSTITUTUL DE CHIMIE, MECC, MD; INSTITUTUL DE FIZICĂ APLICATĂ, MD; UNIVERSITATEA DE STAT DIN TIRASPOL, MD</p> <p>(72) Inventatori: LOZOVAN Vasile, MD; FONARI Marina, MD; KRAVȚOV Victor, MD; SIMINEL Nikita, MD; COROPCEANU Eduard, MD; KULIKOVA Olga, MD; COSTRIUCOVA Natalia, MD</p> <p>(73) Titulari: INSTITUTUL DE CHIMIE, MECC, MD; INSTITUTUL DE FIZICĂ APLICATĂ, MD; UNIVERSITATEA DE STAT DIN TIRASPOL, MD</p> <p>(74) Mandatar autorizat: JOVMIR Tudor</p>	

**(54) Polimer coordinativ unidimensional al cadmiului (II) in baza liganzilor 1,2-bis(piridin-4-ilmetilen)hidrazină și acid 2-aminobenzoic, care manifestă activitate fotoluminescentă și capacitate de schimb al moleculelor de solvent**

(57) Rezumat:

1  
Invenția se referă la chimie, în particular la un compus coordinativ fotoluminescent al cadmiului(II) cu structură polimerică unidimensională.

Conform invenției, se revendică compusul  $[Cd(2-aba)_2(4-bphz)]_n \cdot 0,75n(dmf)$ , unde 2-aba este acidul 2-aminobenzoic deprotonat, 4-bphz este 1,2-bis(piridin-4-ilmetilen)hidrazină și dmf este dimetilformamidă. Compusul manifestă o

2  
activitate fotoluminescentă, sensibilă la eliminarea sau schimbul moleculelor de solvent din cavitățile structurii polimerice.

Compusul poate fi utilizat in domeniul senzorilor pentru detectarea moleculelor oaspete de dimensiuni mici prin solvatare.

Revendicări: 3

Figuri: 6

MD 4776 B1 2021.11.30

### **Declarația privind asumarea răspunderii**

Subsemnatul, declar pe răspundere personală că materialele prezentate în teza de doctorat sunt rezultatul propriilor cercetări și realizări științifice. Conștientizez că, în caz contrar, urmează să suport consecințele în conformitate cu legislația în vigoare.

Siminel Nikita

Data

PERSONAL INFORMATION

**Nikita Siminel**

 (Moldova)  
 +373 6 769-34-65  
 siminel.n@gmail.com

Sex Male | Date of birth 17/11/1987 | Nationality Moldovan

STUDIES APPLIED FOR

**Studii de Doctorat**

WORK EXPERIENCE

- 08/2018–Present **Cercetător științific**  
 Institutul de Fizica Aplicata, Laboratorul Fizica Compușilor Semiconductori “Sergiu Rădăuțan”, Chisinau (Moldova)
- 08/2012–08/2016 **Cercetător științific**  
 Sheffield Hallam University, Materials and Engineering Research Institute, Sheffield (United Kingdom)  
**Chimia Computatională a materialelor de ambalare biodegradabile**
- 09/2007–06/2012 **Asistent de Cercetare**  
 Laborator acreditat „Cristale unice și stocuri pe baza lor”, Universitatea Nationala de Tehnologie și Cercetare "MISiS", Moscova (Russia)

EDUCATION AND TRAINING

- 2010–2012 **Studii de Master**  
 Universitatea Nationala de Tehnologie și Cercetare "MISiS" (Национальный Исследовательский Технологический Университет "МИСиС"), Moscova (Russia)  
**Teza:** "Proprietăți optice ale cristalelor de tantalat lantanum-galiu"  
**Facultatea:** Institutul de Materiale Noi și Nanotecnologii  
**Programul de studii:** Fizica Cristalului Opticii și Acoustoelectronicii
- 2006–2010 **Studii de licență**  
 Universitatea nationala de Tehnologie și Cercetare "MISiS" (Национальный Исследовательский Технологический Университет "МИСиС"), Moscova (Russia)  
**Facultatea:** Institutul de Materiale Noi și Nanotecnologii  
**Specializarea:** Fizica Tehnica

PERSONAL SKILLS

Mother tongue(s) Russian

Foreign language(s)

	UNDERSTANDING		SPEAKING		WRITING
	Listening	Reading	Spoken interaction	Spoken production	
Romanian	C1	C1	B2	B2	B2

English	C2	C2	C1	C1	C1
IELTS in 2012, score 7.5					

Levels: A1 and A2: Basic user - B1 and B2: Independent user - C1 and C2: Proficient user  
 Common European Framework of Reference for Languages

Digital skills	SELF-ASSESSMENT				
	Information processing	Communication	Content creation	Safety	Problem-solving
	Proficient user	Proficient user	Proficient user	Proficient user	Independent user

Digital skills - Self-assessment grid

ADDITIONAL INFORMATION

Publications

1. N.Kozlova; O.Buzanov; A.Kozlova; E.Zabelina; V.Shayapov; N.Siminel Radiation-induced defects and dichroism in  $\text{La}_3\text{Ga}_{5.5}\text{Ta}_{0.5}\text{O}_{14}$ , Radiation&Applications 2016 vol.1(3) 171-176, 10.21175/RadJ.2016.03.032
2. N.Kozlova; O.Buzanov; I.Didenko; A.Kozlova; N.Siminel; E.Zabelina Lanthanum-gallium tantalate: Heterogeneity and point defects, 12<sup>th</sup> Europhysical Conference on Defects in Insulating Materials 2015, 10.1088/1757-899X/80/1/012026
3. V.Verlan; I.Culeac; O.Bordian; V.Zubareva; I.Bulhac; M.Iovu; M.Enachescu; N.Siminel; V.Nedelea Luminescence Properties of a Novel  $\text{Eu}^{3+}$  Dinuclear Coordination Compound, 4<sup>th</sup> International Conference on Nanotechnologies and Biomedical Engineering 2019, 10.1007/978-3-030-31866-6\_33
4. N.Siminel; V.Nedelea; K.Sushkevich; A.Siminel; A.Micu; L.Kulyuk Radiative Recombination of Bound Excitons in  $\text{MoSe}_2/\text{I}_2$  Layered Crystals, 4<sup>th</sup> International Conference on Nanotechnologies and Biomedical Engineering 2019, 10.1007/978-3-030-31866-6\_55
5. N. Siminel Investigation into Interlayer Water Structure in  $\text{Na}^+$ - and  $\text{Ca}^{2+}$ -Montmorillonite: A Molecular Dynamics Study, 4<sup>th</sup> International Conference on Nanotechnologies and Biomedical Engineering 2019, 10.1007/978-3-030-31866-6\_135